

**EFFICIENCY ENHANCEMENT OF SOLUTION  
PROCESSABLE ORGANIC LIGHT EMITTING DIODES VIA  
CHARGE INJECTION AND TRANSPORT MODIFICATION**

**NOOR AZRINA BINTI HAJI TALIK SISIN**

**FACULTY OF SCIENCE  
UNIVERSITY OF MALAYA  
KUALA LUMPUR**

**2016**

**EFFICIENCY ENHANCEMENT OF SOLUTION  
PROCESSABLE ORGANIC LIGHT EMITTING  
DIODES VIA CHARGE INJECTION AND TRANSPORT  
MODIFICATION**

**NOOR AZRINA BINTI HAJI TALIK SISIN**

**THESIS SUBMITTED IN FULFILMENT OF THE  
REQUIREMENTS FOR THE DEGREE OF DOCTOR OF  
PHILOSOPHY**

**FACULTY OF SCIENCE  
UNIVERSITY OF MALAYA  
KUALA LUMPUR**

**2016**

To my family  
*For safekeeping my sanity*

University of Malaya

**UNIVERSITY OF MALAYA**

**ORIGINAL LITERARY WORK DECLARATION**

Name of Candidate: **NOOR AZRINA BINTI HAJI TALIK SISIN**

Registration/Matric No: **SHC120095**

Name of Degree: **DOCTOR OF PHILOSOPHY**

Title of ~~Project Paper/Research Report/Dissertation~~/Thesis (“this Work”):

Field of Study: **EXPERIMENTAL PHYSICS**

I do solemnly and sincerely declare that:

- (1) I am the sole author/writer of this Work;
- (2) This Work is original;
- (3) Any use of any work in which copyright exists was done by way of fair dealing and for permitted purposes and any excerpt or extract from, or reference to or reproduction of any copyright work has been disclosed expressly and sufficiently and the title of the Work and its authorship have been acknowledged in this Work;
- (4) I do not have any actual knowledge nor do I ought reasonably to know that the making of this work constitutes an infringement of any copyright work;
- (5) I hereby assign all and every rights in the copyright to this Work to the University of Malaya (“UM”), who henceforth shall be owner of the copyright in this Work and that any reproduction or use in any form or by any means whatsoever is prohibited without the written consent of UM having been first had and obtained;
- (6) I am fully aware that if in the course of making this Work I have infringed any copyright whether intentionally or otherwise, I may be subject to legal action or any other action as may be determined by UM.

Candidate’s Signature

Date: 6/9/2016

Subscribed and solemnly declared before,

Witness’s Signature

Date: 6/9/2016

Name:

Designation:

## ABSTRACT

This research work aims at improving the device efficiency of solution processed OLED and at the same time to do in-depth study on the device charge injection and transport. The first research project demonstrates high efficiency solution process red OLED device by doping small molecules 4,4',4''-tris(N-carbazolyl)-triphenylamine (TcTa) into Poly(9-vinylcarbazole) (PVK) as mixed hole-transporting hosts. The device performance increased from 2 cd/A to 4 cd/A. This is attributed to the energy barrier reduction and better charge balance in the device. The analysis of temperature-dependent hole mobility in PVK:TcTa film indicates that the energetic disorder of PVK:TcTA decreases with increasing concentration of TcTa implying that hole transport is predominately hopping among more ordered TcTa molecules even at low concentration. Second project presents the fabrication of tandem OLED device where a novel solution process charge-generating unit (CGU) using orthogonal solvents is demonstrated. The device efficiency of tandem device shows high current efficiency of 24.2 cd/A at 1000 cd/m<sup>2</sup>, which is more than three-folds higher than that of single device. This increment is attributed to the efficient CGU developed using PVK blended with 2 wt% of small molecule, 1-Bis[4-[N,N-di(4-tolyl)amino]phenyl]-cyclohexane (TAPC). The investigation on the CGU interface revealed that the energy barrier for hole injection from PVK:TAPC is reduced together with the increasing the hole carrier at the interface. The last project reports a novel solution processes Molybdate (MoO<sub>4</sub>) as a hole blocking and electron transport interlayer. It is shown that the efficiency of the Super Yellow-phenylenevinylene (SY-PPV) fluorescent-based devices is significantly improved. The improved device showed a current and luminance efficiency up to 22.8 cd/A and 14.3 lm/W respectively, which is more than two-fold higher compared to the control device. Such efficiency enhancement is attributed to the dual functions of MoO<sub>4</sub>, which serves as a good hole-blocking layer and at the same time able to transport electrons. Ultraviolet Photoelectron Spectroscopy (UPS) measurement shows that the deep lying valence band blocks the excessive holes from leaking into the cathode while low conduction band of MoO<sub>4</sub> allowing the electron to be injected from cathode. The observed dual functions of MoO<sub>4</sub> make transition metal oxide a very attractive candidate for interfacial modification in various organic electronic devices.

## ABSTRAK

Penyelidikan ini bertujuan untuk menambah baik kecekapan peranti OLED berasaskan larutan dan pada masa yang sama menjalankan kajian mendalam mengenai penyuntikan dan pergerakan cas. Projek kajian pertama menunjukkan peranti OLED berwarna merah berasaskan larutan mencapai kecekapan yang tinggi dengan mencampurkan material bermolekul kecil, 4,4',4''-tris(N-carbazolyl)-triphenylamine (TcTa) ke dalam polimer Poly(9-vinylcarbazole) (PVK) sebagai campuran hos penyunting lohong. Kecekapan peranti meningkat daripada 2 cd/A kepada 4 cd/A. Peningkatan ini adalah hasil penurunan aras penghalang tenaga untuk penyuntikan lohong dan juga disebabkan oleh keseimbangan cas di dalam peranti. Analisis pergerakan lohong bersandarkan-suhu di dalam campuran PVK:TcTa menunjukkan tenaga berselerak campuran menurun apabila kepekatan TcTa meningkat, menggambarkan bahawa penyuntikan lohong adalah melalui loncatan melalui susunan molekul TcTa walaupun pada kepekatan yang rendah. Projek kedua menunjukkan fabrikasi peranti berlapis OLED di mana unit penjanaan cas (CGU) berasaskan larutan yang baru menggunakan teknik pelarut orthogonal diperkenalkan. Peranti lapisan bertingkat OLED menunjukkan kecekapan maksimum peranti mencecah 24.2 cd/A pada  $1000 \text{ cd/m}^2$ , iaitu lebih tiga kali peningkatan berbanding dengan satu lapisan peranti OLED. Peningkatan ini adalah disebabkan oleh kecekapan CGU yang dihasilkan menggunakan campuran PVK dan 2 wt% material bermolekul kecil, 1-Bis[4-[N,N-di(4-tolyl)amino]phenyl]-cyclohexane (TAPC). Penyiasatan pada antara muka CGU menunjukkan aras penghalang tenaga untuk penyuntikan lohong pada PVK:TAPC dikurangkan dan pada masa yang sama, kepadatan cas lohong pada antara muka CGU di tingkatkan. Projek terakhir melaporkan larutan baru Molybdate ( $\text{MoO}_4$ ) sebagai lapisan pengantara bertujuan sebagai penghalang lohong dan membenarkan pergerakan elektron. Kecekapan peranti fluoresen Super Yellow-phenylenevinylene (SYPPV) telah meningkat secara signifikan kepada 22.8 cd/A dan 14.3 lm/W yang mana dua kali ganda tinggi daripada peranti kontrol. Peningkatan kecekapan ini adalah disebabkan oleh dwi-fungsi  $\text{MoO}_4$  iaitu sebagai penghalang lohong dan penyuntik elektron. Ukuran menggunakan Ultraviolet Photoelectron Spectroscopy (UPS) menunjukkan jalur valens yang dalam dapat menghalang lohong yang berlebihan daripada keluar melalui katod serta kedudukan jalur konduksi  $\text{MoO}_4$  di bawah katod membenarkan penyuntikan elektron dari katod. Dwi-fungsi  $\text{MoO}_4$  menjadikan logam transisi oksida sebagai bahan yang menarik untuk dijadikan pembolehubah antara permukaan yang boleh digunakan di dalam perbagai peranti organik elektronik.

## ACKNOWLEDGEMENTS

I would like to express my deepest gratitude to all those who gave me the possibility to complete this thesis. I would like to thank my supervisor, Dr. Woon Kai Lin whose suggestions and financial support helped me for the whole duration of research work and thesis writing up. I am deeply indebted to my co-supervisor, Dr. Yap Boon Kar for answering my countless questions, explaining the experimental setup, proof-reading this thesis and giving me encouragement as well as support in difficult times. I want to thank my group-mates and ex-group-mates, Mr. Calvin, Dr. Chua Chong Lim, Dr. Yeoh Keat Hoe and Mr. Wong Wah Seng for helping me throughout these years. I thank Dr. Thomas Whitcher for guiding me in analyzing synchrotron data. A really special mention goes to my lab mates in LDMRC, I do not have enough space to write your names, but you know who you are. You guys rocks!

Last but not least, I would like to thank my family especially my parents who give me the freedom to pursue my study. Thank you for your boundless love and support. Thank you. Arigatou!

## TABLE OF CONTENTS

<b>ABSTRACT</b> .....	<b>IV</b>
<b>ABSTRAK</b> .....	<b>V</b>
<b>ACKNOWLEDGEMENTS</b> .....	<b>VI</b>
<b>TABLE OF CONTENTS</b> .....	<b>VII</b>
<b>LIST OF FIGURES</b> .....	<b>X</b>
<b>LIST OF TABLES</b> .....	<b>XVI</b>
<b>LIST OF SYMBOLS AND ABBREVIATIONS</b> .....	<b>XVII</b>
<b>LIST OF APPENDICES</b> .....	<b>XXII</b>
<b>CHAPTER 1: INTRODUCTION</b> .....	<b>1</b>
1.1 Introduction .....	1
1.2 Motivations and objectives .....	2
1.3 Thesis Outline .....	3
<b>CHAPTER 2: LITERTURE REVIEW</b> .....	<b>6</b>
2.1 Introduction .....	6
2.2 Development of Organic Light Emitting Diodes Technology .....	6
2.2.1 Principles in Organic Light-Emitting Diodes.....	10
2.2.2 Charge recombination .....	13
2.2.2.1 Light emission in OLED device .....	13
2.2.2.2 Energy transfer in phosphorescent OLED.....	15
2.2.3 Charge carrier conduction in OLED device .....	17
2.2.3.1 Charge transport .....	19
2.2.3.1.1 Energetic disorder, $\sigma$ .....	19
2.2.3.1.2 Disorder Formalism for carrier transport .....	22
2.2.3.2 Charge injection.....	23
2.2.3.2.1 Injection limited current (ILC).....	23
2.2.3.2.2 Space-Charge-Limited Current (SCLC) .....	25
2.2.4 Electronic properties of organic interface .....	26
2.2.4.1 Metal/organic interface .....	27
2.2.4.2 Organic/organic interface .....	29
2.2.4.3 Internal charge transfer in mixed organic system.....	30
2.2.5 OLED structure .....	32
2.2.5.1 Single layer structure .....	32
2.2.5.2 Multilayer structure .....	34
2.2.5.3 Tandem Structure with Charge Generation Unit.....	36
<b>CHAPTER 3: METHODOLOGY</b> .....	<b>39</b>
3.1 Introduction .....	39

3.2	Substrate patterning process.....	39
3.3	Standard single OLED fabrication process .....	41
3.4	Electrical measurement .....	42
	3.4.1 Current density-Voltage-Luminance ( <i>J-V-L</i> ) measurement.....	42
	3.4.2 Time of Flight (ToF) Measurement .....	44
3.5	Optical measurement.....	46
	3.5.1 Absorption spectroscopy measurement.....	46
	3.5.2 Photoluminescence (PL) measurement .....	47
	3.5.3 Atomic Force Microscopy (AFM) measurement .....	48
	1.1.1 Dual Beam Focus Ion Beam (FIB).....	49
	3.5.4 Transmission Electron Microscopy (TEM) .....	50
	3.5.5 UPS/XPS measurement.....	51
	3.5.6 Inductively Coupled Plasma / Mass Spectrometry (ICP/MS).....	57
	<b>CHAPTER 4: EFFECT OF MIXED HOLE-TRANSPORTING HOST ON RED PHOSPHORESCENT OLEDs.....</b>	<b>58</b>
4.1	Introduction .....	58
4.2	Sample preparation for measurement.....	60
	4.2.1 Time of Flight (ToF) Measurement .....	60
	4.2.2 Energetic disorder, $\sigma$ measurement .....	60
	4.2.3 PhOLED device fabrication and measurement .....	62
4.3	Results and Discussions .....	63
	4.3.1 ToF mobility.....	63
	4.3.2 Mechanism of charge transport in PVK:TcTa mixture.....	67
	4.3.3 Energetic disorder, $\sigma$ .....	69
	4.3.4 Morphology via AFM topography .....	73
	4.3.5 Effect of blending system on Red PhOLED device efficiency.....	75
	4.3.6 Electroluminescence emission measurement .....	79
4.4	Chapter summary .....	80
	<b>CHAPTER 5: HIGH EFFICIENCY TANDEM OLEDs WITH FULLY SOLUTION PROCESSABLE CHARGE GENERATING UNIT.....</b>	<b>81</b>
5.1	Introduction .....	81
5.2	Experimental details.....	82
	5.2.1 Single and Tandem OLED device fabrication .....	82
	5.2.2 Charge generation unit (CGU) only device fabrication .....	85
5.3	Experimental results.....	87
	5.3.1 AFM topography images.....	87
	5.3.2 <i>J-V-L</i> characteristic of single and tandem devices .....	90
	5.3.3 Electroluminescence (EL) emission spectra .....	96

5.3.4 UV-Vis measurement.....	97
5.3.4.1 Transmittance of CGU.....	97
5.3.4.2 Validation of orthogonal film formation .....	98
5.3.5 Mechanism of charge generation and transport in CGU.....	100
5.3.5.1 <i>J-V</i> characterization .....	100
5.3.5.2 CGU hetero-junction interface study.....	101
5.3.5.2.1 HATCN <sub>6</sub> /PVK Interface.....	102
5.3.5.2.2 HATCN <sub>6</sub> /PVK:TAPC Interface.....	105
5.3.5.2.3 Discussion .....	108
5.4 Chapter summary .....	108
<b>CHAPTER 6: SOLUTION PROCESSABLE MOLYBDATE AS A CATHODE INTERLAYER FOR SUPER YELLOW OLEDs.....</b>	<b>110</b>
6.1 Introduction.....	110
6.2 Experimental procedure .....	112
6.3 Results and discussions .....	115
6.3.1 Atomic concentration .....	115
6.3.2 OLED Device performance.....	116
6.3.2.1 Full device performance .....	116
6.3.2.2 Single carrier device performance .....	121
6.3.3 Energy level.....	123
6.3.3.1 SYPPV/MoO <sub>4</sub> interfaces .....	123
6.3.3.2 SYPPV/MoO <sub>4</sub> /LiF/Al interfaces .....	127
6.3.4 AFM morphology.....	128
6.4 Chapter summary .....	129
<b>CHAPTER 7: CONCLUSION AND FUTURE RECOMMENDATION .....</b>	<b>130</b>
7.1 Conclusion .....	130
7.2 Future works .....	133
<b>REFERENCES.....</b>	<b>134</b>
<b>LIST OF PUBLICATIONS AND PAPERS PRESENTED .....</b>	<b>151</b>
<b>APPENDIX A .....</b>	<b>153</b>
<b>APPENDIX B.....</b>	<b>154</b>
<b>APPENDIX C .....</b>	<b>155</b>
<b>APPENDIX D .....</b>	<b>156</b>
<b>APPENDIX E.....</b>	<b>157</b>

## LIST OF FIGURES

Figure 2.1 Energy level diagram of a simple typical OLED structure. $E_h$ and $E_e$ at the cathode and anode respectively refer to the injection barriers for hole and electron into the emissive layer. IP represents the ionization potential of emissive layer material. EA stands for electron affinity, indicating on how capable a material is to bind an electron. ....	11
Figure 2.2 The physical processes involve in organic materials electroluminescence. ...	12
Figure 2.3 Jablonski diagram depicting the energy transfer for the fluorescence and phosphorescence of organic material. $S_0$ , $S_1$ and $T_1$ are the ground state, singlet and triplet excited state respectively. $\kappa_{ISC}$ , $\kappa_F$ and $\kappa_P$ are the rate of intercrossing, fluorescence emission rate and phosphorescence emission rate respectively.....	15
Figure 2.4 Förster energy transfer process. ....	16
Figure 2.5 Two different energy transfers in Dexter energy transfer process. ....	17
Figure 2.6 Schematic representation of the molecular orbital splitting and quasi-continuous bands of occupied and unoccupied states in pi-conjugated materials. Adapted from (Schols, 2011). ....	18
Figure 2.7 Density of states (DOS) distribution in disorder organic material. The charge transport sites are represented as discrete states (shown as dashes). ....	20
Figure 2.8 Schematic diagram of hopping transport in an organic semiconducting device. ....	21
Figure 2.9 Energy diagram of a semiconductor showing definition of band edges (CBM/LUMO and VBM/HOMO), vacuum level $E_{VAC}$ , work function (WF), energy gap ( $E_g$ ), ionization potential (IP) and electron affinity (EA).....	27
Figure 2.10 Metal/organic semiconductors interface (a) before and (b) after making contact. ....	28
Figure 2.11 Multilayer OLED device with organic-organic heterojunction formed between hole transport layer/emissive layer/electron transport layer. ....	30
Figure 2.12 The internal interface charge transfer doping model; (a) spatial model and (b) development of the corresponding band energy diagram separating dipole formation and thermodynamic Fermi level equalization where band bending has been neglected. $E_{FM}$ and $E_{FD}$ are the Fermi level position, free of substrate influence. Adapted from (T. Mayer et al., 2012). ....	32

Figure 2.13 (a) Typical single layer OLED device structure built-up from patterned ITO anode electrode, emissive layer (organic material) and Al cathode (b) The energy levels for the structure. Adapted from (Koch, 2007).....	33
Figure 2.14 (a) Energy level diagram and (b) device structure of multilayer OLED device. In this device, PEDOT: PSS is used as HTL and 2,7 bis(diphenylphosphoryl)-9,9'-spirobifluorene (SPPO13) as ETL. The cathode consists of LiF/Al.....	36
Figure 2.15 An example of tandem OLED structure and respective energy level used in this thesis research work. The first and second unit of single structure is connected with CGU unit in the intermediate structure. ....	37
Figure 2.16 Energy level alignment for charge generation unit in tandem at different conditions, where (a) when no external bias applied, (b) forward bias condition (recombination) and (c) reverse bias (charge generation) adapted from (Kröger et al., 2007). ....	38
Figure 3.1 (a) Standard patterned ITO substrate used in experimental work, (b) The dimension of the pattern used for ITO patterning and (c) photolithography mask used.	40
Figure 3.2 Standard OLED fabrication process. Adapted from <a href="http://www.ossila.com/pages/organic-photovoltaic-opv-and-organic-light-emitting-diode-oled-fabrication-manual">http://www.ossila.com/pages/organic-photovoltaic-opv-and-organic-light-emitting-diode-oled-fabrication-manual</a> .....	42
Figure 3.3 Schematic diagram of J-V-L laboratory set-up. ....	43
Figure 3.4 Typical <i>J-V-L</i> characteristic of the OLED device. ....	43
Figure 3.5 ToF measurement laboratory set-up. The figure also depicted the principle on measuring time transit ( $t_{tr}$ ) from the sample (polymer), where $t_{tr}$ is the time where the first sheet charge arrived at the counter electrode.....	45
Figure 3.6 Typical transient photoconductivity of ToF measurement. (a) A double linear graph with (i) Ideal ToF profile (ii) Non-dispersive transient and (iii) dispersive ToF signal, whereas (b) Double log of dispersive transient ToF transient.....	46
Figure 3.7 Schematic diagram of the typical operation principle of UV-Vis spectroscopy.....	47
Figure 3.8 Schematic diagram of PL measurement technique for LS50B spectrometer.	48
Figure 3.9 Film morphology in (left) 3D and (right) 2D measured using AFM tapping mode.....	49
Figure 3.10 (a) Illustration of H-bar FIB technique. Material on opposite sides of area of interest is FIB-milled until it is electron transparent for TEM measurement. (b) SEM	

image showing a sample that was mechanically thinned and glued to TEM half grid. Adapted from (J. Mayer et al., 2011). .....	50
Figure 3.11 (Left) Schematic diagram of the basic operation of XPS/UPS measurement. (Right) The excitation of an individual electron from the energy level to the vacuum level. ....	52
Figure 3.12 Example of XPS peak of Molybdenum trioxide ( $\text{MoO}_3$ ) where the spin-orbital coupling of $3d_{5/2}$ and $3d_{3/2}$ can be determined. ....	53
Figure 3.13 Principle of UPS adapted from (H. Ishii & Seki, 1997). The left is the UPS spectra for metal (Au) . The right is the spectra for organic layer deposited on the metal (Au) substrate. ....	55
Figure 3.14 Example of UPS measurement to determine the material electronic energy levels. ....	56
Figure 3.15 The relative energy diagram constructed from the data in Figure 3.14. ....	56
Figure 3.16 ICP/MS instrumental setup. ....	57
Figure 4.1 The (a) energy levels and (b) device structure fabricated in the experimental works. ....	63
Figure 4.2 Transient photoconductivity of pure PVK thin films. The transient was captured at 300 K and at the electric field of $6.7 \times 10^5$ V/cm. A featureless signal could indicate a dispersive hole transport shown in the double linear plot (inset). Thus, a double logarithmic curve was plotted to find the plateau, which corresponds to the transit time of the hole transport. ....	64
Figure 4.3 Mobility vs. $E^{1/2}$ result curves for 0 wt %, 10 wt %, 20 wt % , 30 wt % and 50 wt % concentrations for temperature range 200 K to 340 K. ....	66
Figure 4.4 Extrapolated hole mobility of TcTa and PVK blended with TcTa concentration varied from 0 wt % to 50 wt % in room temperature at $1 \times 10^6$ V/cm <sup>2</sup> . ..	67
Figure 4.5 Four different regimes in host-guest system. Adapted from (Yimer et al., 2009). ....	69
Figure 4.6 $\ln \mu$ vs. $E^{1/2}$ curves for 0 wt %, 10 wt % , 20 wt % , 30 wt % and 50 wt % concentrations when subjected to temperatures range 200 K to 340 K. ....	70
Figure 4.7 (a) $\ln \mu_0$ vs. $1/T^2$ for 0 wt %, 10 wt % , 20 wt % , 30 wt % and 50 wt % concentrations of TcTa (red line is the fitted line for reference) (b) $\sigma$ versus concentration of TcTa (0 wt % to 50 wt %). ....	71

Figure 4.8 (i) 2D morphology and (ii) phase image of thin film of (a) pristine PVK (0 wt%), (b) mixed hosts with 5 wt% TcTa and (c) pristine TcTa (100 wt%).....	74
Figure 4.9 Current density-Voltage-Luminance characteristics of the red devices fabricated with different TcTa concentrations ( 0 wt % - 100 wt %) .....	76
Figure 4.10 (a) Current Efficiency versus Current Density of the devices. (b) Power Efficiency versus Current Density of the devices. ....	77
Figure 4.11 The current density of hole only devices with different concentrations of TcTa. ....	78
Figure 4.12 Normalized electroluminescence of red devices with 0 to 100 wt% TcTa concentrations together with normalized photoluminescence intensity of TcTa and PVK in the equal mixture (red line shown inset).....	80
Figure 5.1 (a) Device structures and (b) chemical structures of the material applied in this work.....	84
Figure 5.2 Schematic diagram of the fabricated CGU device. HATCN <sub>6</sub> has a strong electron affinity, hence electron from PVK: TAPC is easily removed and injected into cathode. PEDOT: PSS is used to provide a high conductivity path for holes while SPPO13:Cs <sub>2</sub> CO <sub>3</sub> assists the electron injection into cathode. Considering the high conductivity of the PEDOT: PSS and SPPO13: Cs <sub>2</sub> CO <sub>3</sub> layers, most voltage drop would have been originated from the PVK:TAPC/ HATCN <sub>6</sub> heterojunction. ....	86
Figure 5.3 3D (left) and 2D (right) AFM images of (a) PVK, (b) PVK: TAPC (1 wt %), (c) PVK: TAPC ( 2 wt %), (d) PVK: TAPC ( 10 wt %), (e) Al/HATCN <sub>6</sub> and (f) Al/HATCN <sub>6</sub> /PVK: TAPC (2 wt %). ....	89
Figure 5.4 (a) Brightness vs. voltage and (b) Current density vs. voltage of single and tandem devices. ....	91
Figure 5.5 (a) Current efficiency vs. brightness and (b) Power efficiency vs. brightness of single and tandem devices. ....	93
Figure 5.6 The energy levels for the full tandem devices. ....	94
Figure 5.7 The normalized electroluminescent (EL) spectra of the single unit and the tandem OLED with 2 wt % TAPC in PVK viewed in the normal direction at voltage of 12 V. ....	97
Figure 5.8 Optical transmittance of charge generating layer consists of Al / HATCN <sub>6</sub> / PVK: TAPC (2 wt%) spin coated on top of glass. ....	98

Figure 5.9 (a) HATCN <sub>6</sub> dissolved in acetonitrile absorbance spectrum before and after wash with chlorobenzene, (b) PVK: TAPC (2 wt %) film absorption before and after solubility tests. ....	99
Figure 5.10 Log-log curves for J-V characteristic of 0 wt% and 2 wt% TAPC. Both devices exhibits ohmic and SCLC regions as shown by the red and blue lines respectively. ....	101
Figure 5.11 XP spectra of nitrogen, N1s lines at HATCN <sub>6</sub> /PVK interface with varying PVK film thickness. ....	102
Figure 5.12 UP spectra of the HATCN <sub>6</sub> /PVK interface with varying PVK thickness. (a) HECO and (b) LECO representing the work function and HOMO level respectively. (c) Full diagram of the HATCN <sub>6</sub> /PVK interface mapped out from UPS and XPS spectra. ....	104
Figure 5.13 Tauc plot from absorbance spectrum to calculate energy band gap for PVK and PVK:TAPC.....	105
Figure 5.14 XP spectra of the nitrogen N1a lines at HATCN <sub>6</sub> /PVK interface with varying PVK:TAPC film thickness.....	106
Figure 5.15 UP spectra of the HATCN <sub>6</sub> /PVK:TAPC interface with varying PVK thickness. (a) HECO and (b) LECO representing the work function and HOMO level respectively. (c) Full diagram of the HATCN <sub>6</sub> /PVK:TAPC interface mapped out from UPS and XPS spectra. ....	107
Figure 6.1 MoO <sub>3</sub> in (a) DI water and (b) diluted NaOH and DI water solution forming molybdate solution. ....	112
Figure 6.2 Photoluminescence of the SYPPV/ MoO <sub>4</sub> thin film indicates negligible change of the spectra shape indicating minimum damage to the SYPPV. ....	115
Figure 6.3 (a) Wide XPS spectra and (b) the narrow scan and deconvolution of Mo 3d <sub>3/2</sub> , 3d <sub>5/2</sub> .....	116
Figure 6.4 Current Efficiency-Brightness-Power efficiency, (b) Current density versus Voltage of the devices. ....	117
Figure 6.5 Electroluminescence (EL) emission for the device with and without MoO <sub>4</sub> . ....	118
Figure 6.6 (a) Current Efficiency-Brightness-Power efficiency, (b) Current density versus Voltage of the fabricated devices.....	119
Figure 6.7 The device performance fabricated with only NaOH and MoO <sub>4</sub> . ....	120

Figure 6.8 (a) Current Efficiency-Brightness-Power efficiency, (b) Current density versus Voltage of the devices with different MoO <sub>4</sub> concentrations; 0.5 wt%, 0.25 wt %, 0.15 wt %.	121
Figure 6.9 Single carrier dominating devices. The hole current in hole dominating device (ITO/PEDOT:PSS/SY-PPV/MoO <sub>4</sub> /Au) decreases as MoO <sub>4</sub> is added. The electron current is almost the same as MoO <sub>4</sub> is added (device (ITO/LiF/SY-PPV/MoO <sub>4</sub> /LiF/Al).	122
Figure 6.10 UPS spectra of (a) secondary electron cutoff (SEC) region (b) The valence band maximum (VBM) region of SYPPV/MoO <sub>4</sub> .	124
Figure 6.11 The energy levels of MoO <sub>4</sub> on top of SYPPV mapped out from UPS measurement.	125
Figure 6.12 Full energy alignment diagram of SY-PPV/ MoO <sub>4</sub> /LiF/Al interfaces showing the mechanism of electron injection from the cathode into the emissive layer.	127
Figure 6.13 AFM surface morphology of (a) SYPPV, (b) MoO <sub>4</sub> and (c) SYPPV/MoO <sub>4</sub> spin coated on top of glass.	128

## LIST OF TABLES

Table 2.1 Summary of the works that contributes to the OLED technology. ....	9
Table 2.2 Low work function metals used as cathode in organic device. ....	34
Table 4.1 Parameters for hole transport in pure PVK and PVK: TcTa extracted from data in Figure 4.7 (a). ....	72
Table 5.1 Values of $R_S$ from AFM measurements for different concentration of TAPC in PVK. ....	90
Table 5.2 Device efficiency of the fabricated devices in this work. ....	96
Table 5.3 Thickness variation measured using Profilometer. ....	100
Table 7.1 The comparison of fabricated OLED device in this thesis work with the literature. ....	132

## LIST OF SYMBOLS AND ABBREVIATIONS

AFM	:	Atomic Force Microscopy
Al	:	Aluminum
Alq <sub>3</sub>	:	Tris(8-hydroxyquinolino)aluminum
Au	:	Gold
BE	:	Binding Energy
BHJ	:	Bulk heterojunction
Ca	:	Calcium
CBM	:	Conduction Band Minimum
CGL	:	Charge Generating Layer
CGU	:	Charge Generating Unit
CIE	:	Commission internationale de l'Eclairage
CsF	:	Cesium Fluoride
CT	:	Charge transfer
CuPC	:	Copper phthalocyanine
C <sub>60</sub>	:	Fullerene
DOS	:	Density of State
EA	:	Electron Affinity
EIL	:	Electron Injection Layer
E <sub>F</sub>	:	Fermi Level Energy
E <sub>g</sub>	:	Optical Band gap
EL	:	Electroluminescence
ETL	:	Electron Transport Layer
FIB	:	Focus Ion Beam
FN	:	Fowler-Nordheim

F <sub>4</sub> -TCNQ	:	2,3,5,6-Tetrafluoro-7,7,8,8-tetracyanoquinodimethane
FESEM	:	Field Emission Scanning Electron Microscopy
GDM	:	Gaussian Disorder Model
HATCN <sub>6</sub>	:	1,4,5,8,9,11-hexaazatriphenylene hexacarbonitrile
HBL	:	Hole Blocking Layer
HECO	:	High energy cut-off
HOMO	:	Highest Occupied Molecular Orbital
HTL	:	Hole Transport Layer
ICP/MS	:	Inductively coupled plasma mass spectroscopy
ICT	:	Integer charge transfer
ID	:	Interface dipole
IE	:	Ionization Energy
ILC	:	Injection limited current
IPA	:	Isopropyl Alcohol
IP	:	Ionization Potential
Ir(piq) <sub>2</sub> (acac)	:	bis(1-phenyl-isoquinoline)(acetylacetonato)iridium(III) (
Ir(ppy) <sub>3</sub>	:	fac-tris(2-phenylpyridine)iridium
ISC	:	Intersystem crossing
ITO	:	Indium Tin Oxide
J-V-L	:	Current density-Voltage-Luminance
KE	:	Kinetic energy
LECO	:	Low energy cut-off
LEU	:	Light-Emitting Unit
LiF	:	Lithium Fluoride
Liq	:	8-hydroxyquinolatithium
LUMO	:	Lowest Unoccupied Molecular Orbital

MA	:	Miller-Abrahams
MoO <sub>3</sub>	:	Molybdenum tri-Oxide
NaOH	:	Sodium Hydroxide
NPB	:	N-(1-1-naphtyl)-N-phenyl-amino]biphenyl
OH	:	Hydroxyl
OLED	:	Organic Light Emitting Diode
OOH	:	Organic-Organic Heterojunction
OXD-7	:	1,2,5-oxadiazole
PBD	:	2-(4-biphenyl)-5-(4-tert-butylphenyl)-1,3,4 oxadiazole
PEDOT:PSS	:	Poly(3,4 -ethylenedioxy-thiophene) –Poly (styrene sulfonate)
PL	:	Photoluminescence
Poly-TPD	:	poly(4-butylphenyl- diphenyl-amine
PPV	:	poly-(para-phenylene vinylene)
PtOEP	:	2,3,7,8,12,13,17,18-octaethyl-21H,23H-porphine platinum
PVK	:	Poly(9-vinylcarbazole)
P3HT	:	Poly(3-hexylthiophene)
RS	:	Richardson-Schottky
SCLC	:	Space-Charge-Limited Current
SOC	:	Spin orbital coupling
SPPO13	:	2,7-bis(diphenylphosphoryl)-9,9'-spirobifluorene
SY-PPV	:	Super Yellow-phenylenevinylene
TAPC	:	1,1-bis-(4-bis(4-tolyl)-aminophenyl) cyclohexene
TcTa	:	4,4',4''-tris(N-carbazolyl)-triphenylamine
TEM	:	Transmission Electron Microscopy
ToF	:	Time-of-Flight
TMO	:	Transition Metal Oxide

TPD	:	N-N- diphenyl-N,N'bis (3-methylphenyl)-1,1'-biphenyl-4-4'-diamine
UHV	:	Ultra-high vacuum
UPS	:	Ultraviolet Photoelectron Spectroscopy
UV-Vis	:	Ultraviolet-visible
XPS	:	X-ray Photoemission Spectroscopy
mm	:	Millimeter
VBM	:	Valence Band Maximum
V	:	Voltage
$\mu\text{m}$	:	Micrometer
nm	:	nanometer
$\Phi$	:	Work function
$\sigma$	:	Energetic Disorder
$\mu$	:	Mobility
wt %	:	Weight percentage
hv	:	Energy of incident photon
$\alpha$	:	Absorption coefficient
eV	:	Electron volt
$\eta_{\text{EQE}}$	:	Electroluminescence quantum efficiency
$\gamma$	:	Charge carrier balance
$\eta_{\text{st}}$	:	Fraction of spin-allowed excitons
$q_{\text{eff}}$	:	Effective quantum efficiency of emitting material
$\eta_{\text{out}}$	:	Optical out-coupling efficiency
$\mathcal{K}_{\text{ISC}}$	:	Rate of intercrossing
$\mathcal{K}_{\text{P}}$	:	Fluorescence emission rate
$\mathcal{K}_{\text{F}}$	:	Phosphorescence emission rate

$\varepsilon$	:	Site energy relative to the center of the density of state
$N_0$	:	Total density of states
$d$	:	Film thickness
$\beta$	:	Poole-Frenkel slope
$E$	:	Electric field
$\mu_0$	:	Mobility extrapolated to zero field.
$\phi_B$	:	Interface potential barrier height
$\varepsilon_0$	:	Vacuum permittivity
$\varepsilon_r$	:	Organic dielectric constant
$k_B$	:	Boltzmann's constant
$q$	:	Elementary electronic charge
$T$	:	Absolute temperature
$m^*$	:	Free electron mass
$h$	:	Planck's constant
$E_h$	:	Hole injection barrier
$E_e$	:	Electron injection barrier
$S_0$	:	Ground state
$S_1$	:	Singlet state
$T_1$	:	Triplet state

## LIST OF APPENDICES

Appendix A	TEM for thickness measurement.....	156
Appendix B	High-resolution optical microscopy for SYPPV and SYPPV/ MoO <sub>4</sub> film.....	157
Appendix C	ICP/MS measurement for MoO <sub>4</sub> .....	158
Appendix D	Band gap measurement using Tauc Plot.....	159
Appendix E	XPS for O1s peak for MoO <sub>4</sub> film.....	160

University of Malaya

## CHAPTER 1: INTRODUCTION

### 1.1 Introduction

The initial breakthrough of organic electroluminescence in the 1960's has become a great catalyst for the development for organic light emitting diode (OLED) device. The underlying of this discovery is the realization that the intrinsic properties of the organic materials and the related interfaces determine the performance of the OLED devices. The performance of highly efficient OLED device depends on several key factors namely the charge-carrier transport, carrier injection, charge balance, charge confinement as well as optical out-coupling in the device. There have been considerable studies done to gain understanding and knowledge about this subject in the past. There is a need for more works required to further improve the performance of the device. In order to achieve this goal, proper understanding on the electrical conduction mechanism as well as the interfaces in these materials is urgently needed.

One of the widely used classes of organic materials is polymer, which has large molecular weight having a carbon-chain backbone such as poly (N-vinyl carbazole) (PVK). Its ability to form a very good film with good solubility in organic solvent rendering the solvent a very attractive choice. The other widely used material is small-molecules, which has lower molecular weight and fewer organic functional groups compared to polymer. Small-molecules have the advantage over polymer with higher mobility, stability, and efficiency (fabricated by thermal evaporation). However, this class of material suffers from intrinsic problems such as low solubility and the tendency to crystallize especially when the solution-processable technique is used. Polymer-small molecule mixture based OLED has been successfully demonstrated with enhanced

device performance. However, in-depth study, especially on the mixture concentration and electronic structure, are still interesting to look into.

Thermal evaporation technique exhibits a critical drawback due to expensive multiple vacuum deposition equipment used. Thus the exploration for solution-processable materials draws wide interest in this research area. In conventional OLED device, there is at least one active organic electronic material presented, where the energy barrier exists only between the electrodes. In multilayer OLED such as tandem OLED, there will be energy barrier between the electrodes as well as the transporting layers that will block the carrier injection as well as ohmic loss due to intrinsic insulating behavior of organic semiconducting materials.. Thus, maximizing the carrier injection and transport simultaneously minimizing the energy loss becomes a challenge in fabricating the organic device.

## **1.2 Motivations and objectives**

To date, organic semiconductor materials are surpassing inorganic material in a large-area and low-cost production of optoelectronics field owing to their wide range tailor-made materials. The OLED device has in fact already been in consumer market quite for a quite a while, especially for display applications. Considering lighting applications, OLED device gains much attention due to its profound feature such as lightweight, non-glaring, flexible (bending) as well as environmentally friendly (mercury-free). White OLED has been demonstrated to be on par with widely used fluorescent tube (Reineke et al., 2009). However, the process for device fabrication suffers from high-cost and fabrication complexity. Solution process seems to be a better candidate than conventional vacuum deposition process. However, not many works thus far demonstrated the high device efficiency of OLED devices via solution process. Thus, the research works presented in this thesis focus on enhancing the solution-

processable OLED device via different structures as well as the materials.

The objectives of the research work presented in this thesis are:

- i- To investigate the effect in charge injection and transport at the anode/EML interface by doping small molecule materials in the emissive layer and to study the charge transport characteristic in PVK:TcTa blending mixture.
- ii- To study the effects of mixing co-host in p-type charge generation unit (CGU) in solution processed tandem OLED device. Efficiency enhancement in term of charge generation, charge injection and charge transport at CGU interface (doped p-type / n-type) is investigated.
- iii- To improve device efficiency via solution process Molybdate ( $\text{MoO}_4$ ) as hole blocking and electron transporting layer and to study the interface of SYPPV/ $\text{MoO}_4$ /LiF/Al.

### 1.3 Thesis Outline

This thesis covers 6 chapters that discuss the effects of modifying charge injection and transport material at the interface and the effects in OLED device efficiency. The history of organic electroluminescence and the overview of OLED research that has been done to date are briefly discussed in Chapter 1. In addition to that, the motivations, as well as the objectives of this research study, are also presented.

In Chapter 2, the introduction to organic semiconductors such as the electronic structures, energy levels and the energy transfer of the materials are discussed. The theoretical background, the operation principles of the OLED device as well as the fabrication process are also included in detail. This chapter ended with discussions of charge transfer and transport mechanism as well as the interface involved in the OLED device.

Chapter 3 describes the general preparation of OLED devices as well as the experimental techniques involved in this study. The background theory of each experimental approach is briefly explained.

The results disclosed in this thesis are presented in three different chapters starting with Chapter 4. Chapter 4 reports the effects of adding small molecule material, tris(4-carbazoyl-9-ylphenyl)amine (TcTa) as hole transporting co-hosts material in the emissive layer. The effect of co-hosts on the hole injection layer and the improvement on device efficiencies are also presented. The temperature dependent mobility via ToF was studied to describe the mobility, energetic disorders and their effects on device efficiencies. In addition to that, the effects of film morphology as well as the energy barrier for hole injection on the OLED device is also discussed.

Chapter 5 demonstrates the improvement of tandem green phosphorescent OLED device by utilizing doped p-type/n-type charge generation units (CGU) heterojunction. The improvement has been made when the p-type CGU, PVK is co-doped with small molecule material; 1,1-bis-(4-bis(4-tolyl)-aminophenyl) cyclohexene (TAPC). The focus is to investigate the effects of doping small concentration of TAPC in p-type CGU layer on the charge generation, injection as well as the transport properties, which are closely related to the tandem OLED efficiencies. The energy alignments for both doped and un-doped layer are also presented.

Chapter 6 is dedicated to address the effects of a solution process Molybdate ( $\text{MoO}_4$ ) as hole blocking layer (HBL) in the hole-driven OLED device (SY-PPV). The device improvement is discussed on the relation of EML/HBL/cathode interfaces. This chapter also presents one of the highest efficiency solution process-able yellow fluorescent to date.

Finally, Chapter 7 summarized the overall research work done in this thesis and the possible future works to further improve the OLED device.

University of Malaya

## CHAPTER 2: LITERTURE REVIEW

### 2.1 Introduction

This chapter discusses the organic materials used and the physics behind organic light emitting diodes (OLED) in-depth. Firstly, the history of the OLED device is presented in order to describe the initial developments that have been carried out as well as materials development utilized in the OLED device. The basic principles in OLED device include the charge transport and injection, charge recombination, energy transfer and the interface energy level alignment. These are discussed in this chapter. This chapter ends with explanation of the device structure, typically used in OLED device.

### 2.2 Development of Organic Light Emitting Diodes Technology

In 1963, Martin Pope *et al* created the first organic light emitting diodes (OLEDs) using anthracene crystal (Pope, Kallmann, & Magnante, 1963). Following that, in 1965, Helfrich and Schneider observed EL by utilizing anthracene crystal of 1 mm to 5 mm thick as EL layer. However, this device required several hundred volts to operate due to the thicker layer used (Helfrich & Schneider, 1965). This discovery did not gain much interest due to the high voltage needed. In 1982, Vincent *et.al* demonstrated a low operating voltage of anthracene-based EL device by reducing the thickness to 0.6  $\mu$ m. This reduces the working voltage to 30 V (Vincett, Barlow, Hann, & Roberts, 1982). However, despite the thinner EL film used, the device quantum efficiency was still very low, which was less than 1 %.

A major development was then presented by C.W Tang and S.A Van Slyke in 1987, where an organic light emitting diode based on tris(8-hydroxyquinolinato)aluminum ( $\text{Alq}_3$ ) together with N-N- diphenyl-N,N'bis (3-

methylphenyl)-1,1'-biphenyl-4,4'-diamine (TPD) was demonstrated. The device has a brightness of over  $1000 \text{ cd/m}^2$  with a low driving voltage and an external efficiency of 1% (Tang & VanSlyke, 1987). This was the first work that initiated the reduction in operation voltage and improvement in device efficiency, which led to the huge development in OLED until today. Subsequently, in 1988, multilayer OLED was presented by Adachi *et.al.* The active layer is sandwiched between the electron transport layer (ETL) and hole transport layer (HTL) (Adachi, Tokito, Tsutsui, & Saito, 1988).

In 1990, the first polymer LED (PLED) was demonstrated by Burroughess *et.al* at the Cavendish Laboratory in Cambridge. The device was fabricated using precursor conjugated polymer poly-(para-phenylene vinylene) (PPV) by spin coating the polymer on top of indium tin oxide (ITO) (Burroughes et al., 1990). This work also added a new discovery in OLED development by using a wet process to fabricate device. In 1992, Heeger and co-workers showed that OLED device can be fabricated on a plastic substrate rather than a glass substrate (Cao, Treacy, Smith, & Heeger, 1992; Gustafsson et al., 1992). Another great discovery was made by Forrest *et.al.*, where they found that phosphorescent dyes are capable of converting both singlet and triplet excitons into light resulting in a higher efficiency with quantum efficiency less than 25 % (Gu, Shen, Burrows, & Forrest, 1997). Following the ideas of the phosphorescent material, in 1998, Baldo *et.al* showed the first phosphorescent OLED (PhOLED) generated using phosphorescent organometallic dopants, (PtOEP) doped into Alq<sub>3</sub> layer (M. A. Baldo et al., 1998). In 2002, Huang *et.al* demonstrated the idea of p-type doped HTL and n-type doped ETL in p-i-n structure. The device exhibited a high luminance and efficiency at a low operating voltage (J. Huang et al., 2002). The development of device efficiency continued as Reineke's group later showed that WOLED device is comparable to a fluorescent tube with device efficiency up to  $90 \text{ lm/W}$  at  $1000 \text{ cd/m}^2$  (Reineke et al., 2009).

In term of OLED fabrication process, vacuum deposition method is still in demand compared to the wet process. Vacuum deposition processes enable few layers to be deposited on top of each other without removing the under layer and thus open up numerous ways to manipulate the structure in order to increase device efficiency. For example, the first white OLED (WOLED) consists of a tri-layer device with each layer emitting red, blue and green emission respectively, has been successfully demonstrated via vacuum deposited process (J Kido, Kimura, & Nagai, 1995). Wet processing methods such as spin-coating, blade coating as well as inkjet printing are cheaper compared to costly vacuum deposition process and can be easily incorporated in flat panel, flexible displays technologies and ambient light sources. However, the main challenge for solution process method is the solubilization limitation where in multi-layer device the upper layer wash out or mixed with the underneath layer. In order to achieve multilayer structures via solution process, researcher has applied orthogonal solvents, for example, the water/alcohol as orthogonal solvents (Gong, Wang, Moses, Bazan, & Heeger, 2005; F. Huang, Shih, Shu, Chi, & Jen, 2009; Ye, Shao, Chen, Wang, & Ma, 2011). Cross-linking after deposition of the layer has been explored in order to provide a material with a covalently bound structure that is highly resistant to the processing solvent (B. Ma et al., 2007; Png et al., 2010; Yang, Müller, Neher, & Meerholz, 2006; Zhong, Liu, Huang, Wu, & Cao, 2011).

The common organic materials used can be divided into polymers and small molecules. Unlike polymer suffers that from the reproducibility, poly-dispersity, as well as the difficulty to purify, small molecule tend to be easier to synthesize and purified (Ahn et al., 2012; Brown et al., 2003; Deng et al., 2006). Using small molecule material, Jou *et al.* demonstrated high efficiency solution processed single WOLED. The maximum efficiencies of the fabricated device ranging from 1.4 to 5.6 lm/W (brightness from 4400 to 15 2000 cd/m<sup>2</sup>) by varying small molecule as hosts in the co-

doped red, green and blue emissive layer. This work showed that small molecule host outperformed polymer host which exhibits maximum efficiency of merely 0.9 lm/W (3060 cd/m<sup>2</sup>). This enhancement is attributed to the small molecule materials that exhibit low electron injection energy barrier from the hole blocking layer and high hole energy barrier to the emissive layer (Jou, Sun, Chou, & Li, 2005). Other than using single host, Jou's group also reported the use of binary hosts of 4,4'-bis(carbazol-9-yl)biphenyl (CBP) which is small molecule host and blue light emitting polyfluorene-derived copolymer of poly[9,9-dioctylfluorenyl-2,7-diy]alt-co-(9-hexyl-3,6-carbazole) (PF-9HK) as assisting host in the emissive layer. The green and red dopants were also doped in the emissive layer to produce WOLED with maximum efficiency of 4.2 lm/W at 802 cd/m<sup>2</sup>. This is due to the additional host (PF-9HK), which halves the energy barrier for holes to be injected into the emitting zone (Jou, Sun, Chou, & Li, 2006). Table 2.1 summarized the works that been explained in this section.

**Table 2.1** Summary of the works that contributes to the OLED technology.

OLED works (novelty)	Method used	Device performance	References
The first work on reduction in driving voltage using ITO/Diamine /NPD/Mg:Ag structure	Vacuum deposit	1.5 lm/W, 1000 cd/m <sup>2</sup> with driving voltage below 10 V.	Tang & VanSlyke, 1987
Multilayer OLED with structure Mg/TPD/EML/PV/Au	Vacuum deposit	Applied voltage 60 V for light emission.	Adachi, Tokito, Tsutsui, & Saito, 1988
First polymer LED (PLED) using PPV.	Vacuum deposit	EQE ~8%	Burroughes et al., 1990
Flexible LED using soluble conducting polymers PET/PANI/MEH-PPV/Ca	Solution process	EQE 1%	Cao, Treacy, Smith, & Heeger, 1992
First phosphorescent OLED (PhOLED) using phosphorescent organometallic dopants, (PtOEP) doped into fluorescent dye	Vacuum deposit	EQE 23%	M. A. Baldo et al., 1998
Introduced p-type doped HTL and n-type doped ETL in p-i-n structure	Vacuum deposit	Achieved 1000 cd/m <sup>2</sup> using 2.9 V, maximum efficiency of 3 cd/A	J. Huang et al., 2002

High efficiency WOLED	Vacuum deposit	90 lm/W at 1000 cd/m <sup>2</sup>	Reineke et al., 2009
WOLED using small molecule host	Solution process	5.6 lm/W, 15 2000 cd/m <sup>2</sup>	Jou, Sun, Chou, & Li, 2005
WOLED using binary hosts (co-host)	Solution process	4.2 lm/W at 802 cd/m <sup>2</sup>	Jou, Sun, Chou, & Li, 2006)

### 2.2.1 Principles in Organic Light-Emitting Diodes

With the new discoveries made almost every year, the development of OLED has already reached the level where they can be regarded as an alternative to inorganic LED (Brunet, Colón, & Clearfield, 2015). There are commonly two different OLED structures namely single layer OLED and multilayer OLED device. These two structures and materials used will be explained in details in the last section in this chapter. For a simple OLED structure, it normally consists of anode, active layer (also known as light emitting layer) and cathode. Figure 2.1 shows the simplest energy level alignment in OLED device. A glass coated with a transparent anode, normally ITO is used as the substrate. In respect to vacuum level of the sample, the work function,  $\Phi$  of anode needs to be low in order to align with the Highest Occupied Molecular Orbital (HOMO) of the emissive layer (organic layer) to allow hole injection. On the other hand, the  $\Phi$  of cathode is required to be high in order to inject the electrons into the Lowest Unoccupied Molecular Orbital (LUMO) of the emissive layer. The emissive layer can be made up from several types of molecules such as small molecules, polymers or light emitting liquid crystals. Finally, cathode (e.g aluminum) is deposited on top of the emissive layer.

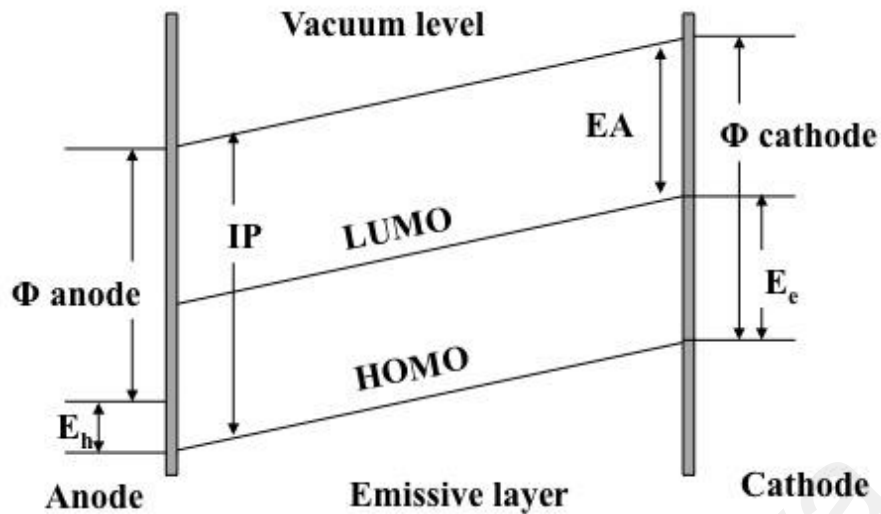


**Figure 2.1** Energy level diagram of a simple typical OLED structure.  $E_h$  and  $E_e$  at the cathode and anode respectively refer to the injection barriers for hole and electron into the emissive layer. IP represents the ionization potential of emissive layer material. EA stands for electron affinity, indicating on how capable a material is to bind an electron.

When an external bias voltage is applied to the device, an electric field builds up. Holes and electrons are injected into the emissive layer from anode and cathode respectively. The injected charges move from molecule to molecule by hopping conduction. If both carriers meet by columbic attraction, they can recombine in the active layer to produce excitons. Normally, the carriers are captured in a form known as charge transfer (CT) state before excitons are formed in a single molecule. Subsequently, the excitons are relaxed from excited states to ground states producing light depending on the energy difference between the excited states and the ground states (Reineke & Baldo, 2012). This process is named as electroluminescence because the light emission occurs as a result of electric field. Figure 2.2 depicts the steps involve in the light emission process: start with (i) charge injection, (ii) charge migration, (iii) excitation formation, (iv) light emission, and (v) light extraction. In order to achieve high efficiency OLED device, it is paramount important to ensure that each step operates in maximal efficiency. Each step is different in the organic materials as the

electronic states in organic materials are highly localized and the charge carrier mobility is orders of magnitude lower compared to inorganic material (Shiang & Duggal, 2007). The OLED device consists of different materials for each different layer with each material exhibiting different behaviors that may affect the device efficiency. For example, due to different electrons and holes mobilities of the materials, the recombination sites tend to be close to either one electrode. Anode and cathode quenching can affect the device efficiency.

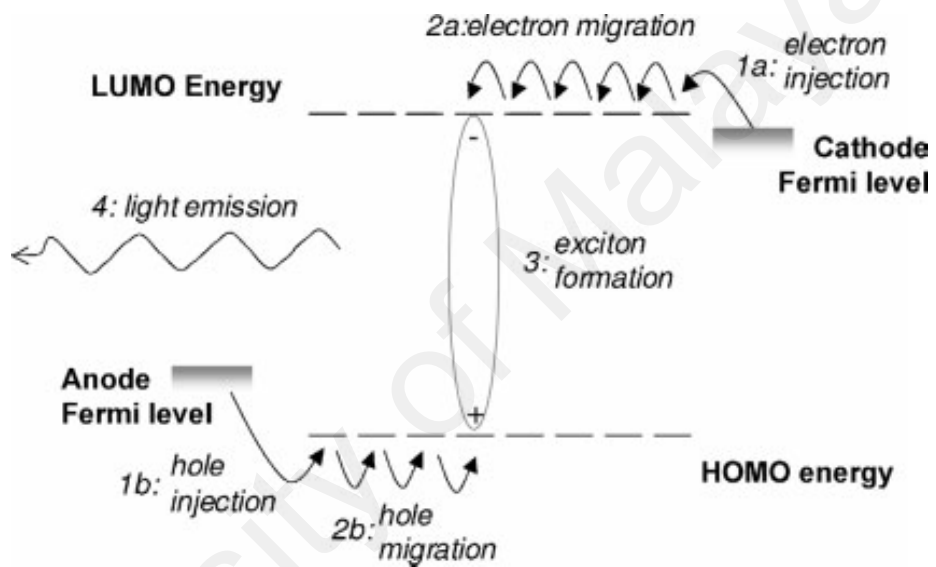


**Figure 2.2** The physical processes involve in organic materials electroluminescence.

In OLED, the ratio of number of emitted photons to charge injected is described as electroluminescence quantum efficiency ( $\eta_{EQE}$ ), which can be expressed as:

$$\eta_{EQE} = \gamma * \eta_{st} * q_{eff} * \eta_{out} \quad \text{Equation 2.1}$$

where  $\gamma$  is the efficiency of charge carrier within the layer,  $\eta_{st}$  is the fraction of spin-allowed excitons,  $q_{eff}$  is the radiatively effective quantum efficiency of emitting material and  $\eta_{out}$  represents the optical out-coupling efficiency.

## 2.2.2 Charge recombination

### 2.2.2.1 Light emission in OLED device

Considering two electrons system in excited molecules of OLEDs, the net spin value of the excited molecule may have total spin either  $S = 0$  or  $S = 1$ , depending on the spin angular momentum of the two electron. Excited state with spin value  $S=0$  corresponds to singlet excited state. The light emission from this state is regarded as singlet emission (fluorescence) with internal quantum efficiency at 25 % according to spin-statistics. The lifetime of fluorescence radiative decay is in the range of 1 to 10 ns (O'Brien, Baldo, Thompson, & Forrest, 1999). While for spin value  $S=1$  is called triplet excited state which reflects the triplet emission (phosphorescence) which consists of 75 % randomly formed excitons. In pure aromatic hydrocarbon, the lifetimes of phosphorescence decay can be in the millisecond range. However, radiatively phosphorescence emission normally cannot be observed in room temperature (Z. R. Li, 2015). It is also considered as non emissive due to spin selection rules. Thus, most of the light emission in organic molecule originates from fluorescence emission instead of phosphorescence. By introducing heavy metal atom into the organic molecule, the intersystem crossing (ISC) between singlet and triplet could be enhanced and the lifetime of the triplet excited state can be shortened (M. A. Baldo et al., 1998). This enhancement produced efficient phosphorescent OLEDs with 100 % internal quantum efficiency.

Jablonski diagram in Figure 2.3 illustrates the process of fluorescence and phosphorescence in OLEDs. In organic molecule, the transition between electronic states takes place via light absorption that raises the molecule to a higher excited state. After the light absorption, an electron is promoted from ground state  $S_0$  to vibrational level of the excited states depending on the photon energy. The transition could jump to  $S_1$  or higher singlet states,  $S_n$ . After the vertical transition, the molecules undergo fast

phonon relaxation in the order of femtosecond reaching the minimum point before making another vertical transition into the ground state  $S_0$ . This process is called fluorescence. The lifetime for this radiative recombination are in the range of  $10^{-9}$  to  $10^{-7}$  seconds. Alternatively, the system could encounter spin conversion to triplet states called ISC. This non-radiative transition occurs in a range of  $10^{-10}$  to  $10^{-8}$  seconds (Valeur & Nuno, 2012). However, the delayed fluorescence (about  $10^{-12}$  seconds) is also possible if the singlet and triplet state splitting is small. Triplet excitons can undergo transition from the triplet state back to the excited singlet state. Emission from the triplet state is often called phosphorescence. Phosphorescence resembles fluorescence but with the radiative lifetime much longer which is in the range of  $10^{-3}$  to  $10^{-2}$  seconds due to transition to the ground state is spin-forbidden by the spin selection rule. However, the radiative lifetime can be shortened using heavy atoms (Köhler & Bässler, 2009). It is normally very difficult to detect the absorption or emission from the triplet excited state. The emission observed in photoluminescence of materials without heavy atoms are all originated from singlet states. The extensively used phosphorescent materials are rare metal complex; red emitting PtOEP (M. A. Baldo et al., 1998), green-emitting Ir(ppy)<sub>3</sub> (M. A. Baldo, Lamansky, Burrows, Thompson, & Forrest, 1999) and blue emitting FlrPic (Adachi, Baldo, Forrest, & Thompson, 2000). The presence of a heavy metal such as Platinum (Pt) and Iridium (Ir) can enhance the spin-orbital coupling (SOC) in a molecule. This SOC process mixes both singlet and triplet states in a way that the triplet exhibits some singlet behavior allowing it to recombine radiatively (M. Baldo & Segal, 2005). Thus, via phosphorescent guest-host system, triplet excitons can be harvested and theoretically 100 % internal quantum efficiency can be achieved.

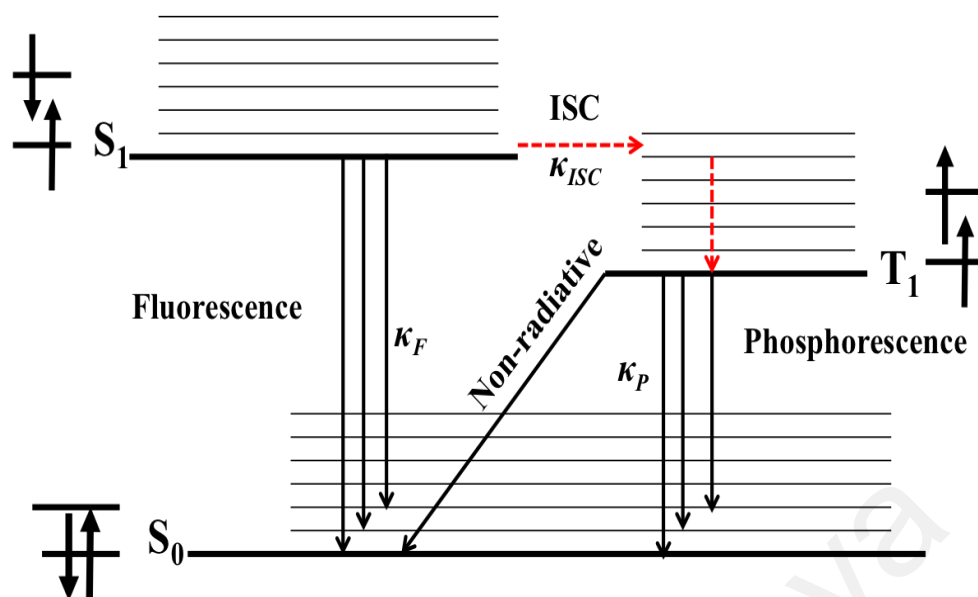


**Figure 2.3** Jablonski diagram depicting the energy transfer for the fluorescence and phosphorescence of organic material.  $S_0$ ,  $S_1$  and  $T_1$  are the ground state, singlet and triplet excited state respectively.  $\kappa_{ISC}$ ,  $\kappa_F$  and  $\kappa_P$  are the rate of intersystem crossing, fluorescence emission rate and phosphorescence emission rate respectively.

#### 2.2.2.2 Energy transfer in phosphorescent OLED

In phosphorescent OLED, host-guest system is normally applied where the charge recombination mainly occurs in the host molecules (Yersin, 2004). The excitons energy from the recombination on the host molecule is then transferred to the guest. This energy transfer can occur via Förster and/or Dexter mechanism which describes the radiation-less energy transfer from the excited state of one molecule (donor/acceptor) to another (acceptor/donor) (Zuniga, 2011).

Förster process (Förster, 1959) is illustrated in Figure 2.4. In this process, only energy transfers between singlet-singlet excited states participate. This process originates from the interaction among the electronic dipoles of the two molecules (host and guest molecules). Förster energy transfer occurs when there is a strong overlap of guest absorption spectrum with the emission spectrum of the host. Exciton in the blend can transfer the excitation energy via a smaller optical gap with typical distance of 1 –

10 nm and typical transfer time <1 ns. Despite a short distance of energy transfer, Förster energy can be expected to dominate as the distance is increased beyond 1 nm.

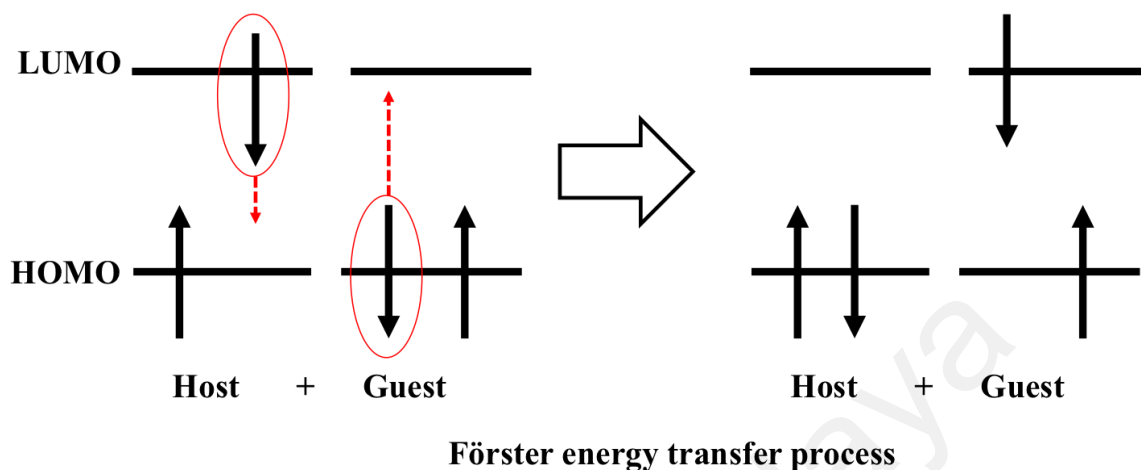


**Figure 2.4** Förster energy transfer process.

Dexter energy transfer is the exchange of the hole and electron between the molecules (Dexter, 1953). The exchange process allows the singlet or triplet excited states of the host to transfer energy to its next nearest guest molecules (shown in Figure 2.5). As a result, the process requires the direct overlap between the molecular orbitals. This type of energy transfer only operates at a short distance of 0.6 nm to 2 nm between the host and the guest. Dexter energy transfer rate is a function of  $e^{-\frac{2r}{L}}$  where  $r$  is the guest-host separation and  $L$  is the sum of Van der Waals radius.

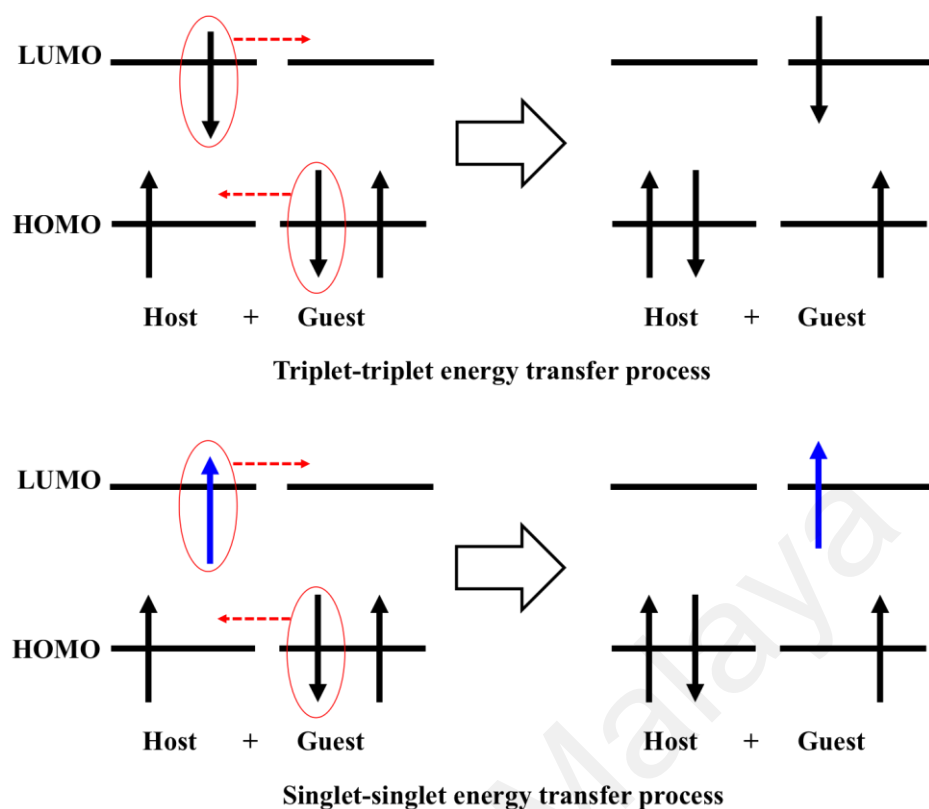


**Figure 2.5** Two different energy transfers in Dexter energy transfer process.

### 2.2.3 Charge carrier conduction in OLED device

Organic materials are hydrocarbon molecules. There are two different classes of organic material used in this thesis namely polymer and small molecules materials. The polymeric system is built-up of a long chain-like molecule with a long carbon backbone, where different functional side groups can be attached to this backbone. On the other hand, a small molecule is a material with a lower molecular weight than the polymer with definite molecular weight. All the organic semiconducting materials are conjugated which implies the existence of single and double carbon bonds. In conjugated organic materials, there are three electrons in the outer shell of the carbon atoms occupied by hybridized  $sp^2$ -orbitals in the backbone plane that contributes to the single  $\sigma$ -bonding of the carbon. The fourth electron is placed in a  $p_z$ -orbital of the carbon, which form the  $\pi$ -bonding that is a weaker bond than  $\sigma$ -bonding. The combination of these two orbitals resulted in a double carbon bond. In this formation,

the electrons belong to  $\pi$ -orbitals, which are formed by the overlapping  $p_z$ -orbitals, and are delocalized over the conjugated part of the molecules. This delocalization phenomenon is called as  $\pi$ -conjugation. The occupied molecular  $\pi$ -orbital with the highest energy is called HOMO which is equivalent to the valence band in crystalline semiconductor, whilst the unoccupied molecular  $\pi$ -orbital or  $\pi^*$ -orbital with the lowest energy is called LUMO which is equivalent to the conduction band of the crystalline semiconductor. Figure 2.6 depicts the phenomenon of the molecular orbital splitting. In the ground state, all bonding orbitals up to HOMO are filled with two electrons of opposite spins while the antibonding orbitals from the LUMO onwards are unoccupied. Excited states (neutral) can be formed when an electron is promoted from HOMO to the LUMO, for example via the light absorption in a molecule (Heinz Bäsler & Köhler, 2011).

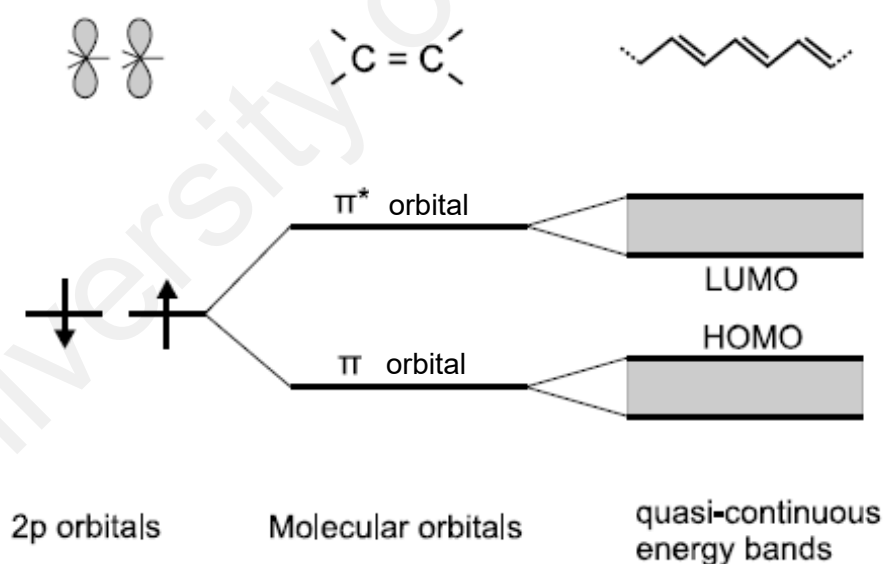


**Figure 2.6** Schematic representation of the molecular orbital splitting and quasi-continuous bands of occupied and unoccupied states in pi-conjugated materials. Adapted from (Schols, 2011).

The conjugated organic material is often amorphous as a result of disordered packing. The  $\pi$ -conjugated system of overlapping  $p_z$ -orbitals can be interrupted by

various defects such as polymer defects, polymer twist as well as from side group vibration and rotation. Such interruptions divided the polymer into separate electronic states that are localized at the particular *sites* where the charge transport takes place through the hopping process.

### 2.2.3.1 Charge transport

A pure organic semiconductor is intrinsically zero *net* charge. In order to produce a high efficiency OLED device, the *extrinsic* carrier is required to be injected into the material. In addition to that, the conjugated polymer normally used in OLED is highly disordered where the charge transport occurs via intermolecular hopping process (Kanemitsu, 1993), unlike the band transport as seen in the inorganic material. The hopping process occurs as the charge carrier tunnels quantum mechanically to the adjacent molecules in the material and sometimes even to non-adjacent molecules. This disordered polymer exhibits a poor charge transport properties and can be affected by trap states either from intrinsic (e.g structural defect) or extrinsic (e.g chemical impurity) trap (Poplavskyy, Su, & So, 2005). Thus, a specific chemical structure and morphology play a crucial role in determining the charge carrier transport properties (Coropceanu et al., 2007).

#### 2.2.3.1.1 Energetic disorder, $\sigma$

In conjugated organic material, electrons and holes reside at LUMO and HOMO respectively. However, due to the presence of disorder (each molecule see slightly different environment), the energy levels of HOMO and LUMO between identical molecules might differ slightly. This is called an *energetic disorder* and the random position of the sites is called *positional disorder*. The random distribution of the site energies where the charge hopping takes place is named as a density of state (DOS).

The charge hopping between localized states is represented by Gaussian distribution as shown in the relation (H. Bässler, 1993):

$$g(\varepsilon) = \frac{N_0}{\sigma\sqrt{2\pi}} \exp\left(-\frac{\varepsilon^2}{2\sigma^2}\right) \quad \text{Equation 2.2}$$

where  $N_0$  is the total density of states,  $\sigma$  is the variance of the distribution and  $\varepsilon$  is the site energy measured in relative to the center of the density of state. Figure 2.7 illustrates the DOS distribution of HOMO/LUMO levels in disordered organic material, where the hopping site is depicted as dashes.

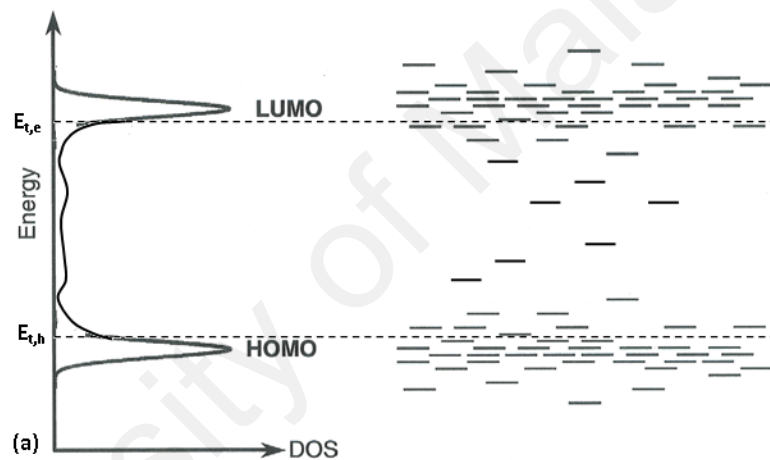


**Figure 2.7** Density of states (DOS) distribution in disorder organic material. The charge transport sites are represented as discrete states (shown as dashes).

Figure 2.8 shows the hopping transport of organic material, which is localized to a single molecule. It is shown that the electrons is injected from the Aluminum (Al) cathode into the LUMO level of the material while holes in the counter electrode is injected from the ITO into the HOMO of the material before forming the excitons via columbic attraction. The variance of distribution of energy level in the materials is dependent on the molecular interaction as well as the disorder of the material, whilst the

transfer rate of the charges is obtained from the energy difference and the distance between hopping sites (Shinar & Savvateev, 2004).

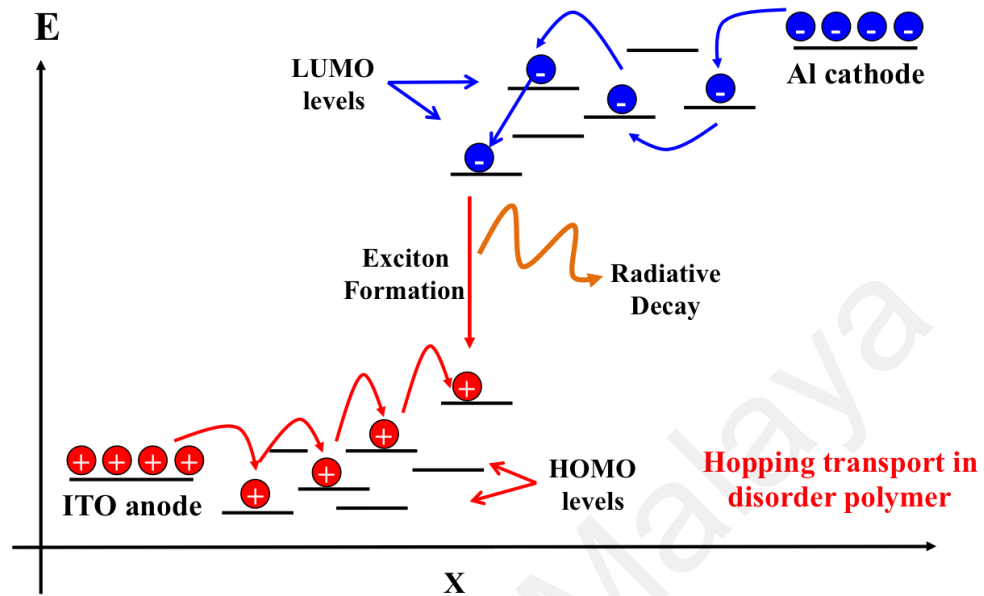


**Figure 2.8** Schematic diagram of hopping transport in an organic semiconducting device.

A hop upward in energy is a phonon-absorbed process while downward hop is a phonon releasing mechanism. The phonon-assisted hopping was reported by Conwell (Conwell, 1956) and Mott (N. F. Mott & Gurney, 1964; Nevil.F Mott & Davis, 1979). A description for the transition rate between the hopping site is proposed by Miller-Abrahams (MA) (Miller & Abrahams, 1960). The model describes the jump rate,  $v_{ij}$  between two sites,  $i$  and  $j$ :

$$v_{ij} = v_o \exp(-2\gamma a) \begin{bmatrix} \exp\left(-\frac{\varepsilon_i - \varepsilon_j}{KT}\right) \exp\left(\pm \frac{eEa}{KT}\right) & \varepsilon_i - \varepsilon_j > 0 \\ 1 & \varepsilon_i - \varepsilon_j < 0 \end{bmatrix} \quad \text{Equation 2.3}$$

where  $E$  is the applied electric field,  $a$  is the intersite distance,  $k$  is the Boltzmann constant,  $T$  is the carrier temperature for hopping transport in Kelvin,  $v_o$  is the

maximum attempt to hop frequency which is in the range of phonon frequency. This model describes the upward hops are thermally activated but the downward hops do not acquire any activation energy and hence is often considered as phonon release.

### 2.2.3.1.2 Disorder Formalism for carrier transport

Other than previously stated transport models, there are quite a number of reports on disorder organic transport studies using the disorder formalism developed by Bässler's group, known as Gaussian Disorder model (GDM) (H. Bässler, 1993). In this disorder formalism, the charges hop from one localized state to another. The sum of all those localized states gives rise to a Gaussian distribution. The relation in GDM is described as:

$$\mu(E, T) = \mu_{\infty} \left[ - \left[ \frac{2\sigma}{3k_B T} \right]^2 \right] \exp \left\{ C \left[ \left[ \frac{\sigma}{k_B T} \right]^2 - \Sigma^2 \right] E^{1/2} \right\} \quad \text{Equation 2.4}$$

where C is an empirical constant of Gaussian disorder in both position and energy with width of  $\Sigma$  and  $\sigma$  respectively. The parameter  $\sigma$  is related to distribution parameters such as energetic width of the DOS. GDM model has been successfully applied to poly (phenylethylene) (PPV) and its derivatives (Hertel, Bässler, Scherf, & Hörhold, 1999; Im, Bässler, Rost, & Hörhold, 2000; Inigo et al., 2004).

Bässler's GDM predicts the temperature and field dependence of charge carrier mobility in polymer. Monte Carlo (MC) simulations relate the non-Arrhenius temperature dependence of hopping mobility and Poole-Frenkel electric field dependence as:

$$\mu(T, E) = \mu(E=0) \exp\left(-\frac{T_0^2}{T^2}\right) \exp(\beta\sqrt{E}) \quad \text{Equation 2.5}$$

Where  $\mu(E=0)$  is zero field mobility,  $\beta$  is the field amplification factor. The carrier mobility in these materials is dependent on the temperature. This hopping transport is

thermally activated where the charge carrier mobility increases with the temperature. This temperature aided the charge carrier to overcome the barriers resulting from the energetic disorder.

### 2.2.3.2 Charge injection

#### 2.2.3.2.1 Injection limited current (ILC)

Charge transport in the OLED device is often limited by the injection in the low current region and greatly depend on the interface between metal/organic layers (Shinar & Savvateev, 2004). The behavior of this interface is influenced by few factors such as injection height barrier, the applied bias and temperature, interfaces dipole as well as the band bending or Fermi level pinning (Arkhipov, von Seggern, & Emelianova, 2003; Bokdam, Çakır, & Brocks, 2011; Hisao Ishii, Sugiyama, Ito, & Seki, 1999; Yan & Gao, 2002).

In ILC region, the spatial electric field,  $E$  distribution is assumed to be uniform, where  $E(x) = \left[ \frac{V}{d} \right]$ . The ILC can be distinguished from other region (for example SCLC) by the electric field at the charge-injecting contact as  $E(x=0) = \left[ \frac{V}{d} \right]$  for ILC, whereas  $E(x=0) = 0$  for SCLC. The prominent models for ILC is commonly based on two models namely: (i) Richardson-Schottky (RS) for thermionic emission (Sze, 2006) (ii) Fowler-Nordheim (FN) for tunneling (Fowler & Nordheim, 1928). For organic device, RS emission is applicable under high electric field with high temperature while FN tunneling is for a low electric field (Matsumura, Akai, Saito, & Kimura, 1996; Parker, 1994).

In RS model, it is assumed that once the electron gained enough thermal energy (to cross the potential maximum), it can be injected into the polymer. At high electric field,

the metal work function is reduced and this lowered the Schottky barrier height known as image force lowering. The RS equation can be described as:

$$J = A^*T \exp \left\{ -\frac{\Phi_B}{k_B T} \right\} \exp \left\{ \frac{\left[ \frac{q^3 V}{4 \pi \epsilon_0 \epsilon_r d} \right]^{1/2}}{k_B T} \right\} \quad \text{Equation 2.6}$$

where  $\phi_B$ ,  $\epsilon_0$ ,  $\epsilon_r$  and  $d$  are the interface potential barrier height, vacuum permittivity, organic dielectric constant and film thickness respectively.  $k_B$  is Boltzmann's constant,  $q$  is the elementary electronic charge,  $T$  is the absolute temperature and  $A^*$  is the Richardson-Schottky constant ( $A^* = 4\pi qm^*k_B^2/h^3$ ), where  $m^*$  is the free electron mass and  $h$  is Planck's constant.

In the other hand, FN formulation ignores image charge effect. When field emission dominates, the current density versus voltage ( $J$ - $V$ ) characteristic are described as:

$$J = AF^2 \exp \left\{ -\frac{8\pi \sqrt{2m^*} \Phi_B^{3/2}}{3hqE} \right\} \quad \text{Equation 2.7}$$

where  $E$  is the applied electric field and  $A$  in ( $A/V^2$ ) is a rate coefficient defined that contains a tunneling prefactor and the rate of current back flow (Davids, Campbell, & Smith, 1997).  $A$  is deduced as (Kao & Hwang, 1981):

$$A = \frac{q^3}{8\pi h \Phi_B} \quad \text{Equation 2.8}$$

### 2.2.3.2.2 Space-Charge-Limited Current (SCLC)

When current injection is not limited by contact barrier, the contact is called Ohmic contact. In this region, the  $J$ - $V$  behavior is described by Ohm's Law (Lampert & Mark, 1970; Sze, 2006):

$$J = qN\mu \frac{V}{d} \quad \text{Equation 2.9}$$

where  $q$  is the electronic charge,  $N$  is the charge carrier density,  $\mu$  is the mobility,  $V$  is the applied bias and  $d$  is the sample thickness.

At low voltage, the electrical field due to the injected carriers is insignificant compared to that due to the bias applied. When the injected carrier density increased, the field due to the carriers increased and dominates, and thus the current becomes space-charge limited. At this region, the device is not limited by injection barrier, but by the transport of charge through organic material (Jain et al., 2001; Marinov, Deen, & Iniguez, 2005; Roichman, Preezant, & Tessler, 2004).

Space charge limited current (SCLC) takes place when the transit time of excess injected charge is lower than the bulk dielectric relaxation time (Kondo, 2007). Under this regime, SCLC is describe via Mott-Gurney law (N. F. Mott & Gurney, 1964):

$$J = \frac{9}{8} \varepsilon_r \varepsilon_0 \mu \frac{E^2}{d} \quad \text{Equation 2.10}$$

where  $J$  is the current density,  $E$  is the electric field,  $d$  is the layer thickness,  $\varepsilon_r$  is the dielectric constant (3.5 for organic material),  $\varepsilon_0$  is the permittivity in free space.

This model is applied by assuming the device exhibits ohmic contact, is dependent on the bulk materials parameters and independent on the field. In  $J$ - $V$  curve, the characteristic of SCLC regime is nearly quadratic with exponents slightly larger than 2.

#### 2.2.4 Electronic properties of organic interface

Basically, an interface between the solids of two different materials can be formed via (i) the contact of two different solids or ii) the deposition of one material on the solid surface of the other material. In OLED, the most common interfaces are formed between metal/organic and organic/organic material. These two interfaces gain an intense interest in a relation to the development of the OLED devices (Hisao Ishii et al., 1999).

In OLED, a misalignment of the injections between metal Fermi level ( $E_F$ ) and the HOMO or LUMO will lead to non-ohmic contact and thus limits the charge injection and transport into the devices resulting in imbalance charge carrier. Therefore, in-depth study in the energy level alignment between the materials is of paramount importance. This section governs the energy level alignment at organic/organic and metal/organic interfaces that is included in the thesis framework.

In order to understand the terms used for electronic structure, Figure 2.9 illustrates the energy diagram of semiconductor with the assumption that there is no net charge accumulation at or near the surface. The definition of conduction band minimum (CBM) / LUMO, valence band maximum (VBM) /HOMO, vacuum level ( $E_{vac}$ ), work function (WF), energy gap ( $E_g$ ), ionization potential (IP) and electron affinity (EA) are shown. HOMO and LUMO terms have been used many times in previous sections, which depict a single-particle injection and transport through the organic semiconductor. The energy gap ( $E_g$ ) of the material is known as the difference between these HOMO and LUMO levels. Vacuum level ( $E_{vac}$ ) is defined as the energy level of an electron with zero kinetic energy (relatively to the sample surface) positioned within a “few nanometers” outside the solid. The nanometers distance is defined as a distance that is sufficient enough for electron to have the full impact of the surface dipole (will

be explained in the next section). While the ionization potential (IP) corresponds to energy difference between  $E_{\text{vac}}$  and VBM/HOMO level. This is the minimum energy required to remove an electron from the system. On the other hand, the energy gained by releasing an electron from the  $E_{\text{vac}}$  to CBM/LUMO is known as electron affinity (EA). The range of EA and IP of organic and inorganic electrons are in the range of 2-4 eV and 4.5-6.5 eV respectively. Lastly, the work function (WF) is depicted as the energy required to remove an electron from Fermi level ( $E_{\text{F}}$ ) to  $E_{\text{vac}}$  (Kahn, 2015).

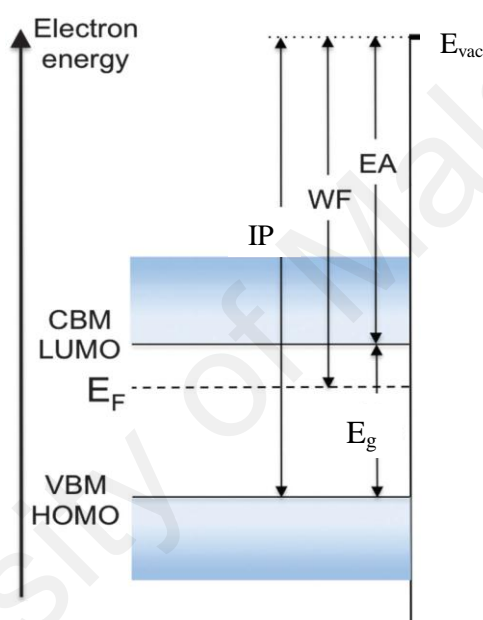


**Figure 2.9** Energy diagram of a semiconductor showing definition of band edges (CBM/LUMO and VBM/HOMO), vacuum level  $E_{\text{vac}}$ , work function (WF), energy gap ( $E_{\text{g}}$ ), ionization potential (IP) and electron affinity (EA).

#### 2.2.4.1 Metal/organic interface

When organic polymer is in contact with the conductive substrate, the vacuum shift is often observed as shown in Figure 2.10. This shifting was first explained using the Integer Charge Transfer (ICT) model (Braun, Salaneck, & Fahlman, 2009). ICT model suggests that the energy level alignment between organic and conductive substrate system with very weak interfacial interaction can be determined via the

substrate work function ( $\Phi_{\text{SUB}}$ ) and the charge transfer states ( $E_{\text{ICT}}$ ) energy of the organic material.

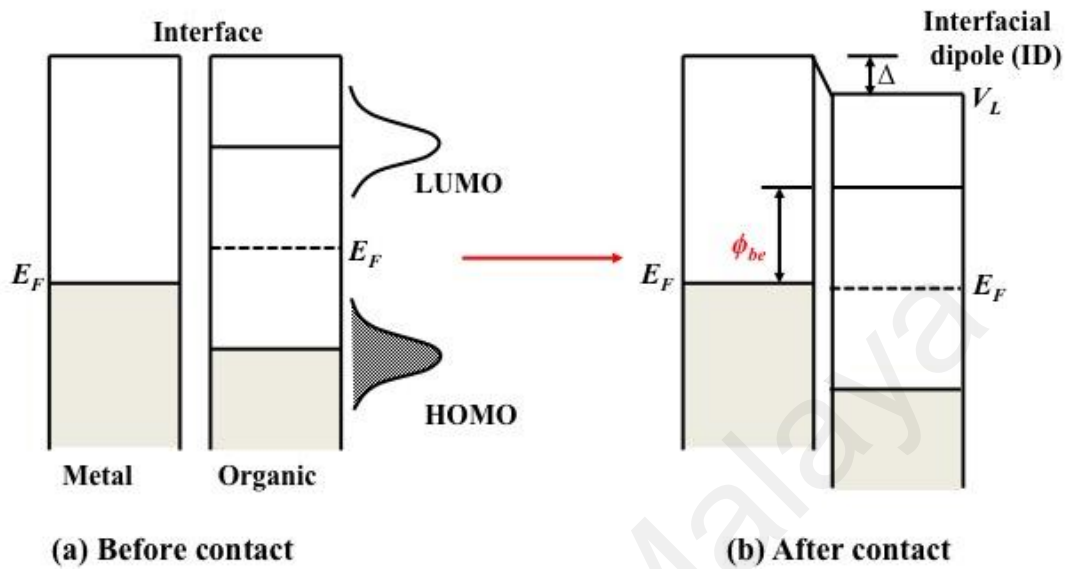


**Figure 2.10** Metal/organic semiconductors interface (a) before and (b) after making contact.

However, it is shown that the  $E_F$  pinning energy emerges naturally in the organic semiconductor gap rather than the energy separation from HOMO and LUMO onsets as the respective polaron-binding energies. Using UPS measurement, Blakesley *et al* showed that, the charge transfer from metal/substrate into empty states in the disorder organic semiconductor result in band bending (Blakesley & Greenham, 2009). Charge transfer occurs from the electrodes into a small DOS, up to several hundred meV into the band gap. This band bending is demonstrated to only rely on the effective work functions (WF) of the electrode (work function with vacuum shift) and the electronic structure (Lange et al., 2011).

In the case of thin layer, vacuum level shift leads to formation of electric dipole layer. Polarization of molecules, charge transfer across the interface, interfacial chemical reaction and push back effect are among the parameters that influenced the origin of dipole layer formation (Loppacher, 2012). Push back effect occurs due to

changes of the substrate surface dipole induced by the adsorbate. The adsorption of organic molecules that attracted to the surface via van der Waals forces resulting a lateral displacement of electronic charge. This displacement pushes back the electron density of the metal substrate that previously extended into a vacuum (Santato & Rosei, 2010). It is also shown that  $\pi$ -electron systems and polar end-group substitutions in the  $\pi$ -conjugated molecules deposited at the surface of a polymeric film is able to form dipole layers, which result in IP and EA of that particular film (Heimel, Salzmann, Duhm, & Koch, 2011).

#### **2.2.4.2 Organic/organic interface**

Organic/organic interface or organic-organic heterojunction (OOH) is a vital part, which fundamentally built up the OLED device especially in multilayer OLED structure. The energy offsets between the electronic levels of two different materials will impact the charge transport as well as the formation and diffusion of excitons due to the difference of their respective IP and EA (Hisao Ishii et al., 1999). In OLED device, excitons recombination occurs at or near the interface of both electron and hole transport layers. Figure 2.11 depicts a multilayer device with detailed energy levels of the device. When external bias is applied, electron and hole are injected and transported to the interface of the electron transport layer (ETL) and hole transport layer (HTL). With optimal energy level alignment in the emissive layer, these charge carriers can efficiently recombine radiatively and emit photons. A large offset between the LUMO of HTL and HOMO of ETL with the EL allows an effective charge confinement and thus enhancing the probability of forming the radiative excitons.

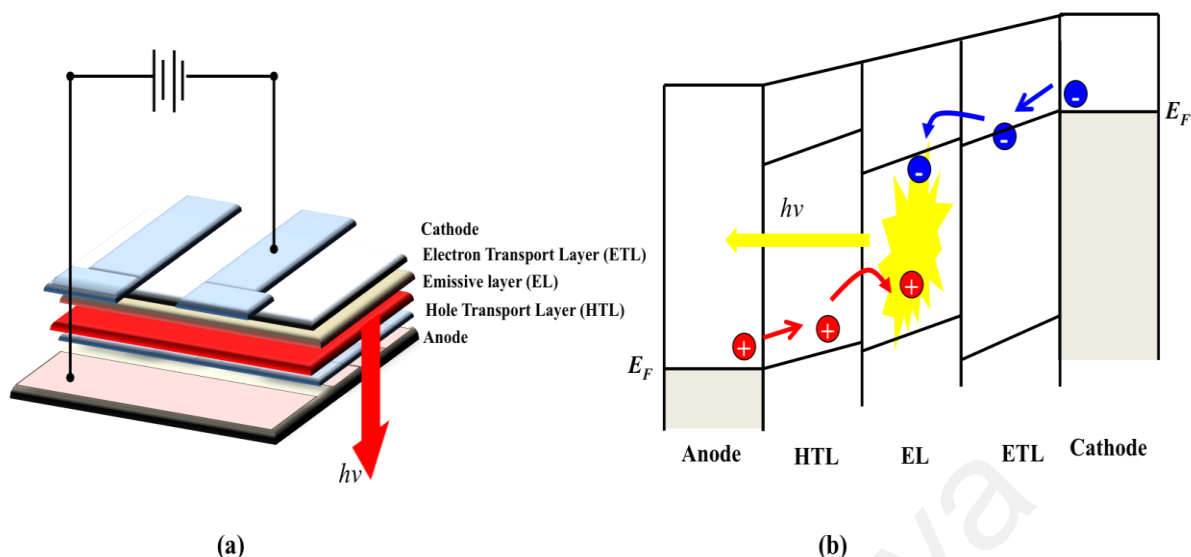


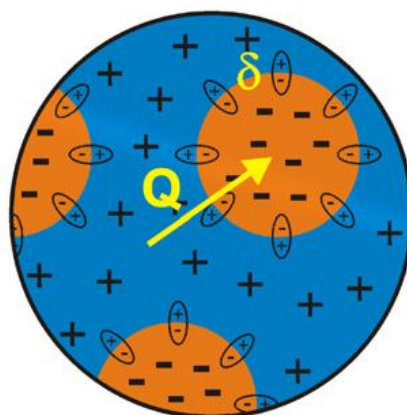
**Figure 2.11** Multilayer OLED device with organic-organic heterojunction formed between hole transport layer/emissive layer/electron transport layer.

Organic-organic heterojunction consists of at least two organic compounds where the first material hereby is known as A, and second material hereby is known as B. There are three main types of OOH in organic device namely A/B-type hetero-structures (A is deposited on top of B or vice versa), A:B-type hetero-structures (A co-deposited with B) as well as monolayer-based hetero-structures (Hinderhofer & Schreiber, 2012). Organic/organic interface exhibits few similar features with metal/organic interface such as the interface dipole (ID). Braun *et.al* shows that the vacuum level of fullerene ( $C_{60}$ ) and poly(3-hexylthiophene) interface shifted upward almost  $\sim 0.6$  eV due to interfacial dipole which implies the charge transfer occurs at the interface from P3HT to  $C_{60}$  (Braun et al., 2009). The main contributor to the ID in an organic/organic interface originates from the charge transfer across the interface that creates permanent dipole across an interface (Gao, 2010).

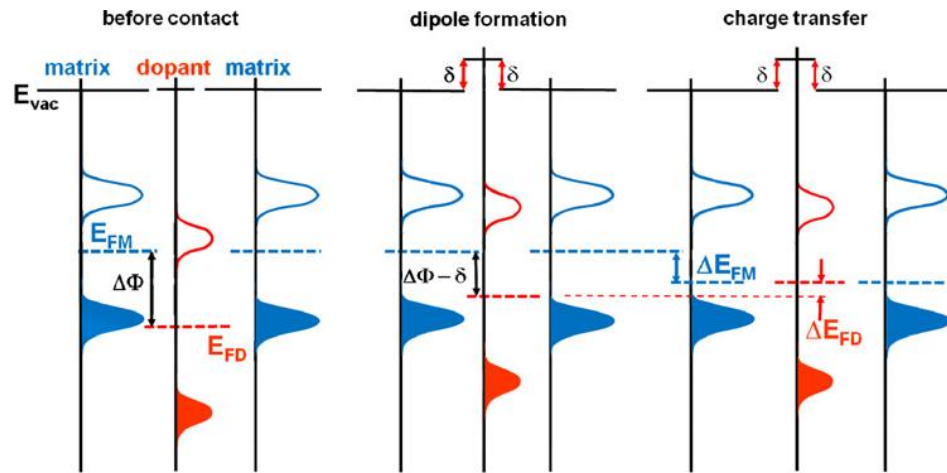
### 2.2.4.3 Internal charge transfer in mixed organic system

Mixed organic semiconductor materials system (doping) is typically described using ICT. In a case of p-type doping, a matrix molecule transfers an electron from its

HOMO to the dopant's LUMO (Braun et al., 2009). In this model, single dopant molecules are assumed to dissolve in the host matrix and p-dopant LUMO is positioned below the HOMO of the host material. However, single dispersed molecules model cannot be applied when there is phase separation between the dopants within the organic material. Thus, Mayer's group proposed a model called the internal interface charge transfer doping model. This model describes the Fermi levels of two-mixed material aligned at the internal interfaces. The magnitude of the internal interface dipole potential drops can be estimated from the dipoles measured at matrix/dopant bilayer interfaces (T. Mayer et al., 2012). Figure 2.12 illustrates model for such mixed phases. In Figure 2.12, the blue and orange regions represent the work function difference between the matrix materials and the dopant precipitates respectively. It is illustrated that the dopant precipitates is compensated by the formation of an interface dipole potential  $\delta$  and charge transfer  $Q$  between the two phases. This charge transfer results in Fermi level movements in the matrix ( $\Delta E_F^M$ ) and the dopant phase ( $\Delta E_F^D$ ). It is shown in Figure 2.12 (b) that the band bending has been ignored due a small characteristic influenced as compared to the extension of space charge regions induced by the equalization of the Fermi level.



(a)



(b)

**Figure 2.12** The internal interface charge transfer doping model; (a) spatial model and (b) development of the corresponding band energy diagram separating dipole formation and thermodynamic Fermi level equalization where band bending has been neglected.  $E_{FM}$  and  $E_{FD}$  are the Fermi level position, free of substrate influence. Adapted from (T. Mayer et al., 2012).

## 2.2.5 OLED structure

### 2.2.5.1 Single layer structure

As described in section 2.2.1, the simplest OLED structure is single OLED that consists of a single emissive layer sandwiched between two electrodes of different work function. A typical single OLED structure is depicted in Figure 2.13.

ITO is commonly used as conductive anode substrate for OLED because of its high transparency and low resistivity. Most of OLED material exhibits HOMO of  $\sim 5.0$  eV to 6.0 eV. Thus, it is compulsory for the anode to have a high work function in order to eliminate the energy barrier for hole injection into OLED material. The measured work function of un-modified ITO substrate is about 4.3 eV (Chou & Wen, 2012). This number is very low compared to the HOMO energy of the OLED material. Thus, an extensive research work has been done in order to modify the ITO work function (Irfan, Graber, So, & Gao, 2012; H. Kim, Lee, Park, & Park, 2002; Nüesch, Kamarás, & Zuppiroli, 1998; Ow-Yang et al., 2014).

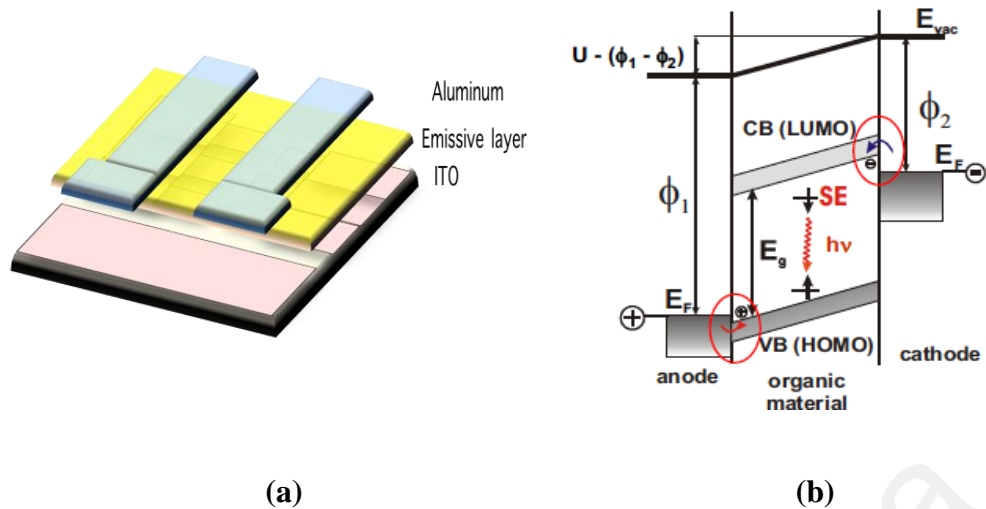


**Figure 2.13** (a) Typical single layer OLED device structure built-up from patterned ITO anode electrode, emissive layer (organic material) and Al cathode (b) The energy levels for the structure. Adapted from (Koch, 2007).

One of the widely used methods is by exposing the ITO substrate to oxygen plasma (X. M. Ding et al., 2000; Irfan, James Turinske, Bao, & Gao, 2012; Wu, Wu, Sturm, & Kahn, 1997). This method is also been applied in this thesis work. It is demonstrated that this method is able to increase the ITO surface work function for up to 6.1 eV (Irfan, Graber, et al., 2012). Besides oxygen plasma, inductively coupled plasma (ICP) with  $CF_4$  gas on the ITO surface can also be used to increase the work function of ITO for up to  $\sim 0.8$  eV (C. Kim et al., 2005). Other than that, the ITO surface work function can also be tuned between 4.90 to 5.40 eV by modifying with phosphonic acid (Sharma, Haldi, Hotchkiss, Marder, & Kippelen, 2009). On the other hand, there are also few works to replace the ITO with another material such as patterned glycerol-doped poly(3,4 -ethylenedioxy-thiophene) –poly (styrene sulfonate (G-PEDOT) (W. H. Kim et al., 2002; W. Kim, Kushto, Kim, & Kafafi, 2003) and also by using bilayer of glycerol monostearate (GMS)/ PEDOT: PSS as an anode (W. Zhang et al., 2013).

For counter electrode, the cathode is typically a low work function metal to efficiently inject electrons into the organic layer. Table 2.1 shows the most commonly used low work function metal in organic device. As shown in Table 2.2, the work

function of Calcium (Ca) is as low as -2.9 eV, which is a very good candidate as cathode. However, Ca is easily oxidized to CaO (Keuning, van de Weijer, Lifka, Kessels, & Creatore, 2012) and results in degradation of organic device. Thus, Al is chosen due to its low price as well as providing a good stability for the device (C.H & Dong Liang Tao, 2007).

**Table 2.2** Low work function metals used as cathode in organic device.

<b>Metal</b>	<b>Work function (eV)</b>
Gold (Au)	- 5.1
Aluminum (Al)	- 4.28
Magnesium (Mg)	- 3.7
Indium (In)	- 4.1 to 4.2
Silver (Ag)	- 4.6
Calcium (Ca)	- 2.9
Chromium (Cr)	- 4.3
Copper (Cu)	- 4.7

Single-layer solution-processed PhOLED is a promising structure for OLED device attributes to its simplicity of device fabrication. However, the efficiency of such device is generally poorer than double-layer PhOLEDs due to exciton quenching at the cathode (Burin & Ratner, 2000; Kuik, Koster, Dijkstra, Wetzelaer, & Blom, 2012). Generally, balancing carrier injection into the emissive layer as well as increasing the rate of the excitons is very important to achieve highly efficient OLEDs (Aizawa et al., 2014; S. Wang et al., 2015).

#### **2.2.5.2 Multilayer structure**

It is well known that OLED is a current-driven device that suffers from operational life-time that decreases with increasing current density (Liao, Klubek, & Tang, 2004; Matsumoto et al., 2003). It is also necessary to increase the luminous efficiency as well as power efficiency at higher brightness. This often suffers from the charge imbalance in the device. These issues become a motivation to the researcher in this field to come out with a better OLED device, for example via fabricating multilayers device and

specifically the latest multi-unit device (namely tandem device).

Multilayer OLEDs is invented to overcome the charge balance problems as previously discussed. Figure 2.14 shows an example of multilayer device with respective energy level. The device is constructed from a few organic thin films sandwiched between the electrodes. A hole transporting/injecting layer (HTL) and electron transporting/injecting layer (ETL) are inserted into the device to balance the charge injection and transport as well as to control the recombination process in the device. For HTL, poly (3,4-ethylene-dioxythiophene (PEDOT:PSS) and Copper phthalocyanine (CuPc) are usually selected. As previously discussed, ITO is known to have a relatively low work function compared to the HOMO or IP of most organic materials, thus, the number of holes is controlled by Schottky barrier height at the interface, limiting the number of holes injected. The addition of PEDOT:PSS as hole transport layer (HTL) could reduce the energy difference or energy barriers between ITO and the emissive layer for efficient charge injection as well as lowering the device operating voltage. Recently, Chen *et. al* demonstrated PEDOT:PSS doped Graphene Oxide (PEDOT-GO) as hole injection layer for quantum dots based LED. By doping GO, the energy offset between HTL and emissive layer was lowered resulting in six folds enhancement compared to undoped PEDOT device. (Jing Chen et al., 2015). 4,7-diphenyl-1,10-phenanthroline (BPhen) and 1,3,5-tris(1-phenyl-1H-benzimidazol-2-yl)benzene (TPBi) are among the commercialized ETL materials normally chosen as ETL for better electron injection from cathode. For further enhancement, hole blocking layer (HBL) and electron blocking layer (EBL) could also be added in order to confine the charges in the active layer. Subsequently, a very thin electropositive and low work function metals such as lithium fluoride (LiF) or cesium fluoride (CsF) together with a thick aluminum are used as the cathode.

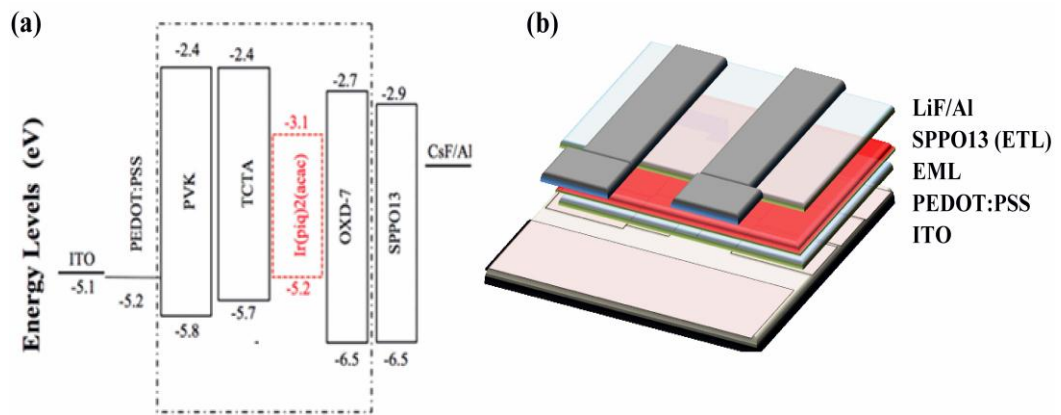


**Figure 2.14** (a) Energy level diagram and (b) device structure of multilayer OLED device. In this device, PEDOT: PSS is used as HTL and 2,7 bis(diphenylphosphoryl)-9,9'-spirobifluorene (SPP013) as ETL. The cathode consists of LiF/Al.

### 2.2.5.3 Tandem Structure with Charge Generation Unit

The technological advancement of OLED structure device is further continued by the introduction of a tandem OLED, one of the promising concept to reduce the device driving current at high luminance. The first reported tandem OLED is by Kido *et.al* (Junji Kido et al., 2003). Tandem OLED consists of vertically stacked two or multiple light-emitting units (LEU) connected by CGL as shown in Figure 2.15. In contrast to the conventional OLED, the presence of CGL permits multiple photons emission from injected electron and hole, thus achieving higher luminance at a lower current density (Y. Chen & Ma, 2012). Recently, Yamaoka *et.al* presented a high-resolution OLED display using blue/yellow tandem structure and RGBY subpixels, with the world's lowest level of power consumption (Yamaoka et al., 2015). However, tandem OLED device developments are still hindered by CGU bottleneck, having a large voltage drops, lack of good optical transparency and operational stability (Chan et al., 2007; Kanno, Holmes, Sun, Kena-Cohen, & Forrest, 2006; Liao & Klubek, 2008; H. Zhang, Dai, & Ma, 2007).

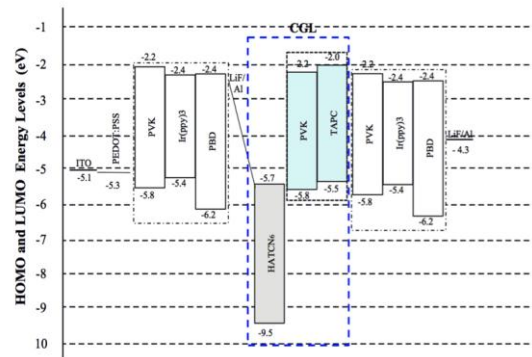
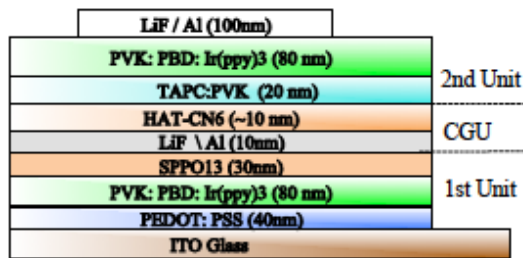


**Figure 2.15** An example of tandem OLED structure and respective energy level used in this thesis research work. The first and second unit of single structure is connected with CGU unit in the intermediate structure.

In the early stages, CGU was made up from layers of a metal-doped or metal-oxide layer forming a p-n junction (Chang, Chen, Hwang, & Chen, 2005; Liao et al., 2004). Tsutsui *et.al* (Tsutsui & Terai, 2004) showed that p-n doped (Mg-doped Alq<sub>3</sub> and V<sub>2</sub>O<sub>5</sub>) connecting layer acts as bipolar charge spouting zone and the additional generated charges that can be injected into the adjacent layers. This connecting junction forms a large band bending and assists the charges to be injected into adjacent EL unit via tunneling process. Figure 2.16 illustrates the tunneling process from p-n doping layers. Using n-doped ETL/p-doped HTL structure, Kroger *et al.* proposed a working mechanism for p-n junction-based CGL where the charge generation process takes place at the junction interface. Electrons are tunneled from HOMO states of HTL via a narrow depletion region at the interface to the LUMO states of ETL (Kröger et al., 2007).

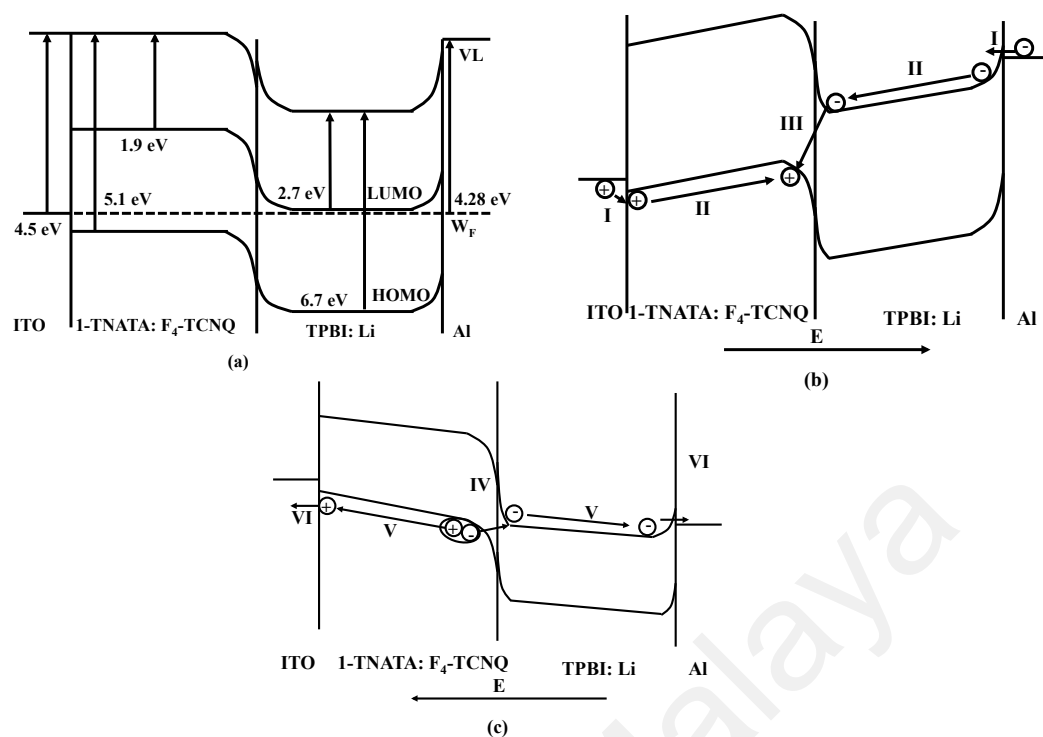


**Figure 2.16** Energy level alignment for charge generation unit in tandem at different conditions, where (a) when no external bias applied, (b) forward bias condition (recombination) and (c) reverse bias (charge generation) adapted from (Kröger et al., 2007).

Using the same structure, Liu *et.al* demonstrated a stable CGL based on a p-doped/n-doped structure combining a hole transport layer, [N-(1-1-naphthyl)-N-phenyl-amino]biphenyl (NPB) with an electron extraction layer, 2,3,5,6-Tetrafluoro-7,7,8,8-tetracyanoquinodimethane (F<sub>4</sub>-TCNQ) as p-doped and 8-hydroxyquinolatithium (Liq)/Al as n-doped layer. The device shows a high efficiency with enhanced lifetime (J. Liu et al., 2013). Recently, an optimal interconnector for tandem OLED built up from n-type/bulk heterojunction (BHJ) /p-type structure where bulk heterojunction was realized using electron acceptor material. The device efficiency of 57.5, 126.8 and 52.7 lm/W for red, green and blue device respectively, have been obtained (Sun, Chen, et al., 2015). However, most of the tandem device is fabricated stepwise using expensive vacuum evaporation process rather than solution process. Thus, in this research work, we take this as a challenge to fabricate tandem OLED with minimum vacuum deposit process, especially for charge generation unit.

## CHAPTER 3: METHODOLOGY

### 3.1 Introduction

In this chapter, the process of fabricating OLED devices and, measurement equipments are presented. The first part of this chapter describes patterning of ITO substrate involving photolithography, etching and stripping process. This chapter also explains how the measurement was carried out for electrical measurement such as Current density-Voltage-Luminance ( $J$ - $V$ - $L$ ) measurement and Time-of-Flight (ToF) measurement. Ultraviolet-visible (UV-Vis) spectroscopy for absorbance measurement, Photoluminescence (PL) spectroscopy, and Atomic Force Microscopy (AFM) measurement are also described. The explanation on Focus Ion Beam (FIB) in combination with HR-TEM for cross sectioning and measuring a very thin layer from the fabricated device is also included in this chapter. The technique of measuring the energy level of the compound and interfacial behavior using *In situ* ultraviolet photoelectron spectroscopy (UPS) and X-ray Photoemission Spectroscopy (XPS) are also presented. Inductively Coupled Plasma Mass Spectrometer (ICP/MS) for elemental detection is described in the end of the chapter.

### 3.2 Substrate patterning process

The same pattern of ITO substrates is depicted in Figure 3.1 throughout the experimental work. The patterning process of ITO substrates follows the standard lithography process. ITO coated glass substrates were purchased from Luminescence Technology Corporation, Taiwan. The thickness of ITO coated on top of the glass is 120 nm and the dimension of the glass substrates was 1.1 mm x 15 mm x 20 mm. The patterned ITO consists of six different pixels as depicted in Figure 3.1 (b). Prior the patterning process, the substrates were cleaned using deionized waster (DI), acetone, isopropyl alcohol (IPA) and DI water sequentially in an ultrasonic bath for 10 minutes

each. Positive photoresist (AZ5214E) was then spin coated on top of ITO coated substrate at 4000 rpm and then annealed at 105 °C for 1 minutes 45 seconds in order to remove the residual solvent in the photoresist. Using Oriel 87431 contact mask aligner, the substrates were then exposed under mercury lamp with *i*-line (365 nm) output through a chrome photo mask (Figure 3.1 (c)). In order to develop a pattern, AZ developer diluted with DI water with 1:2 volumetric ratios was prepared.

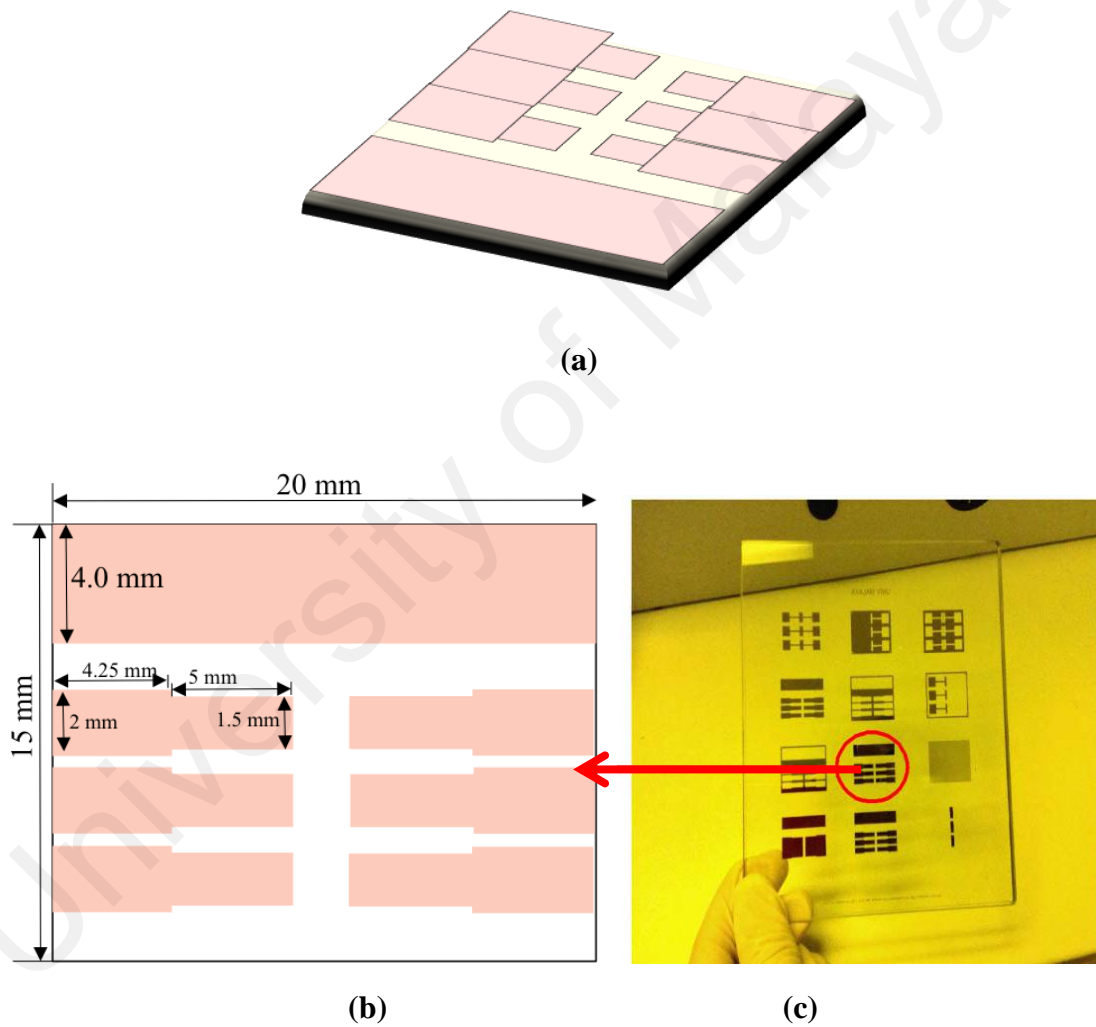


**Figure 3.1** (a) Standard patterned ITO substrate used in experimental work, (b) The dimension of the pattern used for ITO patterning and (c) photolithography mask used.

The exposed substrates were then immersed in diluted AZ developer for 1 minute to create the desired pattern. Following that, the substrates were then baked in the oven at 110 °C for 10 minutes, to ensure a good adhesion between the developed patterned and

substrates. Subsequently in order to remove the unwanted part, the patterned substrates were then etched using hydrochloric acid (HCl) diluted in DI water with 1:1 volumetric ratio. Diluted HCl was heated at 80 °C before dipping the substrates for a few seconds. After etching process, the photoresist was then stripped using sodium hydroxide (NaOH). Finally, the patterned substrates were rinsed thoroughly using DI water, followed by acetone, IPA, and DI water subsequently.

### **3.3 Standard single OLED fabrication process**

The OLED fabrication process for single device normally involves spin coating organic materials and ended with vacuum depositing cathode, Aluminum (Al). For electrical measurement, connection legs are attached to ensure there is a connection at each pixel. Figure 3.2 shows the standard OLED fabrication process. To fabricate single OLED device, the patterned ITO substrate was first treated with oxygen plasma at 35 W for 5 minutes to remove contaminants and to increase the ITO work function as the anode and more importantly to improve surface wettability using highly reactive oxygen radicals. Subsequently, hole transport layer (HIL) was spin coated on top of ITO substrate. The aqueous dispersion of PEDOT: PSS is commonly used as HIL for the standard device. PEDOT: PSS was spin-coated on the substrate forming 40 nm thin films. Then, the substrate was transferred into N<sub>2</sub> environment glove-box and was annealed at 150 °C for 10 minutes. Next, OLED material was spin coated on top of PEDOT: PSS. To complete the device fabrication, the deposition of electron injection material (EIL) and Al cathode was deposited on top of the organic material with a shadow mask. The deposition of these materials was done under vacuum  $2.4 \times 10^{-4}$  mbar. Finally, to protect the materials from the moisture and environment contaminants, the device was encapsulated using U.V curable epoxy and glass lid. The OLED device was then connected with connection legs to be measured.

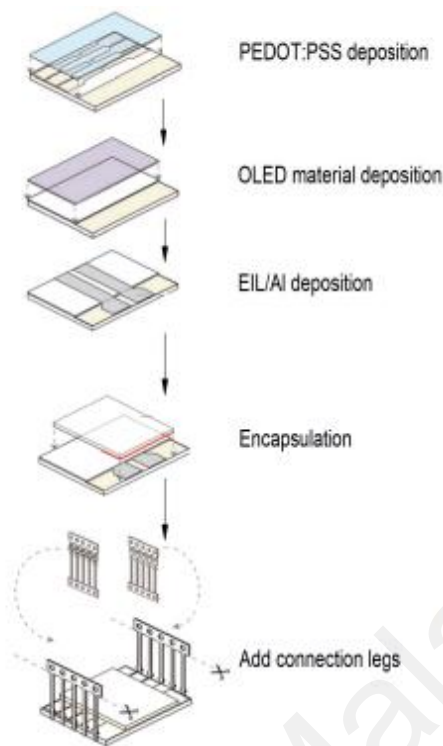


**Figure 3.2** Standard OLED fabrication process. Adapted from <http://www.ossila.com/pages/organic-photovoltaic-opv-and-organic-light-emitting-diode-oled-fabrication-manual>.

### 3.4 Electrical measurement

The most important characteristic for the OLED device is the measurement of device efficiency. The charge mobility and the width of Gaussian density of states can be investigated using temperature dependent Time of Flight (ToF) measurement.

#### 3.4.1 Current density-Voltage-Luminance ( $J$ - $V$ - $L$ ) measurement

$J$ - $V$ - $L$  measurement is the most basic but powerful tool for OLED device efficiency measurement. All the devices were tested using the same measurement setup described here as shown in Figure 3.3. A device is placed in a black box and then subjected to the external bias voltage from Keithley 236 source-meter-unit (SMU). Both current and brightness/luminance are then detected by Konica Minolta CS-200 chroma-meter (which is integrated with SMU) simultaneously. The chroma-meter is also

connected to a black boxed to ensure a fully dark environment for measurement. The measurement is controlled using a Labview computer program.

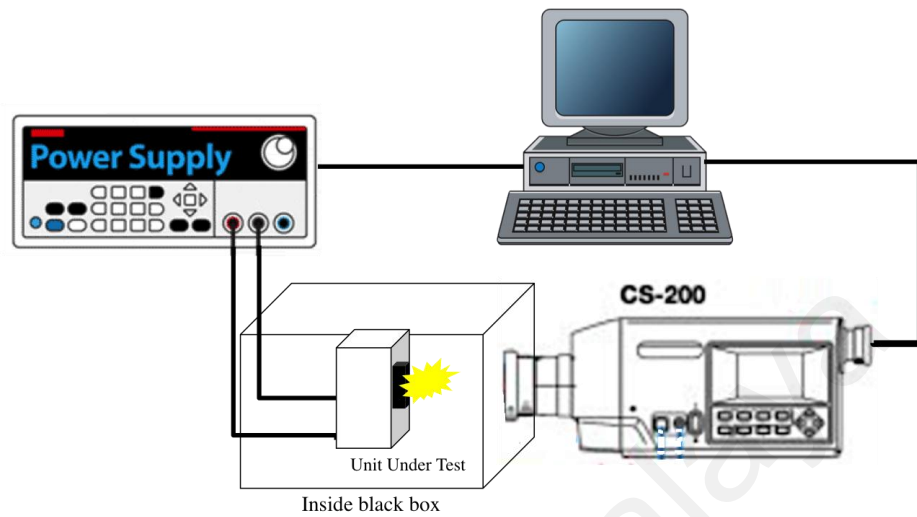


**Figure 3.3** Schematic diagram of J-V-L laboratory set-up.

Figure 3.4 shows an example of *J-V-L* characteristic of a red phosphorescent OLED. The current density of the device rises significantly as the light output starts when the external bias is applied. At this voltage, the charge carriers are injected from both electrodes

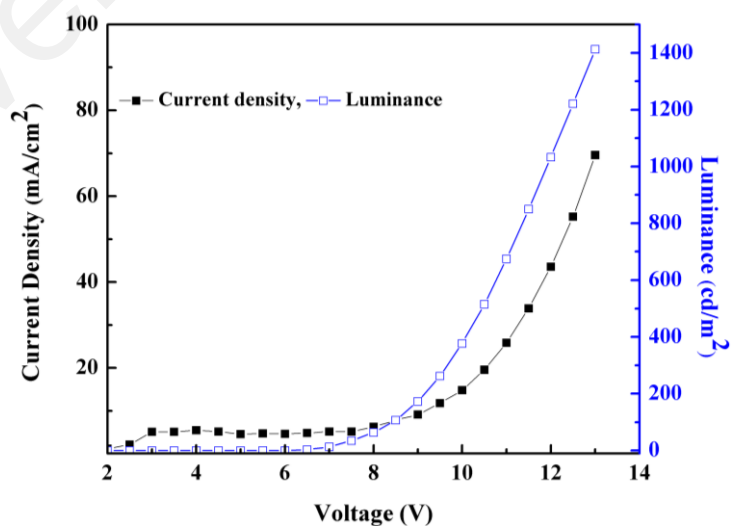


**Figure 3.4** Typical *J-V-L* characteristic of the OLED device.

The efficiencies can be easily extracted and calculated from the raw  $J$ - $V$ - $L$  data.

Current efficiency (cd/A) from luminance can be calculated using:

$$\eta_{CE} = \frac{\text{Luminance } (L)}{\text{Current density } (J)} \quad \text{Equation 3.1}$$

Whilst, the power efficiency or luminous efficacy (lm/W) can be calculated from:

$$\eta_{PE} = \frac{\eta_{CE} * \pi}{V} \quad \text{Equation 3.2}$$

where  $V$  is the operating voltage.

### 3.4.2 Time of Flight (ToF) Measurement

In this work, ToF was used to measure field and temperature dependence mobility. For ToF measurement, the device for testing is typically prepared by sandwiching the film (polymer) between ITO and Al as electrodes. The sample was mounted on the temperature controlled vacuum chamber HCS622VXY. Dissociation of exciton under applied electric field gives rise to free carriers (photocurrent). The photocurrent transient was detected with a digital oscilloscope triggered by the laser pulse. In the set-up shown in Figure 3.5, the charge carriers are generated by pulses excited from a nitrogen laser NL 100 with a peak wavelength of 337 nm and FWHM 3.5 nm. The optical pulse was split into two beams by a beam splitter. The reflected light was incident on the THORLABS DET 25K/M GaP Biased Detector with a detection range of 150-550 nm. The transmitted laser light was used to excite the ITO side of the sample. Under external direct current (DC) bias from Keithley 2600B series Source Meter Unit (SMU), the time-resolved current across external load resistor due to sheet charge carrier drifting across the film is observed. Most polymers have strong absorption,  $\alpha \geq 1 \times 10^5 \text{ cm}^{-1}$  and absorb strongly in the region of 300 to 400 nm. In order to study the hole transport (positive charge), the device tested were positively biased and it was reversed biased in order to study the electron mobility.

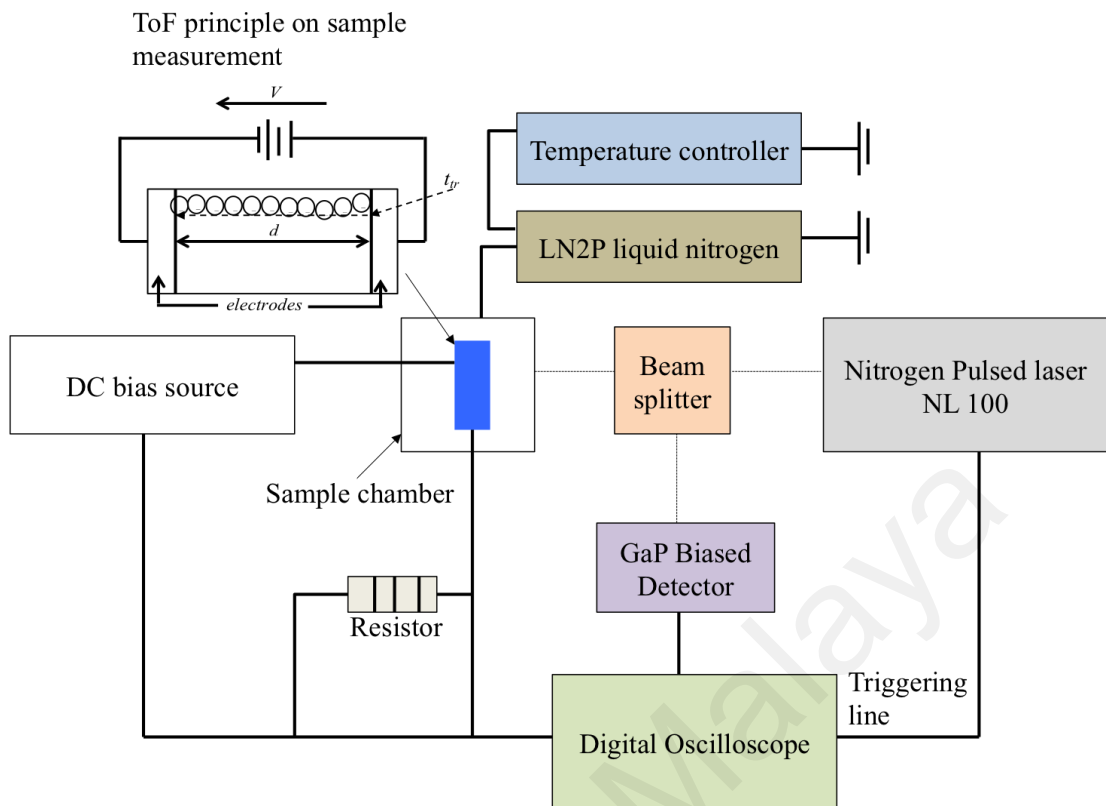


**Figure 3.5** ToF measurement laboratory set-up. The figure also depicted the principle on measuring time transit ( $t_{tr}$ ) from the sample (polymer), where  $t_{tr}$  is the time where the first sheet charge arrived at the counter electrode.

As illustrated in Figure 3.5, the resistor was used in series with the samples. The resistor value was kept as small as possible so that the RC constant does not overshadow the transient signal. The voltage drop across the resistor was monitored by an Agilent Technologies Infinii Vision DSO-X-3052A Digital Oscilloscope, which was synchronized with the GaP biased detector. It was then converted into a time-varying photocurrent by dividing with the value of the load resistance. Instec Inc. mK1000 and LN2-P liquid nitrogen cooling system were connected to the temperature controlled vacuum stage to control the temperature. Figure 3.6 shows the typical ToF transient observed. In (a), profile in (i) depicts the ideal ToF theoretically, where photocurrent shows a sudden drop to zero. This abrupt drop indicates the arrival of the first carrier sheet at the opposite electrode. Transient time ( $t_{tr}$ ) provides the information to calculate the mobility of the film. However, in real practice, the carrier diffusion can broaden the

charges sheet during the movement across the device, thus produces the profiles in (ii) and (iii). Non-dispersive transient is often obtained from pure semiconducting polymers shown in (ii). For polymers that exhibit defects and traps, dispersive transient is often seen as illustrated in (iii). For all cases, the  $t_{tr}$  could be determined from the asymptotes intersection from log-log plots of photocurrent versus times as shown in (b).

From the ToF transient curve, the mobility,  $\mu$  is then determined from the equation:

$$\mu = \frac{d^2}{t_{tr} V} \quad \text{Equation 3.10}$$

where  $V$  is the bias applied and  $d$  is the polymer film thickness.

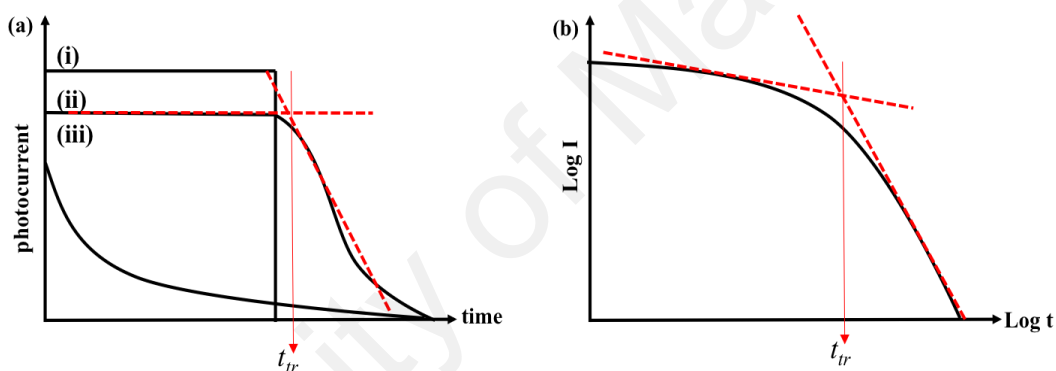


**Figure 3.6** Typical transient photoconductivity of ToF measurement. (a) A double linear graph with (i) Ideal ToF profile (ii) Non-dispersive transient and (iii) dispersive ToF signal, whereas (b) Double log of dispersive transient ToF transient.

### 3.5 Optical measurement

#### 3.5.1 Absorption spectroscopy measurement

Perkin Elmer PE750 UV-Vis are used to measure optical absorption on a thin film sample with a resolution of 1 nm . The absorbance ( $A$ ) of a material is defined as:

$$A = \text{Log}_{10} \frac{I_0}{I} \quad \text{Equation 3.11}$$

where  $I_0$  is the incident light while  $I$  is the transmitted light.

The absorbed energy resulted in the electronic transition from ground state to higher energy orbital if the absorption wavelength corresponds to the energy difference between these orbitals. In the range of 200 nm to 800 nm (for organic material),  $\pi \rightarrow \pi^*$  and  $n \rightarrow \pi^*$  transitions may happen. The basic schematic diagram of the UV-Vis spectroscopy set-up is shown in Figure 3.7. The light source is directed to the monochromator before the light is dispersed via two gratings. This dispersed light go through a small opening slit and split into two identical beams. A blank sample substrate as a reference is placed in one beam of the spectrometer. One of the beams (reference beam) passes via the reference substrate and the second beam passes through the measured sample. Both beams intensities are measured at the same time and compared by the detector. Finally, the sample absorbance output is plotted across the UV-Vis wavelength.

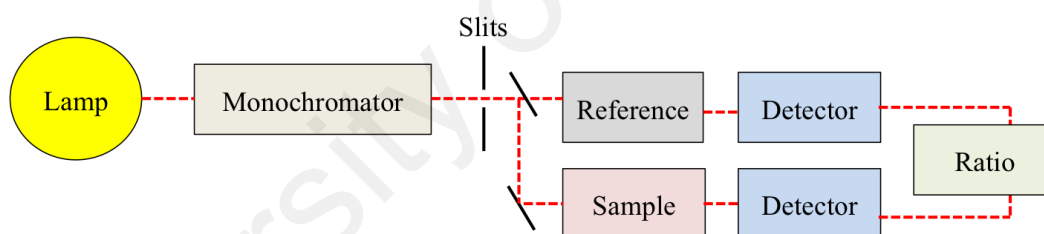


**Figure 3.7** Schematic diagram of the typical operation principle of UV-Vis spectroscopy.

### 3.5.2 Photoluminescence (PL) measurement

PL measurement was carried out using Perkin Elmer LS50B fluorescence spectrometer at room temperature. The PL emission spectra were recorded for fixed excitation wavelength. PL measurement is used to study the electronic and optical transition of the light emitting polymer thin film. When the material is absorbed with sufficient energy from the source, the electron in a compound is excited to a higher energy. In order for this excitation to occur, the excitation energy (normally in

wavelength) must have the same energy or greater than the energy difference between the initial state and the next higher energy state with a lifetime of  $\sim 10^9$  s (Guilbault, 1973). Figure 3.8 shows the operation set-up of the PL spectrometer measurement. The sample (polymer thin film) is placed in the center of the sample holder and the Xenon light source goes through the excitation monochromator. The beam passes through the small opening slits, travel through the excitation filter before incident onto the sample. The emission from the sample is then traveled into an emission monochromator via slits before reaching a detector. The output signal emission spectrum is plotted across the wavelength.

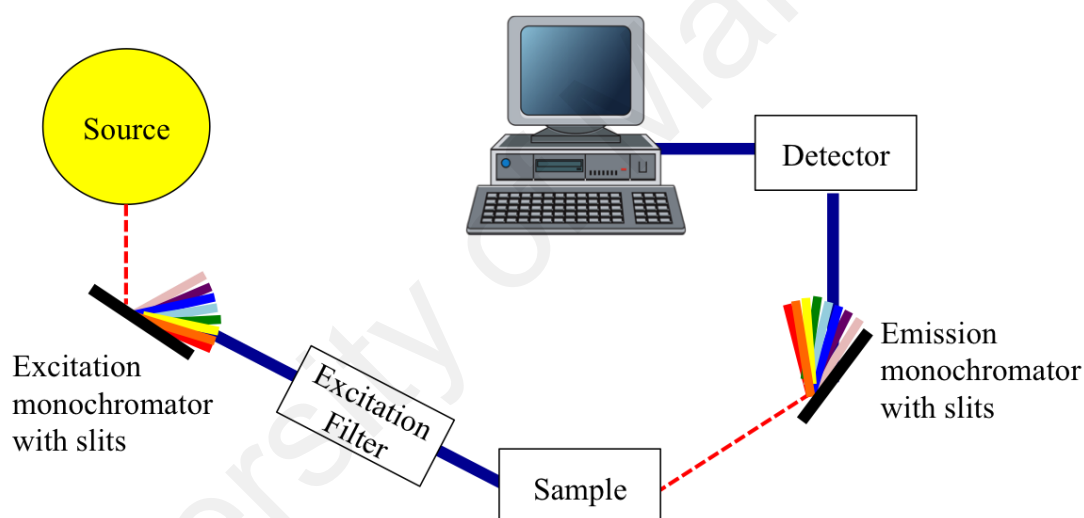


**Figure 3.8** Schematic diagram of PL measurement technique for LS50B spectrometer.

### 3.5.3 Atomic Force Microscopy (AFM) measurement

In this research, the AFM measurement was carried out via NT-MDT NTEGRA-Prima and NX10 (Park System) operating at tapping mode. The cantilever tip is oscillating at high frequency ( $\sim 50$ k to 500 kHz) and taps at the sample surface. Depending on the surface topography, the amplitude of the tip oscillation changes. For example, the top oscillation amplitude decreases when there is a bump on the surface and inversely, the amplitude increases when encountering a cavity. The changes of the

amplitude will result in surface morphology of the sample. In tapping mode, AFM can also performed phase measurement, where the phase differences of the vibrating cantilever are measured. The phase difference can be observed when the cantilever tip is scanning material with different adhesion/ friction/ elasticity. The inelastic energy transfer from the cantilever tip to the sample surface is proportional to the phase shift (Mart ínez & Garc ía, 2006). Figure 3.9 shows an example of the surface morphology measurement in 3D and 2D carried out via tapping mode.

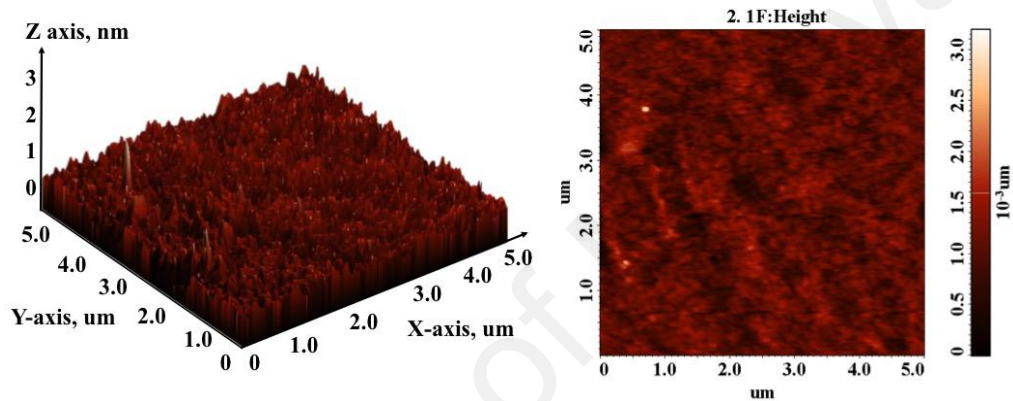


**Figure 3.9** Film morphology in (left) 3D and (right) 2D measured using AFM tapping mode.

### 1.1.1 Dual Beam Focus Ion Beam (FIB)

Dual Beam Focus Ion Beam (FIB) in this thesis experiments was used to prepare a lamella sample for Transmission Electron Microscopy (TEM). Figure 3.10 (a) illustrates the directions for FIB preparation and TEM measurement respectively. The sample is meant to measure a very thin thickness that could not be measured using profiler meter. For this, sample was spin coated on top of the substrate and coated with platinum before proceed with FIB. Using FIB, two trenches were cut one from each side, leaving a thin electron-transparent lamella as shown in Figure 3.10 (b). This technique is known as H-bar FIB. The sample was then directly removed from the trench via lift-out technique

using micromanipulator tip. This sample was then transferred to carbon-coated TEM grid (J. Mayer, Giannuzzi, Kamino, & Michael, 2011).

The basic principle of FIB is by using ions instead of electrons. The ion source, normally Gallium ions are extracted and ionized using high pressure. These ions are then accelerated in the range of 0.5 – 30 keV and focused on the sample via electrostatic lenses.

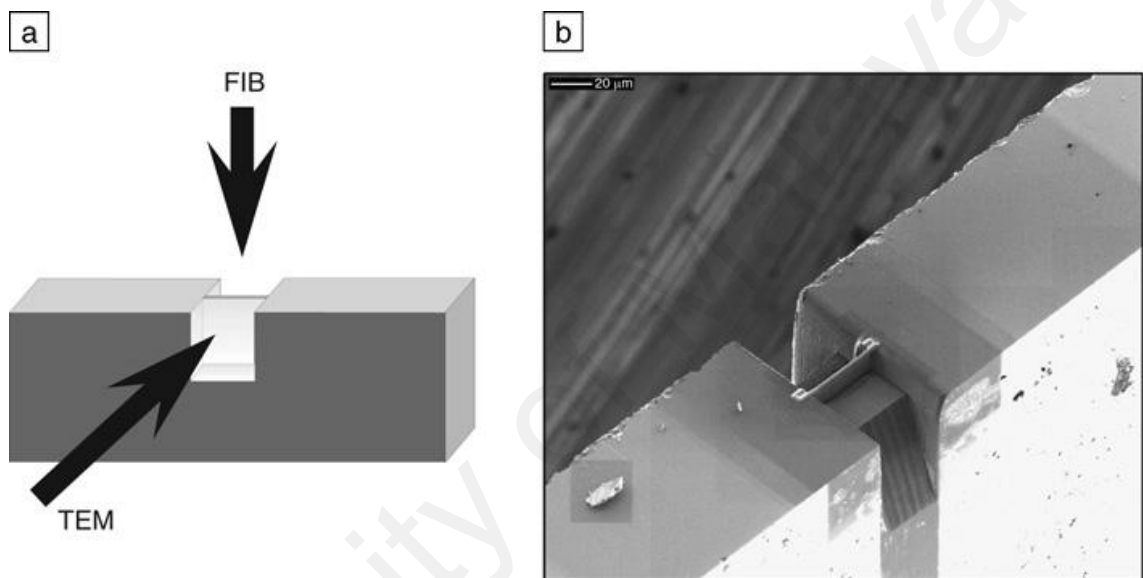


**Figure 3.10** (a) Illustration of H-bar FIB technique. Material on opposite sides of area of interest is FIB-milled until it is electron transparent for TEM measurement. (b) SEM image showing a sample that was mechanically thinned and glued to TEM half grid. Adapted from (J. Mayer et al., 2011).

### 3.5.4 Transmission Electron Microscopy (TEM)

In this work, the Transmission Electron Microscopy (TEM) JEOL JEM 2100F was used to capture a high resolution image and to measure the thickness of a very thin layer in the fabricated device. The structure of thin solid film viewed in cross section can be studied by making the sample surface perpendicular to the electron beam. Using this orientation, the image of the substrate, the thin film layers, and the interfaces can be captured either simultaneously or individually (Bravman & Sinclair, 1984).

The difference between TEM and other optical microscope is the usage of electrons as beam source instead of light. For TEM, high acceleration voltage up to 300 kV was used. When an electron beam passes through the sample, the electron are scattered. The scattered electrons are then being focused into an image or diffraction pattern (depending on the operation mode) via an electromagnetic lens.

### 3.5.5 UPS/XPS measurement

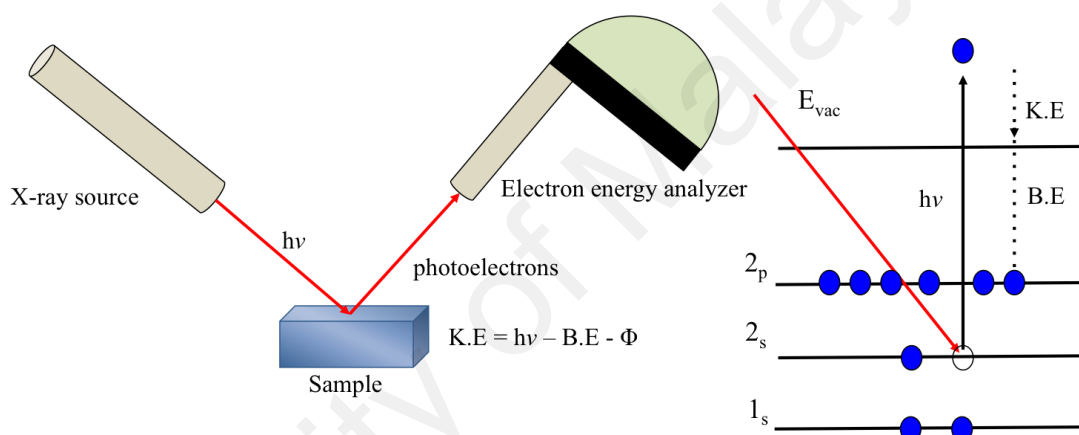
In this work, X-ray Photoemission Spectroscopy (XPS) / *In situ* Ultraviolet Photoelectron Spectroscopy (UPS) are used to probe the structural, chemical formations, surface and identifying electronic information of the material. This technique requires the samples to be loaded in ultra-high vacuum (UHV) conditions with pressure below  $2.7 \times 10^{-8}$  Pa. UHV condition can reduce the possibility of surface contamination by a gas molecule. The difference between XPS and UPS is the source energy. XPS applies 1000 to 2000 eV (high energy x- rays) while UPS uses the energy from ultraviolet rays, which only range from 10 to 40 eV. Thus, electrons from atom core levels are injected in XPS. The valence electron bound in the atoms/molecules as well as solids outer shells are ejected in UPS.

In this technique (shown in Figure 3.11 (left)), the sample surface is subjected to UV radiation or to x-ray photon energy together with the pass energy. Highly energetic x-ray photons knock out the core electron of the atoms from the sample surface as shown in Figure 3.11 (right). This ejected electron is known as photoelectron. The electrons leaving the sample are detected by spectrometer based on their kinetic energy. The analyzer is normally operates as in energy window known as the pass energy, which only accepting the electrons that having an energy within the range of this window. Thus, to maintain a constant energy resolution, the pass energy is fixed throughout the measurement. In this measurement, we used Thermo VG Scientific-Alpha110 electron

energy analyzer to detect the ejected electron. The emitted electrons have measured kinetic energy given as:

$$\text{K.E} = h\nu - \text{B.E} - \Phi \quad \text{Equation 3.13}$$

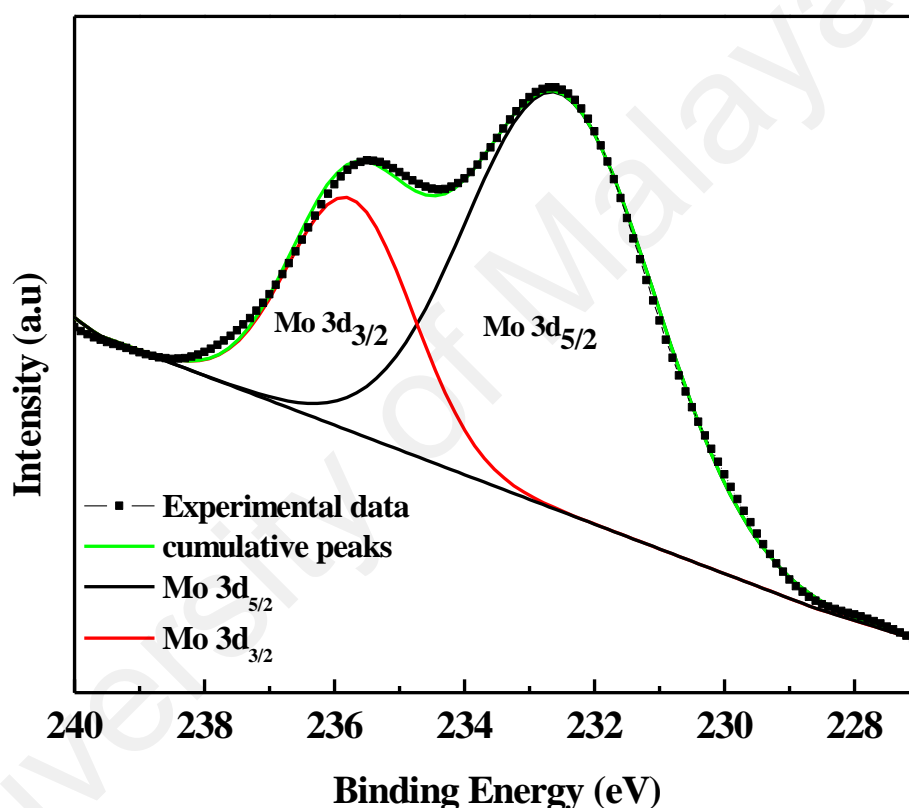
where  $h\nu$  is the energy of the photon and  $\Phi$  is the work function of the spectrometer. BE is the binding energy of the atomic orbital from which the electron originates. BE may regard as the energy difference between the initial and final states after the photoelectron has left the ion.



**Figure 3.11** (Left) Schematic diagram of the basic operation of XPS/UPS measurement. (Right) The excitation of an individual electron from the energy level to the vacuum level.

XPS measurement is used to probe on the core level binding energies (BE) (due to the high energy required to ionize the core-level) of the atoms as well as the chemical shifts in different chemical environment of the measured materials. It is known that BE is dependent on the orbital, the nucleus as well as the element from which it originated. In addition to that, BE location also represents the electron density of the elements. If the electronegativity is high, the atom electron density is reduced (i.e less shielded from the effective nuclear charge) and the core levels of the atoms can be detected at higher binding energies. BE also tends to be consistent with the oxidation state, where more

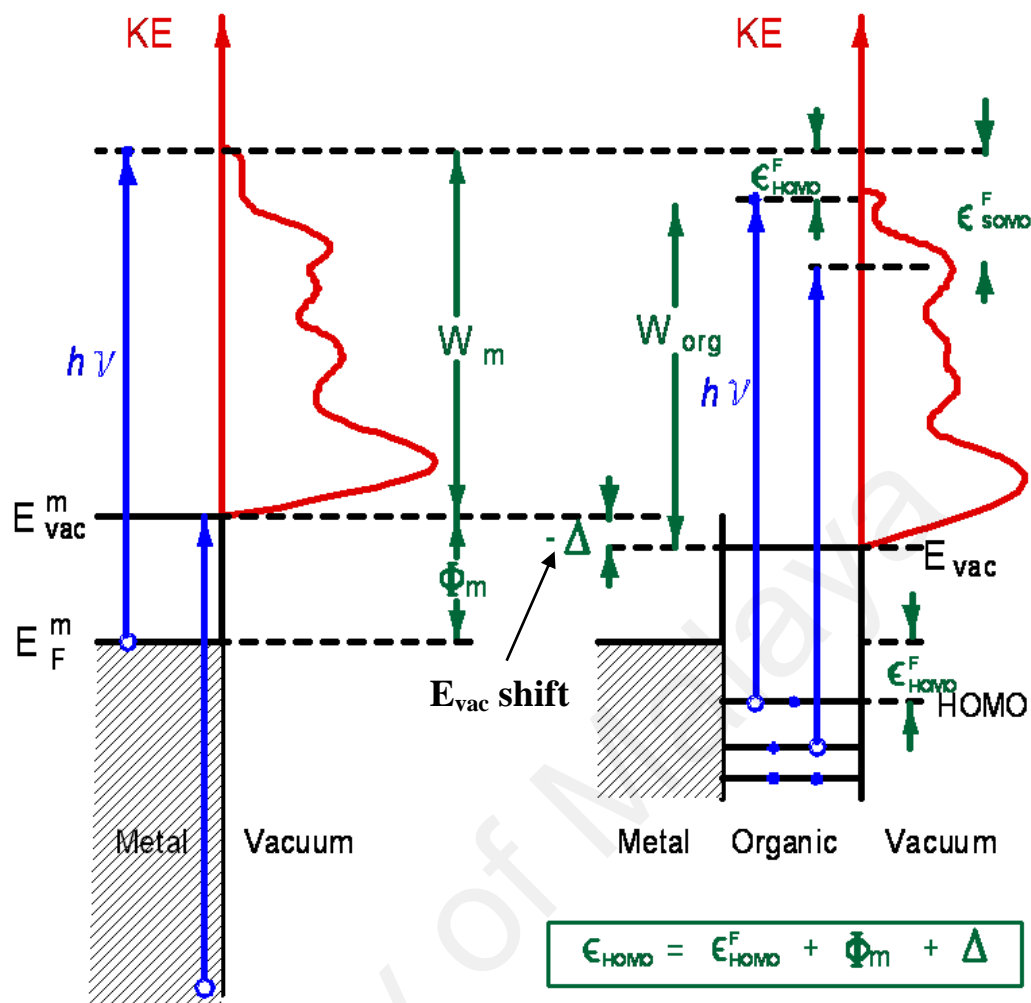
positive oxidation state exhibits a higher BE. These sensitivities make XPS very useful for identifying and measuring the chemical reactions that occur. Figure 3.12 shows an XPS example of the material used in this work. The peak detected is then de-convolute to show the specific chemical states of the element and the relative composition of constituents in the surface region. National Institute of Standards and Technology (NIST) provides a large database of the XPS measurement and specific BE for each element.



**Figure 3.12** Example of XPS peak of Molybdenum trioxide (MoO<sub>3</sub>) where the spin-orbital coupling of 3d<sub>5/2</sub> and 3d<sub>3/2</sub> can be determined.

In order to observe the valence level of electrons, the lower energy irradiation source from Ultraviolet Spectroscopy (UPS) was used. UPS technique is used to measure the material valence-level density of states and thus provide an insight into electron exchange events. Even though only low energy irradiation source is adapted for UPS, the UV-photons exhibit higher photo-ionization cross-section with valence electrons

compared to X-rays. The low energy used for UPS results in a dense convolution of peaks as shown in Figure 3.13. In this thesis work, for UPS measurement, gold is used as a reference. Fermi level ( $E_F$ ) corresponds to zero binding energy (by definition) and the depth below the Fermi level implies the relative energy of the ion remaining after electron emission. Figure 3.13 illustrates the energy level alignment of metal/organic interface using UPS. The left figure shows the metal (Au) photoemission whilst the right figure illustrates photoemission from the organic layer deposited on metal substrate. The low energy cutoff (vertical line) shown in Figure 3.14 corresponds to the vacuum level ( $E_{vac}$ ) of the sample surface. When organic material is deposited on the metal, there is vacuum level shift ( $\Delta$ ) observed due to the presence of a dipole moment at the interface (shown by the black arrow in Figure 3.14). The main feature of organic material which is the material HOMO energy level ( $\xi_{HOMO}^F$ ) can also be observed in the spectra. The HOMO level indicates the hole energy barrier of the material below the Fermi level from the substrates (in this case gold substrate). The LUMO of the material can be determined if the material energy band gap is known.



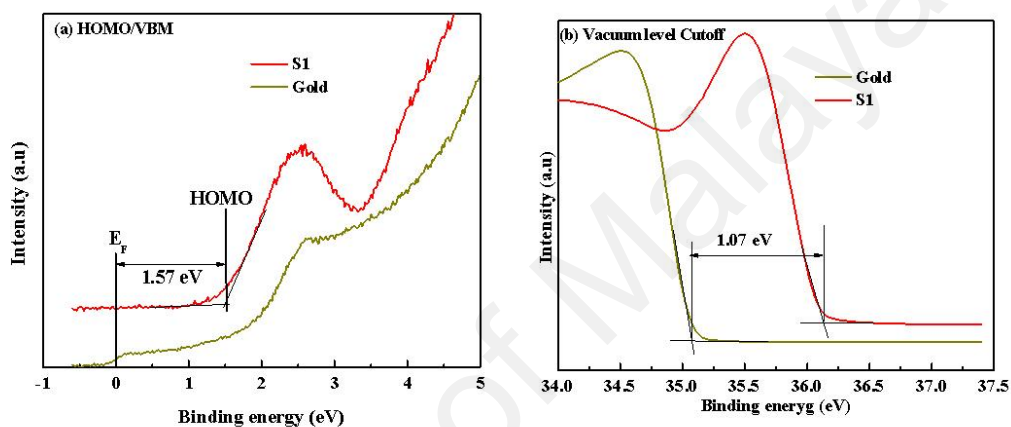
**Figure 3.13** Principle of UPS adapted from (H. Ishii & Seki, 1997). The left is the UPS spectra for metal (Au). The right is the spectra for organic layer deposited on the metal (Au) substrate.

Figure 3.14 shows an example of the measured HOMO or VBM spectra as well as the work function of S1, which was deposited on Gold (Au) substrate. These two material characteristics are determined via linear extrapolation of the energy cutoff regions depicted in (a) and (b). Figure 3.14 is illustrated as a function of binding energy relative to the Au. The raw data in kinetic energy is converted to binding energy via Equation 3.13. In Figure 3.15 (a), the HOMO level of S1 emerges at 1.57 eV below the  $E_F$  of Au. While the work function of the material in Figure 3.14 (b) shows the spectra shifts toward higher binding energy. This implies that the vacuum level of S1 is lower

than that of the Au by 1.07 eV. Figure 3.15 depicts a simple energy level alignment constructed from spectra shown in Figure 3.16. From the value obtained from the spectra, the ionization potential of S1 can be determined using the relation:

$$\text{Ionization potential} = h\nu - (\text{cutoff} - E_{\text{HOMO}}) \quad \text{Equation 3.14}$$

where  $h\nu$  is the photon energy used during the measurement.



**Figure 3.14** Example of UPS measurement to determine the material electronic energy levels.

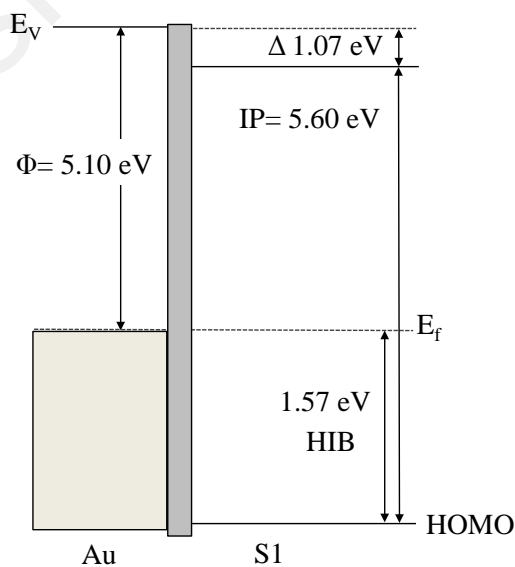


**Figure 3.15** The relative energy diagram constructed from the data in Figure 3.14.

### 3.5.6 Inductively Coupled Plasma / Mass Spectrometry (ICP/MS)

Inductively Coupled Plasma / Mass Spectrometry (ICP/MS) in this thesis work was used to compliment the XPS measurement result, which is to identify the elements in the solution prepared. This equipment is the combination of a high-temperature ICP (Inductively Coupled Plasma) source with a mass spectrometer (MS). ICP source role is to convert the atoms of the elements to ions in the sample. If there are different ions detected, these ions were then separated and detected by MS. Figure 3.17 shows the instrumental setup of ICP/MS. Plasma is produced when the radio frequency (RF) passing through the load coil creates an intense magnetic field, which then interacts on a tangential flow of gas. This process ionized the gas. When there is an electron source from high voltage sparks, very high temperature plasma will be discharged at the end of the tube. The ICP torch is positioned horizontally to generate positive ions instead of photons. The ions are produced and then directed into the MS via the interface region and the elements component will be detected by a detector.

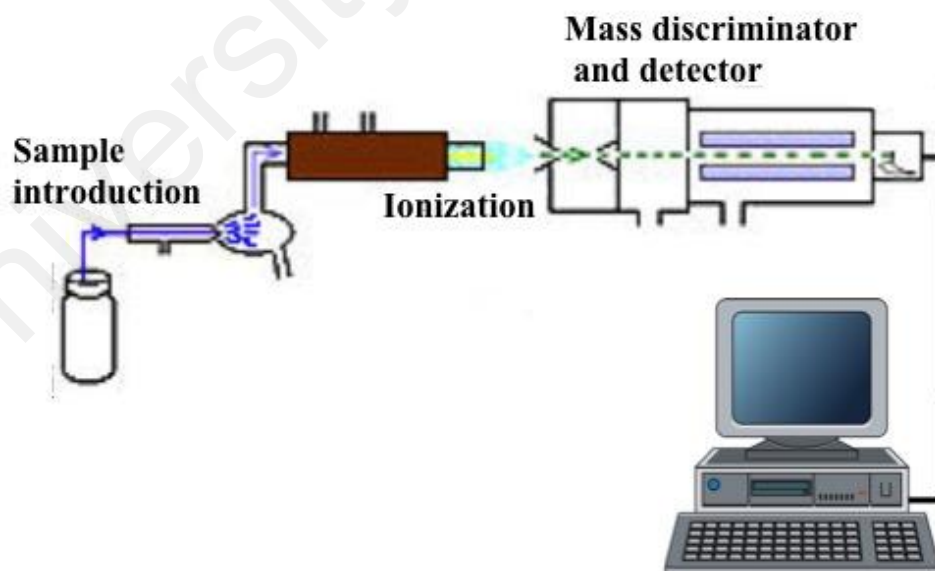


Figure 3.16 ICP/MS instrumental setup.

## CHAPTER 4: EFFECT OF MIXED HOLE-TRANSPORTING HOST ON RED PHOSPHORESCENT OLEDs

### 4.1 Introduction

In OLED, blending the hole and electron transporting host materials are often used to balance the charge density and transport (Song & Lee, 2015; Yook & Lee, 2014; L. Zhang et al., 2015; X. Zhang et al., 2012). It is well known that mixture of materials can form percolative charge transport or traps depending on the energy levels of the materials sites (Grover, Srivastava, Kamalasanan, & Mehta, 2012; Yamada, Sato, Tanaka, & Kaji, 2010). Previous works have shown that incorporation of 7 % tris(4-carbazoyl-9-ylphenyl)amine (TcTa) as co-dopant in poly(9-vinylcarbazole) (PVK) resulted in 43 % enhanced current efficiency in white PhOLED (Lee, Liu, Lee, Chae, & Cho, 2010). The improvement of the device was explained on the basis of triplet energy and the enhancement of hole carrier transport mobility. However, there is no careful study to differentiate the contributions of efficiency enhancement. The mobility is often modeled with hopping transport in disordered energy system with a Gaussian density-of-state (DOS) distribution (Wolf, Bässler, Borsenberger, & Gruenbaum, 1997; Yimer, Bobbert, & Coehoorn, 2009). The change in mobility results from the changes in the DOS hopping sites width (Raj Mohan, Joshi, & Singh, 2008; Scheinert & Paasch, 2014). By mixing different materials of different DOS widths, the resulting DOS may have widened (Wolf et al., 1997) and may as well have narrowed (Raj Mohan et al., 2008).

Hence, in this chapter, the effects of blending hole-transporting materials, by mixing TcTa with PVK as hole blended transporting material was investigated. TcTa has the highest occupied molecular orbital (HOMO) level of 5.7 eV (Yeoh, Ng, Chua, Azrina Talik, & Woon, 2013), which is 0.1 eV shallower than HOMO of PVK at 5.8 eV

(So et al., 2007). Hence, TcTa is expected to induce shallow traps in the hole transport mechanism. The concentration of TcTa is increased from 0 wt % to 50 wt % with the corresponding reduction in the PVK concentration. There has been a lot of works done on the mobility and transport properties of polymer and small molecules (C. Li, Duan, Sun, Li, & Qiu, 2012; Novikov & Vannikov, 2009; Tong, Tsang, Tsung, Tse, & So, 2007; Van der Auweraer, De Schryver, Borsenberger, & Bassler, 1994). However, there is insufficient report on the correlation between the mixture effect on the anode interface and injection, mobility, energetic disorder and film homogeneity.

This chapter presents a detailed experimental study on the effects of blending system in the OLED device. PVK blend with TcTa and 1,2,5-oxadiazole (OXD-7) was used as co-host for hole and electron hosts respectively, for the deep red iridium complex based device. The ratio of OXD-7 remained the same for all fabricated devices. Red phosphorescent emitter bis(1-phenyl-isoquinoline)(acetylacetonato) iridium(III) ( $\text{Ir}(\text{piq})_2(\text{acac})$ ) ( $E_T = 2.1 \text{ eV}$ ) which has a lower triplet energy than the PVK ( $E_T = 2.5 \text{ eV}$ ) was chosen in order to eliminate the triplet exciton energy back transfer loss in the device. It is shown that the optimum ratio of 5 wt % TcTa in PVK is the optimum ratio to achieve high OLED efficiency. TcTa helps to improve the hole and electron balances hence resulting in higher luminescence efficiency. TcTa was reported to have provided more localized regime with lower energy barrier for hole injection at PEDOT:PSS and emissive layer interface. A correlation between the  $\sigma$  and film morphologies suggests that blending of TcTa molecules in the film changes not only the film homogeneity and roughness but also the energetic disorder.

## 4.2 Sample preparation for measurement

All materials were purchased and used as received without further purification. PVK (average  $M_w = 1,100,000$  g/mol) was purchased from Sigma-Aldrich. TcTa, 2,7-bis(diphenylphosphoryl)-9,9'-spirobifluorene (SPPO13) and OXD-7 were purchased from Lumtech. Ir(piq)<sub>2</sub>(acac) was obtained from American Dye Inc.

### 4.2.1 Time of Flight (ToF) Measurement

ITO/organic layer/Al device structure was used for Time of Flight (ToF). The organic layer consists of PVK doped TcTa (with TcTa concentration varied from 0 wt % to 50 wt %) dissolved in chlorobenzene. The layer was spin coated on top of ITO to get a thickness of  $\sim 1$   $\mu\text{m}$  before Al cathode was deposited on top of it. Field and temperature dependence of mobility for the samples was determined using ToF technique carried out in vacuum. A sample was mounted on the temperature controlled vacuum stage HCS622VXY. A nitrogen laser NL 100 with the peak wavelength of 337 nm and FWHM 3.5 nm was used as an excitation source. The optical pulse was split into two beams by a beam splitter. The reflected light was incident on the THORLABS DET 25K/M GaP Biased Detector with a detection range of 150-550 nm. It was used to detect the on-set of pulsed laser for synchronization with the Agilent Technologies Infinii Vision DSO-X-3052A Digital Oscilloscope. The transmitted laser light was used to excite the ITO side of the sample. The photocurrent transient was detected with a digital oscilloscope triggered by the laser pulse. Instec Inc. mK1000 and LN2-P liquid nitrogen cooling system was connected to the temperature controlled vacuum stage to control the temperature.

### 4.2.2 Energetic disorder, $\sigma$ measurement

The energetic disorder,  $\sigma$  and the mobility field as well as temperature dependence of the PVK:TcTa mixture are measured using temperature dependence mobility via ToF

(Matsusue, Suzuki, & Naito, 2005; Naka, Okada, Onnagawa, Yamaguchi, & Tsutsui, 2000).  $\sigma$  can be related to the distribution parameters such as density of states (DOS) energetic width (Kreouzis et al., 2006). In order to obtain the  $\sigma$ ,  $\mu_0$  (zero field mobility), is required. The zero field mobility  $\ln \mu$  ( $E=0$ ) for each temperature was extracted from the y-intercept of a straight-line fit to the plot  $\ln \mu$  versus  $\sqrt{E}$  via the Poole-Frenkel equation (Frenkel, 1938) :

$$\ln \mu = \ln \mu_0 + \beta \sqrt{E} \quad \text{Equation 4.1}$$

where  $\beta$  is a slope of Poole-Frenkel plot and  $E$  is the electric field strength within the device defined by  $\left[ \frac{V}{d} \right]$ .  $\mu_0$  corresponds to the mobility from experiment extrapolated to zero field ( $E = 0$ ).

Using Bässler Gaussian Disorder Model (GDM) (H. Bässler, 1993) when  $E = 0$ , it is proposed that zero field mobility would exhibit a non-Arrhenius temperature dependence as in :

$$\mu(0, T) = \mu_\infty \exp - \left[ \frac{2\sigma}{3k_B T} \right]^2 \quad \text{Equation 4.2}$$

where  $\mu_\infty$  is the prefactor mobility (the mobility at zero field and infinite temperature),  $k_B$  is Boltzmann's constant and  $T$  is the temperature.

By plotting  $\ln \mu_0$  vs.  $1/T^2$ ,  $\mu_\infty$  can be obtained from the y-intercept and the  $\sigma$  can be deduced from the slope based on the following equation (H. Bässler, 1993):

$$\ln \mu_0 = \ln \mu_\infty - \left[ \frac{2\sigma}{3k_B} \right]^2 \frac{1}{T^2} \quad \text{Equation 4.3}$$

### 4.2.3 PhOLED device fabrication and measurement

The device structure consists of ITO (100 nm) / PEDOT:PSS (Al 4083) (40 nm) / EML (75nm) / SPPO13 (20 nm) / CsF (1 nm) / Al (100 nm). Figure 4.1 shows the energy levels and the device structure used throughout the experiment. The EML layer for the device is PVK: TcTa :OXD-7:Ir(piq)<sub>2</sub>(acac) with a blending ratio of 70 - x : x : 24 : 6 where x is the concentration of TcTa varying from 0 wt % , 5 wt % , 10 wt % , 30 wt % , 50 wt % , 70 wt % and 100 wt % with respect to PVK. Pre-patterned ITO was ultrasonically cleaned using deionized (DI) water, acetone, isopropyl alcohol and then DI water again for 10 minutes, followed by oxygen plasma treatment for 5 minutes. Next, 40 nm of PEDOT: PSS was spin-coated on top of the substrates and immediately baked in N<sub>2</sub> glovebox environment for 10 minutes at 150 °C. The EML dissolved in chlorobenzene was spin coated on top of PEDOT: PSS and then baked at 80 °C for 30 minutes. Following that, 20 nm of SPPO13 dissolved in isopropyl alcohol was spin coated on top of EML. Next, 1 nm of CsF and 100 nm of Al were vacuum deposited at a base pressure of  $2.5 \times 10^{-4}$  mbar without breaking the vacuum. All the devices were encapsulated using UV curable epoxy and glass lid.

The film thickness was measured using P-6 profilometer (KLA-Tencor). Electroluminescence and photoluminescence intensities were measured using SM442 Spectrometer and Perkin Elmer Luminescence Spectrometer LS50B respectively. For AFM, a single layer of emissive layer (with different TcTa concentrations) was spin coated on top of ITO glass. The surface morphology of the films was investigated via Atomic Force Microscopy (AFM, NT-MDT NTEGRA-Prima). The sample absorption was measured using Perkin Elmer PE750 UV-Vis. The device current-brightness-voltage characteristics were measured using Konica Minolta Cs-200 integrated with Keithley 276 source meter.

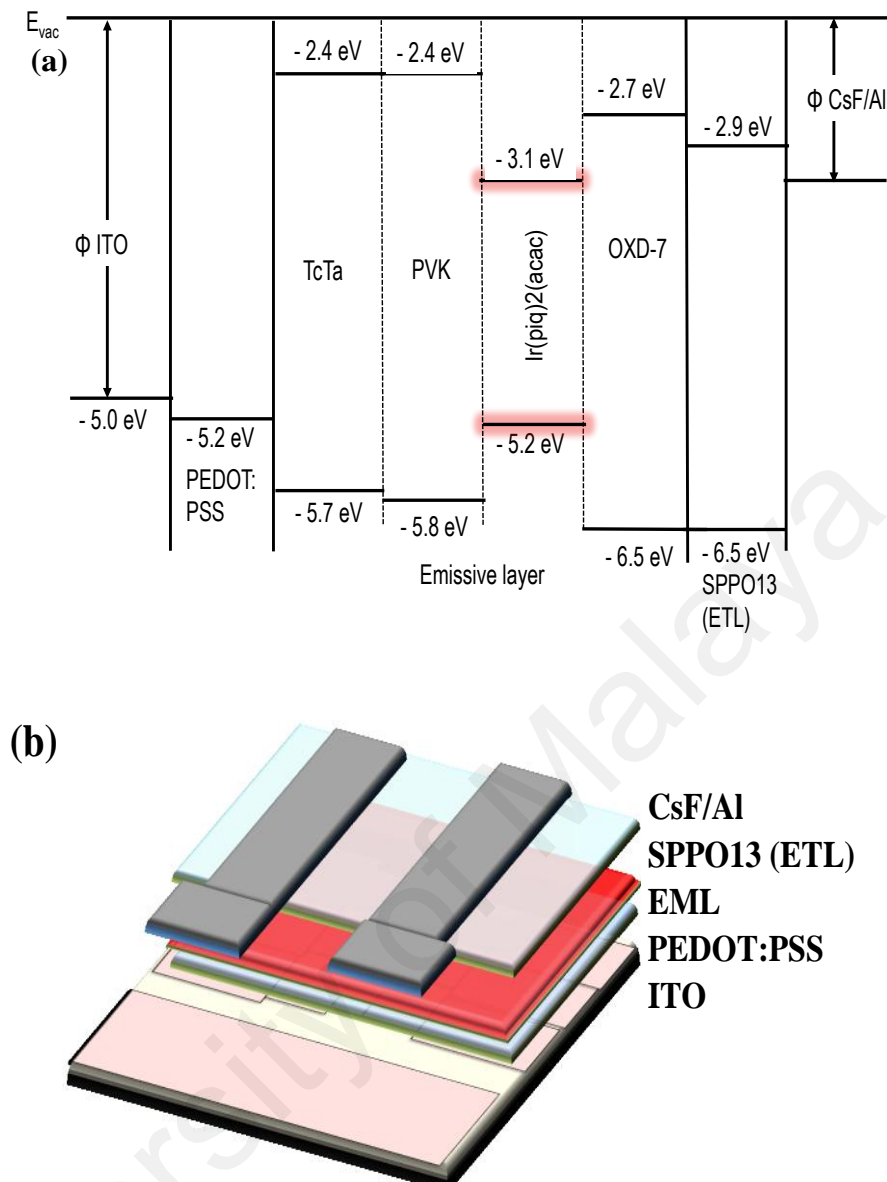


**Figure 4.1** The (a) energy levels and (b) device structure fabricated in the experimental works.

## 4.3 Results and Discussions

### 4.3.1 ToF mobility

The curve for mobility measurement of PVK film using ToF is shown in Figure 4.2. It shows the photocurrent transients at 300K for 0 wt % TcTa in a log-log scale and linear-linear scale in the inset.

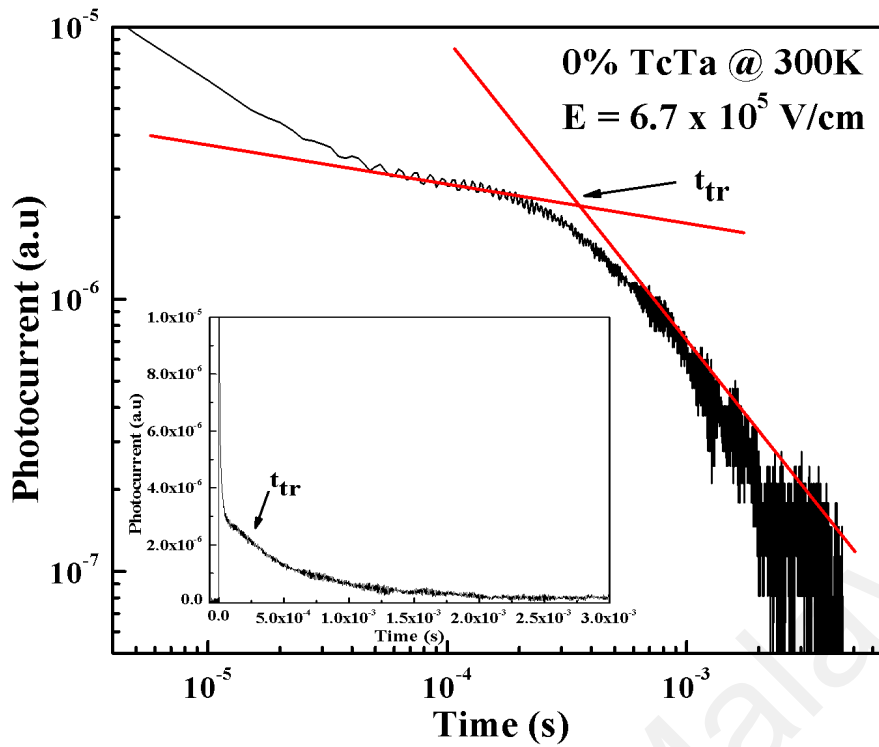


**Figure 4.2** Transient photoconductivity of pure PVK thin films. The transient was captured at 300 K and at the electric field of  $6.7 \times 10^5$  V/cm. A featureless signal could indicate a dispersive hole transport shown in the double linear plot (inset). Thus, a double logarithmic curve was plotted to find the plateau, which corresponds to the transit time of the hole transport.

The intersection of asymptotes to the plateau and tailing edge of the photocurrent transients indicates the carrier transit time ( $t_{tr}$ ), which is the arrival time of the first carrier at the counter electrode. The mobility,  $\mu$  at room temperature is calculated from the equation:

$$\mu = \frac{d^2}{V t_{tr}} \quad \text{Equation 4.4}$$

where  $d$  is the polymer film thickness,  $V$  is the voltage applied and  $t_{tr}$  is the transient time from ToF measurement.

Figure 4.3 shows the result of mobility versus  $\sqrt{E}$  for 0 wt %, 10 wt %, 20 wt %, 30 wt% and 50 wt% TcTa samples. ToF measurement for sample more than 50 wt % of

TcTa could not be performed due to poor film-forming and strong molecular aggregation properties of small molecule (Höfle, Pfaff, et al., 2014). The mobility versus  $\sqrt{E}$  curves for different concentrations exhibits the electrical field dependence of hole mobility follows the PF behavior shown in Equation (2.5). Note that for 10 wt % and 20 wt % blend system, the mobility is shown at higher electric field ( $> 1750 \text{ V}^{1/2}/\text{cm}$ ) compared to 30 wt % and 50 wt % blend system due to low electric field dependent mobility of the blend system.

The dependence of hole mobility with electric field implies that the mobility may be influenced by charge-carrier hopping in positional and energetical disorder of hopping sites, as suggested by Bässler (H. Bässler, 1993). In disordered material, the charge carrier is transported via hopping conduction where each molecule is considered as a transport site for charge conduction. The results also show the hole transport is thermally activated hopping as evident from the temperature dependent hole mobility.

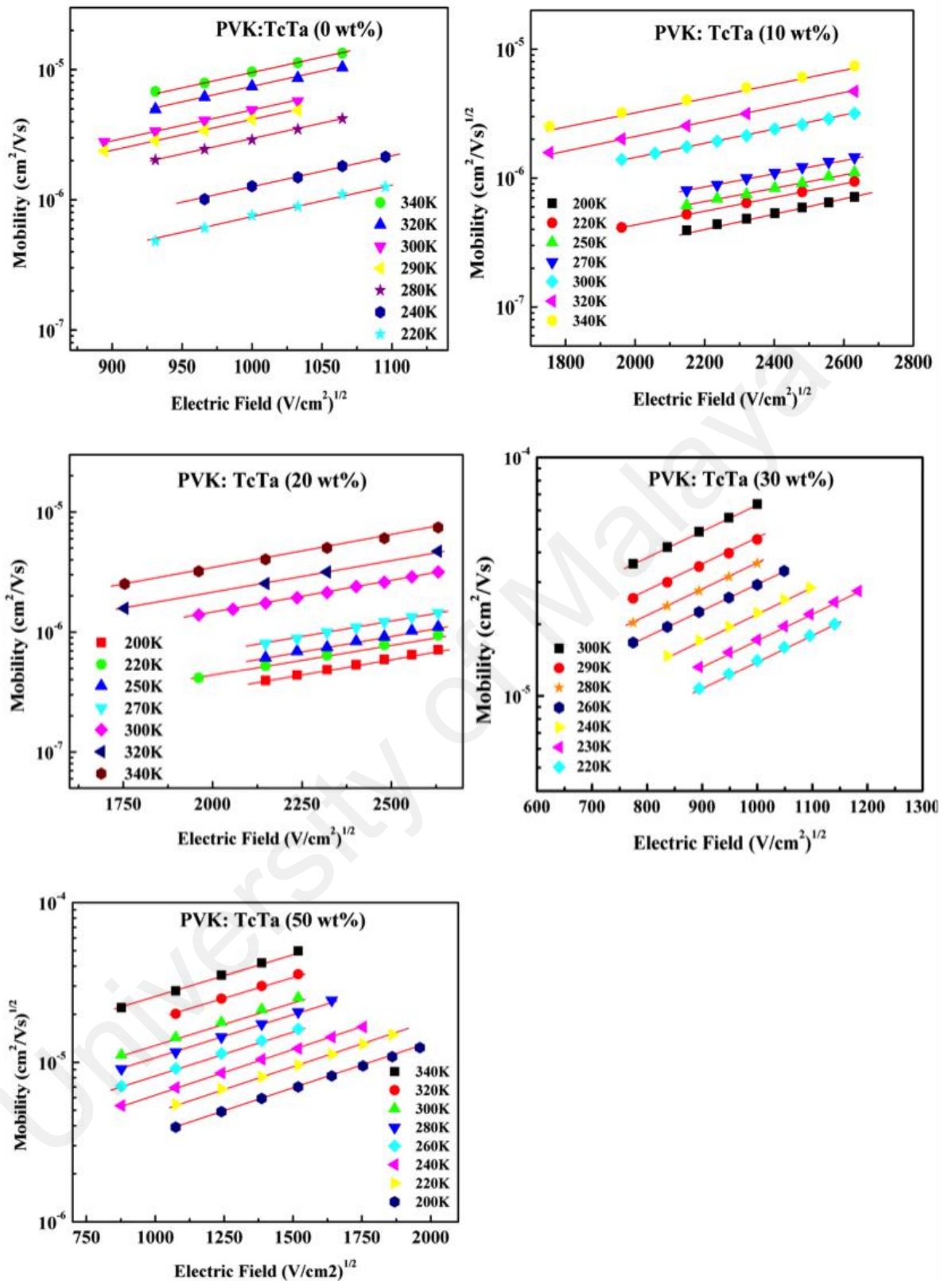


**Figure 4.3** Mobility vs.  $E^{1/2}$  result curves for 0 wt %, 10 wt %, 20 wt % , 30 wt % and 50 wt % concentrations for temperature range 200 K to 340 K.

The mobility at room temperature from the curve in Figure 4.3 was extracted at  $1 \times 10^6 \text{ V/cm}^2$  for different concentrations of TcTa (0 wt % – 50 wt %) and plotted in Figure 4.4. Note that there is intermediate mobility at 5 wt %, 25 wt % and 45 wt% added (not shown in Figure 4.3). These mobilities are measured at room temperature in order to establish a trend.

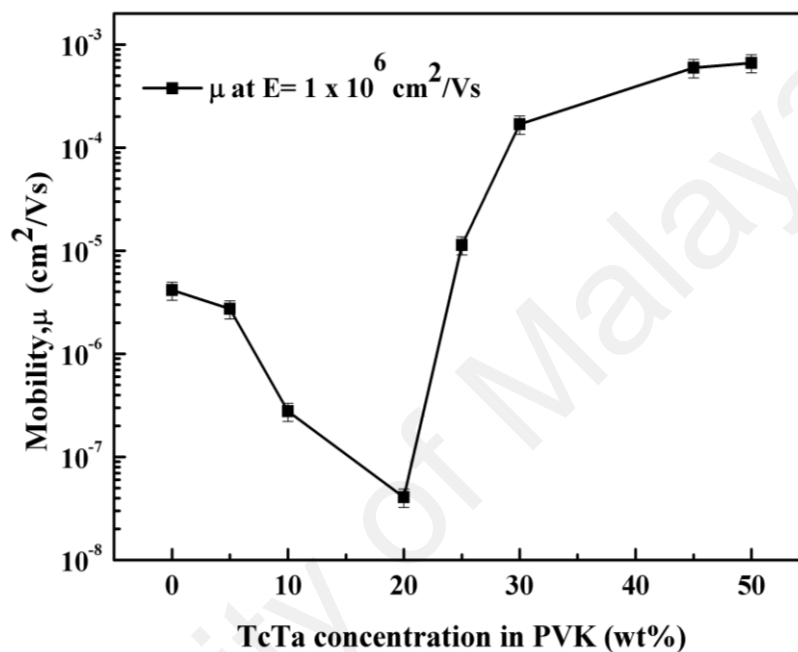


**Figure 4.4** Extrapolated hole mobility of TcTa and PVK blended with TcTa concentration varied from 0 wt % to 50 wt % in room temperature at  $1 \times 10^6 \text{ V/cm}^2$ .

#### 4.3.2 Mechanism of charge transport in PVK:TcTa mixture

Figure 4.4 shows that the mobility of pristine PVK is  $4.15 \times 10^{-6} \text{ cm}^2/\text{Vs}$ , which is consistent with the published data (Pai, Yanus, & Stolka, 1984). The mobility reduces from to  $3.86 \times 10^{-8} \text{ cm}^2/\text{Vs}$  when the concentration of TcTa increases from 0 wt % to 20 wt %. However, the mobility increased to  $6.65 \times 10^{-4} \text{ cm}^2/\text{Vs}$  when TcTa concentration increases to 50 wt %. Almost the same behavior has been reported when PVK is doped with small molecules materials (Borsenberger, 1998). At 50 wt% TcTa, the mobility are measured to be in the range of  $10^{-4} \text{ cm}^2/\text{Vs}$ , which is comparable to the reported pristine TcTa mobility reported at  $1.5 \times 10^{-4} \text{ cm}^2/\text{Vs}$  (Xiao et al., 2011). This is explained by the

transition from traps controlled hopping transport to hopping via both materials. At low concentration of TcTa in PVK ( $\leq 20$  wt %), TcTa could initially act as shallow traps.

The idea of shallow trap is best understood using Miller-Abrahams equation which is the transfer rate of hole between molecule  $i$  and  $j$  with equation given as below (Miller & Abrahams, 1960):

$$v_{ij} = v_o \exp(-2\gamma a) \begin{bmatrix} \exp\left(-\frac{\epsilon_i - \epsilon_j}{KT}\right) \exp\left(\pm \frac{eEa}{KT}\right) & \epsilon_i - \epsilon_j > 0 \\ 1 & \epsilon_i - \epsilon_j < 0 \end{bmatrix} \quad \text{Equation 4.4}$$

where  $E$  is the applied electric field,  $a$  is the intersite distance,  $k$  is the Boltzmann constant,  $T$  is the carrier temperature for hopping transport in Kelvin,  $v_o$  is the maximum attempt to hop frequency which is in the range of phonon frequency.

At  $100^\circ\text{C}$  with  $E = 6.7 \times 10^5$  V/cm, the intersite hopping distance and intersite hopping energy difference between a given TcTa molecule and PVK molecule is  $\sim 0.3$  nm and  $0.1$  eV respectively (Preezant & Tessler, 2006; Woon et al., 2015). There is probability that the trapped hole on a TcTa molecule could hop onto the next PVK molecule. This becomes more important as more TcTa energy sites are available. At low concentration of TcTa, transport of charge trapped in TcTa is slow resulting in lower mobility. As the concentration of TcTa increases, there are more TcTa energy sites available. Some charge carriers begin to hop between these sites. At higher concentration, which is more than 20 wt %, the hopping transport is dominated by TcTa, which results in a higher mobility transport.

PVK:TcTa blending system could be considered as host-guest system. The mechanism of ToF mobility trend in Figure 4.4 could be described as hopping in four different regimes as illustrated in Figure 4.5. In the first regime (Figure 4.5 (a)), since the concentration of TcTa (guest) is still smaller compared to PVK, charge carrier could

hop among the PVK (host) site. As the concentration of TcTa increases, charge carrier mobility decreases (Figure 4.5 (b)). When the concentration of TcTa is sufficiently large ( $\geq 20$  wt %), there is a large overlap between the upper tail of PVK DOS with lower tail of TcTa DOS, resulting in molecules of both materials to participate in charge carrier transport ((Figure 4.5 (c)). When the TcTa concentration is higher than that of PVK, the mobility is then dominated by TcTa sites ((Figure 4.5 (d)). The blending of organic materials may be influenced by the energetic disorder width,  $\sigma$  of the blend system hopping site, which will be discussed in the next section.

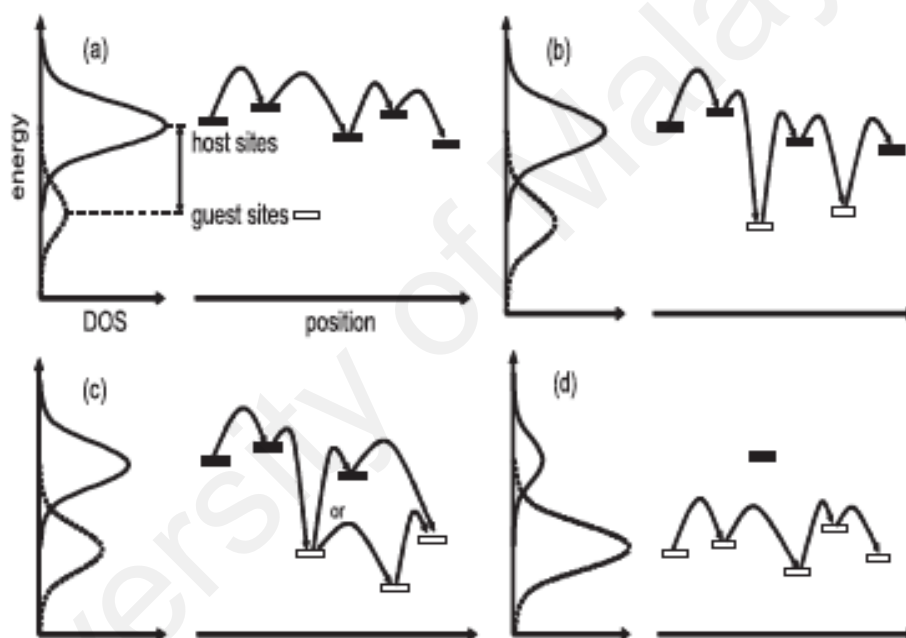


**Figure 4.5** Four different regimes in host-guest system. Adapted from (Yimer et al., 2009).

### 4.3.3 Energetic disorder, $\sigma$

To calculate the energetic disorder, temperature dependence mobility was studied. In  $\mu$  ( $E=0$ ) for each temperature was first extracted from the y-intercept of a straight-line fit to the plot  $\ln \mu$  versus  $\sqrt{E}$  via the Poole-Frenkel equation. The curve for  $\ln \mu$  ( $E=0$ ) versus electric field is shown in Figure 4.6. All mobility trends display poole-frenkel type dependence whereby the mobility increases with electric field as shown in in the

graph ( $\ln \mu$  vs.  $E^{1/2}$ ). The increasing mobility in  $\ln \mu$  vs.  $E^{1/2}$  could be observed for all concentrations and could be attributed to the tilting of density of states by the applied potential that result in decreasing energetic barrier as seen by the charge carriers.

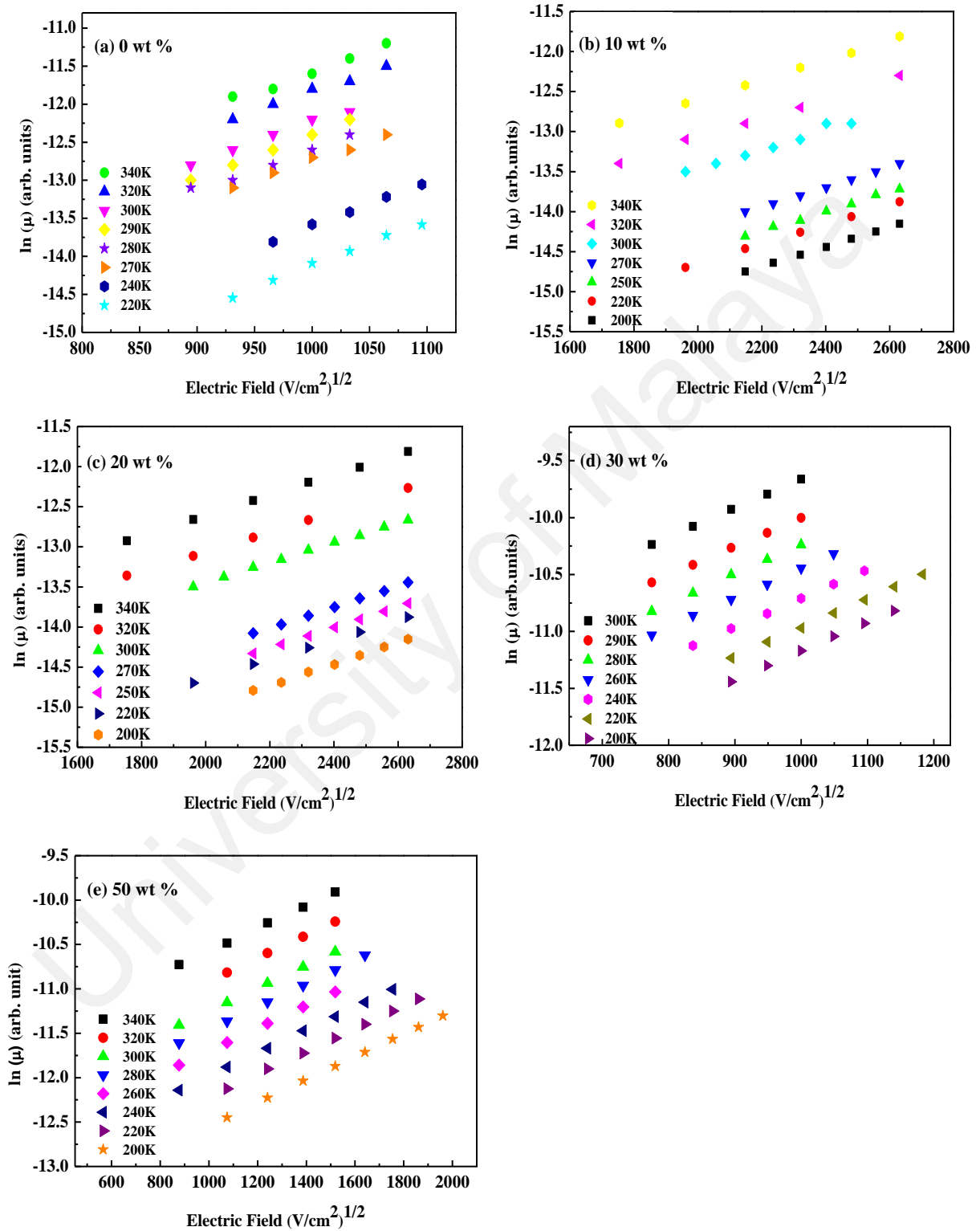


**Figure 4.6**  $\ln \mu$  vs.  $E^{1/2}$  curves for 0 wt %, 10 wt %, 20 wt %, 30 wt % and 50 wt % concentrations when subjected to temperatures range 200 K to 340 K.

Figure 4.7 (a) shows the  $\ln \mu_0$  vs.  $1/T^2$  graph for different concentrations of TcTa in PVK while Figure 4.7 (b) shows the energetic disorder for different concentration extracted from (a). Table 4.1 shows the derived values of  $\mu_\infty$  and  $\sigma$  derived from the fitting data. It can be observed that the slope (indicating the  $\sigma$  of the mixture) reduces with increasing concentration of TcTa.

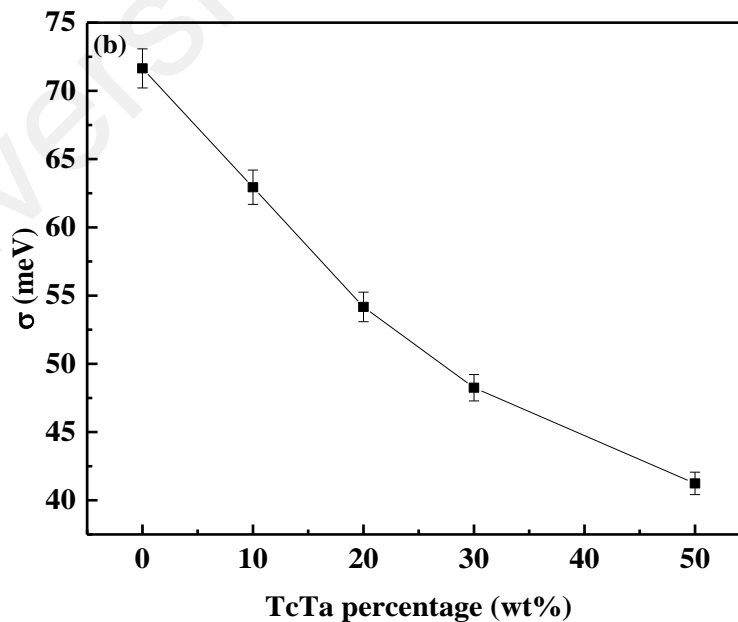
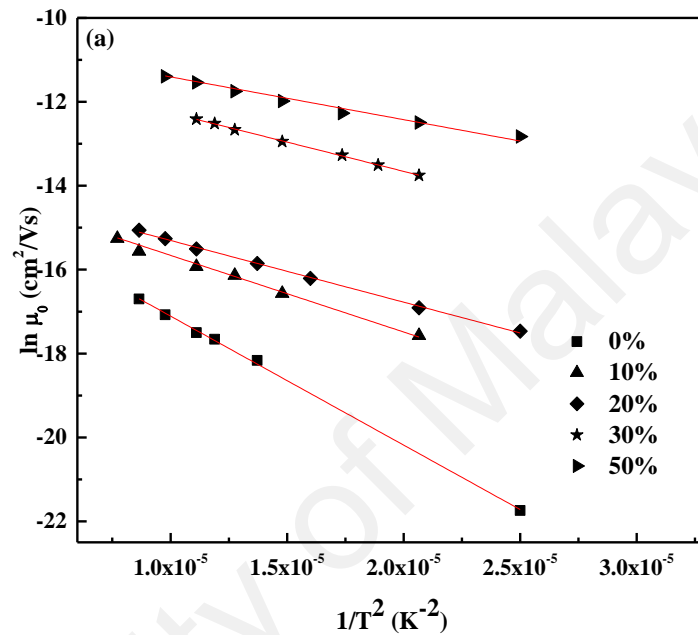


**Figure 4.7** (a)  $\ln \mu_0$  vs.  $1/T^2$  for 0 wt %, 10 wt %, 20 wt %, 30 wt % and 50 wt % concentrations of TcTa (red line is the fitted line for reference) (b)  $\sigma$  versus concentration of TcTa (0 wt % to 50 wt %).

**Table 4.1** Parameters for hole transport in pure PVK and PVK: TcTa extracted from data in Figure 4.7 (a).

TcTa percentage in PVK (wt%)	$\ln u_{\infty}$ (cm <sup>2</sup> /Vs)	$\sigma$ (meV)
0	-14.03	71.65
10	-13.83	62.94
20	-13.19	50.17
30	-10.87	48.25
50	-10.38	41.23

As shown in Figure 4.7 (b), the  $\sigma$  for pristine PVK film is 71.65 meV, which is almost the same as demonstrated by Borsenberger et.al (Wolf et al., 1997). The  $\sigma$  for sample with 50 wt % PVK doped with TcTa decreases down to 41.23 meV. The  $\sigma$  of pure TcTa reported is 35.28 meV (Noh, Suman, Hong, & Lee, 2009). In a mixed-hole transporting host, holes would hop between TcTa and PVK. Thus, energetic disorder,  $\sigma$  is expected to increase. A superimposed disorder Gaussian density of states is expected, with one Gaussian DOS for free carriers (PVK) and one for trapped carriers (TcTa). However, even at 10 wt % TcTa, the  $\sigma$  decreased from 71.65 meV (pristine PVK) to 62.94 meV. Given  $\sigma$  of pure TcTa and PVK are 35.28 meV and 71.65 meV respectively, ~16 % of PVK energy sites from the upper tail of Gaussian DOS overlap with the TcTa energy sites. Any hole carriers found themselves at the upper tail of PVK Gaussian DOS will have 50 % chance to hop onto the lower tail of TcTa Gaussian DOS. This can explain the reduction of  $\sigma$  in the mixture when the concentration of TcTa is sufficiently high. However, this does not explain the reduced  $\sigma$  even at 10 wt %. This led us to suggest the possibility of phase segregation even at low concentration.

If phase segregation occurs, charge transport in these films could take place via a mixture of ordered (TcTa) and less ordered regions (PVK). On the other hand, all zero field mobility values (shown in Table 4.1) extrapolated at infinite temperature,  $\mu_{\infty}$  increase with increasing concentrations of TcTa in PVK. The result presented here is in

agreement with the result demonstrated when an amorphous glass of the neat compound was replaced by a dispersive transport molecule in an “inert polymer” (Van der Auweraer et al., 1994). Vannikov *et. al* demonstrated that the reduction of  $\sigma$  and an increment of  $\mu_{\infty}$  when a polymer is doped with triphenylamine (Vannikov, Kryukov, Tyurin, & Zhuravleva, 1989) could be attributed to an increase of polaron binding energy (carrier interaction with phonons) (Van der Auweraer et al., 1994). Recently, Mohan *et. al* demonstrated via Monte Carlo simulation that the overall  $\sigma$  is dependent on the system morphology. The energetic disorder,  $\sigma$  is reduced with the presence of ordered regions in the disordered material (Mohan, Singh, & Joshi, 2012; Raj Mohan & Joshi, 2006). In order to find the correlation between morphology the charge carrier transport, the films were subjected to AFM measurement.

#### 4.3.4 Morphology via AFM topography

Figure 4.8 shows 2D morphology and the phase images of these films probed via AFM. The root mean square roughness,  $R_s$  is increased from 0.224 nm to 0.647 nm or 1.057 nm as 5 wt% or 100 wt% of TcTa is blended. From the phase contrast imaging, we could determine whether there is any presence of aggregation as a result of difference between adhesion and viscoelasticity. It also can be seen in Figure 4.8 (c) that with 100 wt% TcTa, the film appears to exhibit multi-branching tree-like form. Such could indicate that TcTa tends to form crystal dendrite and displays a tendency to be higher order than amorphous PVK. In the phase image of 5 wt % TcTa, it can be observed that there is a difference in phase contrast imaging which could indicate the onset of phase segregation.

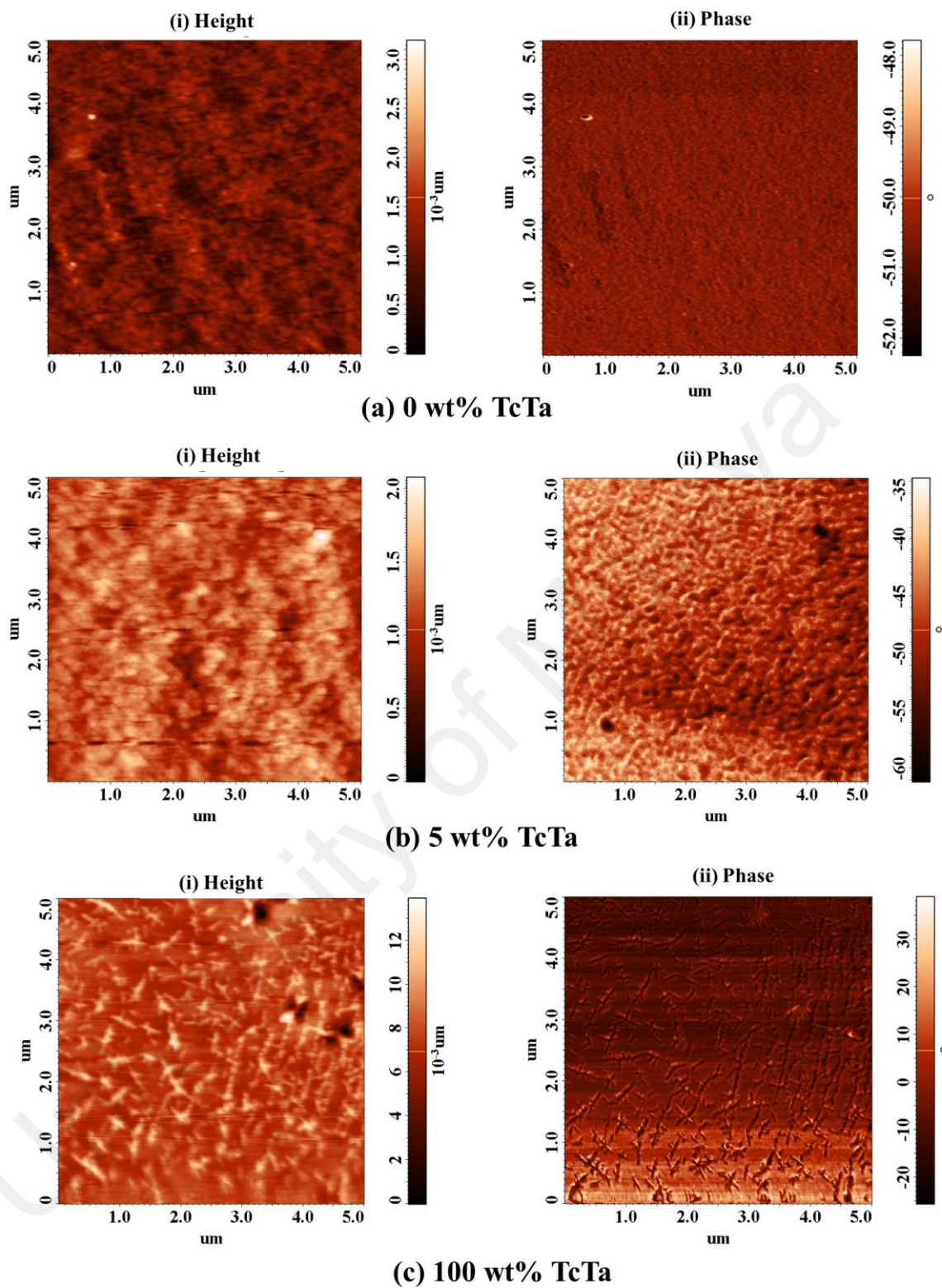
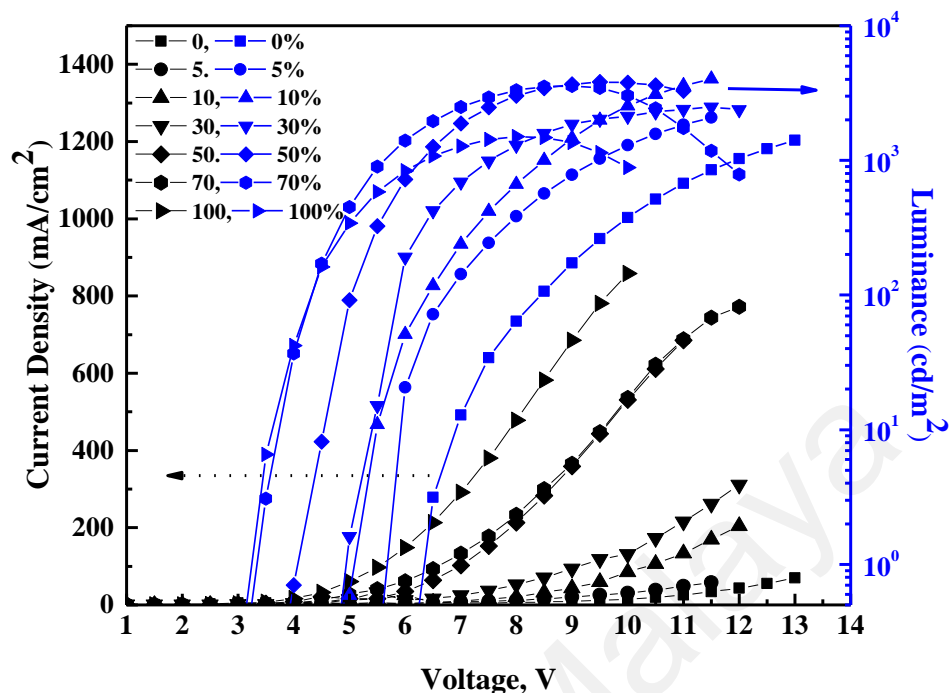


**Figure 4.8** (i) 2D morphology and (ii) phase image of thin film of (a) pristine PVK (0 wt%), (b) mixed hosts with 5 wt% TcTa and (c) pristine TcTa (100 wt%).

From the data that have been collected up to this point, we could conclude that the charge carrier mobility is influenced by not only the disorder but also the system morphology configuration. In addition to that, Poplavskyy *et al.* explained that the ToF measurement is not the only parameter that is relevant to the real device performance and but also the magnitude of steady state conduction current and other processes such as injection from contact as well as the charge trapping (Poplavskyy *et al.*, 2005).

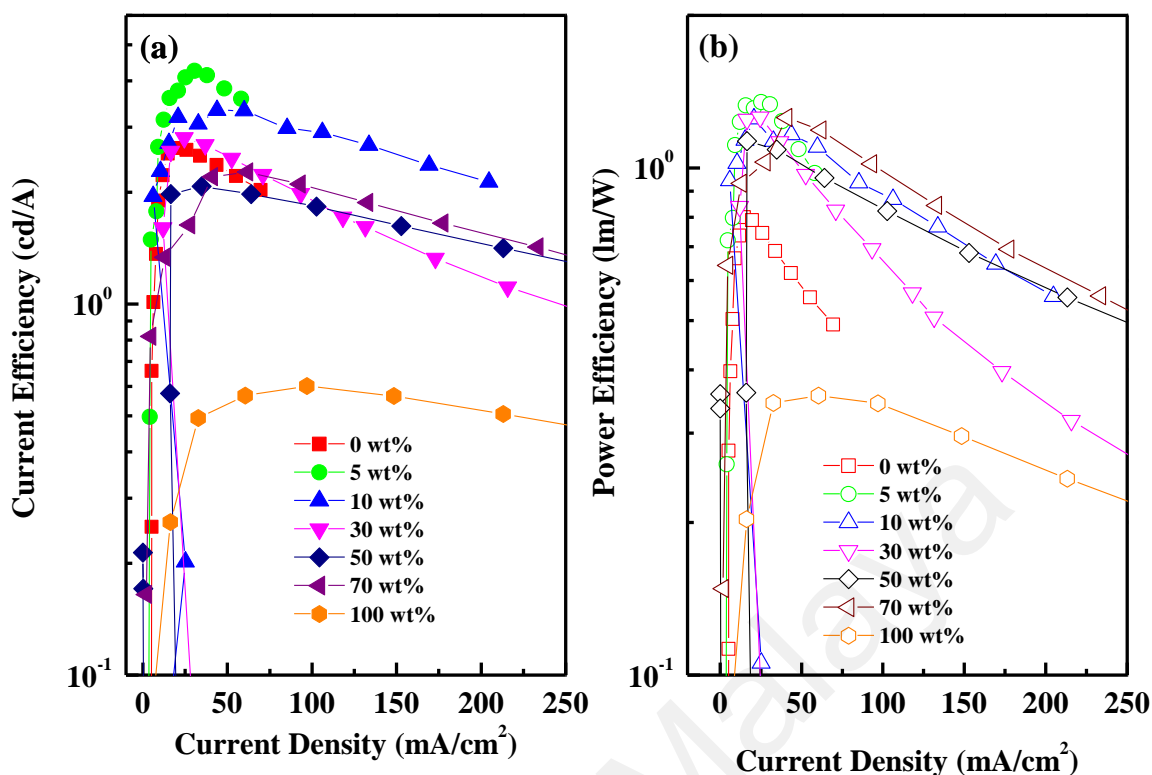
#### 4.3.5 Effect of blending system on Red PhOLED device efficiency

Figure 4.9 shows the curve of Current density- Voltage- Luminance ( $J$ - $V$ - $L$ ) for the fabricated device with different TcTa concentrations in PVK. The current density of the device increased as the concentration of TcTa increased. The increase may be attributed to the high exciton concentration formed, which originates from the increment of hole accumulations. It is also shown that the devices with TcTa doped in the emissive layer exhibit a higher current flow compared to the device without TcTa. A higher applied voltage is necessary for the device with lower TcTa concentration to get the same current density. To get  $100 \text{ mA/cm}^2$ , only 5.5 V is required for 100 wt% TcTa compared to 12.7 V for 0 wt%. The turn on voltage ( $V_{\text{on}}$ ) decreases with increasing concentration of TcTa indicating reduced injection barrier from PEDOT:PSS to emissive layer. The  $V_{\text{on}}$  (at  $1 \text{ cd/m}^2$ ) for 100 wt% TcTa is only 3.2 V which is much lower compared to that of 0% TcTa at 6.3 V. This is surprising since the difference in HOMO levels between PVK and TcTa is small ( $\sim 0.1 \text{ eV}$ ). The effect of current density enhancement is reflected in the device current efficiency, depicted in Figure 4.10.



**Figure 4.9** Current density-Voltage-Luminance characteristics of the red devices fabricated with different TcTa concentrations ( 0 wt % - 100 wt %)

Figure 4.10 shows the current efficiency and power efficiency versus current density for both devices with and without TcTa. By doping TcTa into the emissive layer, the turn-on voltage reduces and the brightness increases. Besides that, the efficiency of the device with TcTa is also higher compared to the device without TcTa. At 20 mA/cm<sup>2</sup>, the device with 5 wt % TcTa shows the highest current efficiency of up to 4.16 cd/A, which is 100 % higher than the device without TcTa with only 2.6 cd/A. This increment is higher compared to the reported 43 % increment (Lee et al., 2010) when TcTa is added into the emissive layer.



**Figure 4.10** (a) Current Efficiency versus Current Density of the devices. (b) Power Efficiency versus Current Density of the devices.

The effectiveness of blending TcTa in PVK is shown up to 30 wt %, where the current efficiency is higher compared to the control device (0 wt %). Adding more TcTa (> 30 wt %) apparently reduced the current efficiency to lower than that of the control device. This may be attributed by a large shift of the charge carrier balance. As the hole injection barrier from PEDOT:PSS to emissive layer reduces, there would be more holes accumulated in the emissive layer. Thus, the hole population outnumbers that of the electron (as no changes made for electron part). This result implies that 5 wt % of TcTa added in the device is sufficient to enhance the hole and electron charge balance and thus improve the device efficiency. On the contrary, it is observed that the power efficiency remains relatively stable over a large range of TcTa concentration, between 10 wt % to 70 wt %. Poor device current efficiencies may be attributed to the structural defect densities. When the volume of TcTa is higher than PVK, the mixture tends to easily crystallize. To gain more insight on the effect of different concentrations of TcTa

in hole carrier, hole dominating devices have been fabricated. Figure 4.11 shows the characteristic of hole dominating devices with polymer film consists of PVK:TcTa:OXD-7:Ir(piq)<sub>2</sub>acac).

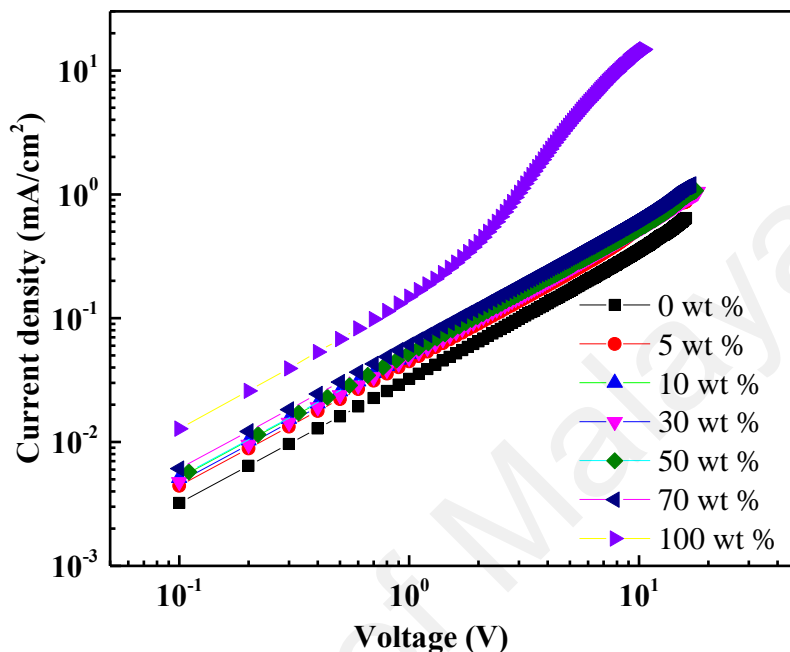


**Figure 4.11** The current density of hole only devices with different concentrations of TcTa.

It is shown in Figure 4.11 that the holes currents increase with increasing concentration of TcTa from 0 wt % to 100 wt %. The drastic increment of current density for 100 wt % of TcTa may have been assisted by the shallower HOMO level of TcTa. Surprisingly, the current density from the real OLED device apparently does not follow the trend of the current for the mobility device (mobility decrease when 5 wt% until 20 wt% TcTa added and then increases). A possible reason for almost independence of the current density on mobility is that the current density depends on the energetic barrier at the injecting contact of PEDOT:PSS and mixed TcTa: PVK interface. The injection barrier from PEDOT:PSS to PVK:TcTa may be slowly reduced as the concentration of TcTa is added into PVK.

#### 4.3.6 Electroluminescence emission measurement

Figure 4.12 shows the normalized electroluminescence (EL) of the devices with 0 wt % to 100 wt % TcTa concentrations as well as photoluminescence (PL) of equal mixture of SPPO13 and TcTa. The PL blend of TcTa and SPPO13 are different from that of pristine materials. This dictates that PL of the mixture is exciplex in origin. The EL peak at 610 nm corresponds to Ir(piq)<sub>2</sub>(acac) emission mainly due to carrier trapping at the dopant sites. With TcTa concentration higher than 30 wt %, a new emission peak is observed at 490 nm. In this experiment, SPPO13 functions as a hole blocking layer. With increasing hole current and mobility, more holes travel further into the device, accumulating at the emissive and SPPO13 interface layer. Recombination could occur between electrons at the SPPO13 layer and holes at the emissive layer. The detection of a new peak in EL spectra corresponds to the exciplex peak, which indicates holes accumulating at the TcTa and SPPO13 interface. This also results in a change of the CIE coordinates. At 1000 cd/m<sup>2</sup>, the CIE coordinates are (0.68, 0.31) for 0 wt % devices, (0.67, 0.32) for 70 wt % devices and (0.64,0.32) for 100 wt % devices.

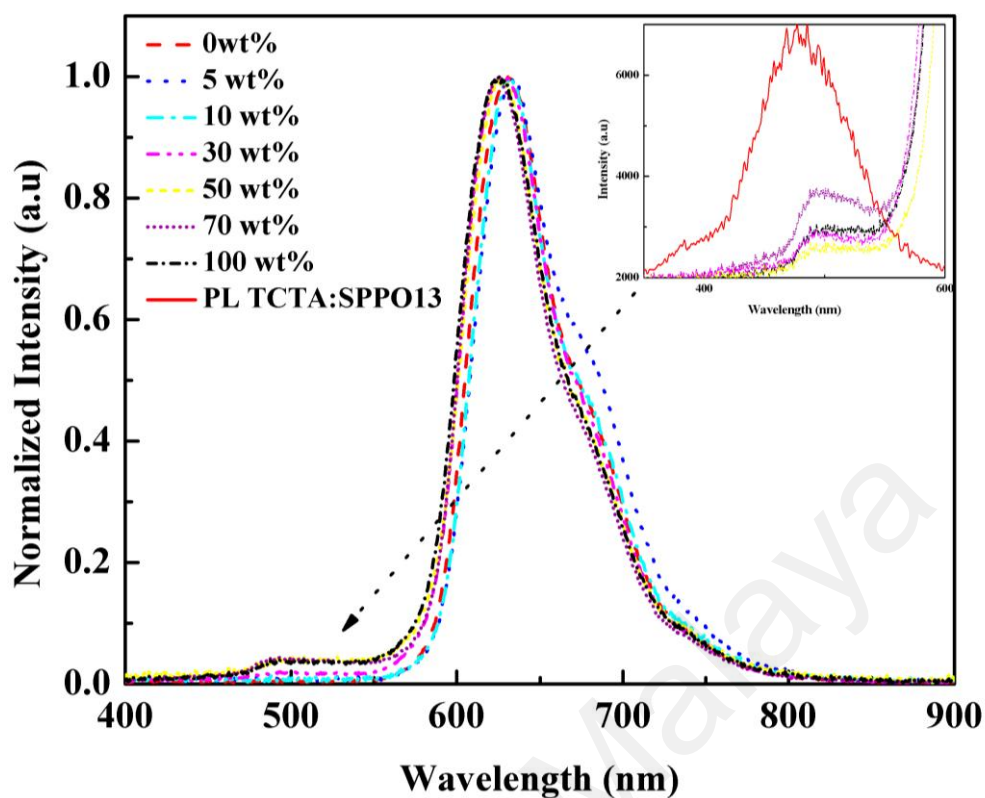


**Figure 4.12** Normalized electroluminescence of red devices with 0 to 100 wt% TcTa concentrations together with normalized photoluminescence intensity of TcTa and PVK in the equal mixture (red line shown inset).

#### 4.4 Chapter summary

Doping a very small amount of TcTa into PVK improves the device efficiency. This results in a 100 % improvement in current efficiency of red phosphorescent OLED. Since the current in our case is injection controlled, we do not see the influence of mobility on the current. However, the device efficiency shows the dependence on the carrier mobility to produce good charge balance. TcTa may have assisted in hole injection from the PEDOT:PSS by providing a localized region with lower energy. The energetic disorder decreases with increasing concentration of TcTa implying that hole transport is predominately hopping among the more ordered TcTa molecules even at low concentration. Film morphology also plays a very crucial role in determining the transport property where a smooth film surface is required to ensure uniform carrier injection at the interface.

## CHAPTER 5: HIGH EFFICIENCY TANDEM OLEDs WITH FULLY SOLUTION PROCESSABLE CHARGE GENERATING UNIT

### 5.1 Introduction

A number of research works has been engineered to design high performance tandem OLED with efficient CGU. Most of these CGLs heavily relied on vacuum deposition method. Forming a bi-layer film using solution process method is not an easy task due to intermixing problem (Baumann & Rudat, 2013; Jiangshan Chen et al., 2012; Zhong, Duan, Huang, Wu, & Cao, 2011). In order to reduce the device-processing cost and to simplify the fabrication process, it is highly desirable to reduce the vacuum deposition process to the minimum. Apparently, most of the works done for the solution processed OLED focused on the emissive layer (Gather, Jin, Mello, Bradley, & Meerholz, 2009; B. Liu et al., 2013; Yook & Lee, 2013; You et al., 2009; X. Zhang et al., 2012) but not much on the CGL. Only the latest research by T.Chiba *et. al* (Chiba, Pu, Sasabe, Kido, & Yang, 2012) utilized a hybrid CGL consisting of solution processed poly(4-butylphenyl-diphenyl-amine (Poly-TPD) with vacuum deposited molybdenum tri-oxide ( $\text{MoO}_3$ ). However there is no research work done on fully solution processable CGLs reported thus far.

In this chapter, a solution processable green LEU tandem PhOLED connected using doped *p*-type/*n*-type CGL is presented. The CGL consists of 1,4,5,8,9,11-hexaazatriphenylene hexacarbonitrile ( $\text{HATCN}_6$ ) as the *n*-type layer and small molecule material; 1,1-bis-(4-bis(4-tolyl)-aminophenyl) cyclohexene (TAPC) with polymer, poly PVK as the mixed *p*-type layer. Extensive investigations on improving OLED device by mixing small molecule has been demonstrated, owing to small molecules well-known characteristics such as higher charge carrier mobility, stability as well as the efficiency (Hellerich et al., 2013; Mao et al., 2011; Yook & Lee, 2014). The application of small

molecule doped with polymer binder demonstrated the possibility of utilizing as a mixed host in emissive layer in order to improve the hole injection and transportation. Most of the time, large weight ratio (10 - 60 wt %) is applied (Suh, Chin, Kim, Kang, & Lee, 2003; Suo, Yu, Deng, Lou, & Jiang, 2008; X. Zhang et al., 2012). Large weight ratio of such a mixture tends to exhibit phase separation, which is detrimental to OLED device (Jiangshan Chen et al., 2012; Keum, Ha, & Kim, 2006; Smith et al., 2012). Since doping of small molecule-polymer is rarely employed in heterojunction layer especially as CGL, it is interesting to explore the effect of a very small percentage of small molecule in polymer acting as heterojunction layer. Thus, in this work, doped *p*-type (small molecule: polymer)/*n*-type heterojunction integrated as CGL layer in tandem OLED is demonstrated. From this structure, two-folds enhanced efficiency up to 24 cd/A (7.5 lm/W) at 1000 cd/m<sup>2</sup> was achieved for tandem device, compared to the single emitting unit. The efficient charge generation could be attributed to lower energy barrier for hole injection at CGU interface, high vacuum level shift as well as high carrier accumulation arises from the addition of TAPC into PVK.

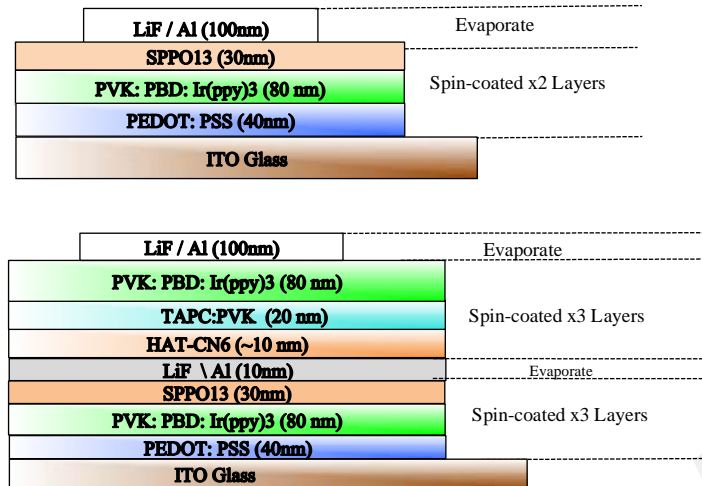
## 5.2 Experimental details

### 5.2.1 Single and Tandem OLED device fabrication

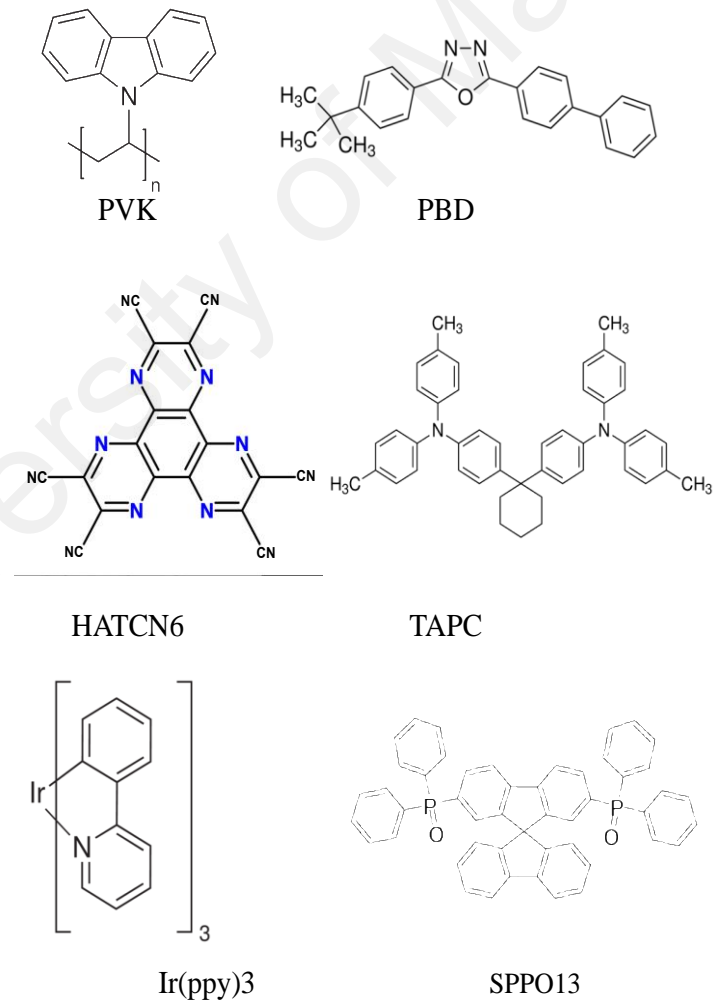
PEDOT:PSS (AI4083) was purchased from H.C. Starck. TAPC, HATCN<sub>6</sub> and fac-tris(2-phenylpyridine)iridium (Ir(ppy)<sub>3</sub>) were purchased from Luminescence Technology (Taiwan). PVK and 2-(4-biphenyl)-5-(4-tert-butylphenyl)-1,3,4 oxadiazole (PBD) were obtained from Sigma Aldrich. All materials were purchased and used as received without further purification. The device structure consists of indium tin oxide (ITO) / PEDOT: PSS, (40 nm) / PVK:PBD (70:30 w/w): Ir(ppy)<sub>3</sub> (1wt%) (80 nm) / LiF (1nm) / Al (10 nm) / HATCN<sub>6</sub>, (10 nm) / TAPC: PVK (30 nm) / PVK: PBD (70:30 w/w): Ir(ppy)<sub>3</sub> (1wt%) (80nm) / LiF (1nm) / Al (100nm).

Figure 5.1 shows (a) device structure and (b) the chemical structures of the materials used in this work. Mixed hosts of PVK:TAPC were blended in chlorobenzene by varying TAPC concentration of 0 wt %, 1 wt %, 2 wt % and 10 wt % . ITO coated glass substrates were routinely cleaned before subjected to oxygen plasma treatment for 5 minutes. 40 nm of PEDOT:PSS was spin coated on the substrates and immediately baked in N<sub>2</sub> environment for 10 minutes at 150 °C. The emissive material was dissolved in chlorobenzene, subsequently spin coated onto the PEDOT:PSS coated substrate to produce a 80 nm thick film and baked at 80 °C for 30 minutes. Following that, 1 nm interlayer consisting of LiF and 10 nm of Al layers were vacuum deposited under  $2.4 \times 10^{-4}$  mbar. 10 nm of HATCN<sub>6</sub>, dissolved in acetone, was spin-coated onto the sample. HATCN<sub>6</sub> is insoluble in chlorobenzene. Therefore, PVK: TAPC could be spin coated on top of HATCN<sub>6</sub> without dissolving the layers underneath. PVK: TAPC was spin-coated onto the sample to form a layer of 20 nm film. The film was baked at 100 °C for 30 minutes before the second 80 nm emissive layer was spin coated on top of it. Finally, ~1 nm of LiF and 100 nm Al was sequentially vacuum deposited at a base pressure of  $2.4 \times 10^{-4}$  mbar.

(a)



(b)



**Figure 5.1** (a) Device structures and (b) chemical structures of the material applied in this work.

### 5.2.2 Charge generation unit (CGU) only device fabrication

To elucidate the mechanism of charge generation in CGU, devices consists of ITO / PEDOT:PSS (40 nm) / PVK: X wt% TAPC (where X is either 0 or 2) (30 nm)/ HATCN<sub>6</sub> (10 nm) /SPPO13:Cs<sub>2</sub>CO<sub>3</sub> (20 nm) : LiF (1 nm) /Al (100 nm) was fabricated. Figure 5.2 shows the schematic diagram of CGU device energy level used in this work. The structure is introduced to simulate the sequence in a real tandem device, which is when the device is reversed bias. To ensure ohmic contact, 40 nm of PEDOT: PSS was spin coated onto the cleaned ITO substrates and immediately baked in N<sub>2</sub> environment for 10 minutes at 150 °C. Next, PVK: TAPC (2 wt%) or PVK dissolved in chlorobenzene was spin coated on top of PEDOT: PSS. Subsequently, 10 nm of 0.25 wt % of HATCN<sub>6</sub> in acetone was spin coated onto the PVK: TAPC and baked at 120 °C for 30 minutes. This is followed by spin-coating 5 % Cs<sub>2</sub>CO<sub>3</sub> co-dissolved in SPPO13 film on top of HATCN<sub>6</sub>. Before Cs<sub>2</sub>CO<sub>3</sub> was mixed with SPPO13, 0.05 wt% of Cs<sub>2</sub>CO<sub>3</sub> was dissolved in 2-ethoxyethanol first. The film was then annealed at 100 °C for 20 minutes. Finally, 1 nm of LiF and 100 nm of Al was vacuum deposited.

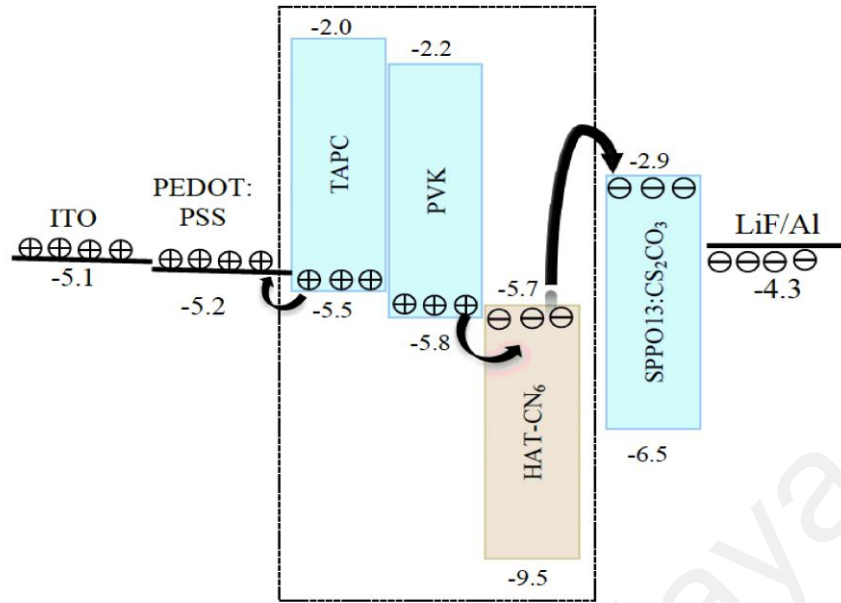


**Figure 5.2** Schematic diagram of the fabricated CGU device. HATCN<sub>6</sub> has a strong electron affinity, hence electron from PVK: TAPC is easily removed and injected into cathode. PEDOT: PSS is used to provide a high conductivity path for holes while SPPO13:Cs<sub>2</sub>CO<sub>3</sub> assists the electron injection into cathode. Considering the high conductivity of the PEDOT: PSS and SPPO13: Cs<sub>2</sub>CO<sub>3</sub> layers, most voltage drop would have been originated from the PVK: TAPC/ HATCN<sub>6</sub> heterojunction.

In order to calculate the carrier mobility,  $\mu$  a well-known Mott-Gurney SCLC equation was used (N. F. Mott & Gurney, 1964):

$$J = \frac{9}{8} \epsilon_r \epsilon_0 \mu \frac{E^2}{L} \quad \text{Equation 5.1}$$

where  $J$  is the current density,  $E$  is the electric field, and  $L$  is the organic layer thickness. Since the polymer matrix in organic thin film is normally influenced by a randomly oriented dipoles, the carrier mobility is described using the Poole-Frenkel equation as below:

$$\mu(E) = \mu_0 \exp(\beta \sqrt{E}) \quad \text{Equation 5.2}$$

where  $\mu_0$  is the zero-field mobility and  $\beta$  is the Poole-Frenkel factor.

From equation (5.1) and (5.2), the field dependent SCLC can be calculated by:

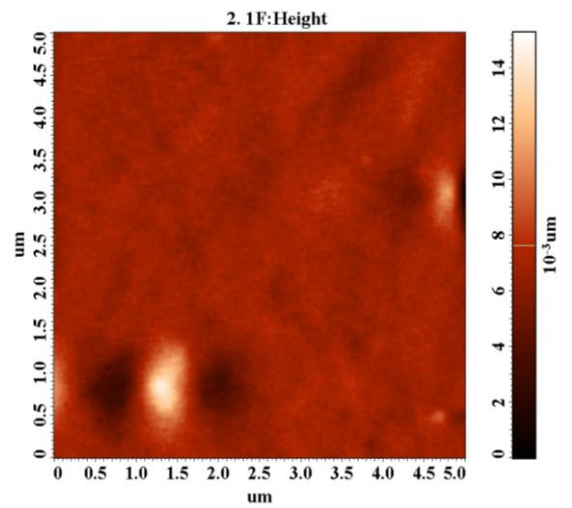
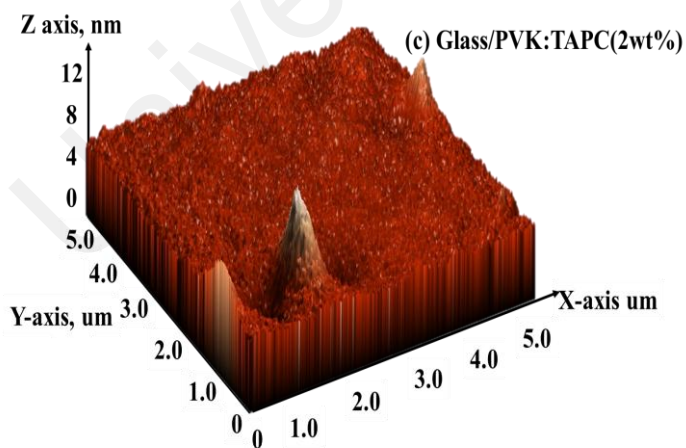
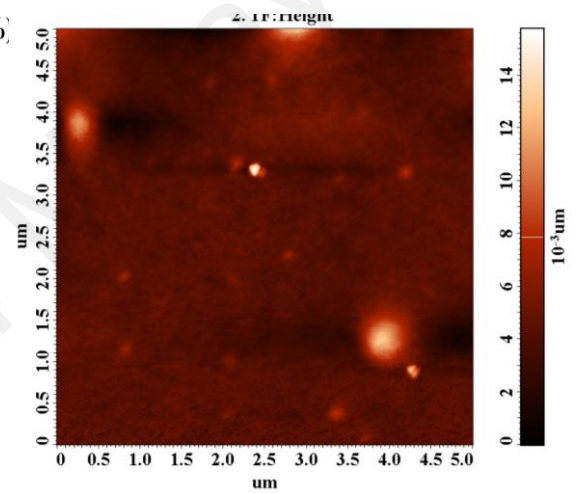
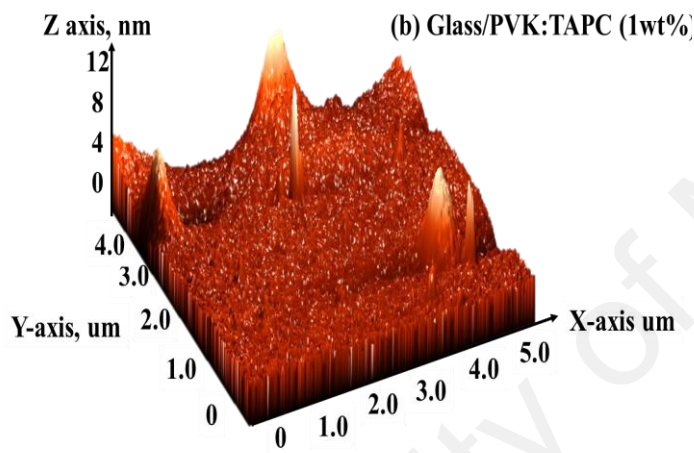
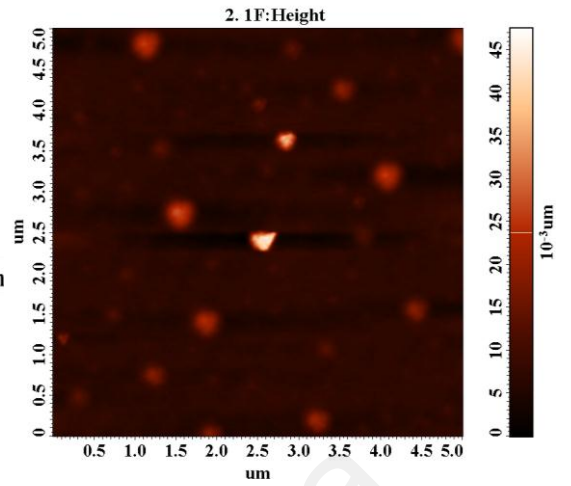
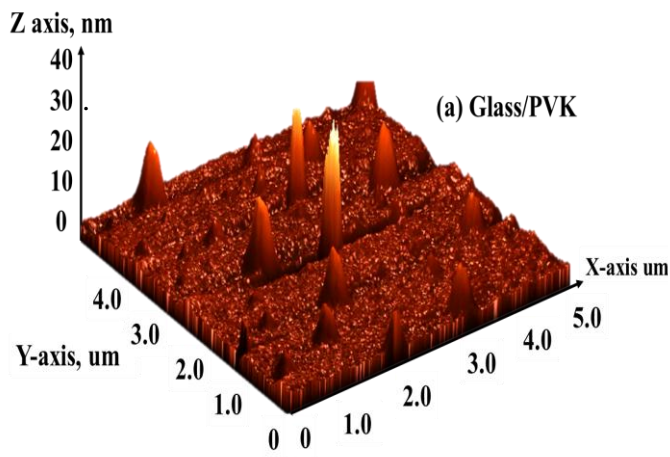
$$J_{\text{SCLC}} = \frac{9}{8} \epsilon_r \epsilon_0 \mu \frac{E^2}{L} \mu_0 \exp(-\beta \sqrt{E}) \quad \text{Equation 5.3}$$

To further study the CGU interfaces, XPS and UPS measurement were carried out. For this measurement, a series of PVK and PVK:TAPC solution were prepared by varying the solution concentrations (0.02 mg/ml, 0.01 mg/ml, 0.015 mg/ml and 0.005 mg/ml). The organic thin film was then spin coated on top of the ITO glass with the same spin coating speed. In all the UPS and XPS spectra, the Fermi energy level ( $E_F$ ) is referred to as the zero Binding Energy (BE). The work function and ionization energy (IE) of all films were determined by a linear extrapolation of the High and Low electron cutoff respectively to the background intensity line. For absorption measurement, HATCN<sub>6</sub>/PVK: TAPC solution was spin coated on top of clean ITO glass and annealed. Perkin Elmer PE750 Lambda UV-Vis-NIR was used to measure the material absorbance and to estimate the energy band gap.

### 5.3 Experimental results

#### 5.3.1 AFM topography images

Figure 5.3 (a) - (c) shows the spin coated polymer-small molecule blend films examined under the atomic force microscopy (AFM) images illustrated in 3D (left) and 2D (right) images. The root mean square ( $R_s$ ) of each film is listed in Table 5.1. It could be seen from these images that the surface become smoother when PVK is doped with TAPC. The  $R_s$  (in Table 5.1) of the film decreases when TAPC concentration increases from 0 wt% to 2 wt%. The AFM results also show a smooth mixed film implying that there is no significant phase separation in the small molecule – polymer mixture. However, when we added a large percent of TAPC (10 wt%), the surface become very rough.



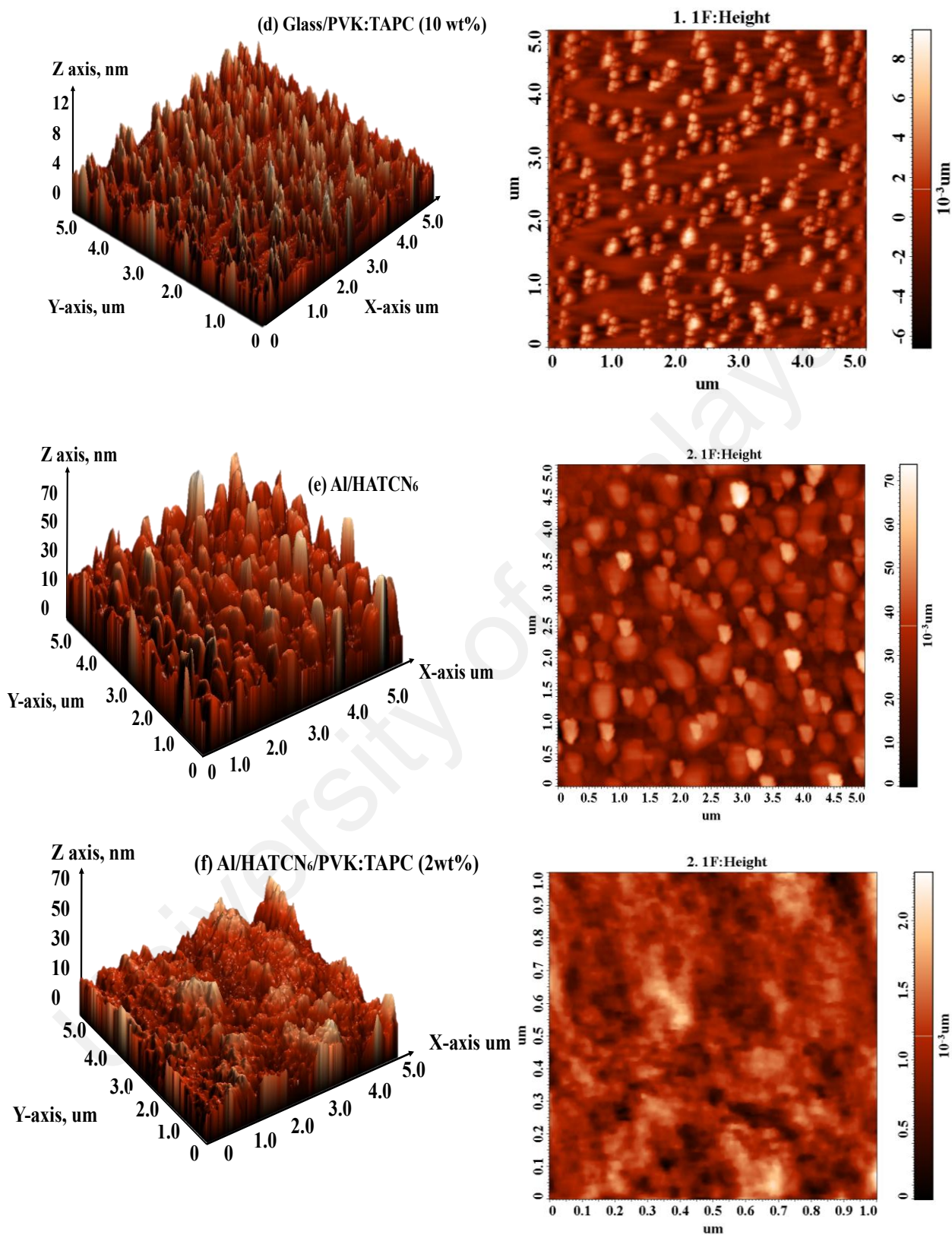


**Figure 5.3** 3D (left) and 2D (right) AFM images of (a) PVK, (b) PVK: TAPC (1 wt %), (c) PVK: TAPC ( 2 wt %), (d) PVK: TAPC ( 10 wt %), (e) Al/HATCN<sub>6</sub> and (f) Al/HATCN<sub>6</sub>/PVK: TAPC (2 wt %).

Figure 5.3 also illustrates the AFM images of (e) Al / HATCN<sub>6</sub> and (f) Al / HATCN<sub>6</sub> / PVK: TAPC (2 wt%), which corresponds to the layers of the CGU in tandem OLED fabricated in this work. By spin coating PVK: TAPC on top of Al/HATCN<sub>6</sub>, significant improvement in surface morphology is observed. Al/HATCN<sub>6</sub>/PVK:TAPC layer shows R<sub>s</sub> of 0.275 nm, compared with the Al/HATCN<sub>6</sub> with R<sub>s</sub> of 8.849 nm. These results demonstrated that PVK: TAPC (2 wt %) on top of Al/HATCN<sub>6</sub> acts as planarization layer overcoming the roughness of Al/HATCN<sub>6</sub>. This helps to improve the hole injection.

**Table 5.1** Values of R<sub>s</sub> from AFM measurements for different concentration of TAPC in PVK.

Film	wt %	R <sub>s</sub> (nm)
PVK	0.0	2.632
PVK: TAPC	1.0	1.050
PVK: TAPC	2.0	0.907
PVK: TAPC	10	2.046
Al/HATCN <sub>6</sub>	0.0	8.849
Al/HATCN <sub>6</sub> /PVK: TAPC	2.0	0.275

### 5.3.2 J-V-L characteristic of single and tandem devices

Figure 5.4 (a) shows the brightness – voltage characteristic of both single unit and tandem devices. The brightness–voltage and current density–voltage characteristics of the fabricated devices are illustrated in Figure 5.4 (a) and (b) respectively.

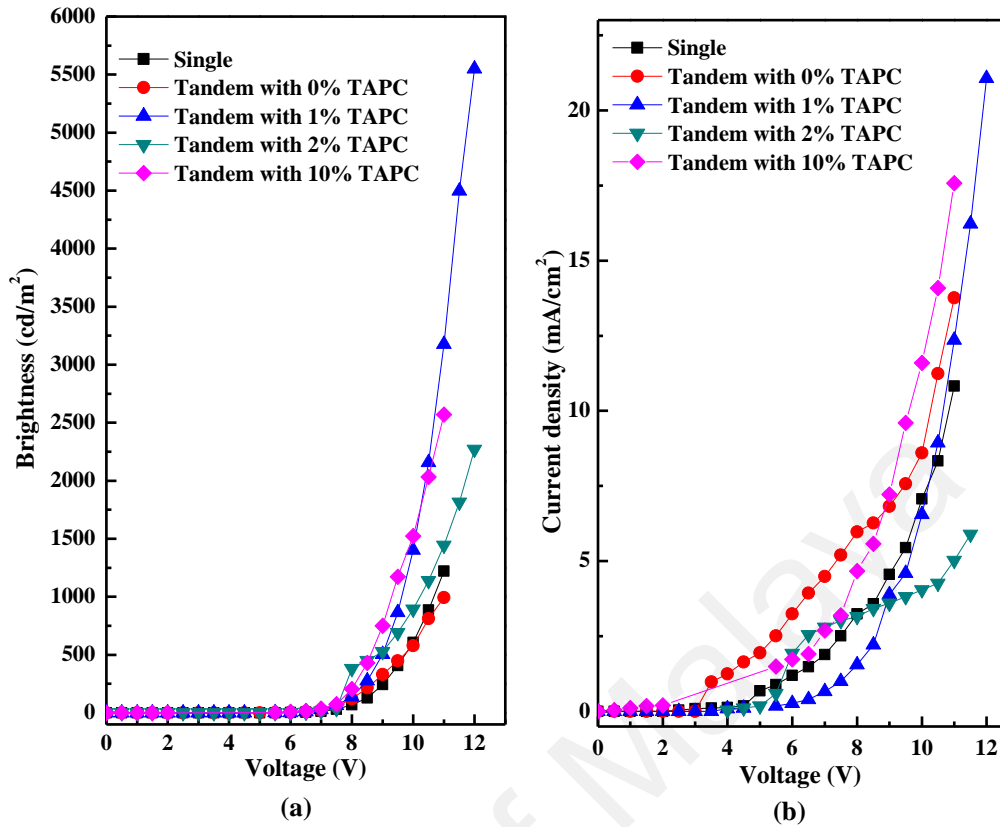


**Figure 5.4** (a) Brightness vs. voltage and (b) Current density vs. voltage of single and tandem devices.

The turn-on voltage (at  $1 \text{ cd/m}^2$ ) in the single device is observed to be at 5.9 V. The turn-on voltages for the tandem OLED with 0 wt %, 1 wt %, 2 wt % and 10 wt % TAPC doped in PVK are 5.2 V, 5.8 V, 5.4 V and 5.5 V respectively. Typically, tandem OLED shows a higher turn-on voltage compared to the single device (Chiba et al., 2012). In our case, the turn-on voltages of the tandem devices are lower than a single unit. Although the efficient charge extraction and charge transfer at the CGL organic–organic interface might result in insignificant voltage drop cross CGL, it is still insufficient to explain the lower turn on voltage observed in our devices. This phenomenon is also observed by Chen et al. using  $\text{LiF} / \text{ZnPc:C60} / \text{MoO}_3$  as CGL in their tandem device (Y. Chen et al., 2011), where the turn-on voltages for the tandem device are actually lower than single unit.

As observed in Figure 5.4 (a), the brightness of all devices is higher than 1000  $\text{cd/m}^2$  at 11 V. Tandem device with 1 wt % TAPC in PVK shows the highest brightness compared to the other devices. In Figure 5.4 (b), tandem device with 10 wt % TAPC shows the highest current density at 16.8  $\text{mA/cm}^2$  compared to the rest of devices at 11 V. The current density of the tandem OLED with 2 wt % TAPC is the lowest at 5.02  $\text{mA/cm}^2$ , compared to 10.8  $\text{mA/cm}^2$ , 13.7  $\text{mA/cm}^2$ , 12.3  $\text{mA/cm}^2$  and for single device, 0 wt % TAPC and 1 wt % TAPC respectively.

Figure 5.5 (a) illustrates the current efficiency of the tandem OLEDs compared to a single OLED. When the ratio of TAPC in PVK increased from 1 wt % to 2 wt %, the current efficiency at 1000  $\text{cd/m}^2$  increased to 19.3  $\text{cd/A}$  and 24.2  $\text{cd/A}$  respectively. However, the efficiency decreased to 11.0  $\text{cd/A}$  when 10 wt % TAPC was added. This might be attributed to the rougher surface morphology shown in Figure 5.3. The current efficiency of these tandem devices are more than doubled compared to the single device that exhibits only 10.7  $\text{cd/A}$ . Figure 5.5 (b) shows that the power efficiencies of the tandem OLED with 2 wt % TAPC is the highest at 7.3  $\text{lm/W}$  which is 2.9 folds of that of single OLED at 2.5  $\text{lm/W}$ . Such improvement magnitude is significant compared to that reported for vacuum deposited CGL devices (Earmme & Jenekhe, 2013).

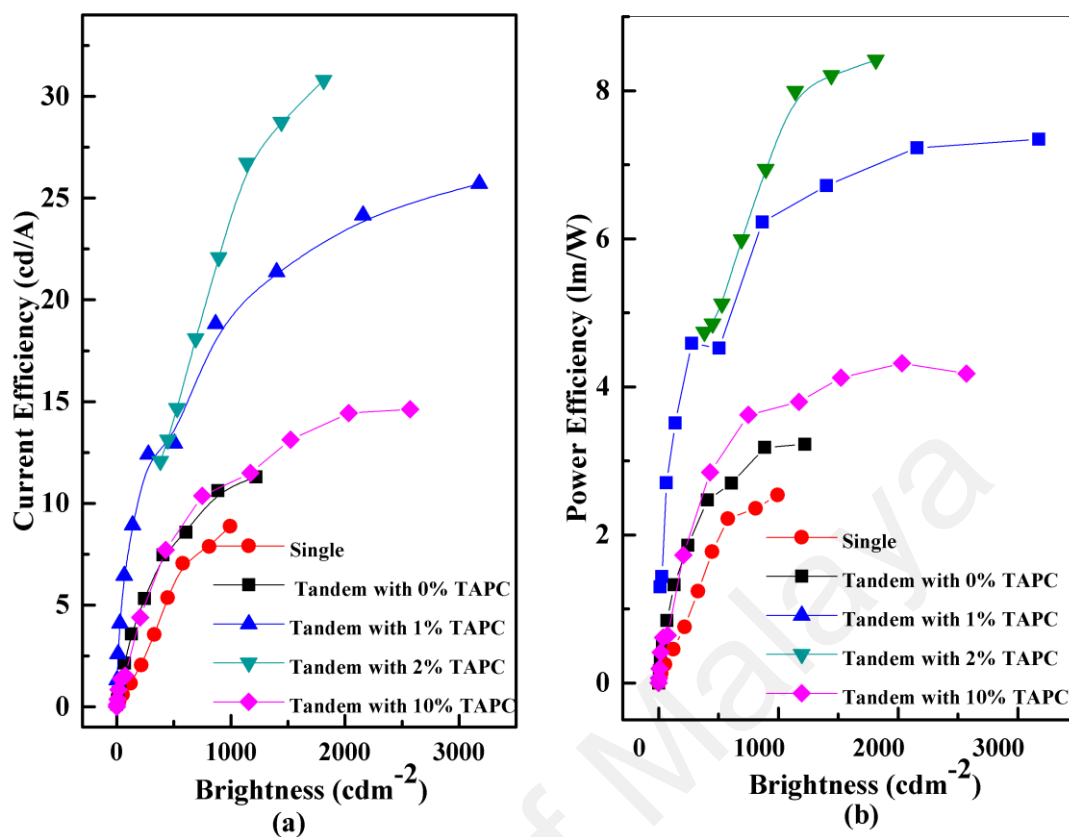


**Figure 5.5** (a) Current efficiency vs. brightness and (b) Power efficiency vs. brightness of single and tandem devices.

Theoretically, when two identical units are connected by CGL, the power efficiency of the device remains unchanged due to the double operational voltage. Adding to that, if there is extra voltage drop across CGL, the power efficiency could even be lower compared to the single device (Sun, Guo, et al., 2015). However, in this work, the power efficiency of the tandem device is higher compared to conventional device, which indicates that the tandem OLED structure possess an excellent charge generation, transport as well as extraction and injection capabilities that would result in negligible voltage drop across the CGL (Y. Chen & Ma, 2012).

Figure 5.6 shows the close match of the HOMO level of PVK at 5.8 eV (S.-J. Kim et al., 2011) and the LUMO level of HATCN<sub>6</sub> at 5.7 eV (Jeon et al., 2012) that could facilitate the electron transfer. We hypothesized that the generated electrons and

holes could be effectively extracted out from CGL and injected into adjacent emissive layer. Under the external electric field, it is expected that the electrons tunnel from the HOMO level of PVK to the LUMO level HATCN<sub>6</sub> via a narrow depletion region at the organic-organic interface, and injected into the 1st emissive layer assisted by LiF / Al as EIL (Chiba et al., 2011). Generated holes in PVK: TAPC are injected into the 2<sup>nd</sup> emission layer. The current efficiency of the tandem OLED improved by almost 3 folds, comparable to the vacuum deposited CGL reported (Chiba et al., 2011). It is most likely that the significant performance improvement in the tandem OLED is due to efficient charge generation and extraction that occurred.

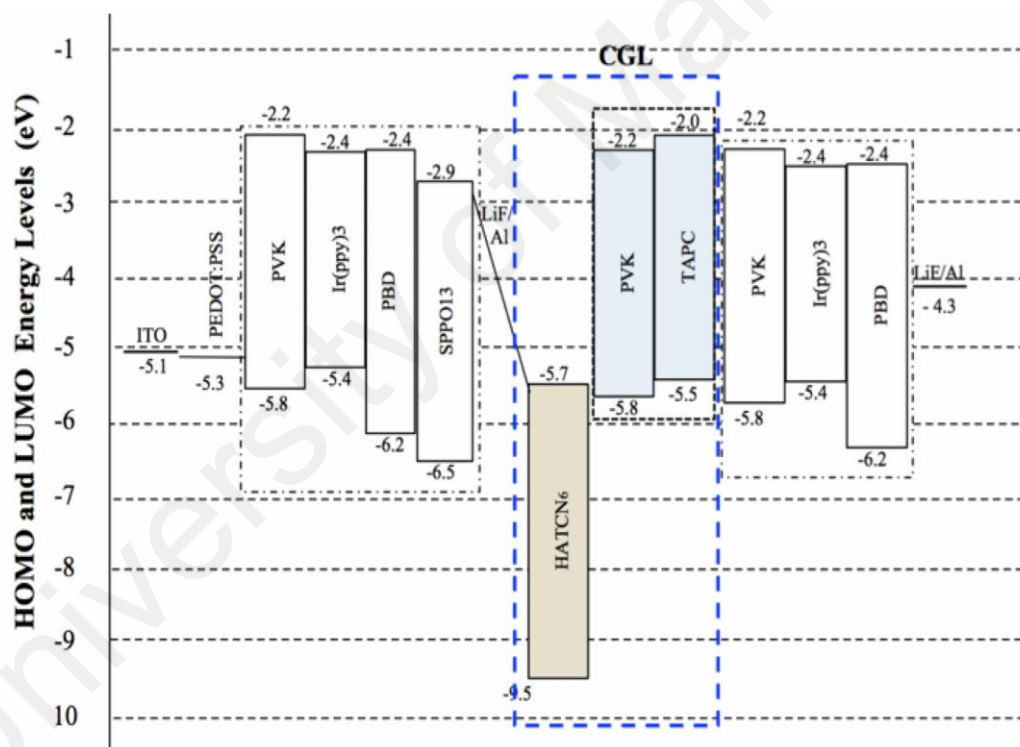


**Figure 5.6** The energy levels for the full tandem devices.

For tandem OLED with 0 wt % TAPC in PVK, the accumulation of holes is expected to occur at the HATCN<sub>6</sub> and PVK interfaces. Holes can be injected into a PVK transporting layer. Doping of 1 wt % and 2 wt % of TAPC in PVK is expected to induce traps for hole transport as the HOMO level of TAPC is at 5.5 eV (Kalinowski,

Cocchi, Virgili, Fattori, & Williams, 2007) while the PVK HOMO level is at 5.8 eV.. Hence, in Figure 5.4, the current density of tandem OLED doped with TAPC is lower than device without doping. The trapped and de-trapping holes could occur at higher applied voltages. Thus, at high voltages, for example at 11 V, the current density is the highest for 0 wt %, followed by 1 wt % and 2 wt % TAPC in tandem devices. However, for 2 wt % and 10 wt % of TAPC, it shows an unusual shape for a diode at a lower voltage. The HOMO level of TAPC is 0.2 eV higher than the LUMO level of HATCN<sub>6</sub> while the HOMO level of PVK is 0.1 eV lower than the LUMO level of HATCN<sub>6</sub>. Since TAPC has a better hole donating property than the PVK, doping of TAPC could increase the hole generation at the HATCN<sub>6</sub>/PVK interface. Hence, our second hypothesis is that there are two mechanisms taking place when sufficient amount of TAPC is doped. The first is the increase of hole generation and the second is the trapping of holes. These could contribute to the unusual S-shape of the *J-V* curve for tandem OLED with 2 wt % TAPC. We also note that at voltages below 8 V, the device is unstable in the sense that the brightness tends to fluctuate randomly. Also noted that the tandem OLED device with 1 wt % TAPC showed much higher brightness and current density compared to other devices with efficiency just slightly lower than that of 2 wt % TAPC in PVK.

Albeit the lower current density of 2 wt % TAPC in PVK compared to pure PVK as *p*-type CGL, this device shows the highest efficiency compared to other fabricated devices. Table 5.2 summarized the efficiency of the device fabricated. To further evaluate the underlying effect of TAPC in the device, CGU only device was fabricated and the electronic structure of the layers was systematically investigated. Only 0 wt% and 2 wt % TAPC in PVK were taken into consideration in order to explain the effect of mixing TAPC in PVK.

**Table 5.2** Device efficiency of the fabricated devices in this work.

Device	TAPC wt % in PVK	V <sub>on</sub> (V)	Current Efficiency (cd/A)	Power Efficiency (lm/W)	CIE (x,y)
<b>Single</b>	-	5.9	10.7	2.5	0.34, 0.55
<b>Tandem</b>	0	5.2	8.9	3.2	0.36, 0.55
	1	5.8	19.3	6.5	0.36, 0.55
	2	5.4	24.2	7.3	0.36, 0.55
	10	5.5	11.0	3.7	0.36, 0.55

### 5.3.3 Electroluminescence (EL) emission spectra

Figure 5.7 shows the normalized electroluminescence (EL) emission spectra of the single unit and the tandem OLED with 2 wt % TAPC viewed in the normal direction at 12 V. Both devices shared an identical peak at 509 nm. The spectral full widths half-maxima for both single and tandem OLED are almost identical. However, the present tandem device does not show any micro-cavity phenomenon indicating good optical transparency of the intermediate connector due to low reflectivity of the CGU. Micro cavity phenomenon results in EL spectrum narrowing, angle dependent spectral change and also deviation from the Lambertian distribution of emission spectroscopy. This phenomenon is normally observed in tandem device if there is metal-based CGUs used, where micro-cavity is formed by highly reflective metal (Leem, Lee, Kim, & Kang, 2008).

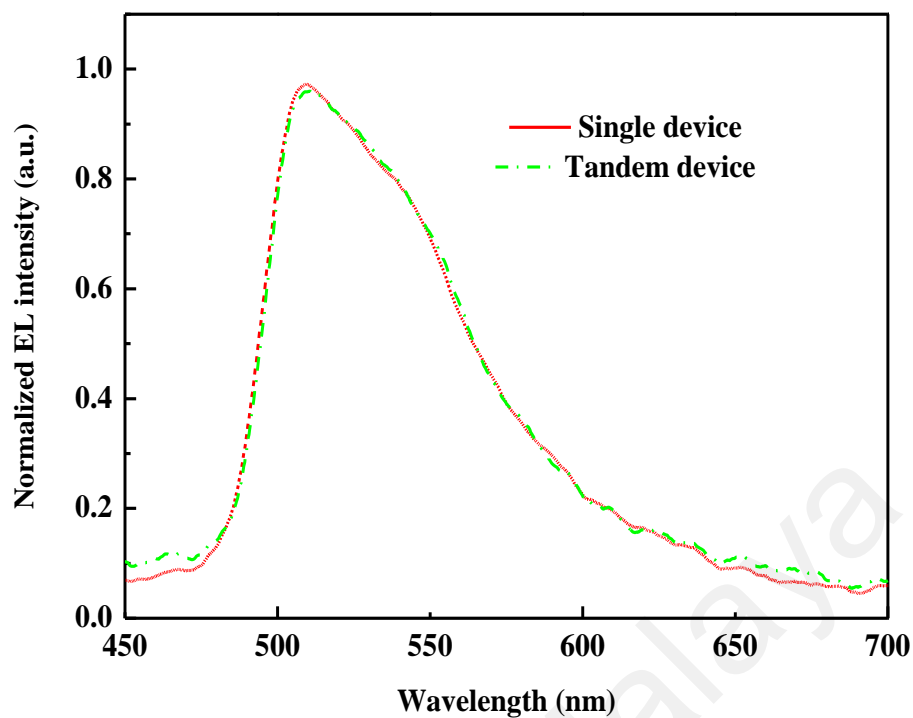


**Figure 5.7** The normalized electroluminescent (EL) spectra of the single unit and the tandem OLED with 2 wt % TAPC in PVK viewed in the normal direction at voltage of 12 V.

### 5.3.4 UV-Vis measurement

#### 5.3.4.1 Transmittance of CGU

Figure 5.8 shows the transmittance spectra of Al/HATCN<sub>6</sub>/PVK: TAPC (2 wt %) with good transmittance over 60 % across the wide visible wavelength ranges (400 – 800 nm). Despite of lower transmission due to presence of thin aluminum, the device is actually performing better in efficiency.

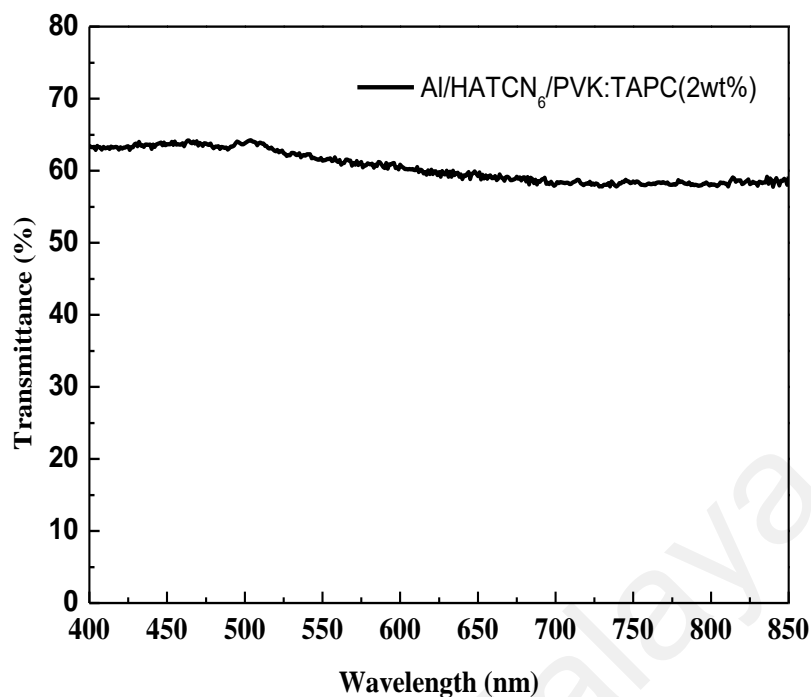


**Figure 5.8** Optical transmittance of charge generating layer consists of Al / HATCN<sub>6</sub> / PVK: TAPC (2 wt%) spin coated on top of glass.

#### 5.3.4.2 Validation of orthogonal film formation

The solubility test for CGL layer was done by spin coating chlorobenzene on the test layer. Chlorobenzene was chosen due to its ability to dissolve almost all organic materials. Figure 5.9 (a) and (b) show the result for HATCN<sub>6</sub> layer and PVK:TAPC (2 wt%) layer that has been spin coated on top of glass substrate. The intensity of HATCN<sub>6</sub> layer maintained, before and after wash with chlorobenzene, which suggests that HATCN<sub>6</sub> could not be washed out by the upper layer whilst the intensity of PVK:TAPC (2 wt%) film reduced after washed partially by chlorobenzene. The PVK used here has a molecular weight higher than 1,000,000 g/mol. Because of its very high molecular weight, it would be more difficult to dissolve in chlorobenzene. These results show that chlorobenzene is sufficient to form CGL layer while maintaining the required thickness to achieve an efficient tandem OLED.

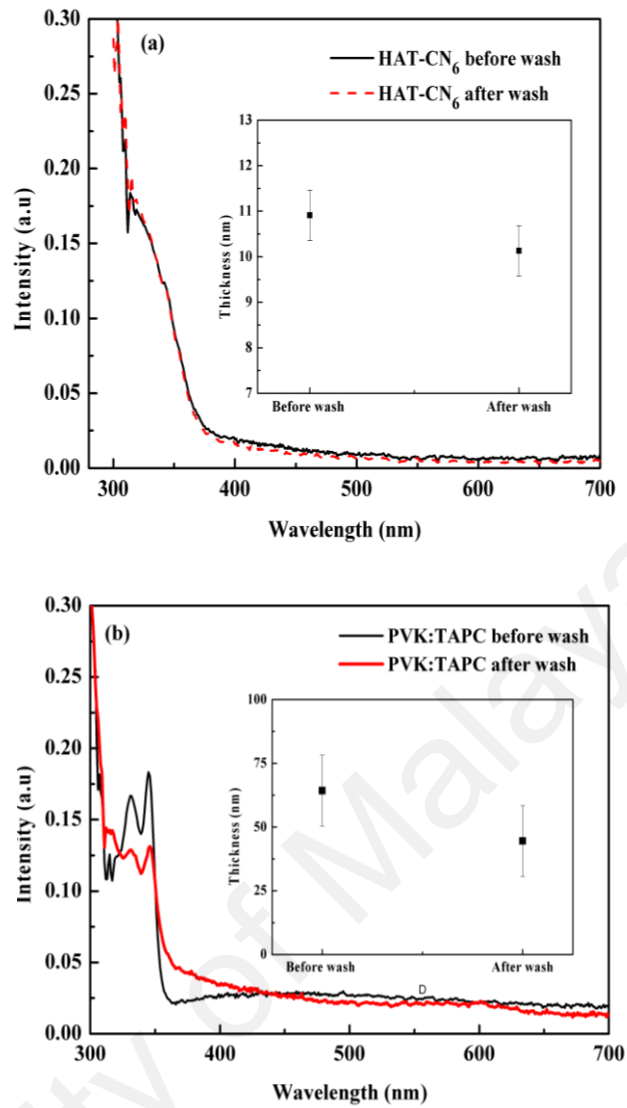


**Figure 5.9** (a) HATCN<sub>6</sub> dissolved in acetonitrile absorbance spectrum before and after wash with chlorobenzene, (b) PVK: TAPC (2 wt %) film absorption before and after solubility tests.

Table 5.3 shows the annealed film thickness variation measured before and after being washed by chlorobenzene. There is no significant change in the thickness of HATCN<sub>6</sub> before and after washing. There is a small reduction of about 20-25 % in PVK:TAPC thickness. As more than 70 % of the original film thickness remains, it is still acceptable in our applications. This results also showed the we have successfully used orthogonal solvent approach to build-up two different layers via solution process.

**Table 5.3** Thickness variation measured using Profilometer.

Sample	Thickness (nm)			
	HAT-CN <sub>6</sub>		PVK:TAPC	
	before wash	after wash	before wash	after wash
1 <sup>st</sup> point	10.61	10.13	62.21	45.95
2 <sup>nd</sup> point	11.53	11.22	61.65	44.27
3 <sup>rd</sup> point	10.21	10.01	62.15	46.55
4 <sup>th</sup> point	10.52	10.32	66.75	48.01

### 5.3.5 Mechanism of charge generation and transport in CGU

#### 5.3.5.1 *J-V* characterization

To further investigate the effect of doped CGU in the device performance, CGU only device was fabricated. The structure of this device is shown in Figure 5.2. Figure 5.10 shows the double log *J-V* characteristic of the CGU with 0 wt % and 2 wt % TAPC in PVK. Both devices exhibit the same trends for both the ohmic and space-charge-limited current (SCLC) regions. The device with 0 wt % TAPC shows a higher current density compared to the device with 2 wt % TAPC. It is not surprising that TAPC reduces the hole mobility as TAPC is expected to introduce hole traps due to its higher lying HOMO level compared to PVK (Schmechel & von Seggern, 2004; von Malm, Steiger, Schmechel, & von Seggern, 2001). The presence of traps induced by TAPC reduces the hole mobility and thus the current density due to the enhanced energetic disorder (Hyun Kim, Yaghmazadeh, Bonnassieux, & Horowitz, 2011; Kumar, Jain, Kapoor, Poortmans, & Mertens, 2003; Tong et al., 2007; Tsung & So, 2008). The effect of TAPC in assisting charge injection is also reflected in lower transition voltage from ohmic to SCLC compared to 0 wt % TAPC device.

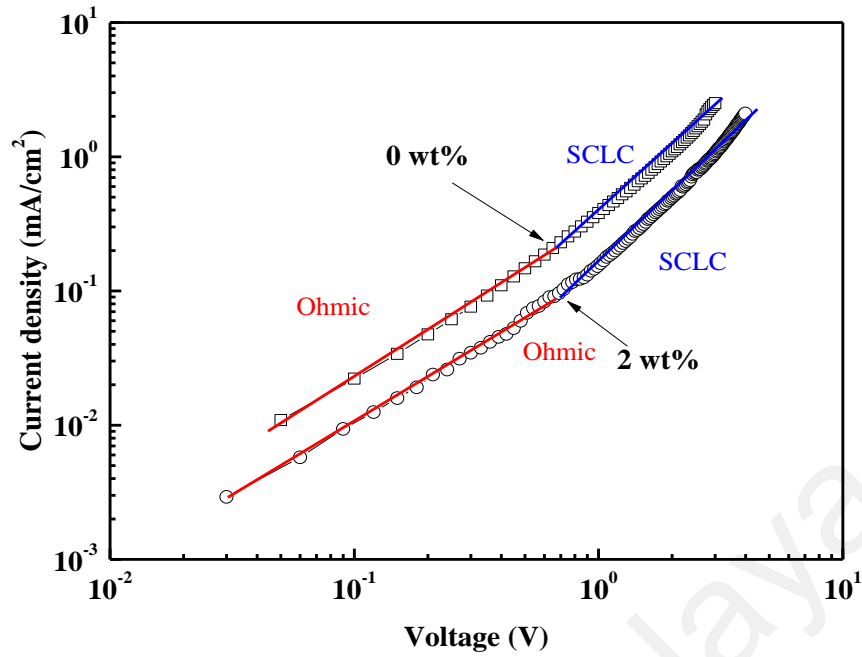


**Figure 5.10** Log-log curves for J-V characteristic of 0 wt% and 2 wt% TAPC. Both devices exhibits ohmic and SCLC regions as shown by the red and blue lines respectively.

From the  $JV$  curve of field dependence SCLC (Figure 5.10), we calculated the carrier mobility based on Poole Frenkel equation shown in Equation 5.1- 5.3. The carrier zero field mobility,  $\mu_0$  and Poole-Frenkel factor,  $\beta$  were then extracted by fitting to the logarithm of  $(J/E^2)$  versus the square root of the electric field graph. The estimated zero field mobility decreased from  $7.99 \times 10^{-6} \text{ cm}^2/\text{Vs}$  to  $3.37 \times 10^{-6} \text{ cm}^2/\text{Vs}$  when 2 wt % of TAPC is added into PVK. The carrier mobility of the CGU decreased about 2.4 times when 2 wt % TAPC was added into PVK. This is attributed to the traps generated when PVK is mixed with TAPC. (B. Li, Chen, Zhao, Yang, & Ma, 2011). Even though there is traps introduced, the carrier transport can still occur as high electric field is applied across the device.

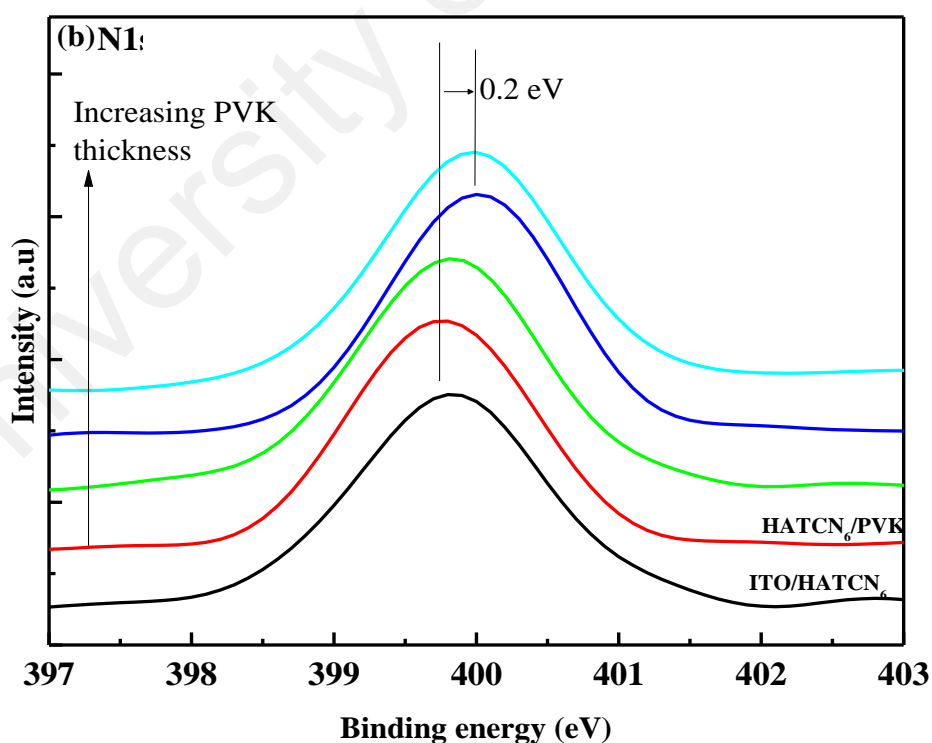
### 5.3.5.2 CGU hetero-junction interface study

Study on electronic structure and energy level alignment for the CGU interfaces is further investigated using XPS and UPS measurement. The structure for CGU

organic/organic interface studied here are HATCN<sub>6</sub>/PVK and HATCN<sub>6</sub>/PVK: TAPC (2 wt %) interface.

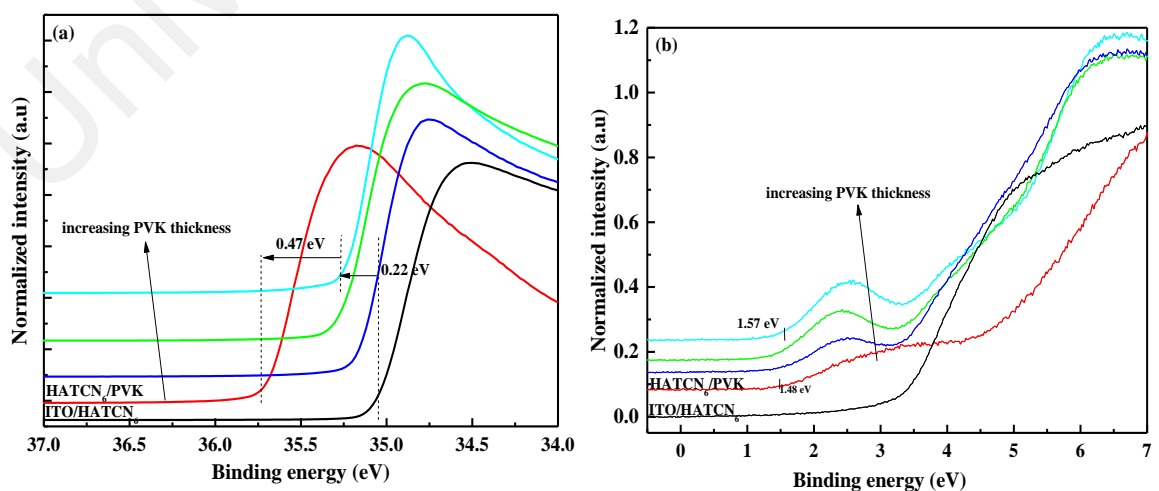
### 5.3.5.2.1 HATCN<sub>6</sub>/PVK Interface

The investigation starts with the first interface between HATCN<sub>6</sub> and PVK. A layer of 10 nm of HATCN<sub>6</sub> was spin coated first prior spin coat PVK film. The thickness of PVK on top of HATCN<sub>6</sub> is varied to observe PVK bulk characteristic. In order to observe the variation peak for N1s, BE was re-calibrated using Carbon 1s with BE at 284.6 eV. Figure 5.11 shows the nitrogen N1s peak from HATCN<sub>6</sub> / PVK interface. It is shown that the N1s peak centre of the thickest PVK film shifts to lower energy as the PVK film decreases, suggesting that the HOMO level is bending upward closer to Fermi energy at the interface. This implies that the bending magnitude of PVK at the interface is 0.20 eV upward.



**Figure 5.11** XP spectra of nitrogen, N1s lines at HATCN<sub>6</sub>/PVK interface with varying PVK film thickness.

The high-energy cut-off (HECO) in Figure 5.12 (a) is used to calculate the work function of the PVK layers. It is calculated that the work function difference between ITO/HATCN<sub>6</sub> and the thickest PVK (4.3 eV) layer deposited on HATCN<sub>6</sub> is 0.22 eV. This implies 0.22 eV work function difference between substrate and PVK bulk. Figure 5.12 (b) depicts the low energy cutoff (LECO) that represents the difference between the HOMO level of PVK and the Fermi level, which in this case is measured to be 1.57 eV at the interface. Taken the work function of the thickest PVK layer to be 4.3 eV, the ionization potential (IE) of PVK was calculated to be 5.87 eV which is close to the value of 5.9 eV shown in literature (Herlocker et al., 2000). Figure 5.12 (c) shows the full diagram based on the XPS and UPS spectrums of the interface. From UV-Vis absorption coefficient plotted over the photon energy (in Figure 5.13), the bandgap of PVK is measured to be 3.45 eV which is comparable the literature (Benchaabane et al., 2014). This value placed the LUMO level of PVK at 3.30 eV. Since the ITO/HATCN<sub>6</sub> interface energy level was not measured, the energy level characteristic of this material is fully adapted from the literature (Kang, Kim, Kim, Seo, & Park, 2011). Taking the bulk work function of HATCN<sub>6</sub> at 5.95 eV, the IE of PVK (5.87 eV) and the bulk dipole (0.2 eV), the hole injection barrier from HOMO to Fermi level is calculated to be 0.14 eV.



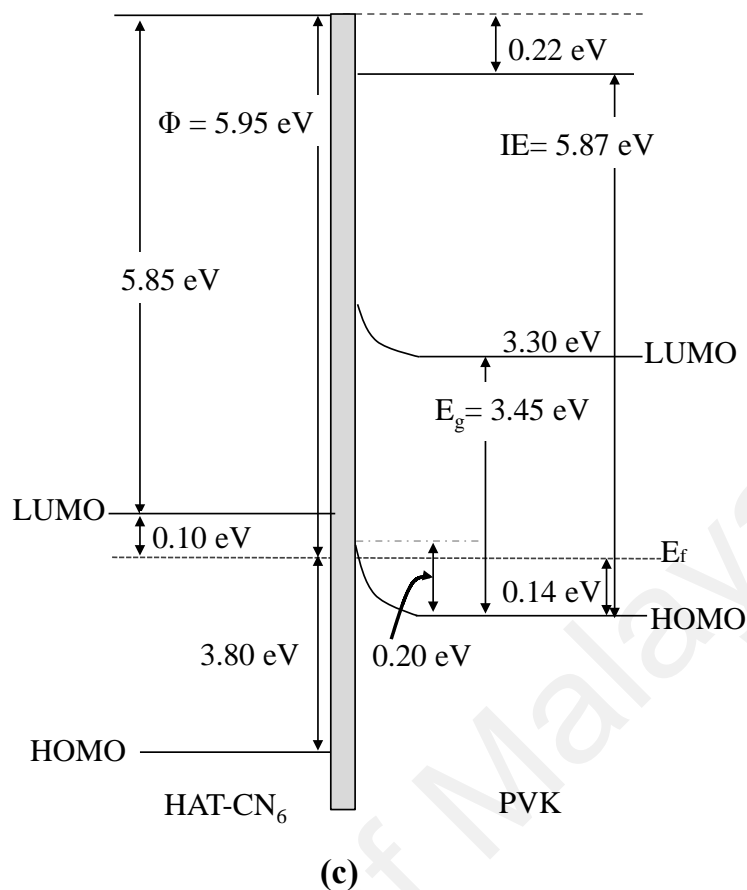


**Figure 5.12** UP spectra of the HATCN<sub>6</sub>/PVK interface with varying PVK thickness. (a) HECO and (b) LECO representing the work function and HOMO level respectively. (c) Full diagram of the HATCN<sub>6</sub>/PVK interface mapped out from UPS and XPS spectra.

Figure 5.13 corresponds to the band-gap of the material. It can be seen that the band gap of PVK: TAPC increased 0.04 eV compared to PVK. However, since the band-gap of amorphous p-type of semiconductor does not easily change even when doped with other material, this number is considered merely as an instrument error.

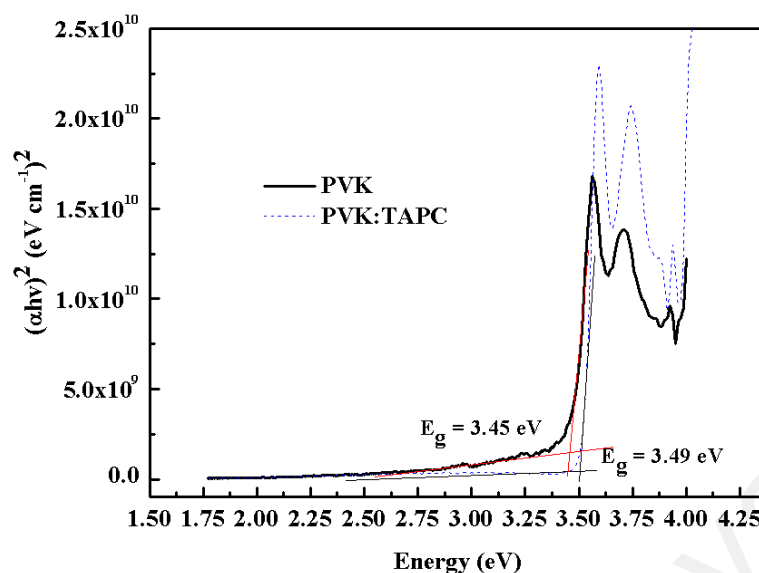


**Figure 5.13** Tauc plot from absorbance spectrum to calculate energy band gap for PVK and PVK:TAPC.

#### 5.3.5.2.2 HATCN<sub>6</sub>/PVK:TAPC Interface

Similar to HATCN<sub>6</sub>/PVK interface, once again the Carbon 1s centre peak was first aligned at 284.6 eV to observe the variation peak for N1s. It is shown in Figure 5.14 that the peak centre of N1s in the thickest PVK film shifts to a lower energy which is similar to HATCN<sub>6</sub>/PVK interface, suggesting that the HOMO level is also bending upward closer to Fermi energy. It is observed that the total energy shift and the bending magnitude of PVK:TAPC at the interface is 0.40 eV upward. The high and low cut-offs for the UP spectra of HATCN<sub>6</sub>/PVK:TAPC interface are shown in Figure 5.15 together with a band diagram illustrating the energy levels at the interface. The work function of PVK:TAPC calculated from HECO spectra is 4.15 eV. The work function difference between ITO/HATCN<sub>6</sub> and the thickest PVK:TAPC layer is 0.28 eV, which is higher compared to PVK layer (0.22 eV) shown before.

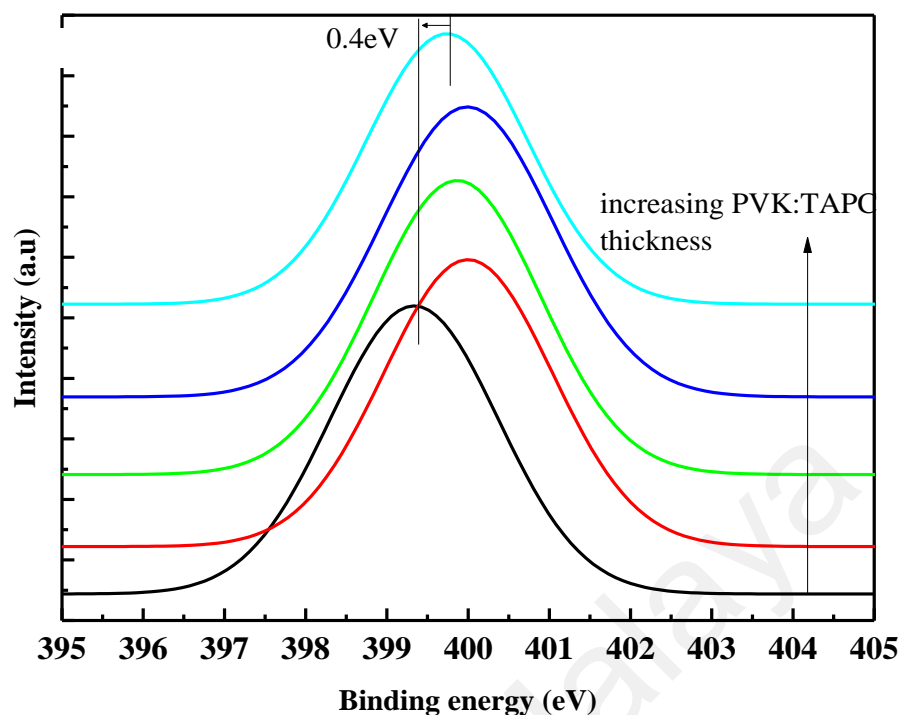


**Figure 5.14** XPS spectra of the nitrogen N1s lines at HATCN<sub>6</sub>/PVK interface with varying PVK:TAPC film thickness.

LECO part shown in Figure 5.15 (b) measured the difference between the HOMO level of PVK:TAPC and the Fermi level, to be 1.60 eV at the interface. By taking the work function of thickest PVK:TAPC layer at 4.15 eV, the IE of PVK:TAPC was calculated to be 5.75 eV, which is lower compared to PVK. Figure 5.15 (c) shows the full diagram based on the XPS and UPS spectrums of the interface. The bandgap is 3.45 eV ( shown in Figure 5.13), putting the LUMO level of PVK:TAPC at 3.37 eV. It could also be seen that the magnitude of band bending at the interface increases up to 0.20 eV as TAPC is doped in PVK. With bulk work function of HATCN<sub>6</sub> at 5.95 eV, the IE of PVK:TAPC (5.75 eV) and the bulk dipole (0.28 eV), the hole injection barrier from HOMO to Fermi level is calculated to be 0.08 eV.

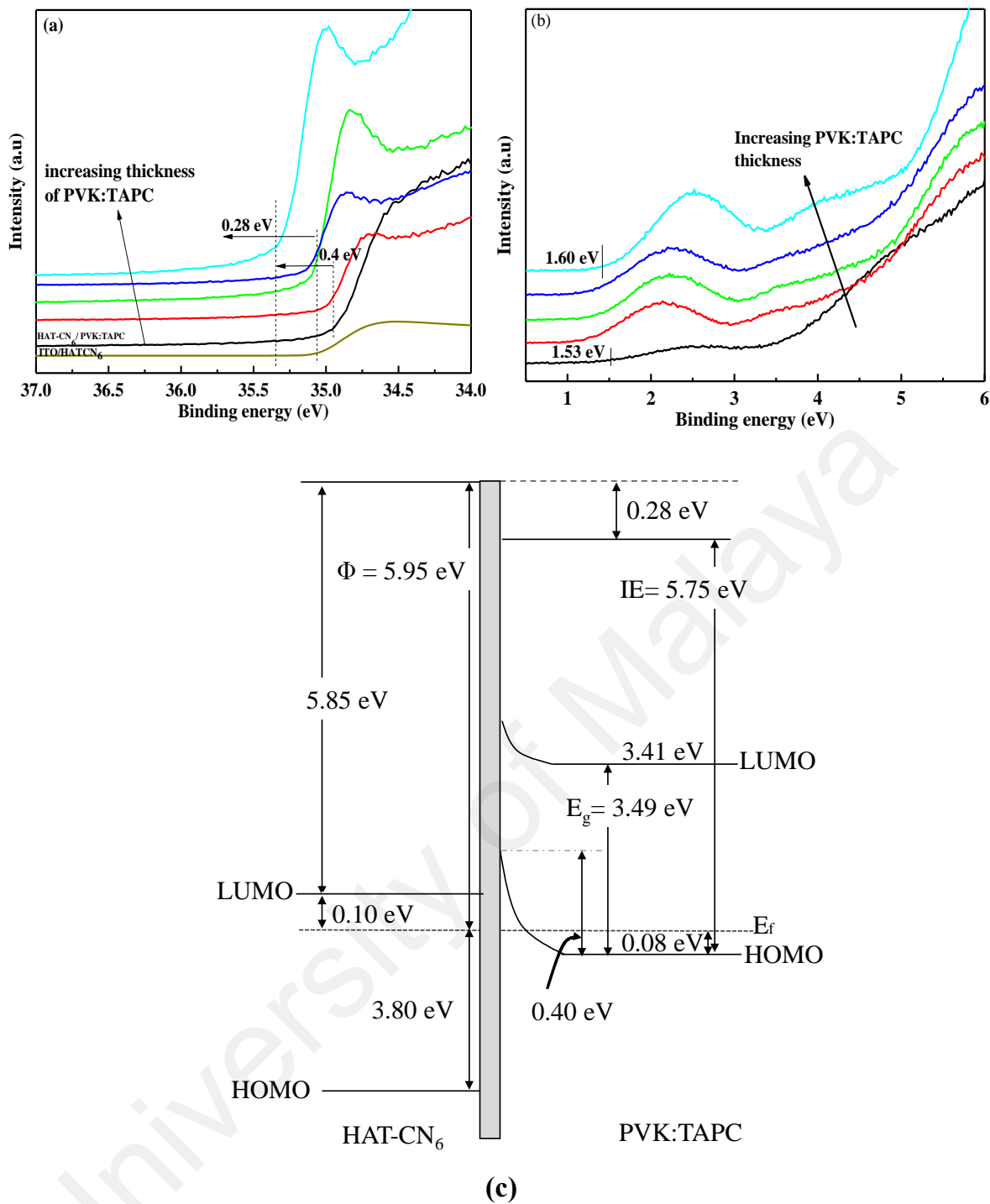


**Figure 5.15** UP spectra of the HATCN<sub>6</sub>/PVK:TAPC interface with varying PVK thickness. (a) HECO and (b) LECO representing the work function and HOMO level respectively. (c) Full diagram of the HATCN<sub>6</sub>/PVK:TAPC interface mapped out from UPS and XPS spectra.

### 5.3.5.2.3 Discussion

Based on the diagram illustrated in Figure 5.12 (c) and 5.15 (c), it is shown that efficient charge generation and injection in CGU are mainly influenced by the energy barrier between LUMO of HATCN<sub>6</sub> and HOMO of PVK or PVK: TAPC. Calculated hole injection barrier PVK:TAPC of 0.08 eV is smaller compared to hole injection barrier of PVK with 0.14 eV . This allows the electron from PVK:TAPC to be easily extracted by HATCN<sub>6</sub> LUMO compared to PVK and forming more efficient charge carrier generation interface. Adding TAPC into PVK increased the hole carrier density generation at the CGU interface since TAPC is widely known as electron donor. High charge accumulation can also be observed in the magnitude of the band bending, where PVK:TAPC exhibits a higher band bending compared to pure PVK which may also be due to increasing charge carrier concentration in PVK:TAPC.

At the interfaces presented here, as the work function of HATCN<sub>6</sub> is greater than that of PVK or PVK:TAPC, the electrostatic potential will be greater in PVK or PVK:TAPC. Thus the electron will be tunneled from PVK or PVK:TAPC to HATCN<sub>6</sub> (H. Wang & Yan, 2010). The tunneling mechanism is expected to occur at the interfaces which is similar to the tunneling process in the organic/organic hetero-junction demonstrated by Kroger et.al (Kröger et al., 2007), where electrons are expected to tunnel through the depletion zone from the HOMO level of the p-type CGU layer (PVK:TAPC) to the LUMO of n-type CGU layer leaving holes in p-type layer to be injected into the adjacent emissive layer via the intermediate Al layer.

## 5.4 Chapter summary

In summary, we have successfully fabricated a tandem OLED via a novel and fully solution processable charge-generating layer. HATCN<sub>6</sub> as the n-type CGL layer has a good solubility in acetonitrile and insoluble in all other types of organic solvent. Hence,

another layer could be spin coated on top of HATCN<sub>6</sub> layer without intermixing problem. The tandem OLED device with two hosts, PVK: TAPC as the *p*-type CGL layer, exhibits a high efficiency with 24.2 cd/A, which is more than doubled compared to the single OLED that exhibits only 10.7 cd/A at 1000 cd/m<sup>2</sup>. Although the presence of traps induced by TAPC reduces the current density of the CGU, it is shown that tandem OLED incorporating CGU with 2 wt% TAPC yielded higher efficiency due to the better electron extraction and reduced injection barrier at HATCN<sub>6</sub>/ PVK: TAPC interfaces shown by XPS and UPS measurements.

University of Malaya

## CHAPTER 6: SOLUTION PROCESSABLE MOLYBDATE AS A CATHODE INTERLAYER FOR SUPER YELLOW OLEDs

### 6.1 Introduction

Transition metal oxides (TMO) have gained increasing interest in organic electronics, due to their abilities to increase device efficiency and stability. Previous studies have shown a significant improvement of device efficiency when a TMO was used as a buffer layer to help increasing the carrier injection from electrodes (Fu, Chen, Shi, & Ma, 2013; Girotto, Voroshazi, Cheyns, Heremans, & Rand, 2011; Kröger et al., 2009; Matsushima, Kinoshita, & Murata, 2007; Maria Vasilopoulou et al., 2011; M. Zhang, Ding, Tang, & Gao, 2011). The limited number of TMO electron injecting layers leads to the development of hydrogenation of TMOs. Hydrogenation reduces  $\text{WO}_3$  to  $\text{WO}_{2.5}$  and  $\text{MoO}_3$  to  $\text{MoO}_{2.7}$  which can be used as electron injection layers in OLED devices (M. Vasilopoulou et al., 2012). The hydrogenation of  $\text{MoO}_3$  creates gap states below the conduction band assisting electron injection from the cathodes (Maria Vasilopoulou et al., 2011).

In organic light-emitting diodes (OLEDs),  $\text{MoO}_3$  is often used at anode interlayer to increase the device efficiency by lowering the hole injection barrier. The hole injection improvement is originated from the ability of  $\text{MoO}_3$  to extract electron from the highest occupied molecular orbital (HOMO) to the ITO anode (Kröger et al., 2009). This creates an accumulation of holes at the organic semiconductor interface and hence an energy bending at that interface (Du et al., 2015; Irfan, Ding, So, & Gao, 2011; Kröger et al., 2009; M. Zhang et al., 2011). Hence,  $\text{MoO}_3$  is an n-type semiconductor. The use of  $\text{MoO}_3$  at the anode interlayer has been widely reported (Lampande et al., 2013; J. Liu et al., 2014; Z. Liu, Helander, Wang, & Lu, 2010). However, the use of  $\text{MoO}_3$  at the cathode side has rarely been investigated. One notable example is the use of

MoO<sub>3</sub>/Ag/MoO<sub>3</sub> as a transparent cathode for OLEDs (Tian, Williams, Ban, & Aziz, 2011). Reduced MoO<sub>3</sub> could be used as an electron injection layer at polymer/Al interface (Maria Vasilopoulou et al., 2011). This is possible as a result of chemically reduction of MoO<sub>3</sub> by the ultrathin aluminum. Ouyang *et al.* demonstrated that MoO<sub>3</sub>/Al can be used as an electron injection layer in inverted OLED (Ouyang et al., 2015). However, the device efficiency with MoO<sub>3</sub> from both reports is not that high. Another example is the use of LiF/MoO<sub>3</sub>/Al as a cathode buffer layer in organic solar cells. As a result, power efficiency was improved from 1.2 % to 3.3 % (Kageyama, Kajii, Ohmori, & Shirota, 2011). Although MoO<sub>3</sub> might be used at the cathode side, to our best of knowledge, there is no report showing high device efficiency OLEDs that use MoO<sub>3</sub> at the cathode side.

In this thesis work, MoO<sub>3</sub> powder was dissolved in DI water and NaOH which chemically producing sodium molybdate (Na<sub>2</sub>MoO<sub>4</sub>). However, from the XPS and ICP-MS measurement (Appendix C), Na could not be detected and thus the solution is then left with Molybdate (MoO<sub>4</sub>). This chapter presents the use of solution processed MoO<sub>4</sub> as the cathode interlayer having a representative yellow emitting poly-(p-phenylenevinylene) (SY-PPV) semiconductor polymer as an emitting layer. By inserting lithium fluoride (LiF) between optimal thickness of solution processed MoO<sub>4</sub> on top of super yellow poly-(p-phenylenevinylene) (SY-PPV) the efficiency of the SY-PPV fluorescent-based devices can be significantly improved by more than two folds. Despite the increased driving voltage, the device showed a current and a luminance efficiency up to 22.8 cd/A and 14.3 lm/W respectively, which is more than two-folds increase in efficiency compared to the control device using LiF/Al at a brightness of 1000 cdm<sup>-2</sup>. UPS is used to analyze the energy alignment between SY-PPV and the solution processed MoO<sub>4</sub> and MoO<sub>4</sub>/LiF/Al interfaces. We found that the solution processed MoO<sub>4</sub> using diluted sodium hydroxide has relatively low ionization

energy, electron affinity and work function decreasing with increasing thickness of  $\text{MoO}_4$ . However, the optical bandgap increases with increasing spin-speed. A large energetic barrier is always present between the SY-PPV and deep lying valence band of  $\text{MoO}_4$ . This is supported by suppression of hole current in hole dominating devices. The ability of thin  $\text{MoO}_4$  ( $\sim 2$  nm) acting as a hole blocking layer while allowing electrons to be transported across the layer and a large upward vacuum shift appeared to be the origin of efficiency enhancement of SY-PPV light-emitting diode when  $\text{MoO}_4/\text{LiF}/\text{Al}$  is used.

## 6.2 Experimental procedure

To prepare solution processed  $\text{MoO}_4$ , 15 mg of  $\text{MoO}_3$  powder (Sigma Aldrich) was dissolved in 1ml of 0.12 M of sodium hydroxide (NaOH) to form sodium  $\text{MoO}_3$  solution. The mixture is stirred for a few minutes in room temperature. 2 v % of Zonyl surfactant was added into the solution to assist the film wetting (Höfle, Schienle, et al., 2014; Vosgueritchian, Lipomi, & Bao, 2012). Figure 6.1 shows the  $\text{MoO}_3$  solution before and after added with NaOH. A crystal clear solution was produced when NaOH was added into the solution of  $\text{MoO}_3$  and DI water. This solution is then become molybdate ( $\text{MoO}_4$ ) solution.

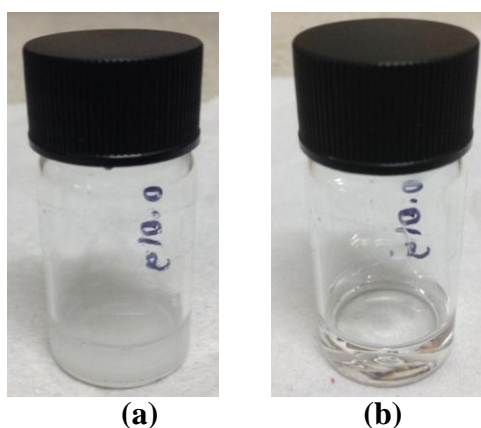


**Figure 6.1**  $\text{MoO}_3$  in (a) DI water and (b) diluted NaOH and DI water solution forming molybdate solution.

The device consists of indium tin oxide (ITO) / poly (3,4-ethylenedioxythiophene):polystyrene sulfonate (PEDOT:PSS) / SY-PPV/  $x$ , where  $x =$  Al (100 nm) or LiF (0.8 nm) /Al (100 nm) or MoO<sub>4</sub>/Al (100 nm) or MoO<sub>4</sub>/LiF (0.8 nm) /Al (100 nm). ITO substrates were cleaned using DI water, acetone, and isopropyl alcohol sequentially in the ultrasonic bath followed by oxygen plasma treatment with 35 W for 5 minutes. 40 nm PEDOT:PSS was then spin coated on top of ITO followed by annealing at 150 °C for 10 minutes in N<sub>2</sub> environment. Yellow emissive layer (PDY-132 from Merck) was then spin coated on top of PEDOT:PSS forming a 80 nm film followed by annealing at 100 °C. MoO<sub>4</sub> solution was spin coated on top of the emissive layer and annealed at 100 °C for 10 minutes. The thickness of MoO<sub>4</sub> can be changed by varying the spin-coating speed (2K, 5K, 8K and 10K rpm). Finally, cathode was vacuum deposited through a shadow mask under  $2.4 \times 10^{-4}$  mbar pressure.

All devices were encapsulated using UV curable epoxy and a glass slide. The current ( $J$ ) – voltage ( $V$ ) – brightness ( $L$ ) characteristics were measured using Konica Minolta CS-200. The film thickness was measured using KLA-Tencor P-6 profilometer except for MoO<sub>4</sub> films. Due to the limitation of profilometer, MoO<sub>4</sub> films were measured using Transmission Electron Microscopy (TEM). Dual beam Focus Ion Beam was used to prepare MoO<sub>4</sub> lamella for TEM measurements. The samples were prepared by spin coating the MoO<sub>4</sub> films on top of glass substrates. A layer of platinum was coated on top of it to make the film conductive. The images for thickness measurement TEM are shown in Appendix A. It is shown that thickness for 10K rpm, 8K rpm, 5K rpm and 2K rpm are 2 nm, 3.6 nm, 6.8 nm and 15.7 nm respectively. Atomic force microscopy (AFM) image was taken using an NX10 Park Systems. For X-ray Photoemission Spectroscopy (XPS) / *In situ* ultraviolet photoelectron spectroscopy (UPS), the samples were loaded in ultra-high vacuum conditions with pressure below  $2.7 \times 10^{-8}$  Pa. The photoelectron kinetic energy was measured with a Thermo VG Scientific-Alpha110

electron energy analyzer. The samples were then subjected to UV radiation from the synchrotron at *Synchrotron Light Research Institute at Thailand* to determine the work functions using photon energy of 39.5 eV and pass energy of 10 eV. To determine whether the MoO<sub>4</sub> is chemically changed by the solution process using NaOH, the elemental composition of MoO<sub>4</sub> is determined by the XPS system, with photon energy of 750 eV and Agilent inductively coupled plasma mass spectroscopy 7500 single Turbo system (ICP/MS). A Perkin Elmer PE750 Lambda UV-Vis-NIR was used to measure the material absorbance of the spin-coated thin films in quartz substrates in order to estimate the band gap.

In order to confirm the MoO<sub>4</sub> indeed is covering the SYPPV without de-wetting problem, high-resolution optical microscopy was used to observe the thin film (Appendix B) and photoluminescence (PL) measurement was carried out. PL spectra in Figure 6.2 shows a negligible change of the spectra shape indicating minimum damage to the SYPPV when MoO<sub>4</sub> spin coated on top of the film. In addition to that, there is also no damage observed of SYPPV layer after spin coat MoO<sub>4</sub> due attributes to the different surface properties and polarity of solvents used for SYPPV (dissolved in Toluene (non-polar)) and MoO<sub>4</sub> (dissolved in di-onized water (polar)).

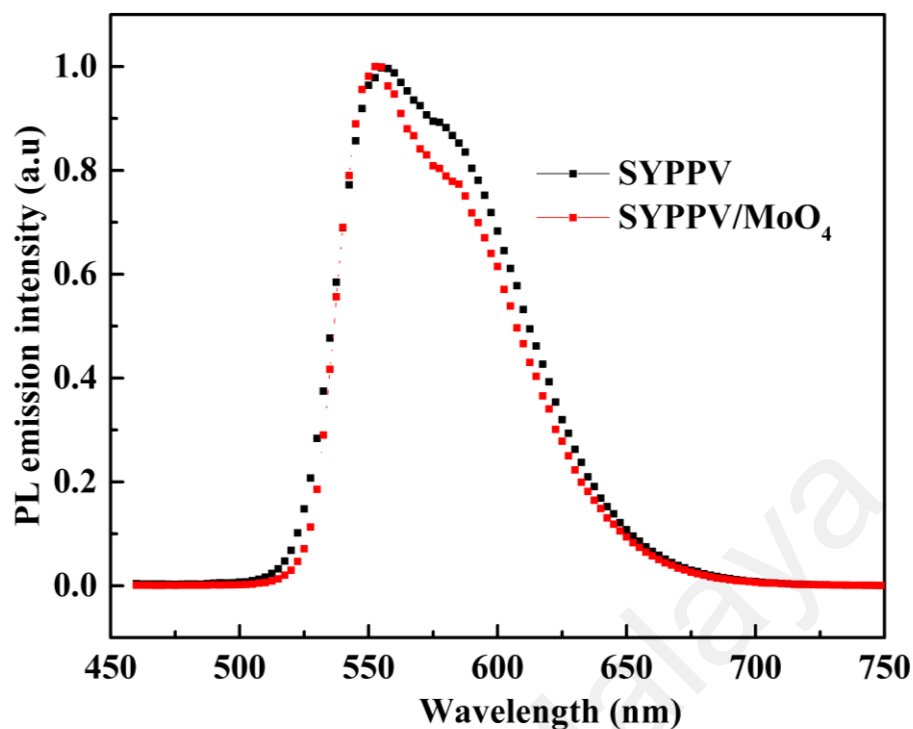


**Figure 6.2** Photoluminescence of the SYPPV/ MoO<sub>4</sub> thin film indicates negligible change of the spectra shape indicating minimum damage to the SYPPV.

### 6.3 Results and discussions

#### 6.3.1 Atomic concentration

XPS measurements were carried out to investigate the chemical composition and the surface electronic structure of the annealed thin film of the solution. Figure 6.3 (a) shows the wide scan of XP spectra for MoO<sub>4</sub> film and (b) narrow scan for Mo 3d, which is the core level of molybdate. The peaks of Mo in Figure 6.3 (b) detected at 235.7 eV and 232.5 eV can be assigned as the Mo 3d<sub>3/2</sub> and 3d<sub>5/2</sub> energy level respectively, which also correspond to the Mo<sup>6+</sup> oxidation state (Buono-Core et al., 2014). The small peaks observed at 235.2 eV and 232.4 eV are also representing the 3d<sub>3/2</sub> and 3d<sub>5/2</sub> doublet spin-orbit coupling that referred to Mo<sup>5+</sup> oxidation states (Whiffen & Smith, 2010). This film comprises of 97 % and 3.3% of Mo<sup>6+</sup> and Mo<sup>5+</sup> respectively. The presence of Mo<sup>5+</sup> states implies the film is slightly under-stoichiometric.

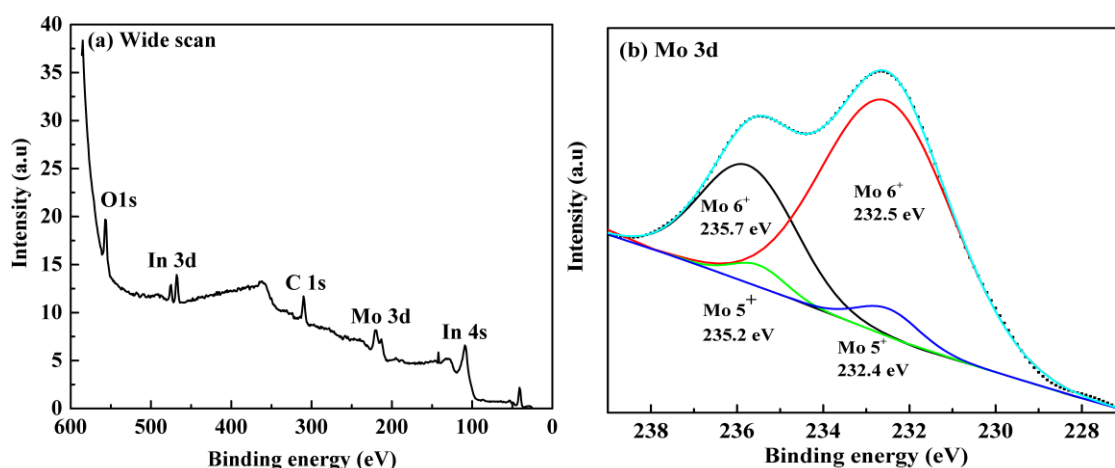


**Figure 6.3** (a) Wide XPS spectra and (b) the narrow scan and deconvolution of Mo 3d<sub>3/2</sub>, 3d<sub>5/2</sub>.

### 6.3.2 OLED Device performance

#### 6.3.2.1 Full device performance

In order to investigate whether MoO<sub>4</sub> can be used at the cathode side, OLED device with and without MoO<sub>4</sub> (0.15 wt % of MoO<sub>4</sub> at 10K rpm) was spin coated on top of SY-PPV. As shown in Figure 6.4 (a) and (b), the performance of the device of MoO<sub>4</sub>/Al exhibits a higher performance compared to the device with only Al cathode. At 1000 cd/m<sup>2</sup>, the maximum device efficiency is 0.15 cd/A (0.03 lm/W) and 1.2 cd/A (0.3 lm/W) for the device of Al and MoO<sub>4</sub>/Al cathode respectively. By using partially reduced MoO<sub>3</sub> Vasilopoulou *et al* demonstrated that the device efficiency can be increased from 0.04 to 0.9 lm/W for Al and MoO<sub>2.7</sub>/Al cathode respectively (Maria Vasilopoulou et al., 2011). Such improvement is still low. It is likely that MoO<sub>4</sub> is chemically reduced by the deposition of merely aluminum (M. Vasilopoulou et al., 2012; Maria Vasilopoulou et al., 2011).

*J-V-L* curve in Figure 6.4 (c) shows that the device with MoO<sub>4</sub>/Al gives a higher brightness but a lower current density compared to the device with Al only. Our observations indicate that electron injection from MoO<sub>4</sub>/Al is very poor. Efficient

electron injection can be enhanced by incorporating a thin LiF between MoO<sub>4</sub> and aluminum. Figure 6.4 (a) and (b) show that the device efficiency is further increased when a layer of LiF is added. The device with MoO<sub>4</sub>/LiF/Al outperformed the device with only LiF/Al. At 1000 cd/m<sup>2</sup>, the LiF/Al device shows an efficiency of 10.1 cd/A with 7.3 lm/W having CIE coordinate of (0.46, 0.53) whilst the device with MoO<sub>4</sub> shows maximum efficiencies up to 22.8 cd/A with 14.3 lm/W having CIE coordinate of (0.48, 0.52). The efficiency shown by MoO<sub>4</sub>/LiF/Al is more than two-fold higher than that of the control device with LiF/Al.

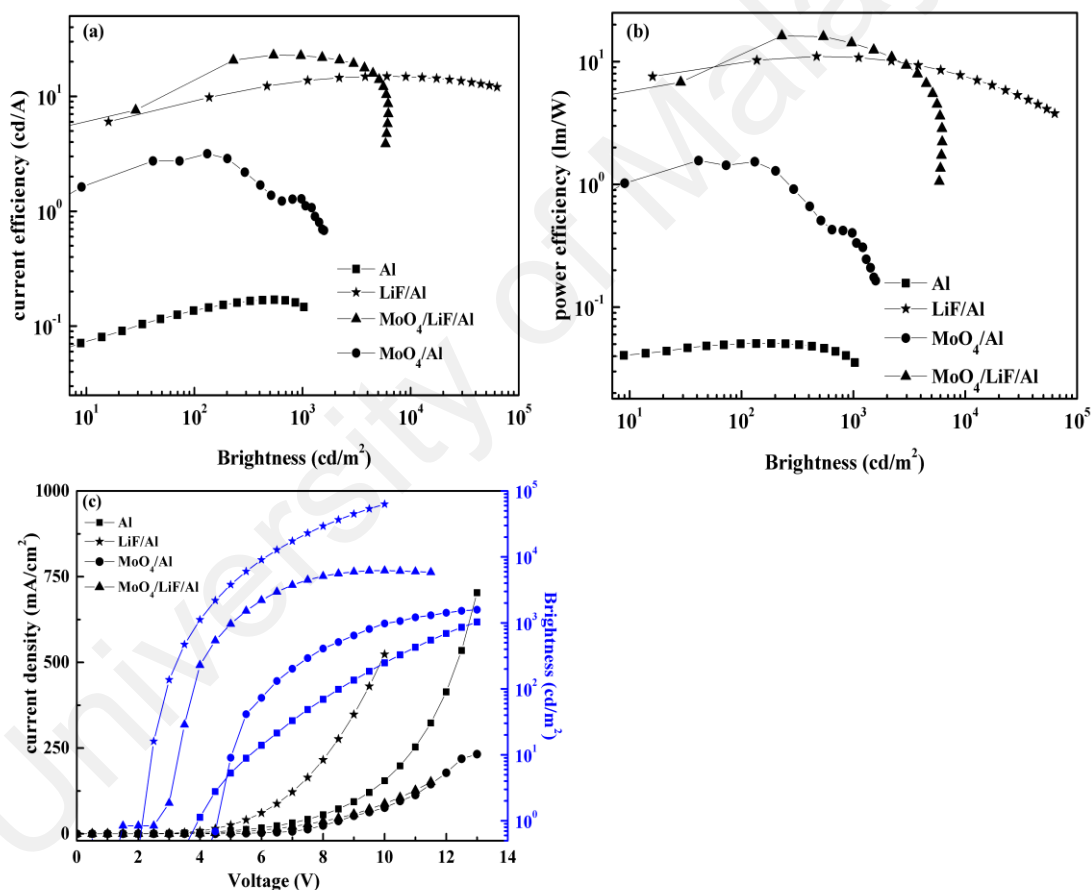


**Figure 6.4** Current Efficiency-Brightness-Power efficiency, (b) Current density versus Voltage of the devices.

Figure 6.4 (c) also shows that in order to achieve 1000 cd/m<sup>2</sup>, 3.8 V and 2.9 V driving voltage is required for MoO<sub>4</sub>/LiF/Al and for LiF/Al device respectively. The

control device shown to exhibit a higher current density compared to the device with MoO<sub>4</sub> layer. There are two possibilities that contribute to a higher driving voltage of MoO<sub>4</sub>/LiF/Al device. First, this might attribute to the addition of MoO<sub>4</sub> layer that may slightly increase the electron energy barrier into the emissive layer (S. Wang et al., 2015). Secondly, there might be a hole accumulation at the emissive/MoO<sub>3</sub> interface (Siboni & Aziz, 2012) as MoO<sub>4</sub> is well known to exhibit a deep valence band. To investigate these hypotheses, we fabricated a single carrier device to observe the carrier injection discusses in next section. The change of CIE coordinates is also reflected in electroluminescence (EL) emission measurement shown in Figure 6.5, which shown the EL emission of the device with MoO<sub>4</sub> is narrowed compared to the device with only LiF/Al.

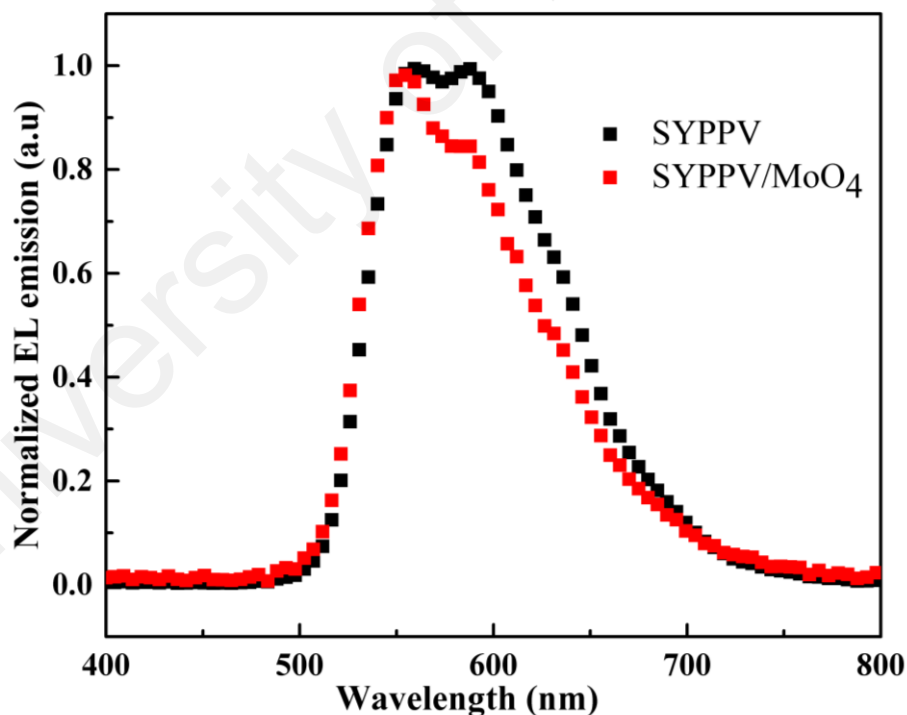


**Figure 6.5** Electroluminescence (EL) emission for the device with and without MoO<sub>4</sub>.

The performance of the OLED devices is also observed to be dependent on MoO<sub>4</sub> thickness and concentration. The performance of device with different thicknesses is

shown in Figure 6.6. It is interesting to observe that, the thinnest  $\text{MoO}_4$  shows the highest efficiency while the thicker are progressively poorer with current efficiency dropping drastically from 22.8 cd/A for 10 K rpm to 13.9 cd/A and 3.5 cd/A at 1000  $\text{cdm}^{-2}$  for 8K rpm and 5K rpm thick  $\text{MoO}_4$  respectively. The decreasing in device efficiency may be attributed by the carrier imbalance in the devices. Current densities for the devices are also compared in Figure 6.6 (b). It is shown that the control device has a higher current density compared to the device with  $\text{MoO}_4$  layer. This result indicates that  $\text{MoO}_4$  has the ability to block excess holes leaking into the cathode and thus reduce the hole current in the device.

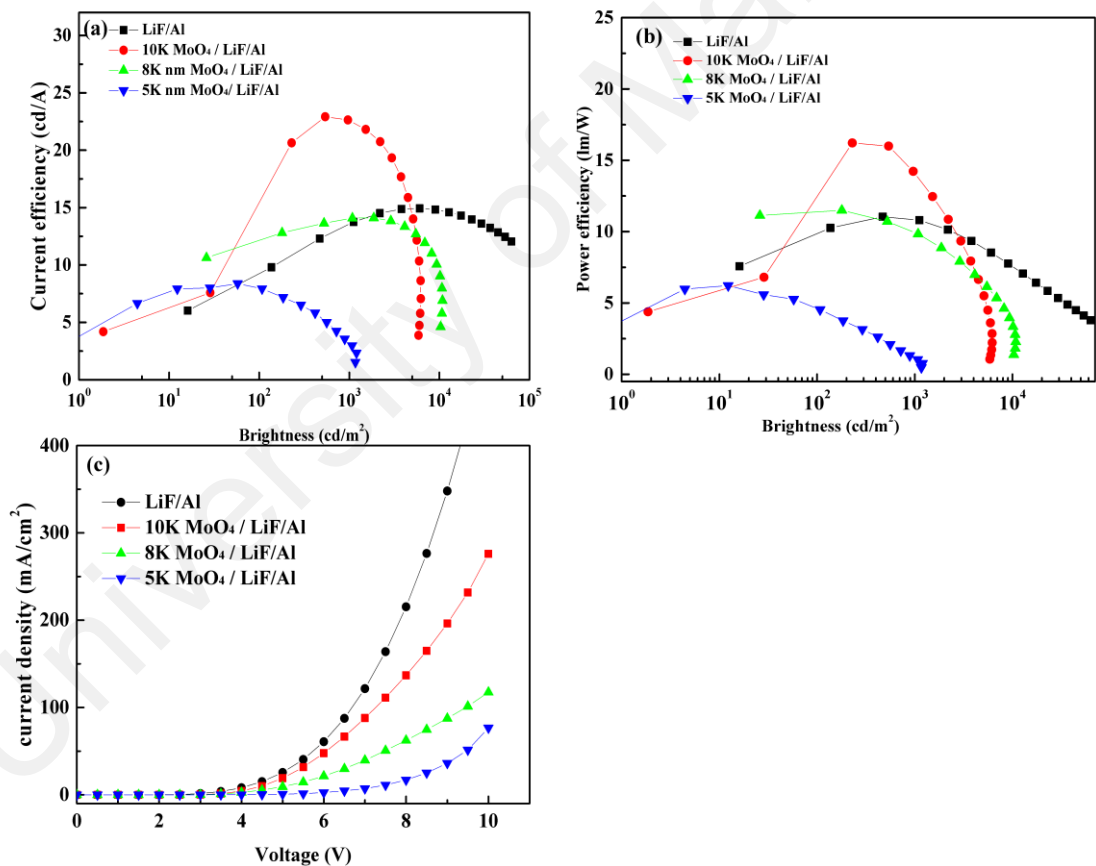


**Figure 6.6** (a) Current Efficiency-Brightness-Power efficiency, (b) Current density versus Voltage of the fabricated devices.

Recently, Wang et al reported enhancement of inverted bottom emission OLED (IBOLED) up to 6 cd/A using NaOH treated with water vapor and carbon dioxide (CO<sub>2</sub>) as EIL. The increasing of device efficiency is attributed to the reduction of electron injection barrier via dipole formation originate from the decomposition of NaOH to sodium carbonate (Na<sub>2</sub>CO<sub>3</sub>) (D. Wang, Wu, Bi, Zhang, & Zhao, 2015). Thus, we attempt to investigate the effect of NaOH (without any treatment) in our device. Figure 6.7 shows the device with NaOH and the device with MoO<sub>4</sub>. For the device with only NaOH solution, the maximum device performance is significantly decreases to 7.8 cd/A with 3.8 lm/W (Figure 6.7 (a-b)). The results in Figure 6.7 (c) show that the current density as well as the device brightness with only NaOH is reduced. This result implies that the residual of NaOH can have adverse effect device and hence the performance of devices with MoO<sub>4</sub> layer.

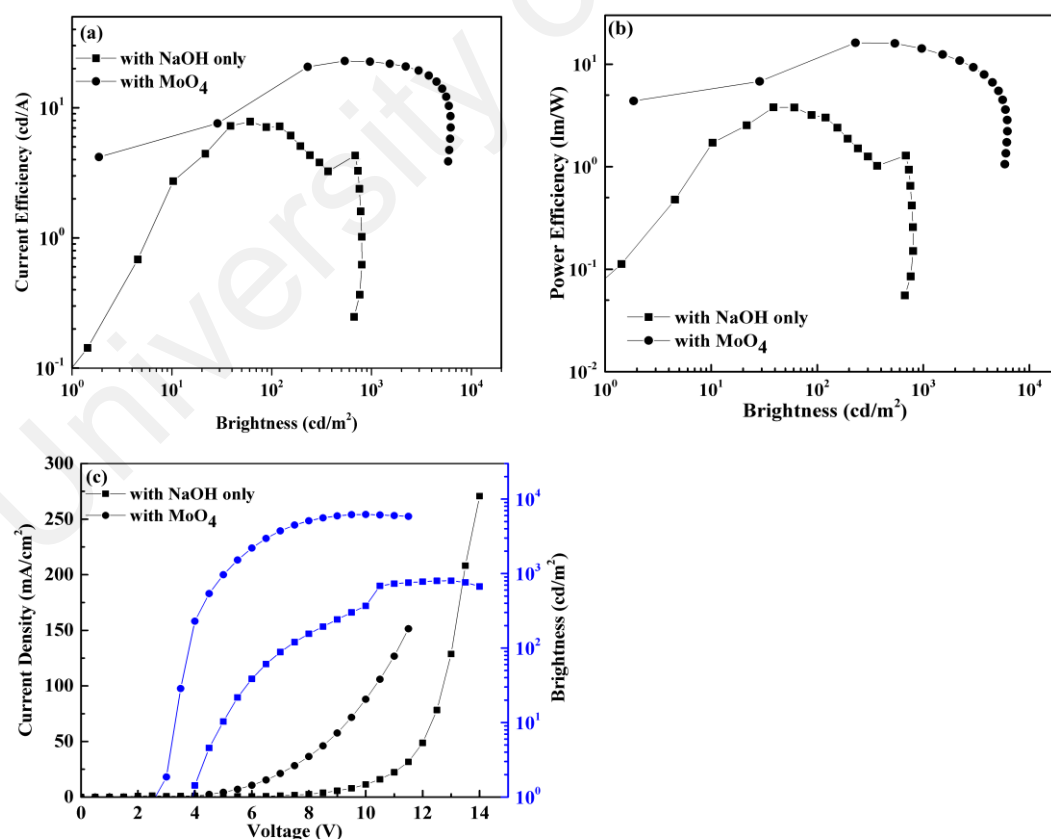


**Figure 6.7** The device performance fabricated with only NaOH and MoO<sub>4</sub>.

To observe the effect of MoO<sub>4</sub> concentration in the solution, we fabricated another devices with different concentrations, namely 0.5 wt%, 0.25 wt% and 0.15 wt%. Figure 6.8 shows the device performance for the devices. It is found that, the lower the concentration of MoO<sub>4</sub>, the higher device performance. As depicted in Figure 6.8 (a), at 1000 cd/m<sup>2</sup>, the device shows current efficiency 22.8 cd/A, 15.1 cd/A, and 9.3 cd/A for 0.5 wt%, 0.25 wt % and 0.15 wt% respectively. Whilst for power efficiency, the device for 0.5 wt%, 0.25 wt% and 0.15 wt% gives 14.3 lm/W, 11.6 lm/W and 5.9 lm/W respectively. The device with 0.15 wt% MoO<sub>4</sub> shown in Figure 6.8 (b) shows the highest current density compared to the other devices. This might indicate that 0.15 wt % MoO<sub>4</sub> is the optimal concentration which is sufficient to block hole carrier in the emissive layer. Adding more MoO<sub>4</sub> decreased the current resulting in charge imbalance and reduced device efficiency. The increasing of turn-on voltage (V<sub>on</sub>) observed for the device with MoO<sub>4</sub> may due to the insulating behavior of MoO<sub>4</sub>.

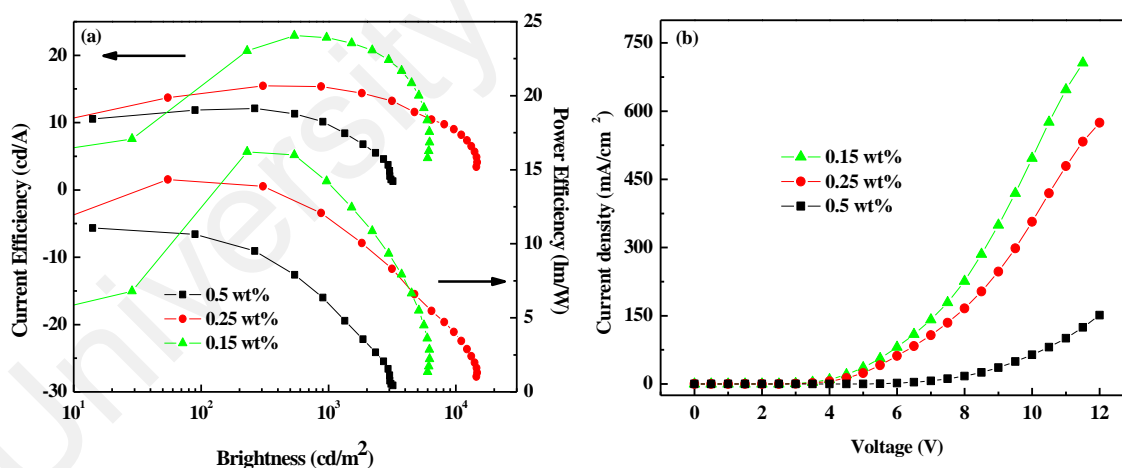


**Figure 6.8** (a) Current Efficiency-Brightness-Power efficiency, (b) Current density versus Voltage of the devices with different MoO<sub>4</sub> concentrations; 0.5 wt%, 0.25 wt %, 0.15 wt %.

### 6.3.2.2 Single carrier device performance

In order to understand the role of MoO<sub>4</sub> at the cathode side, the electron dominating devices with structure of ITO/LiF/SY-PPV/LiF/Al and ITO/LiF/SY-

PPV/MoO<sub>4</sub>/LiF/Al were fabricated. If MoO<sub>4</sub> serves as an electron injector when negative bias is applied at MoO<sub>4</sub>/LiF/Al, significant electron current should be detected. Figure 6.9 shows the electron dominating current for the devices. Both devices show almost the same electron dominating current, which implies that MoO<sub>4</sub> exhibits electron-transporting behavior. In Figure 6.4 (c), the device current decreases with the addition of MoO<sub>4</sub> layer. This suggests a reduction of hole current, which might originate from hole blocking behavior of MoO<sub>4</sub>. To confirm this, we fabricated hole dominating device structure that consists of ITO/PEDOT:PSS/SY-PPV/MoO<sub>4</sub>/Au and without MoO<sub>4</sub> as a control. The ITO/PEDOT is biased at a positive voltage while MoO<sub>4</sub>/Au is biased at the negative voltage. If MoO<sub>4</sub> serves as a hole-transporting layer, there will be no significant decrease in current. Figure 6.9 shows that the hole current is reduced at low driving voltage when MoO<sub>4</sub> is added. This reduction indicates that hole carrier is blocked by MoO<sub>4</sub> layer.

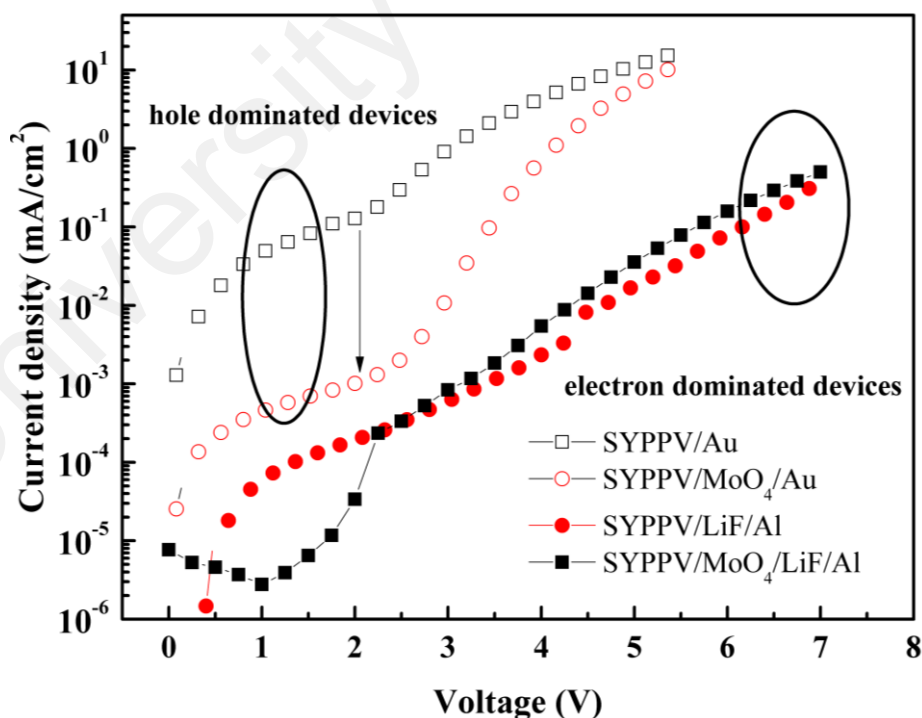


**Figure 6.9** Single carrier dominating devices. The hole current in hole dominating device (ITO/PEDOT:PSS/SY-PPV/MoO<sub>4</sub>/Au) decreases as MoO<sub>4</sub> is added. The electron current is almost the same as MoO<sub>4</sub> is added (device (ITO/LiF/SY-PPV/MoO<sub>4</sub>/LiF/Al).

There have been numerous researches indicate that hole accumulation occurs at the organic semiconductor/MoO<sub>3</sub> interface (H. Ding, Gao, Kim, Subbiah, & So, 2010; Irfan et al., 2011; X. Liu, Wang, Yi, & Gao, 2014; C. Wang, Irfan, & Gao, 2014). The presence of hole accumulation can increase the driving voltage by virtue of increased electrostatic repulsion of holes at that interface. This might explain the observed increased driving voltage in the OLED devices. However, at a higher voltage, for example 5V, MoO<sub>4</sub> becomes more and more hole transporting. It is quite possible that quantum tunneling of holes at high voltage is happening. For quantum tunneling, this requires the thickness of MoO<sub>4</sub> to be sufficiently thin. The thickness of 10K rpm of MoO<sub>4</sub> is ~2 nm as determined by TEM measurement. We speculate that quantum tunneling might be the reason why the efficiency drops significantly at a higher voltage. As stated before, the thickness of 8K rpm, 5K rpm and 2K rpm are 3.6 nm, 6.8 nm and 15.7 nm respectively

### **6.3.3 Energy level**

#### **6.3.3.1 SYPPV/MoO<sub>4</sub> interfaces**

UPS study was done on the energy alignment at the cathode interfaces in order to understand the role of MoO<sub>4</sub>. The samples that consist of different thicknesses of MoO<sub>4</sub> on SY-PPV were subjected to UPS measurements. Figure 6.10 (a) shows the UPS of high-energy cut-off (HECO) which is used to calculate the work function. While, Figure 6.10 (b) is the low energy cutoff (LECO) represents the valence band maximum (VBM) of the material. The work function and VBM positions were determined by linear extrapolations of the straight lines as shown in the figure.

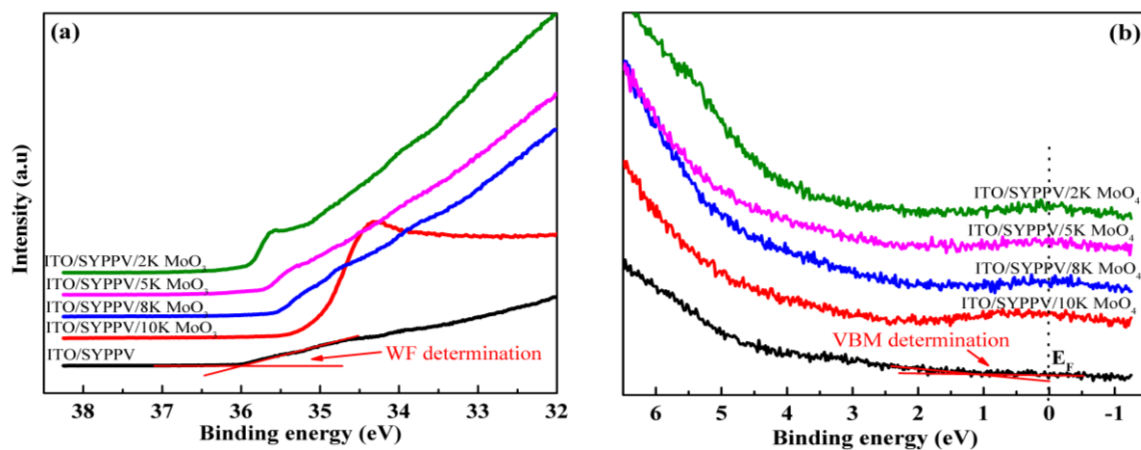


**Figure 6.10** UPS spectra of (a) secondary electron cutoff (SEC) region (b) The valence band maximum (VBM) region of SYPPV/MoO<sub>4</sub>.

In Figure 6.10 (a), the initial HECO position of SY-PPV ( $\Phi = 3.90$  eV) moves towards a lower BE to 4.90 eV (for 10K). Deposition of a thicker MoO<sub>4</sub> layer ( $\leq 8$ K rpm) slowly shifts the cutoff position to a higher binding energy (BE) which changes the surface work function until it reduced to - 4.10 eV, at 2K rpm MoO<sub>4</sub>. The movement of the work function is influenced by the position of the VBM of the material. In Figure 6.10 (b), VBM for ITO/SY-PPV is at  $\sim 0.90$  eV below the Fermi level ( $E_F$ ). The deposition of MoO<sub>4</sub> on top of SY-PPV shifts the value of the VBM and re-arranges the band diagram of the material. From figure 6.10 (b), the VBM onset for 10K rpm, 8K rpm, 5K rpm and 2K rpm is determined to be 2.34 eV, 2.45 eV, 2.67 eV and 2.71 eV respectively.

From the UPS measurement, the energy levels of the MoO<sub>4</sub> with different thicknesses on top of SY-PPV layer are mapped out as shown in Figure 6.11. The HOMO onset of 0.90 eV below Fermi level ( $E_F$ ) corresponds to 4.80 eV Ionization Energy (IE) of SY-PPV. With a band gap of 2.45 eV (Appendix D) and  $\Phi$  of 3.90 eV, the LUMO level of SY-PPV is placed at 1.55 eV above the  $E_F$ . By depositing MoO<sub>4</sub> on top of SY-PPV, there is a gradual change in IE of MoO<sub>4</sub>, which decreases from 7.24 eV for 10K rpm to 6.90 eV when the rpm reduced to 2K rpm. The IE and EA change as

much as 0.34 eV and 0.18 eV respectively when the MoO<sub>4</sub> thickness increases. The highest EA, IE and work function obtained here are 4.2 eV, 7.2 eV and 4.9 eV respectively. These values are almost consistent with the values reported for solution process MoO<sub>3</sub> (Hammond et al., 2012). However, these values gradually decreased as the MoO<sub>4</sub> film increased. It has been reported that the value of  $\Phi$  and IE of MoO<sub>4</sub> reduced significantly when it is exposed to moisture and various adsorbate in air (Meyer et al., 2012; C. Wang et al., 2014).

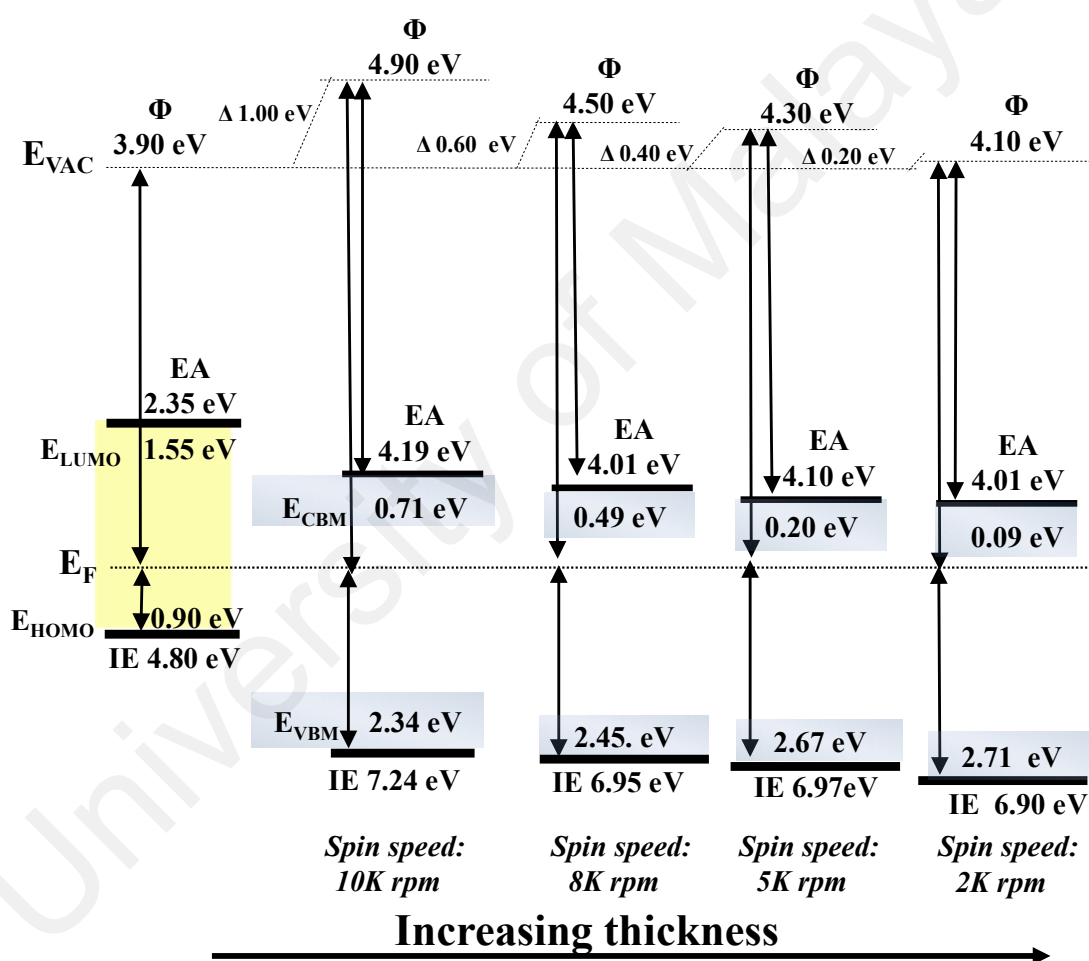


**Figure 6.11** The energy levels of MoO<sub>4</sub> on top of SYPPV mapped out from UPS measurement.

Although the MoO<sub>4</sub> thin films are annealed and sealed inside the plastic containers inside the glovebox before the UPS measurement, full removal of adsorbed water from

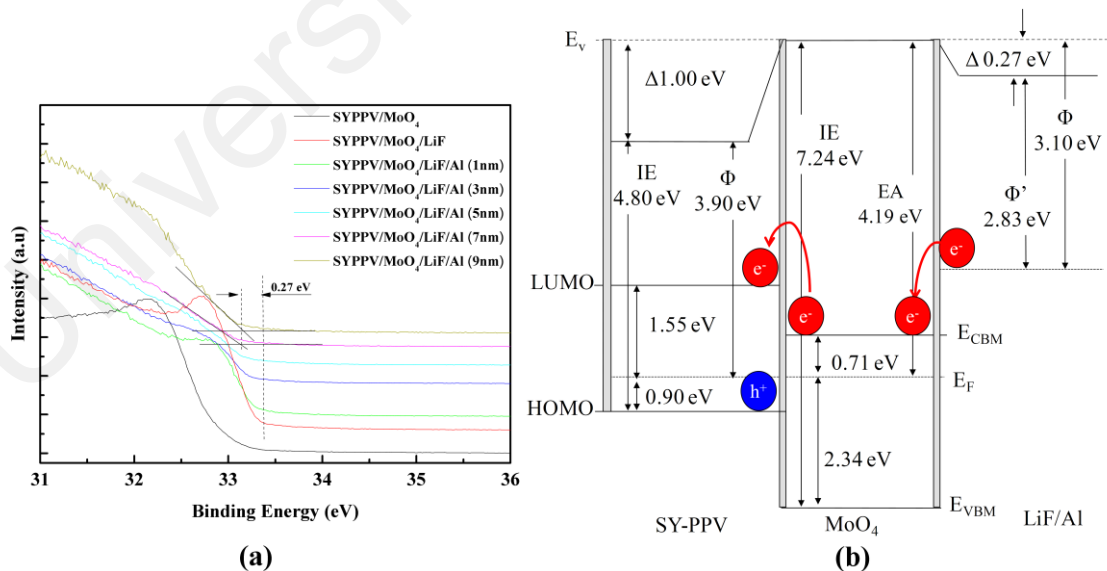
diluted NaOH might not be possible especially for a thick film. The absorbed water has the effect of reducing the EA and IE. Indeed the presence of water in the solution-processed MoO<sub>4</sub> film under XPS was observed (O1s Peak in Appendix E). The optical band-gap also changes with varying spin-coating speed. The thinnest MoO<sub>4</sub> film spin coated at 10K rpm has the widest band-gap 3.05 eV. The thickest (2K rpm) MoO<sub>4</sub> film shows a band gap of 2.87 eV (Appendix D). It has been reported that the band gap of MoO<sub>3</sub> is increased with decreasing cluster size (Weber, 1995). The higher spin-speed might have produced a smaller cluster size possibly due to faster evaporation at a higher spin-speed. Hence, the band gap increases. The highest electron affinity (EA) is obtained when a 10K rpm MoO<sub>4</sub> layer is deposited, which is 4.19 eV. From the band gap measured, the conduction band (CB) of the material can be determined. The CB of the films slowly reduced to 0.71 eV, 0.49 eV, 0.20 eV and 0.09 eV for 10K, 8K, 5K and 2K rpm MoO<sub>4</sub> film respectively from the Fermi level.

Figure 6.11 shows that the energy levels of the SY-PPV interface with MoO<sub>4</sub> deposited on top of it. For the thinnest layer of MoO<sub>4</sub>, there is a large vacuum shift as high as 1.00 eV and decreasing with increasing thickness until it reaches a very small shift of 0.20 eV at 2K rpm. Vacuum shift is often resulted from the presence of dipole layer at the interface. Such dipole layer is often a monolayer thick (<1 nm) (Topham, Kumar, & Soos, 2011; Whitcher et al., 2016) This could indicate that there is a very strong thin sheet of negative charges at the MoO<sub>4</sub> interface attracting equally thin sheet of positive charges at SY-PPY forming a dipole moment across the interface. However, for a thicker MoO<sub>4</sub>, the vacuum shift is reduced. This is surprising since interfacial dipole should be independent of the thickness. Whether such reduction is due to depolarization from adsorbed water or clustering size or other unknown effects is beyond the scope of this thesis. These results also indicate that large vacuum shift can be obtained when MoO<sub>4</sub> is very thin. This is in line of reports that the highest

performance enhancement can be obtained using only a very thin (1 nm) of MoO<sub>3</sub> (Chambon et al., 2012)

### 6.3.3.2 SYPPV/MoO<sub>4</sub>/LiF/Al interfaces

Figure 6.12 shows the UPS spectra of LiF/Al on top of 10K rpm MoO<sub>4</sub>/SY-PPV. The work function of the layer was gradually changed when LiF/Al was deposited on top of MoO<sub>4</sub>. When 7 nm of Al layer was deposited, there is 0.27 eV downward shift of vacuum level. No more shifting could be observed when 9 nm Al layer was deposited on top of MoO<sub>4</sub>. This implies that the Al layer has reached the bulk characteristic at 7 nm. Figure 6.12 (b) shows full diagram depicting the energy level across the cathode into the emissive layer, SY-PPV. The position of lower work function of LiF/Al compared to the electron affinity of MoO<sub>4</sub>, making the electron injection from the aluminum into MoO<sub>4</sub> easy. However, there is a large energetic barrier (~0.84 eV) for electron to be transported to LUMO of SYPPV and yet the electron current in electron dominating device is almost unchanged.



**Figure 6.12** Full energy alignment diagram of SY-PPV/ MoO<sub>4</sub>/LiF/Al interfaces showing the mechanism of electron injection from the cathode into the emissive layer.

### 6.3.4 AFM morphology

The film morphology using AFM is shown in Figure 6.13. SY-PPV and MoO<sub>4</sub> has root mean square surface roughness of 0.372 nm and 0.659 nm respectively on the glass substrates. However, when MoO<sub>4</sub> is spin-coated on top of SYPPV at 10 K rpm, several sharp spikes are formed with surface roughness of 2.5 nm. The rougher surface from MoO<sub>4</sub> may help to increase the physical contact with the deposited electrode (W. Ma et al., 2005). Despite a larger electron energetic barrier between SYPPV/MoO<sub>4</sub>, the rough surface would enhance the local electric field intensity (Xu et al., 2014) which help the electron injection.

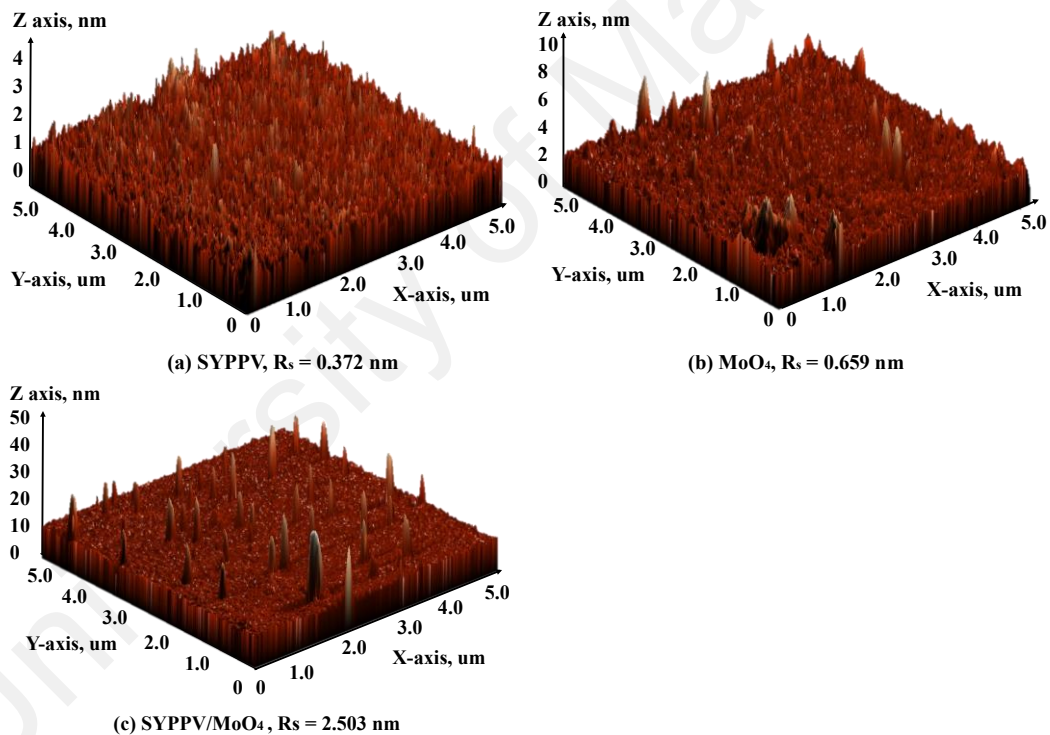


**Figure 6.13** AFM surface morphology of (a) SYPPV, (b) MoO<sub>4</sub> and (c) SYPPV/MoO<sub>4</sub> spin coated on top of glass.

As shown before (Figure 6.6), the thinnest MoO<sub>4</sub> shows the highest efficiency while the thicker are progressively poorer with current efficiency dropping drastically from 22.8 cd/A for 10 K rpm to 13.9 cd/A and 3.5 cd/A at 1000  $\text{cdm}^{-2}$  for 8K rpm and 5K

rpm thick MoO<sub>4</sub> respectively. Since the conduction band of MoO<sub>4</sub> is far lower than the work function of LiF/Al as shown in Figure 6.12 (b), it is safe to assume that electrons can be easily injected into the conduction band of MoO<sub>4</sub> even for a thicker layer of MoO<sub>4</sub>.

#### 6.4 Chapter summary

The use of solution processed MoO<sub>4</sub> at the cathode side is demonstrated in OLEDs. Interfacial energy alignment and charge transporting properties across the MoO<sub>4</sub> are investigated. It was found that the solution processed MoO<sub>4</sub> using diluted NaOH has a relatively low IE and EA reducing further when the thickness of MoO<sub>4</sub> increases. However, the band-gap increases with higher spin-speed. Hole barrier as large as 1.44 eV is found between the SYPPY/MoO<sub>4</sub> interface which might serve as a potential hole blocking layer for LiF/Al cathode. At the same time, the electron current still can flow and almost unhindered compared to LiF/Al cathode. The AFM indicates the presence of sharp spikes that could help electron injection. These result in a large improvement in device efficiency up to 22.8 cd/A with 14.3 lm/W for a yellow fluorescent OLED.

## CHAPTER 7: CONCLUSION AND FUTURE RECOMMENDATION

### 7.1 Conclusion

This thesis presents in-depth studies on the charge transport and injection in three different OLED devices with different interface modifications. The mechanism of device efficiency enhancement were systematically studied and analyzed. Our main findings are concluded in the following paragraph.

First, the study of the hole transport in poly(9-vinylcarbazole) PVK blended with small molecule tris(4-carbazoyl-9-ylphenyl)amine (TcTa) in the emissive layer mixture was discussed. In this study, the interface between PEDOT:PSS/EML was modified. By doping TcTa in PVK, shallow hole traps was introduced which results in lowering the mixture hole mobility. By doping merely 5 wt% of TcTa into PVK as mixed hole-transporting hosts, the efficiency of deep red heterojunction phosphorescent organic light emitting diode increases from 2 cd/A to 4 cd/A suggesting that TcTa molecules assist in hole injection by lowering the hole mobility that allows more hole-electron recombination and increases the device efficiency. On the other hand, the device current observed increases as the TcTa concentration increases, which might be the result of hole injection sensitivity to the hole barrier. TcTa is also observed to provide more localized regime with lower energy barrier for hole injection at PEDOT:PSS and emissive layer interface. The energetic disorder of the blended system reduces from  $\sim 72$  meV at 0 wt% TcTa to  $\sim 41$  meV at 50 wt% TcTa. A correlation between the  $\sigma$  and the film morphologies suggests that the blending of TcTa molecules in the film does not only change the film homogeneity and roughness but also change the energetic disorder.

The hole injection and transport properties is further studied via modification of charge generation layer in tandem OLED presented in Chapter 5. In this chapter, a tandem OLED was fabricated using a novel and fully solution processable as charge-generating layer (CGL). The CGL comprises of two hosts, PVK: TAPC as the *p*-type and HATCN<sub>6</sub> as n-type layer. Orthogonal solvents were utilized for CGL as HATCN<sub>6</sub> layer has a good solubility in acetonitrile and insoluble in all other types of organic solvent. Hence, another layer could be spin coated on top of HATCN<sub>6</sub> layer without intermixing problem. Tandem device exhibits high efficiency with 24.2 cd/A, which is more than doubled compared to the single OLED that exhibits only 10.7 cd/A at 1000 cd/m<sup>2</sup>. The presence of traps induced by TAPC reduces the current density of the CGU. It is shown that tandem OLED incorporating CGU with 2 wt % TAPC yielded a higher efficiency due to better electron extraction and lower injection barrier at HATCN<sub>6</sub>/PVK: TAPC interface compared to HATCN<sub>6</sub>/PVK, shown by XPS and UPS measurement.

In search of other materials for hole blocking and electron transport that offer good solubility in orthogonal solvent, we found MoO<sub>3</sub> can be dissolved in aqueous NaOH producing molybdate (MoO<sub>4</sub>) solution. The material can be dissolved on top of emissive layer without the need to worry about the layer underneath. Thus, in chapter 6, we demonstrated solution processable MoO<sub>4</sub> as cathode modifier. The device fabricated was modified by adding MoO<sub>4</sub> as hole blocking and electron transporting layer before LiF/Al were deposited. Incorporating MoO<sub>4</sub> in the device resulted in a high device efficiency improvement up to 22.8 cd/A with 14.3 lm/W for yellow fluorescent device. Via UPS measurement, we mapped out the interface of SYPPV/MoO<sub>4</sub>/LiF/Al and the mechanism device efficiency was explained on a basis of hole blocking mechanism at SYPPV/MoO<sub>4</sub> and the electron transport at MoO<sub>4</sub>/LiF/Al and interface. This allows

electrons to recombine with hole carrier and thus increases the device charge balance and thus increases the device efficiency.

Table 7.1 compared the performance of the OLED devices fabricated in this thesis work with the state-of-art work reported to date.

**Table 7.1** The comparison of fabricated OLED device in this thesis work with the literature.

Device efficiency of red phosphorescent OLED with doped hosts				
		C.E (cd/A)	P.E (lm/W)	Enhancement (%)
State-of-art work (X. Zhang et al., 2015)	Control device	12.9	5.6	~ 54 % for C.E ~ 66 % for P.E  *Maximum efficiency when 6 wt% of TcTa was added
	Mixed host device (CBP:TcTa)	19.9	9.3	
Thesis work	Control device	2.6	0.8	~ 61.5 % for C.E ~75 % for P.E  *Maximum efficiency when 5 wt% of TcTa was added
	Mixed host device (PVK:TcTa)	4.2	1.4	
Device efficiency of tandem OLED with solution process CGU				
		C.E (cd/A)	P.E (lm/W)	Enhancement (%)
State-of-art work (Höfle et al., 2015)	Control device	10.0	7.0	~ 150 % for C.E ~ 100 % for P.E
	Solution process CGU (ZnO/WO <sub>3</sub> )	25.0	14.0	
Thesis work	Control device	10.7	2.5	~ 126 % for C.E ~192 % for P.E
	Solution process CGU (HATCN <sub>6</sub> /PVK:TAPC)	24.2	7.3	
** Device efficiency with MoO <sub>3</sub> as interlayer				
		C.E (cd/A)	P.E (lm/W)	Enhancement (%)
State-of-art work (Moon, Lee, Huh, & Park, 2015)	Control device (using PEDOT:PSS as HIL)	26.2	10.1	Comparable with control device
	Solution process MoO <sub>3</sub> as HIL (anode side)	25.2	10.6	
Thesis work	Control device	10.1	7.3	~ 125 % for C.E ~ 96 % for P.E
	Solution process Molybdate as HBL (cathode side)	22.8	14.3	

\*\* To author best knowledge, there is no other work reported to date on the usage of solution process MoO<sub>3</sub> as cathode interlayer.

## 7.2 Future works

Based on in-depth studies carried out in this thesis, there are still research gap left that can be improved in the future.

- a. We demonstrated in the first part of this thesis work that by merely doping 5 wt % of TcTa in PVK, an increment of 100 % is achieved for red OLED device attributed to the charge balance in the device. It is also suggested that the improvement is due to the same mobility of hole and electron that allows an efficient recombination. The work presented here mainly discussed on the basis of hole carrier behavior instead of both carriers. It is well known that the characteristic of both carriers, hole and electron need to be taken into account in order to clearly study the OLED characteristic. Thus, a further study on electron carrier in this blending system is needed in the future.
- b. For tandem structure, we presented that with only 2 wt% of TAPC doped in PVK as p-type CGU, an efficient tandem OLED with low turn on voltage is achieved. However, the work presented here is not yet optimized. Thus, for future work, it is worth to do optimization process for the suggested charge generation unit to produce a high tandem device OLED device efficiency. In addition to that, this work can also be extended to fabricate blue, red as well as a white tandem OLED.
- c. For MoO<sub>4</sub> hole blocking layer shown in this thesis work, future work can be done by applying the material to different structures and also to phosphorescent OLED device.

## REFERENCES

- Adachi, C., Baldo, M. A., Forrest, S. R., & Thompson, M. E. (2000). High-efficiency organic electrophosphorescent devices with tris(2-phenylpyridine)iridium doped into electron-transporting materials. *Applied Physics Letters*, 77(6), 904.
- Adachi, C., Tokito, S., Tsutsui, T., & Saito, S. (1988). Organic Electroluminescent Device with a Three-Layer Structure. *Japanese Journal of Applied Physics*, 27(Part 2, No. 4), L713–L715.
- Ahn, S. Il, Kim, W. K., Ryu, S. H., Kim, K. J., Lee, S. E., Kim, S.-H., ... Choi, K. C. (2012). OLED with a controlled molecular weight of the PVK (poly(9-vinylcarbazole)) formed by a reactive ink-jet process. *Organic Electronics*, 13(6), 980–984.
- Aizawa, N., Pu, Y.-J., Watanabe, M., Chiba, T., Ideta, K., Toyota, N., ... Kido, J. (2014). Solution-processed multilayer small-molecule light-emitting devices with high-efficiency white-light emission. *Nature Communications*, 5, 5756.
- Arkhipov, V. I., von Seggern, H., & Emelianova, E. V. (2003). Charge injection versus space-charge-limited current in organic light-emitting diodes. *Applied Physics Letters*, 83(24), 5074.
- Baldo, M. A., Lamansky, S., Burrows, P. E., Thompson, M. E., & Forrest, S. R. (1999). Very high-efficiency green organic light-emitting devices based on electrophosphorescence. *Applied Physics Letters*, 75(1), 4.
- Baldo, M. A., O'Brien, D. F., You, Y., Shoustikov, A., Sibley, S., Thompson, M. E., & Forrest, S. R. (1998). Highly efficient phosphorescent emission from organic electroluminescent devices, 395(6698), 151–154.
- Baldo, M., & Segal, M. (2005). Phosphorescence as a Probe of Exciton Formation and Energy Transfer in Organic Light Emitting Diodes. In W. Brütting (Ed.), *Physics of Organic Semiconductors*. Weinheim, FRG: Wiley-VCH Verlag GmbH & Co. KGaA.
- Bässler, H. (1993). Charge Transport in Disordered Organic Photoconductors -a Monte Carlo Simulation Study. *Physica Status Solidi (B)*, 175(1), 15–56.
- Bässler, H., & Köhler, A. (2011). Charge transport in organic semiconductors. In R. M. Metzger (Ed.), *Unimolecular and Supramolecular Electronics I: Chemistry and Physics Meet at Metal-Molecule Interfaces* (1st ed., Vol. 312, pp. 1–66). New York: Springer-Verlag Berlin Heidelberg.
- Baumann, T., & Rudat, B. (June 13, 2013). Manufacturing of OLEDs – challenges and solutions. Retrieved 1 January, 2015, from <http://www.ledlighting-eetimes.com/content/manufacturing-oleds---challenges-and-solutions>.
- Benchaabane, A., Ben Hamed, Z., Kouki, F., Abderrahmane Sanhoury, M., Zellama, K., Zeinert, A., & Bouchriha, H. (2014). Performances of effective medium model in interpreting optical properties of polyvinylcarbazole:ZnSe nanocomposites.

*Journal of Applied Physics*, 115(13), 134313.

- Blakesley, J. C., & Greenham, N. C. (2009). Charge transfer at polymer-electrode interfaces: The effect of energetic disorder and thermal injection on band bending and open-circuit voltage. *Journal of Applied Physics*, 106(3), 34507.
- Bokdam, M., Çakır, D., & Brocks, G. (2011). Fermi level pinning by integer charge transfer at electrode-organic semiconductor interfaces. *Applied Physics Letters*, 98(11), 113303.
- Borsenberger, P. M. (1998). *Organic Photoreceptors for Xerography*. (P. M. Borsenberger & D. S. Weiss, Eds.) (1st ed.). BOOK, New York, NY: Taylor & Francis.
- Braun, S., Salaneck, W. R., & Fahlman, M. (2009). Energy-level alignment at organic/metal and organic/organic interfaces. *Advanced Materials*, 21(14–15), 1450–1472.
- Bravman, J. C., & Sinclair, R. (1984). The preparation of cross-section specimens for transmission electron microscopy. *Journal of Electron Microscopy Technique*, 1(1), 53–61.
- Brown, P. J., Thomas, D. S., Köhler, A., Wilson, J. S., Kim, J.-S., Ramsdale, C. M., ... Friend, R. H. (2003). Effect of interchain interactions on the absorption and emission of poly(3-hexylthiophene). *Physical Review B*, 67(6), 64203.
- Brunet, E., Colón, J. L., & Clearfield, A. (2015). *Tailored Organic-Inorganic Materials*. (E. Brunet, J. L. Colón, & A. Clearfield, Eds.) (1st ed.). New Jersey: John Wiley & Sons.
- Buono-Core, G. E., Klahn, A. H., Castillo, C., Muñoz, E., Manzur, C., Cabello, G., & Chornik, B. (2014). Synthesis and characterization of thin molybdenum oxide films prepared from molybdenum dioxo tropolonate precursors by photochemical metal-organic deposition (PMOD) and its evaluation as ammonia gas sensors. *Journal of Non-Crystalline Solids*, 387, 21–27.
- Burin, A. L., & Ratner, M. A. (2000). Exciton Migration and Cathode Quenching in Organic Light Emitting Diodes †. *The Journal of Physical Chemistry A*, 104(20), 4704–4710.
- Burroughes, J. H., Bradley, D. D. C., Brown, A. R., Marks, R. N., Mackay, K., Friend, R. H., ... Holmes, A. B. (1990). Light-emitting diodes based on conjugated polymers. *Nature*, 347(6293), 539–541.
- C.H, W., & Dong Liang Tao. (2007). Rare-Earth Complexes and Its Applications in Organic Light Emitting Diodes. In R. W. Buckley (Ed.), *Solid State Chemistry Research Trends* (1st ed., p. 236). New York, NY: Nova Publishers.
- Cao, Y., Treacy, G. M., Smith, P., & Heeger, A. J. (1992). Solution-cast films of polyaniline: Optical-quality transparent electrodes. *Applied Physics Letters*, 60(22), 2711.

- Chambon, S., Derue, L., Lahaye, M., Pavageau, B., Hirsch, L., & Wantz, G. (2012). MoO<sub>3</sub> Thickness, Thermal Annealing and Solvent Annealing Effects on Inverted and Direct Polymer Photovoltaic Solar Cells. *Materials*, 5(12), 2521–2536.
- Chan, M. Y., Lai, S. L., Lau, K. M., Fung, M. K., Lee, C. S., & Lee, S. T. (2007). Influences of Connecting Unit Architecture on the Performance of Tandem Organic Light-Emitting Devices. *Advanced Functional Materials*, 17(14), 2509–2514.
- Chang, C.-C., Chen, J.-F., Hwang, S.-W., & Chen, C. H. (2005). Highly efficient white organic electroluminescent devices based on tandem architecture. *Applied Physics Letters*, 87(25), 253501.
- Chen, J., Pan, J., Huang, Q., Xu, F., Zhang, Z., Lei, W., & Nathan, A. (2015). Graphene oxide/PEDOT:PSS as injection layer for quantum dot light emitting diode. *Physica Status Solidi (a)*, 212(12), 2856–2861.
- Chen, J., Shi, C., Fu, Q., Zhao, F., Hu, Y., Feng, Y., & Ma, D. (2012). Solution-processable small molecules as efficient universal bipolar host for blue, green and red phosphorescent inverted OLEDs. *Journal of Materials Chemistry*, 22, 5164.
- Chen, Y., Chen, J., Ma, D., Yan, D., Wang, L., & Zhu, F. (2011). High power efficiency tandem organic light-emitting diodes based on bulk heterojunction organic bipolar charge generation layer. *Applied Physics Letters*, 98(24), 243309.
- Chen, Y., & Ma, D. (2012). Organic semiconductor heterojunctions as charge generation layers and their application in tandem organic light-emitting diodes for high power efficiency. *Journal of Materials Chemistry*, 22(36), 18718.
- Chiba, T., Pu, Y.-J., Miyazaki, R., Nakayama, K., Sasabe, H., & Kido, J. (2011). Ultra-high efficiency by multiple emission from stacked organic light-emitting devices. *Organic Electronics*, 12, 710–715.
- Chiba, T., Pu, Y.-J., Sasabe, H., Kido, J., & Yang, Y. (2012). Solution-processed organic light-emitting devices with two polymer light-emitting units connected in series by a charge-generation layer. *Journal of Materials Chemistry*, 22(42), 22769.
- Chou, Y.-N., & Wen, T.-C. (2012). Tuning of Indium Tin Oxide Work Function with an Ionic Solid Thin Film in Polymer Light-Emitting Diodes. In *The Electrochemical Society Meeting* (Vol. MA2012-02, p. 3959). The Electrochemical Society.
- Conwell, E. M. (1956). Impurity Band Conduction in Germanium and Silicon. *Physical Review*, 103(1), 51–61.
- Coropceanu, V., Demetrio, A., Filho, S., Olivier, Y., Silbey, R., & Bre, J. (2007). Charge Transport in Organic Semiconductors. *J.Chem. Rev.*, 107, 926–952.
- Davids, P. S., Campbell, I. H., & Smith, D. L. (1997). Device model for single carrier organic diodes. *Journal of Applied Physics*, 82(12), 6319.

- Deng, L., Furuta, P. T., Garon, S., Li, J., Kavulak, D., Thompson, M. E., & Fréchet, J. M. J. (2006). Living Radical Polymerization of Bipolar Transport Materials for Highly Efficient Light Emitting Diodes. *Chemistry of Materials*, 18(2), 386–395.
- Dexter, D. L. (1953). A Theory of Sensitized Luminescence in Solids. *The Journal of Chemical Physics*, 21(5), 836.
- Ding, H., Gao, Y., Kim, D. Y., Subbiah, J., & So, F. (2010). Energy level evolution of molybdenum trioxide interlayer between indium tin oxide and organic semiconductor. *Applied Physics Letters*, 96(7), 73304.
- Ding, X. M., Hung, L. M., Cheng, L. F., Deng, Z. B., Hou, X. Y., Lee, C. S., & Lee, S. T. (2000). Modification of the hole injection barrier in organic light-emitting devices studied by ultraviolet photoelectron spectroscopy. *Applied Physics Letters*, 76(19), 2704.
- Du, Y., Peng, H. Y., Mao, H., Jin, K. X., Wang, H., Li, F., ... Wu, T. (2015). Evolution of the SrTiO<sub>3</sub>-MoO<sub>3</sub> Interface Electronic Structure: An in Situ Photoelectron Spectroscopy Study. *ACS Applied Materials & Interfaces*, 7(21), 11309–14.
- Earmme, T., & Jenekhe, S. A. (2013). Improved electron injection and transport by use of baking soda as a low-cost, air-stable, n-dopant for solution-processed phosphorescent organic light-emitting diodes. *Applied Physics Letters*, 102(23), 233305.
- Förster, T. (1959). 10th Spiers Memorial Lecture. Transfer mechanisms of electronic excitation. *Discussions of the Faraday Society*, 27, 7.
- Fowler, R. H., & Nordheim, L. (1928). Electron Emission in Intense Electric Fields. *Proceedings of the Royal Society A: Mathematical, Physical and Engineering Sciences*, 119(781), 173–181.
- Frenkel, J. (1938). On Pre-Breakdown Phenomena in Insulators and Electronic Semiconductors. *Physical Review*, 54(8), 647–648.
- Fu, Q., Chen, J., Shi, C., & Ma, D. (2013). Room-temperature sol-gel derived molybdenum oxide thin films for efficient and stable solution-processed organic light-emitting diodes. *ACS Applied Materials & Interfaces*, 5(13), 6024–9.
- Gao, Y. (2010). Surface analytical studies of interfaces in organic semiconductor devices. *Materials Science and Engineering: R: Reports*, 68(3), 39–87.
- Gather, M. C., Jin, R., Mello, J., Bradley, D. D. C., & Meerholz, K. (2009). Highly-efficient solution-processed phosphorescent multi-layer organic light-emitting diodes investigated by electromodulation spectroscopy. *Applied Physics B*, 95, 113–124.
- Giroto, C., Voroshazi, E., Cheyns, D., Heremans, P., & Rand, B. P. (2011). Solution-processed MoO<sub>3</sub> thin films as a hole-injection layer for organic solar cells. *ACS Applied Materials & Interfaces*, 3(9), 3244–7.
- Gong, X., Wang, S., Moses, D., Bazan, G. C., & Heeger, A. J. (2005). Multilayer

- Polymer Light-Emitting Diodes: White-Light Emission with High Efficiency. *Advanced Materials*, 17(17), 2053–2058.
- Grover, R., Srivastava, R., Kamalasanan, M. N., & Mehta, D. S. (2012). Percolation dominated electron transport in Tetracyanoquinodimethane mixed 4,7-diphenyl-1,10-phenanthroline thin films. *Organic Electronics*, 13(12), 3074–3078.
- Gu, G., Shen, Z., Burrows, P. E., & Forrest, S. R. (1997). Transparent flexible organic light-emitting devices. *Advanced Materials*, 9(9), 725–728.
- Guilbault, G. G. (1973). *Practical Fluorescence — Theory, Methods and Techniques*. M. Dekker. <http://doi.org/10.1002/food.19760200180>
- Gustafsson, G., Cao, Y., Treacy, G. M., Klavetter, F., Colaneri, N., & Heeger, A. J. (1992). Flexible light-emitting diodes made from soluble conducting polymers. *Nature*, 357(6378), 477–479.
- Hammond, S. R., Meyer, J., Widjonarko, N. E., Ndione, P. F., Sigdel, A. K., Garcia, A., ... Olson, D. C. (2012). Low-temperature, solution-processed molybdenum oxide hole-collection layer for organic photovoltaics. *Journal of Materials Chemistry*, 22(7), 3249.
- Heimel, G., Salzmann, I., Duhm, S., & Koch, N. (2011). Design of Organic Semiconductors from Molecular Electrostatics †. *Chemistry of Materials*, 23(3), 359–377.
- Helfrich, W., & Schneider, W. G. (1965). Recombination Radiation in Anthracene Crystals. *Physical Review Letters*, 14(7), 229–231.
- Hellerich, E. S., Intemann, J. J., Cai, M., Liu, R., Ewan, M. D., Tlach, B. C., ... Shinar, J. (2013). Fluorescent polymer guest:small molecule host solution-processed OLEDs. *Journal of Materials Chemistry C*, 1(34), 5191.
- Herlocker, J. A., Fuentes-Hernandez, C., Ferrio, K. B., Hendrickx, E., Blanche, P.-A., Peyghambarian, N., ... Marder, S. R. (2000). Stabilization of the response time in photorefractive polymers. *Applied Physics Letters*, 77(15), 2292.
- Hertel, D., Bässler, H., Scherf, U., & Hörhold, H. H. (1999). Charge carrier transport in conjugated polymers. *The Journal of Chemical Physics*, 110(18), 9214.
- Hinderhofer, A., & Schreiber, F. (2012). Organic-organic heterostructures: concepts and applications. *Chemphyschem: A European Journal of Chemical Physics and Physical Chemistry*, 13(3), 628–43.
- Höfle, S., Bernhard, C., Bruns, M., Kübel, C., Scherer, T., Lemmer, U., & Colmann, A. (2015). Charge generation layers for solution processed tandem organic light emitting diodes with regular device architecture. *ACS Applied Materials & Interfaces*, 7(15), 8132–7.
- Höfle, S., Pfaff, M., Do, H., Bernhard, C., Gerthsen, D., Lemmer, U., & Colmann, A. (2014). Suppressing molecular aggregation in solution processed small molecule organic light emitting diodes. *Organic Electronics*, 15(1), 337–341.

- Höfle, S., Schienle, A., Bernhard, C., Bruns, M., Lemmer, U., & Colmann, A. (2014). Solution Processed, White Emitting Tandem Organic Light-Emitting Diodes with Inverted Device Architecture. *Advanced Materials*, 26(30), 5155–5159.
- Huang, F., Shih, P.-I., Shu, C.-F., Chi, Y., & Jen, A. K.-Y. (2009). Highly Efficient Polymer White-Light-Emitting Diodes Based on Lithium Salts Doped Electron Transporting Layer. *Advanced Materials*, 21(3), 361–365.
- Huang, J., Pfeiffer, M., Werner, A., Blochwitz, J., Leo, K., & Liu, S. (2002). Low-voltage organic electroluminescent devices using pin structures. *Applied Physics Letters*, 80(1), 139.
- Hyun Kim, C., Yaghmazadeh, O., Bonnassieux, Y., & Horowitz, G. (2011). Modeling the low-voltage regime of organic diodes: Origin of the ideality factor. *Journal of Applied Physics*, 110(9), 93722.
- Im, C., Bäessler, H., Rost, H., & Hörhold, H. H. (2000). Hole transport in polyphenylenevinylene-ether under bulk photoexcitation and sensitized injection. *The Journal of Chemical Physics*, 113(9), 3802.
- Inigo, A. R., Chiu, H.-C., Fann, W., Huang, Y.-S., Jeng, U.-S., Lin, T.-L., ... Chen, S.-A. (2004). Disorder controlled hole transport in MEH-PPV. *Physical Review B*, 69(7), 75201.
- Irfan, I., Graber, S., So, F., & Gao, Y. (2012). Interplay of cleaning and de-doping in oxygen plasma treated high work function indium tin oxide (ITO). *Organic Electronics*, 13(10), 2028–2034.
- Irfan, I., James Turinske, A., Bao, Z., & Gao, Y. (2012). Work function recovery of air exposed molybdenum oxide thin films. *Applied Physics Letters*, 101(9), 93305.
- Irfan, Ding, H., So, F., & Gao, Y. (2011). Oxide insertion layer in organic semiconductor devices. *Journal of Photonics for Energy*, 1(1), 11105.
- Ishii, H., & Seki, K. (1997). Energy level alignment at organic/metal interfaces studied by UV photoemission: breakdown of traditional assumption of a common vacuum level at the interface. *IEEE Transactions on Electron Devices*, 44(8), 1295–1301.
- Ishii, H., Sugiyama, K., Ito, E., & Seki, K. (1999). Energy Level Alignment and Interfacial Electronic Structures at Organic/Metal and Organic/Organic Interfaces. *Advanced Materials*, 11(8), 605–625.
- Jain, S. C., Geens, W., Mehra, A., Kumar, V., Aernouts, T., Poortmans, J., ... Willander, M. (2001). Injection- and space charge limited-currents in doped conducting organic materials. *Journal of Applied Physics*, 89(7), 3804.
- Jeon, W. S., Park, J. S., Li, L., Lim, D. C., Son, Y. H., Suh, M. C., & Kwon, J. H. (2012). High current conduction with high mobility by non-radiative charge recombination interfaces in organic semiconductor devices. *Organic Electronics: Physics, Materials, Applications*, 13(6), 939–944.

- Jou, J.-H., Sun, M.-C., Chou, H.-H., & Li, C.-H. (2005). White organic light-emitting devices with a solution-processed and molecular host-employed emission layer. *Applied Physics Letters*, 87(4), 43508.
- Jou, J.-H., Sun, M.-C., Chou, H.-H., & Li, C.-H. (2006). Efficient pure-white organic light-emitting diodes with a solution-processed, binary-host employing single emission layer. *Applied Physics Letters*, 88(14), 141101.
- Kageyama, H., Kajii, H., Ohmori, Y., & Shirota, Y. (2011). MoO<sub>3</sub> as a Cathode Buffer Layer Material for the Improvement of Planar pn-Heterojunction Organic Solar Cell Performance. *Applied Physics Express*, 4(3), 32301.
- Kahn, A. (2015). Fermi level, work function and vacuum level. *Mater. Horiz.*, 3(1), 7–10.
- Kalinowski, J., Cocchi, M., Virgili, D., Fattori, V., & Williams, J. A. G. (2007). Mixing of Excimer and Exciplex Emission: A New Way to Improve White Light Emitting Organic Electrophosphorescent Diodes. *Advanced Materials*, 19(22), 4000–4005.
- Kanemitsu, Y. (1993). Microscopic nature of hopping charge transport in disordered molecular solids. *Journal of Non-Crystalline Solids*, 164–166, 1271–1274.
- Kang, H., Kim, J.-H., Kim, J.-K., Seo, J., & Park, Y. (2011). Interface Electronic Structure of a Strongly Electron Withdrawing Molecule on an Indium-tin-oxide Surface. *Journal of Korean Physical Society*, 59(5), 3060–3063.
- Kanno, H., Holmes, R. J., Sun, Y., Kena-Cohen, S., & Forrest, S. R. (2006). White Stacked Electrophosphorescent Organic Light-Emitting Devices Employing MoO<sub>3</sub> as a Charge-Generation Layer. *Advanced Materials*, 18(3), 339–342.
- Kao, K.-C., & Hwang, W. (1981). *Electrical transport in solids: with particular reference to organic semiconductors*. Pergamon Press. Retrieved from [https://books.google.com.my/books/about/Electrical\\_transport\\_in\\_solids.html?id=mqZPAQAIAAJ&pgis=1](https://books.google.com.my/books/about/Electrical_transport_in_solids.html?id=mqZPAQAIAAJ&pgis=1)
- Keum, J., Ha, C.-S., & Kim, Y. (2006). Molecularly doped polymeric network nanolayers for organic light-emitting devices. *Macromolecular Research*, 14(4), 401–403.
- Keuning, W., van de Weijer, P., Lifka, H., Kessels, W. M. M., & Creatore, M. (2012). Cathode encapsulation of organic light emitting diodes by atomic layer deposited Al<sub>2</sub>O<sub>3</sub> films and Al<sub>2</sub>O<sub>3</sub>/a-SiN<sub>x</sub>:H stacks. *Journal of Vacuum Science & Technology A: Vacuum, Surfaces, and Films*, 30(1), 01A131.
- Kido, J., Kimura, M., & Nagai, K. (1995). Multilayer white light-emitting organic electroluminescent device. *Science (New York, N.Y.)*, 267(5202), 1332–4.
- Kido, J., Matsumoto, T., Nakada, T., Endo, J., Mori, K., Kawamura, N., & Yokoi, A. (2003). 27.1: Invited Paper: High Efficiency Organic EL Devices having Charge Generation Layers. *SID Symposium Digest of Technical Papers*, 34(1), 964.

- Kim, C., Lee, B., Yang, H. J., Lee, H. M., Lee, J. G., & Shin, H. (2005). Effects of Surface Treatment on Work Function of ITO (Indium Tin Oxide) Films. *Journal of the Korean Physical Society*, 47, 417–421.
- Kim, H., Lee, J., Park, C., & Park, Y. (2002). Surface Characterization of O<sub>2</sub>-Plasma-Treated Indium-Tin-Oxide (ITO) Anodes for Organic Light-Emitting-Device Applications. *Journal of the Korean Physical Society*, 41(3), 395–399.
- Kim, S.-J., Zhang, Y., Zuniga, C., Barlow, S., Marder, S. R., & Kippelen, B. (2011). Efficient green OLED devices with an emissive layer comprised of phosphor-doped carbazole/bis-oxadiazole side-chain polymer blends. *Organic Electronics*, 12(3), 492–496.
- Kim, W. H., Mäkinen, A. J., Nikolov, N., Shashidhar, R., Kim, H., & Kafafi, Z. H. (2002). Molecular organic light-emitting diodes using highly conducting polymers as anodes. *Applied Physics Letters*, 80(20), 3844.
- Kim, W., Kushto, G., Kim, H., & Kafafi, Z. (2003). Effect of Annealing on the Electrical Properties and Morphology of a Conducting Polymer used as an Anode in Organic Light-Emitting Devices. *Journal of Polymer Science: Part B: Polymer Physics*, 41, 2522–2528.
- Koch, N. (2007). Organic electronic devices and their functional interfaces. *Chemphyschem: A European Journal of Chemical Physics and Physical Chemistry*, 8(10), 1438–55.
- Köhler, A., & Bässler, H. (2009). Triplet states in organic semiconductors. *Materials Science and Engineering: R: Reports*, 66(4–6), 71–109.
- Kondo, T. (2007). *Current-Voltage Characteristics of Organic Semiconductors: Interfacial Control Between Organic Layers and Electrodes Current-Voltage Characteristics of Organic Semiconductors: Interfacial Control Between*. Georgia Institute of Technology. (Doctoral Dissertation). Retrieved from <http://hdl.handle.net/1853/16253>
- Kreouzis, T., Poplavskyy, D., Tuladhar, S. M., Campoy-Quiles, M., Nelson, J., Campbell, A. J., & Bradley, D. D. C. (2006). Temperature and field dependence of hole mobility in poly(9,9-dioctylfluorene). *Physical Review B*, 73(23), 235201.
- Kröger, M., Hamwi, S., Meyer, J., Dobbertin, T., Riedl, T., Kowalsky, W., & Johannes, H.-H. (2007). Temperature-independent field-induced charge separation at doped organic/organic interfaces: Experimental modeling of electrical properties. *Physical Review B*, 75(23), 235321.
- Kröger, M., Hamwi, S., Meyer, J., Riedl, T., Kowalsky, W., & Kahn, A. (2009). Role of the deep-lying electronic states of MoO<sub>3</sub> in the enhancement of hole-injection in organic thin films. *Applied Physics Letters*, 95(12), 123301.
- Kuik, M., Koster, L. J. A., Dijkstra, A. G., Wetzelaer, G. A. H., & Blom, P. W. M. (2012). Non-radiative recombination losses in polymer light-emitting diodes. *Organic Electronics*, 13(6), 969–974.

- Kumar, V., Jain, S. C., Kapoor, A. K., Poortmans, J., & Mertens, R. (2003). Trap density in conducting organic semiconductors determined from temperature dependence of J–V characteristics. *Journal of Applied Physics*, *94*(2), 1283.
- Lampande, R., Kim, G. W., Boizot, J., Kim, Y. J., Pode, R., & Kwon, J. H. (2013). A highly efficient transition metal oxide layer for hole extraction and transport in inverted polymer bulk heterojunction solar cells. *Journal of Materials Chemistry A*, *1*(23), 6895.
- Lampert, M. A., & Mark, P. (1970). *Current Injection in Solids* (xiv). Academic Press, New York.
- Lange, I., Blakesley, J. C., Frisch, J., Vollmer, A., Koch, N., & Neher, D. (2011). Band bending in conjugated polymer layers. *Physical Review Letters*, *106*(21), 216402.
- Lee, D.-H., Liu, Y.-P., Lee, K.-H., Chae, H., & Cho, S. M. (2010). Effect of hole transporting materials in phosphorescent white polymer light-emitting diodes. *Organic Electronics*, *11*(3), 427–433.
- Leem, D.-S., Lee, J.-H., Kim, J.-J., & Kang, J.-W. (2008). Highly efficient tandem p-i-n organic light-emitting diodes adopting a low temperature evaporated rhenium oxide interconnecting layer. *Applied Physics Letters*, *93*(10), 103304.
- Li, B., Chen, J., Zhao, Y., Yang, D., & Ma, D. (2011). Effects of carrier trapping and scattering on hole transport properties of N,N'-diphenyl-N,N'-bis(1-naphthyl)-1,1'-biphenyl-4,4'-diamine thin films. *Organic Electronics*, *12*(6), 974–979.
- Li, C., Duan, L., Sun, Y., Li, H., & Qiu, Y. (2012). Charge Transport in Mixed Organic Disorder Semiconductors: Trapping, Scattering, and Effective Energetic Disorder. *The Journal of Physical Chemistry C*, *116*(37), 19748–19754.
- Li, Z. R. (2015). *Organic Light-Emitting Materials and Devices*. (Z. R. Li, Ed.) (2nd Editio). CRC Press. Retrieved from <https://www.crcpress.com/Organic-Light-Emitting-Materials-and-Devices/Li-Li-Meng/9781574445749>
- Liao, L. S., & Klubek, K. P. (2008). Power efficiency improvement in a tandem organic light-emitting diode. *Applied Physics Letters*, *92*(22), 223311.
- Liao, L. S., Klubek, K. P., & Tang, C. W. (2004). High-efficiency tandem organic light-emitting diodes. *Applied Physics Letters*, *84*, 167.
- Liu, B., Xu, M., Tao, H., Ying, L., Zou, J., Wu, H., & Peng, J. (2013). Highly efficient red phosphorescent organic light-emitting diodes based on solution processed emissive layer. *Journal of Luminescence*, *142*, 35–39.
- Liu, J., Wang, J., Huang, S., Shi, X., Wu, X., & He, G. (2013). A highly efficient, transparent and stable charge generation unit based on a p-doped monolayer. *Organic Electronics*, *14*(5), 1337–1343. Journal Article.
- Liu, J., Wu, X., Chen, S., Shi, X., Wang, J., Huang, S., ... He, G. (2014). Low-temperature MoO<sub>3</sub> film from a facile synthetic route for an efficient anode interfacial layer in organic optoelectronic devices. *J. Mater. Chem. C*, *2*(1), 158-

- Liu, X., Wang, C., Yi, S., & Gao, Y. (2014). Effect of oxygen plasma treatment on air exposed MoO<sub>x</sub> thin film. *Organic Electronics*, 15(5), 977–983.
- Liu, Z., Helander, M. G., Wang, Z., & Lu, Z. (2010). Efficient Single-Layer Organic Light-Emitting Diodes Based on C545T-Alq<sub>3</sub> System. *The Journal of Physical Chemistry C*, 114(27), 11931–11935.
- Loppacher, C. (2012). Electronic Properties of Metal/Organic Interfaces. In S. Sadewasser & T. Glatzel (Eds.), *Kelvin Probe Force Microscopy- Measuring and Compensating Electrostatic Forces* (1st ed., pp. 221–241). Berlin Heidelberg: Springer-Verlag Berlin Heidelberg.
- Ma, B., Lauterwasser, F., Deng, L., Zonte, C. S., Kim, B. J., Fréchet, J. M. J., ... Thompson, M. E. (2007). New Thermally Cross-Linkable Polymer and Its Application as a Hole-Transporting Layer for Solution Processed Multilayer Organic Light Emitting Diodes. *Chemistry of Materials*, 19(19), 4827–4832.
- Ma, W., Iyer, P. K., Gong, X., Liu, B., Moses, D., Bazan, G. C., & Heeger, A. J. (2005). Water/Methanol-Soluble Conjugated Copolymer as an Electron-Transport Layer in Polymer Light-Emitting Diodes. *Advanced Materials*, 17(3), 274–277.
- Mao, G., Wu, Z., He, Q., Jiao, B., Xu, G., Hou, X., ... Gong, Q. (2011). Considerable improvement in the stability of solution processed small molecule OLED by annealing. *Applied Surface Science*, 257(17), 7394–7398.
- Marinov, O., Deen, M. J., & Iniguez, B. (2005). Charge transport in organic and polymer thin-film transistors: recent issues. *IEE Proceedings - Circuits, Devices and Systems*, 152(3), 189.
- Martínez, N. F., & García, R. (2006). Measuring phase shifts and energy dissipation with amplitude modulation atomic force microscopy. *Nanotechnology*, 17(7), S167-72.
- Matsumoto, T., Nakada, T., Endo, J., Mori, K., Kawamura, N., Yokoi, A., & Kido, J. (2003). 27.5L: Late-News Paper: Multiphoton Organic EL device having Charge Generation Layer. *SID Symposium Digest of Technical Papers*, 34(1), 979.
- Matsumura, M., Akai, T., Saito, M., & Kimura, T. (1996). Height of the energy barrier existing between cathodes and hydroxyquinoline–aluminum complex of organic electroluminescence devices. *Journal of Applied Physics*, 79(1), 264.
- Matsushima, T., Kinoshita, Y., & Murata, H. (2007). Formation of Ohmic hole injection by inserting an ultrathin layer of molybdenum trioxide between indium tin oxide and organic hole-transporting layers. *Applied Physics Letters*, 91(25), 253504.
- Matsusue, N., Suzuki, Y., & Naito, H. (2005). Charge Carrier Transport in Neat Thin Films of Phosphorescent Iridium Complexes. *Japanese Journal of Applied Physics*, 44(6A), 3691–3694.

- Mayer, J., Giannuzzi, L. A., Kamino, T., & Michael, J. (2011). TEM Sample Preparation and FIB-Induced Damage. *MRS Bulletin*, 32(5), 400–407.
- Mayer, T., Hein, C., Mankel, E., Jaegermann, W., Müller, M. M., & Kleebe, H.-J. (2012). Fermi level positioning in organic semiconductor phase mixed composites: The internal interface charge transfer doping model. *Organic Electronics*, 13(8), 1356–1364.
- Meyer, J., Hamwi, S., Kröger, M., Kowalsky, W., Riedl, T., & Kahn, A. (2012). Transition metal oxides for organic electronics: energetics, device physics and applications. *Advanced Materials (Deerfield Beach, Fla.)*.
- Miller, A., & Abrahams, E. (1960). Impurity Conduction at Low Concentrations. *Physical Review*, 120(3), 745–755.
- Mohan, S. R., Singh, M. P., & Joshi, M. P. (2012). On the Use of Empirical Equation in Extracting Disorder Parameters in Inhomogeneous Organic Thin Films. *The Journal of Physical Chemistry C*, 116(3), 2555–2562.
- Moon, B. S., Lee, S.-H., Huh, Y. H., & Park, B. (2015). Hole-selective and impedance characteristics of an aqueous solution-processable MoO<sub>3</sub> layer for solution-processable organic semiconducting devices. *Journal of the Korean Physical Society*, 66(4), 635–645.
- Mott, N. ., & Davis, E. . (1979). *Electronic processes in non-crystalline materials* (second edi). Oxford: Clarendon Press, Oxford.
- Mott, N. F., & Gurney, R. W. (1964). *Electronic Processes in Ionic Crystals*. (N. F. Mott & R. W. Gurney, Eds.) (2nd ed.). Dover: Dover Publications Inc.
- Naka, S., Okada, H., Onnagawa, H., Yamaguchi, Y., & Tsutsui, T. (2000). Carrier transport properties of organic materials for EL device operation. *Synthetic Metals*, 111–112(null), 331–333.
- Noh, S., Suman, C. K., Hong, Y., & Lee, C. (2009). Carrier conduction mechanism for phosphorescent material doped organic semiconductor. *Journal of Applied Physics*, 105(3), 33709.
- Novikov, S. V., & Vannikov, A. V. (2009). Hopping Charge Transport in Disordered Organic Materials: Where Is the Disorder? *The Journal of Physical Chemistry C*, 113(6), 2532–2540.
- Nüesch, F., Kamarás, K., & Zuppiroli, L. (1998). Protonated metal-oxide electrodes for organic light emitting diodes. *Chemical Physics Letters*, 283(3–4), 194–200.
- O'Brien, D. F., Baldo, M. A., Thompson, M. E., & Forrest, S. R. (1999). Improved energy transfer in electrophosphorescent devices. *Applied Physics Letters*, 74(3), 442.
- Ouyang, S., Xie, Y., Wang, D., Zhu, D., Xu, X., Tan, T., & Fong, H. H. (2015). Aluminum-modified Molybdenum Trioxide for Electron Injection in Inverted Organic Light Emitting Diodes. *Journal of Display Technology*, 11(3), 273–277.

- Ow-Yang, C. W., Jia, J., Aytun, T., Zamboni, M., Turak, A., Saritas, K., & Shigesato, Y. (2014). Work function tuning of tin-doped indium oxide electrodes with solution-processed lithium fluoride. *Thin Solid Films*, 559, 58–63.
- Pai, D. M., Yanus, J. F., & Stolka, M. (1984). Trap-controlled hopping transport. *The Journal of Physical Chemistry*, 88(20), 4714–4717.
- Parker, I. D. (1994). Carrier tunneling and device characteristics in polymer light-emitting diodes. *Journal of Applied Physics*, 75(3), 1656.
- Png, R.-Q., Chia, P.-J., Tang, J.-C., Liu, B., Sivaramakrishnan, S., Zhou, M., ... Ho, P. K. H. (2010). High-performance polymer semiconducting heterostructure devices by nitrene-mediated photocrosslinking of alkyl side chains. *Nature Materials*, 9(2), 152–8.
- Pope, M., Kallmann, H. P., & Magnante, P. (1963). Electroluminescence in Organic Crystals. *The Journal of Chemical Physics*, 38(8), 2042.
- Poplavskyy, D., Su, W., & So, F. (2005). Bipolar charge transport, injection, and trapping studies in a model green-emitting polyfluorene copolymer. *Journal of Applied Physics*, 98(1), 14501.
- Preezant, Y., & Tessler, N. (2006). Carrier heating in disordered organic semiconductors. *Physical Review B*, 74(23), 235202.
- Raj Mohan, S., & Joshi, M. P. (2006). Field dependence of hole mobility in TPD-doped polystyrene. *Solid State Communications*, 139(4), 181–185.
- Raj Mohan, S., Joshi, M. P., & Singh, M. P. (2008). Charge transport in disordered organic solids: A Monte Carlo simulation study on the effects of film morphology. *Organic Electronics*, 9(3), 355–368.
- Reineke, S., & Baldo, M. A. (2012). Recent progress in the understanding of exciton dynamics within phosphorescent OLEDs. *Physica Status Solidi (a)*, 209(12), 2341–2353.
- Reineke, S., Lindner, F., Schwartz, G., Seidler, N., Walzer, K., Lüssem, B., & Leo, K. (2009). White organic light-emitting diodes with fluorescent tube efficiency. *Nature*, 459(7244), 234–8.
- Roichman, Y., Preezant, Y., & Tessler, N. (2004). Analysis and modeling of organic devices. *Physica Status Solidi (a)*, 201(6), 1246–1262.
- Santato, C., & Rosei, F. (2010). Organic/metal interfaces: seeing both sides. *Nature Chemistry*, 2(5), 344–5.
- Scheinert, S., & Paasch, G. (2014). Influence of the carrier density in disordered organics with Gaussian density of states on organic field-effect transistors. *Journal of Applied Physics*, 115(4), 44507.
- Schmechel, R., & von Seggern, H. (2004). Electronic traps in organic transport layers. *Physica Status Solidi (a)*, 201(6), 1215–1235.

- Schols, S. (2011). *Device Architecture and Materials for Organic Light-Emitting Devices: Targeting High Current Densities and Control of the Triplet Concentration*. (S. Schols, Ed.) (1st ed.). Netherland: Springer Dordrecht Heifrlberg London New York.
- Sharma, A., Haldi, A., Hotchkiss, P. J., Marder, S. R., & Kippelen, B. (2009). Effect of phosphonic acid surface modifiers on the work function of indium tin oxide and on the charge injection barrier into organic single-layer diodes. *Journal of Applied Physics*, *105*(7), 74511.
- Shiang, J. J., & Duggal, A. R. (2007). Organic Electroluminescence. In C. Ronda (Ed.), *Luminescence: From Theory to Applications* (pp. 191–217). Weinheim, Germany: Wiley-VCH Verlag GmbH & Co. KGaA.
- Shinar, J., & Savvateev, V. (2004). *Organic Light-Emitting Devices*. (J. Shinar, Ed.). New York, NY: Springer New York.
- Siboni, H. Z., & Aziz, H. (2012). Causes of driving voltage rise in phosphorescent organic light emitting devices during prolonged electrical driving. *Applied Physics Letters*, *101*(17), 173502.
- Smith, J., Zhang, W., Sougrat, R., Zhao, K., Li, R., Cha, D., ... Anthopoulos, T. D. (2012). Solution-processed small molecule-polymer blend organic thin-film transistors with hole mobility greater than 5 cm<sup>2</sup>/Vs. *Advanced Materials (Deerfield Beach, Fla.)*, *24*(18), 2441–6.
- So, F., Krummacher, B., Mathai, M. K., Poplavskyy, D., Choulis, S. A., & Choong, V.-E. (2007). Recent progress in solution processable organic light emitting devices. *Journal of Applied Physics*, *102*(9), 91101.
- Song, W., & Lee, J. Y. (2015). Light emission mechanism of mixed host organic light-emitting diodes. *Applied Physics Letters*, *106*(12), 123306.
- Suh, M. C., Chin, B. D., Kim, M.-H., Kang, T. M., & Lee, S. T. (2003). Enhanced Luminance of Blue Light-Emitting Polymers by Blending with Hole-Transporting Materials. *Advanced Materials*, *15*(15), 1254–1258.
- Sun, H., Chen, Y., Zhu, L., Guo, Q., Yang, D., Chen, J., & Ma, D. (2015). Realization of Optimal Interconnector for Tandem Organic Light-Emitting Diodes with Record Efficiency. *Advanced Electronic Materials*, *1*(11), n/a-n/a.
- Sun, H., Guo, Q., Yang, D., Chen, Y., Chen, J., & Ma, D. (2015). High Efficiency Tandem Organic Light Emitting Diode Using an Organic Heterojunction as the Charge Generation Layer: An Investigation into the Charge Generation Model and Device Performance. *ACS Photonics*, *2*(2), 271–279.
- Suo, F., Yu, J., Deng, J., Lou, S., & Jiang, Y. (2008). Organic electroluminescent characteristics of PS:NPB composite hole transporting layer. *Frontiers of Optoelectronics in China*, *1*(3–4), 323–328.
- Sze, S. M. (2006). *Physics of Semiconductor Devices*. (S. M. Sze & K. K. Ng, Eds.) (2nd Editio). New Jersey: Wiley & Sons, New York.

- Tang, C. W., & VanSlyke, S. A. (1987). Organic electroluminescent diodes. *Applied Physics Letters*, 51(12), 913.
- Tian, B., Williams, G., Ban, D., & Aziz, H. (2011). Transparent organic light-emitting devices using a MoO<sub>3</sub>/Ag/MoO<sub>3</sub> cathode. *Journal of Applied Physics*, 110(10), 104507.
- Tong, K. L., Tsang, S. W., Tsung, K. K., Tse, S. C., & So, S. K. (2007). Hole transport in molecularly doped naphthyl diamine. *Journal of Applied Physics*, 102(9), 93705.
- Topham, B. J., Kumar, M., & Soos, Z. G. (2011). Profiles of Work Function Shifts and Collective Charge Transfer in Submonolayer Metal-Organic Films. *Advanced Functional Materials*, 21(10), 1931–1940.
- Tsung, K. K., & So, S. K. (2008). Carrier trapping and scattering in amorphous organic hole transporter. *Applied Physics Letters*, 92(10), 103315.
- Tsutsui, T., & Terai, M. (2004). Electric field-assisted bipolar charge spouting in organic thin-film diodes. *Applied Physics Letters*, 84(3), 440.
- Valeur, B., & Nuno, B.-S. M. (2012). *Molecular Fluorescence: Principles and Applications*. (B. Valeur & B.-S. M. Nuno, Eds.) (2nd ed.). Weinheim, Germany: John Wiley & Sons.
- Van der Auweraer, M., De Schryver, F. C., Borsenberger, P. M., & Bassler, H. (1994). Disorder in Charge Transport in doped polymers. *Advanced Materials*, 6(3), 199–213.
- Vannikov, A. V., Kryukov, A. Y., Tyurin, A. G., & Zhuravleva, T. S. (1989). Influence of the medium polarity on electron transport in polymer systems. *Physica Status Solidi (a)*, 115(1), K47–K51.
- Vasilopoulou, M., Georgiadou, D. G., Palilis, L. C., Argitis, P., Kennou, S., Sygellou, L., ... Davazoglou, D. (2012). Reduced transition metal oxides as electron injection layers in hybrid-PLEDs. *Microelectronic Engineering*, 90, 59–61.
- Vasilopoulou, M., Palilis, L. C., Georgiadou, D. G., Argitis, P., Kennou, S., Sygellou, L., ... Davazoglou, D. (2011). Reduced molybdenum oxide as an efficient electron injection layer in polymer light-emitting diodes. *Applied Physics Letters*, 98(12), 123301.
- Vincett, P. S., Barlow, W. A., Hann, R. A., & Roberts, G. G. (1982). Electrical conduction and low voltage blue electroluminescence in vacuum-deposited organic films. *Thin Solid Films*, 94(2), 171–183.
- Von Malm, N., Steiger, J., Schmechel, R., & von Seggern, H. (2001). Trap engineering in organic hole transport materials. *Journal of Applied Physics*, 89(10), 5559.
- Vosgueritchian, M., Lipomi, D. J., & Bao, Z. (2012). Highly Conductive and Transparent PEDOT : PSS Films with a Fluorosurfactant for Stretchable and Flexible Transparent Electrodes. *Advanced Functional Materials*, 22, 421–428.

- Wang, C., Irfan, I., & Gao, Y. (2014). Protection of MoO<sub>3</sub> high work function by organic thin film. *Applied Physics Letters*, 105(18), 181602.
- Wang, D., Wu, Y., Bi, R., Zhang, H., & Zhao, D. (2015). Solution-processed sodium hydroxide as the electron injection layer in inverted bottom-emission organic light-emitting diodes. *J. Mater. Chem. C*, 3(16), 3922–3927.
- Wang, H., & Yan, D. (2010). Organic heterostructures in organic field-effect transistors. *NPG Asia Materials*, 2(2), 69–78.
- Wang, S., Wang, X., Yao, B., Zhang, B., Ding, J., Xie, Z., & Wang, L. (2015). Solution-Processed Phosphorescent Organic Light-Emitting Diodes with Ultralow Driving Voltage and Very High Power Efficiency. *Scientific Reports*, 5(July), 12487.
- Weber, R. (1995). Effect of Local Structure on the UV-Visible Absorption Edges of Molybdenum Oxide Clusters and Supported Molybdenum Oxides. *Journal of Catalysis*, 151(2), 470–474.
- Whiffen, V. M. L., & Smith, K. J. (2010). Hydrodeoxygenation of 4-Methylphenol over Unsupported MoP, MoS<sub>2</sub>, and MoO<sub>x</sub> Catalysts †. *Energy & Fuels*, 24(9), 4728–4737.
- Whitcher, T. J., Woon, K. L., Wong, W. S., Chanlek, N., Nakajima, H., Saisopa, T., & Songsiriritthigul, P. (2016). Interfacial behavior of resistive switching in ITO–PVK–Al WORM memory devices. *Journal of Physics D: Applied Physics*, 49(7), 75104.
- Wolf, U., Bäsler, H., Borsenberger, P. M., & Gruenbaum, W. T. (1997). Hole trapping in molecularly doped polymers. *Chemical Physics*, 222(2–3), 259–267.
- Woon, K. L., Hasan, Z. A., Ong, B. K., Ariffin, A., Griniene, R., Grigalevicius, S., & Chen, S.-A. (2015). Triplet states and energy back transfer of carbazole derivatives. *RSC Adv.*, 5(74), 59960–59969.
- Wu, C. C., Wu, C. I., Sturm, J. C., & Kahn, A. (1997). Surface modification of indium tin oxide by plasma treatment: An effective method to improve the efficiency, brightness, and reliability of organic light emitting devices. *Applied Physics Letters*, 70(11), 1348.
- Xiao, L., Chen, Z., Qu, B., Luo, J., Kong, S., Gong, Q., & Kido, J. (2011). Recent progresses on materials for electrophosphorescent organic light-emitting devices. *Advanced Materials (Deerfield Beach, Fla.)*, 23(8), 926–52.
- Xu, W., Zhang, X., Hu, Q., Zhao, L., Teng, X., Lai, W.-Y., ... Bradley, D. D. C. (2014). Fluorene-based cathode interlayer polymers for high performance solution processed organic optoelectronic devices. *Organic Electronics*, 15(6), 1244–1253.
- Yamada, T., Sato, T., Tanaka, K., & Kaji, H. (2010). Percolation paths for charge transports in N,N'-diphenyl-N,N'-di(m-tolyl)benzidine (TPD). *Organic Electronics*, 11(2), 255–265.

- Yamaoka, R., Sasaki, T., Kataishi, R., Miyairi, N., Kusunoki, K., Kaneyasu, M., ... Mori, H. (2015). High-resolution OLED display with remarkably low power consumption using blue/yellow tandem structure and RGBY subpixels. *Journal of the Society for Information Display*, 23(10), 451–456.
- Yan, L., & Gao, Y. (2002). Interfaces in organic semiconductor devices. *Thin Solid Films*, 417(1–2), 101–106.
- Yang, X., Müller, D. C., Neher, D., & Meerholz, K. (2006). Highly Efficient Polymeric Electrophosphorescent Diodes. *Advanced Materials*, 18(7), 948–954.
- Ye, T., Shao, S., Chen, J., Wang, L., & Ma, D. (2011). Efficient phosphorescent polymer yellow-light-emitting diodes based on solution-processed small molecular electron transporting layer. *ACS Applied Materials & Interfaces*, 3(2), 410–6.
- Yeoh, K. H., Ng, C. Y. Bin, Chua, C. L., Azrina Talik, N., & Woon, K. L. (2013). High power efficiency solution-processed double-layer blue phosphorescent organic light-emitting diode by controlling charge transport at the emissive layer and heterojunction. *Physica Status Solidi (RRL) - Rapid Research Letters*, 7(6), 421–424.
- Yersin, H. (2004). Triplet Emitters for OLED Applications. Mechanisms of Exciton Trapping and Control of Emission Properties. In *Transition Metal and Rare Earth Compounds* (Vol. 241, pp. 1–26). Berlin, Heidelberg: Springer Berlin Heidelberg.
- Yimer, Y. Y., Bobbert, P. A., & Coehoorn, R. (2009). Charge transport in disordered organic host–guest systems: Effects of carrier density and electric field. *Synthetic Metals*, 159(21–22), 2399–2401.
- Yook, K. S., & Lee, J. Y. (2013). Solution processed phosphorescent white organic light emitting diodes using a small molecule host material. *Journal of Luminescence*, 143, 432–435.
- Yook, K. S., & Lee, J. Y. (2014). Small molecule host materials for solution processed phosphorescent organic light-emitting diodes. *Advanced Materials (Deerfield Beach, Fla.)*, 26(25), 4218–33.
- You, J.-D., Tseng, S.-R., Meng, H.-F., Yen, F.-W., Lin, I.-F., & Horng, S.-F. (2009). All-solution-processed blue small molecular organic light-emitting diodes with multilayer device structure. *Organic Electronics*, 10(8), 1610–1614.
- Zhang, H., Dai, Y., & Ma, D. (2007). High efficiency tandem organic light-emitting devices with Al / WO<sub>3</sub> / Au. *Applied Physics Letters*, 91, 123504.
- Zhang, L., Cai, C., Li, K. F., Tam, H. L., Chan, K. L., & Cheah, K. W. (2015). Efficient Organic Light-Emitting Diode through Triplet Exciton Reharvesting by Employing Blended Electron Donor and Acceptor as the Emissive Layer. *ACS Applied Materials & Interfaces*, 7(45), 24983–6.
- Zhang, M., Ding, H., Tang, C. W., & Gao, Y. (2011). Strong interface p-doping and band bending in C60 on MoO<sub>x</sub>. *Organic Electronics*, 12(9), 1588–1593.

- Zhang, W., Zhao, B., He, Z., Zhao, X., Wang, H., Yang, S., ... Cao, Y. (2013). High-efficiency ITO-free polymer solar cells using highly conductive PEDOT:PSS/surfactant bilayer transparent anodes. *Energy & Environmental Science*, 6(6), 1956.
- Zhang, X., Guo, X., Chen, Y., Wang, J., Lei, Z., Lai, W., ... Huang, W. (2015). Highly efficient red phosphorescent organic light-emitting devices based on solution-processed small molecular mixed-host. *Journal of Luminescence*, 161, 300–305.
- Zhang, X., Wu, Z., Jiao, B., Wang, D., Wang, D., Hou, X., & Huang, W. (2012). Solution-processed white organic light-emitting diodes with mixed-host structures. *Journal of Luminescence*, 132(3), 697–701.
- Zhong, C., Duan, C., Huang, F., Wu, H., & Cao, Y. (2011). Materials and Devices toward Fully Solution Processable Organic Light-Emitting Diodes †. *Chemistry of Materials*, 23(3), 326–340.
- Zhong, C., Liu, S., Huang, F., Wu, H., & Cao, Y. (2011). Highly Efficient Electron Injection from Indium Tin Oxide/Cross-Linkable Amino-Functionalized Polyfluorene Interface in Inverted Organic Light Emitting Devices. *Chemistry of Materials*, 23(21), 4870–4876.
- Zuniga, C. A. (2011). *Solution-Processable Charge Transport Layers for Phosphorescent OLEDs* (Doctoral dissertation). Retrieved from <http://hdl.handle.net/1853/43671>

## LIST OF PUBLICATIONS AND PAPERS PRESENTED

### Journal Publications:

- (i) **N A Talik**, K L Woon and B K Yap, Effect of mixed hole transporting host on the mobility, Gaussian density of states and efficiencies of a heterojunction phosphorescent organic light emitting diode. *J. Phys. D: Appl. Phys.*, vol. 49 (2016) p. 155103.
- (ii) **N.A. Talik**, K.H. Yeoh, C.Y.B. Ng, C.Y. Tan, B.K. Yap Investigations of solution-processed charge generation unit with low concentration of small molecule doped in p-type / HAT-CN<sub>6</sub> for Tandem OLED, *J. Lumin.*, Vol. 169, Part A, (2016) pg. 61-64.
- (iii) **N.A. Talik**, K.H. Yeoh, C.Y.B Ng, B.K. Yap, K.L. Woon Efficient green phosphorescent tandem organic light emitting diodes with solution processible mixed hosts charge generating layer, *J.Lumin.*, Vol.154, (2014) pg. 345-349.
- (iv) **N.A Talik**, K.L Woon, B.K Yap, W. S. Wong, T.J.Whitcher, N. Chanlek, H. Nakajima, T. Saisopa, and P. Songsiriritthigul, Solution Processable Sodium Molybdate as cathode interlayer For Super-Yellow Organic Light Emitting Diode (**Accepted in J. Phys. D: Appl Phys**)

The following papers finished during this period are either overlap or the subjects are outside the scope of this thesis.

- (i) K H Yeoh, **N A Talik**, T J Whitcher, C Y B Ng, K L Woon, The efficiency enhancement of single-layer solution-processed blue phosphorescent organic light emitting diodes by hole injection layer modification, *Journal Physics D: Applied Physics*, 47 (2014) 205103.

- (ii) Thomas J Whitcher, **Noor Azrina Talik**, Kailin Woon, Narong Chanlek et al. Determination of energy levels at the interface between O<sub>2</sub> plasma treated ITO/P3HT: PCBM and PEDOT : PSS/P3HT : PCBM using angular-resolved x-ray and ultraviolet photoelectron spectroscopy, *Journal Physics D: Applied Physics*, 47 (2014) 055109.
- (iii) T J Whitcher, Wong Wah Seng, **Noor Azrina Talik**, Kailin Woon, Narong Chanlek et al Electrostatic model of the energy-bending within organic semiconductors: Experiment and **simulation Journal of Physics Condensed Matter 28(36):365002 (2016) (Q1)**
- (iv) T J Whitcher, Wong Wah Seng, **Noor Azrina Talik**, Kailin Woon, Narong Chanlek et al Investigation into the Gaussian density of states widths of organic semiconductors, **Journal of Physics D Applied Physics 49(32):325106 (2016)**
- (v) Calvin Yi Bin Ng, Keat Hoe Yeoh, Thomas J. Whitcher, **Noor Azrina Talik**, Kai Lin Woon, Thanit Saisopa, Hideki Nakajima, Ratchadaporn Supruangnet and Prayoon Songsiriritthigul, High efficiency solution processed fluorescent yellow organic light-emitting diode through fluorinated alcohol treatment at the emissive layer/cathode interface, *Journal Physics D: Applied Physics*, 47 (2014) 015106.
- (vi) Thomas J Whitcher, Keat Hoe Yeoh, Yi Bin Calvin Ng, **Noor Azrina Talik** et al, Enhancement of the work function of indium tin oxide by surface modification using caesium fluoride, *Journal Physics D: Applied Physics*, 46 (2013).

#### **Conference attended**

- (i) 3rd International Conference on the Advancement of Materials and Nanotechnology 2013, Penang.

## APPENDIX A

The thickness measurement for MoO<sub>4</sub> film was carried out using Transmission Electron Microscopy (TEM). Figure A1 shows TEM images for all thickness measurement for 10K, 8K, 5K and 2K rpm spin coating speed.

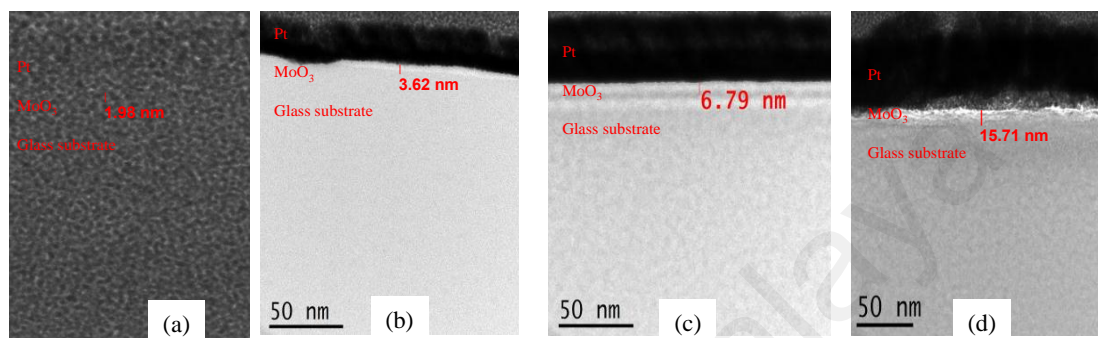


**Figure A1** (a) 10K rpm with thickness of 1.98 nm (b) 8K rpm with thickness of 3.62 nm (c) 5K rpm with thickness of 6.79 nm and (d) 2k rpm thickness with 15.71 nm.

## APPENDIX B

In order to confirm the  $\text{MoO}_4$  film is indeed covering the SYPPV without de-wetting, high optical microscopy and photoluminescence measurement are used to observe the thin film layers. Figure B shows the optical figures of the film after spin coating  $\text{MoO}_4$  layer on top of SYPPV. A smooth surface without any aggregation was obtained which suggests there is no wetting problem. There is also no damage observed of SYPPV layer after spin coat  $\text{MoO}_4$  due to the different surface properties. This is attributed to the different polarity of solvents used for SYPPV (dissolved in Toluene (non-polar)) and  $\text{MoO}_4$  (dissolved in 90 % of di-onized water (polar)).

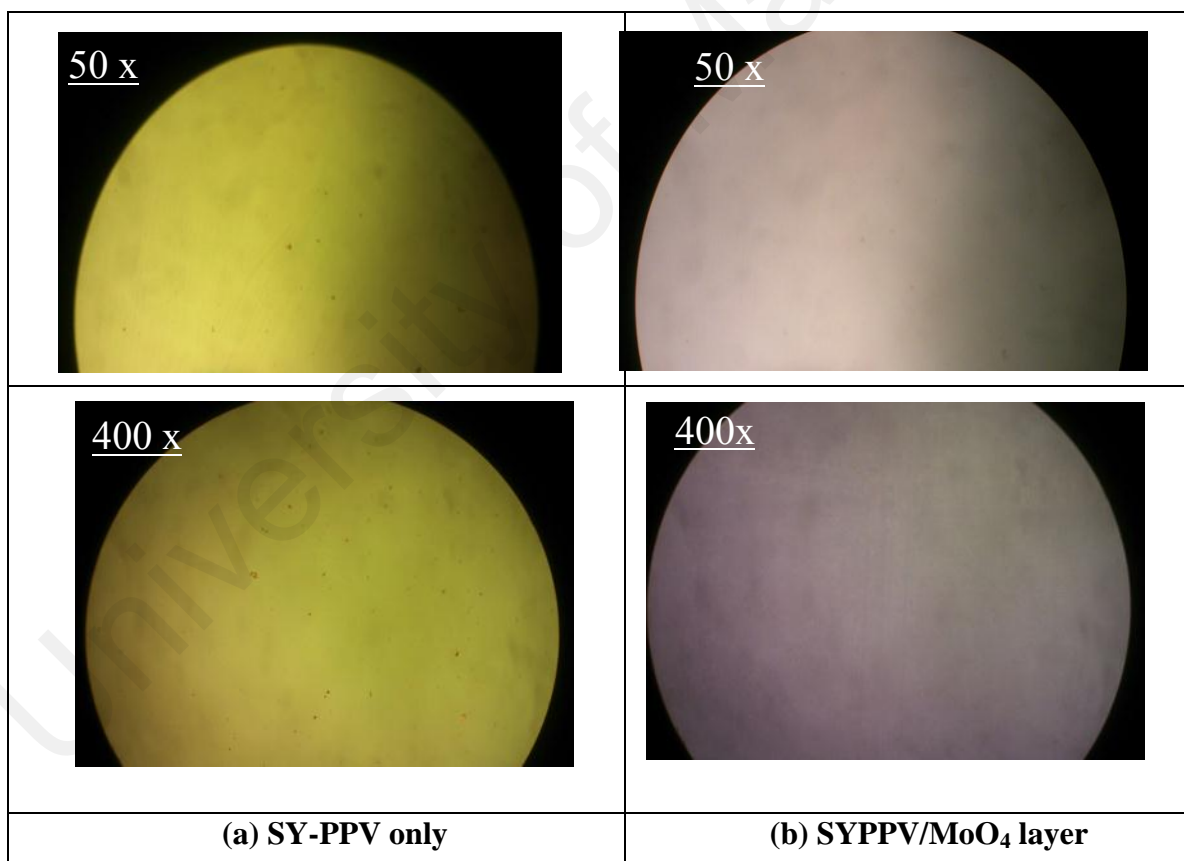
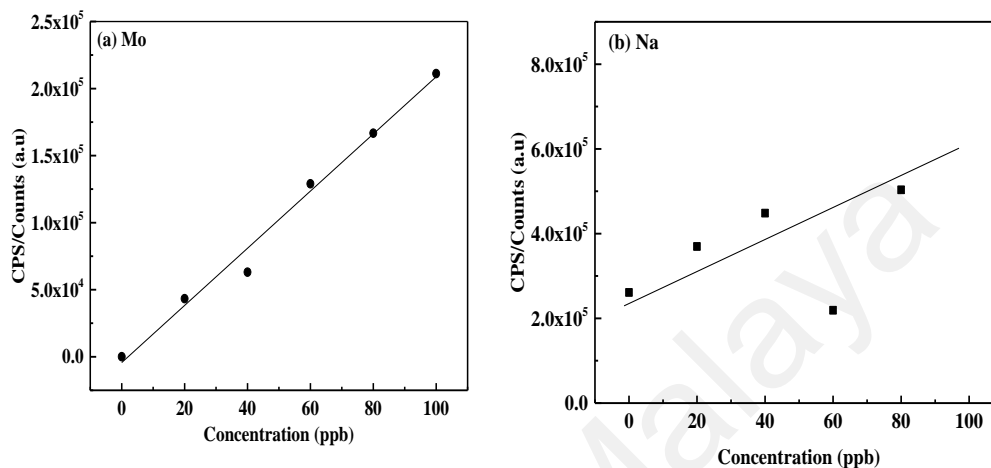


**Figure B** Picture of SYPPV and SYPPV/  $\text{MoO}_4$  under high magnification microscope under reflection mode. (a) SYPPV layer and (b) SYPPV/  $\text{MoO}_4$  layers at 50x magnification and 400x magnification. The change of color with and without  $\text{MoO}_4$  is probably due to reflection of light as a result of presence of high refractive index  $\text{MoO}_4$  thin film.

## APPENDIX C

ICP/MS elemental result shows that there is no sodium (Na) detected, while the solution shows very high concentration of Molybdenum (Mo).



Counts/Elements	Mo / 95	Na / 23
	3977.0	-100.60

(c)

**Figure C** Calibration curves of (a) Mo (Mass : 95) and (b) Na (Mass: 23). The concentration of elements is calculated from the slope and intercept of the calibration curve. (c) Table shows intensity for Mo and Na elements. Negative value of Na implies that Na cannot be detected (less than detection limits).

## APPENDIX D

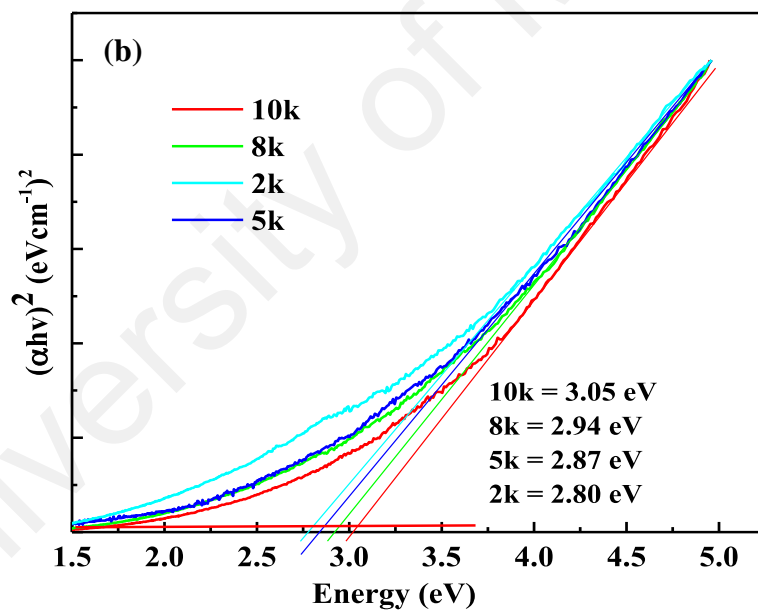
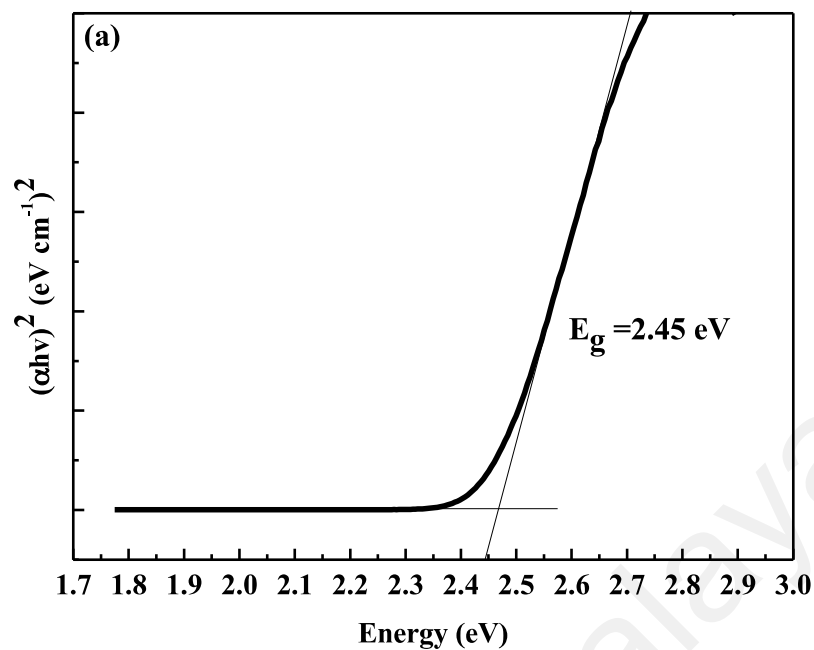


**Figure D** (a) Direct bandgap from UV-Vis shows that SYPPV film has  $E_g = 2.45$  eV and (b) the band gap for  $\text{MoO}_4$  film with different thickness.

## APPENDIX E

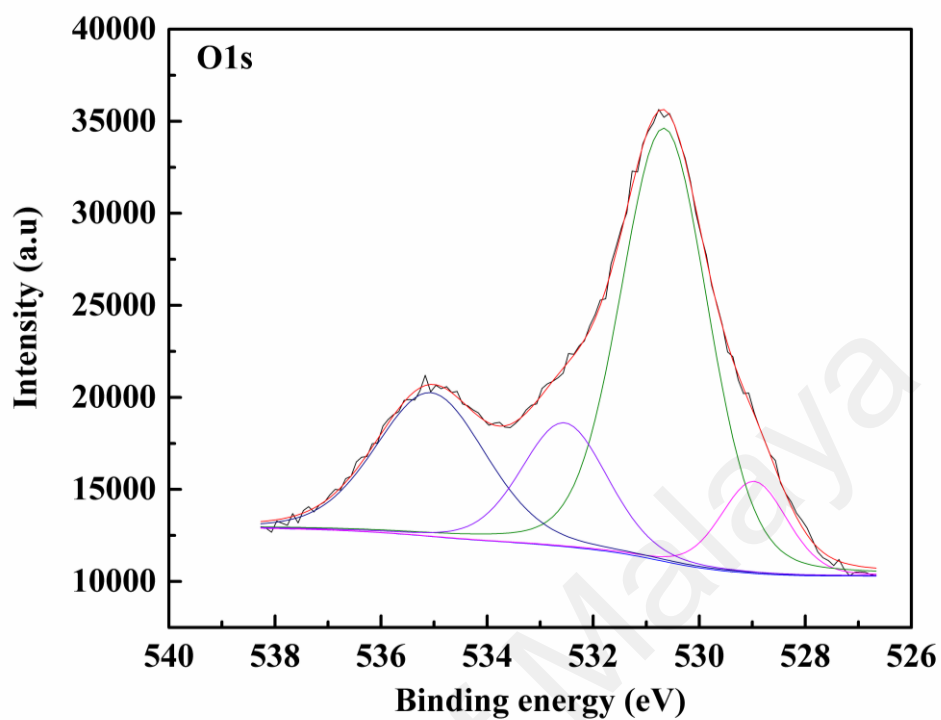


**Figure E** O1s peak from MoO<sub>4</sub> film. The peak at 528.9 eV to 530.6 eV can be assigned to Mo-O bond and 535.1 eV represent H<sub>2</sub>O peak at the sample surface. The peak at 532.5 eV can be assigned to oxygen from glass surface.